STOCHASTIC SIMULATION OF MAIN SHOCK-AFTERSHOCK SEQUENCES AND THEIR USE IN DAMAGE-BASED SEISMIC DESIGN OF REINFORCED CONCRETE STRUCTURES

by

Nithin VL

DEPARTMENT OF CIVIL ENGINEERING

INDIAN INSTITUTE OF TECHNOLOGY GUWAHATI

December, 2019

STOCHASTIC SIMULATION OF MAIN SHOCK-AFTERSHOCK SEQUENCES AND THEIR USE IN DAMAGE-BASED SEISMIC DESIGN OF REINFORCED CONCRETE STRUCTURES

A Thesis Submitted
in Partial Fulfillment of the Requirements
for the Degree of
DOCTOR OF PHILOSOPHY

by

Nithin VL

DEPARTMENT OF CIVIL ENGINEERING

INDIAN INSTITUTE OF TECHNOLOGY GUWAHATI

December, 2019

CERTIFICATE

It is certified that the work contained in the thesis entitled *”Stochastic Simulation of Main shock-Aftershock Sequences and their Use in Damage-Based Seismic Design of Reinforced Concrete Structures”* by *Nithin V.L.* (Roll No.: 136104011) has been carried out under our supervision and that this work has not been submitted elsewhere for a degree.

Date:

(SANDIP DAS)
Assistant Professor
Department of Civil Engineering
Indian Institute of Technology Guwahati
Guwahati

(HEMANT B. KAUSHIK)
Professor
Department of Civil Engineering
Indian Institute of Technology Guwahati
Guwahati

ACKNOWLEDGEMENTS

I express my deep and sincere gratitude to Dr. Sandip Das and Dr. Hemant B. Kaushik who inspired my academic and personal lives with their guidance, encouragement, gracious support and care throughout my work. Their valuable suggestions, effusive cooperation, coordination and encouraging interactions were a great driving force for me to carry out this research work. I would also like to extend my gratitude to all my teachers for broadening and enriching my knowledge.

I am also thankful to all the technical and non-technical staff at Structural Engineering Laboratory, IIT Guwahati for their unconditional and most-willing support during the experiments.

Financial assistance provided by the Ministry of Human Resource Development, Government of India, is greatly acknowledged. I would also like to acknowledge the financial support provided by the Department of Science and Technology, India, under the grant number DST/TSG/STS/2012/55-G.

I am grateful to all my friends, lab mates and well-wishers who made my stay at IIT Guwahati a memorable and pleasant experience.

I am thankful to my parents for their unwavering support and encouragement. Last but not the least, I thank my wife and my son for the patience with which they bore my absence when they needed me the most.

Nithin V.L.

Dedicated to my Wife and Son

Contents

List of Tables

List of Figures

List of Abbreviations and Acronyms

Aft1 = First aftershock ground motion in a MAS sample
Aft2 = Second aftershock ground motion in a MAS sample
Aft3 = Third aftershock ground motion in a MAS sample
CFRRC - Coir fibre and rope reinforced concrete
CoV - Coefficient of variation
EPSDF - Evolutionary power spectral density function
GMPE - Ground motion prediction equation
L-P - Littlewood-Paley
LVDT - Linear varying displacement transducer
MAS - Main shock aftershock sequence
MCE - Maximum credible earthquake
NTHA - Nonlinear time-history analysis
PSV - Pseudo spectral velocity
PSA - Pseudo spectral acceleration
PGA - Peak ground displacement
PGV - Peak ground velocity
PGD - Peak ground displacement
PSDF - Power spectral density function
RC - Reinforced concrete
RMS - Root mean square
RMSD - temporal RMS of displacement
RMSV - temporal RMS of velocity
RMSA - temporal RMS of acceleration
SMD - Strong motion duration
SDOF - Single degree of freedom
SA - Spectral acceleration
THA - Time-history analysis

List of Symbols

$\langle \cdot, \cdot \rangle$ = Inner product

$(\cdot)_{\mathrm{N}}$ = Normalized value of $(\cdot)$ such that the maximum ordinate is unity

$|\cdot|$ = Modulus

a = Scale parameter which controls the frequency content of the wavelet basis

a_j = Scale parameter which controls the frequency content of the wavelet basis corresponding to jth level

$a_{1,j}(b)$, $a_{2,j}(b)$, $a_{3,j}(b)$, $a_{4,j}(b)$ = Regression coefficients of unconditional scaling model for energy arrivals

$a_{1,j}(t)$, $a_{2,j}(t)$, $a_{3,j}(t)$, $a_{4,j}(t)$, $a_{5,j}(t)$ and $a_{6,j}(t)$ = Regression coefficients of conditional scaling model for energy arrivals

$A(t,\omega)$ = Frequency-dependent deterministic slow-varying amplitude modulation or envelope

$A_j(t)$ = Deterministic amplitude modulation specific to the jth level in time domain

b = Shift parameter which localizes the wavelet basis at $t = b$

b_{min} = Minimum value of b of estimated energy arrival curve (Here, $b_{min} = -12$ s)

b_{max} = Maximum value of b of estimated energy arrival curve (Here, $b_{max} = 100$ s)

$\overline{b_i}$ = Transformed b in stretched/shrinked energy arrival curve of ith sample

$b_1(T)$, $b_2(T)$, $b_3(T)$, $b_4(T)$ = Regression coefficients of unconditional PSV scaling model

$b_{1,j}(t)$, $b_{2,j}(t)$, $b_{3,j}(t)$, $b_{4,j}(t)$ & $b_{5,j}(t)$ = Regression coefficients of unconditional scaling model for energy arrivals

$c_1(T)$, $c_1(T)$, $c_1(T)$ & $c_1(T)$ = Regression coefficients of conditional PSV scaling model

$c1$, $c2$ and $c3$ = Regression coefficients of SMD scaling model

d_b = Diameter of the longitudinal reinforcement

D_i = Size of displacement cycle

DI = Park & Ang Damage Index

DI_i = Damage index of ith hinge

$\overline{\mathrm{d}Z}(\omega)$ = Stationary orthogonal incremental process

E_H = Hysteretic energy dissipated at the plastic hinge

E_{H_i} = Cumulative hysteresis energy upto ith event

E_i = Hysteresis energy dissipated at ith hinge

$E_j(b)$ = Energy arrival curve of wavelet coefficients

$\bar{E}_j(b)$ = Smoothed energy arrival curve of wavelet coefficients

$E'_j(b)$ = Energy arrival curve of wavelet coefficients

$\bar{E}'_j(b)$ = Smoothed energy arrival curve of wavelet coefficients

$\hat{E}_j(b)$ = Estimated (smooth) energy arrival using Eq. (3.20) via estimated smoothened regression coefficients

$\hat{E}_{i,j}(\overline{b_i})$ = ith sample of energy arrival of level j modified by GMPE compatibility algorithm

$\hat{E}_{i,j}(b)$ = ith sample for the level-wise energy arrival for a given seismic scenario

$E_j(t)$ = Energy arrival curve of decomposed time-history

$\bar{E}_j(t)$ = Smoothed energy arrival curve of decomposed time-history

$\bar{E}_{\mathrm{Aft},j}(t)$ = Smoothed instantaneous cumulative energy arrival of aftershocks

$\bar{E}_{\mathrm{Main},j}(t)$ = Smoothed energy arrival of decomposed motions of main shock

$\mathrm{E}[\cdot]$ = Statistical expectation

$\hat{E}_{\mathrm{Aft},j}(t)$ = Estimated (median) energy arrival curve for aftershock

$\hat{E}_{\mathrm{Aft},p,j}(t)$ = Estimate energy curve of aftershock for pth sample and jth level

$F(t), \mathbf{F}(t)$ = Ground motion process

$f(t)$ = Ground motion time-history

f = Frequency of structure at the end of an event

f_0 = Frequency of undamaged structure

$f_j(t)$ = Decomposed time-history corresponding to jth level

f_y = Yield strength of reinforcement

$F(\omega)$ = Fourier transform of recorded signal $f(t)$

F_y = Yield strength of structure

g_1, g_2, g_3 = Regression coefficients of empirical scaling model for frequency of damaged structure

h = Focal depth
h_{Main} = Focal depth of main shock
h_{Aft} = Focal depth of aftershock
h_{AS1} = Focal depth of largest aftershock (magnitude-wise)
h_{AS2} = Focal depth of second largest aftershock (magnitude-wise)
h_{AS3} = Focal depth of third largest aftershock (magnitude-wise)
h_{AS4} = Focal depth of fourth largest aftershock (magnitude-wise)
k_i = Realization of a standard normal variate for ith sample
k_p = Realization of a standard normal variate for pth sample
I_i = Indicator parameter which is 1 if up to ith event is considered and is 0 otherwise
l_p = Plastic-hinge length
L = Shear-span of the member
m = Maximum number of events present in any sequence
M = Local Magnitude
M_{Main} = Magnitude of main shock
M_{Aft} = Magnitude of aftershock
M_{AS1} = Magnitude of largest aftershock
M_{AS2} = Magnitude of second largest aftershock
M_{AS3} = Magnitude of third largest aftershock
M_{AS4} = Magnitude of fourth largest aftershock
n = Total number of hinges in the frame
ODI = Overall damage index
$PSV(T)$ = PSV spectral ordinate corresponding to period T
R = Epicentral distance
$\Re$ = Real number
R^2 = Coefficient of determination
$R_{Z,j}(\tau)$ = Autocorrelation function of narrow bandlimited Gaussian whitenoise samples corresponding to jth level
S = Indicator parameter for local site conditions
S_0 = Magnitude of stationary PSDF
SMD = Strong Motion Duration
t = Time-instant
T = Time period
T_j = Pseudo period corresponding to jth level
T_j^{l} = Lower limit of time period for jth level
T_j^{u} = Upper limit of time period for jth level

$V_j(b)$ = Deterministic amplitude modulation corresponding to jth level in wavelet domain

$V'_j(b)$ = Frequency-dependent modulation for the wavelet coefficient process

$V_j(t)$ = Deterministic frequency-dependent slow varying modulation in decomposed time-history domain

$\bar{V}_j(t)$ = Normalized frequency-dependent slow varying modulation in decomposed time-history domain

$W_\psi f(a,b)$ = Wavelet coefficient

$W_\psi f(a_j,b)$ = Wavelet coefficient corresponding to jth level

$x_i(t)$ = ith simulated ground motion sample of a process

x_u = Failure displacement of the structure when subjected to monotonic loading

$X(t)$ = Simulated ensemble

$y_{j,i}(t)$ = A sample of narrow bandlimited motion with frequency range corresponding to the level j

$z_j(b)$ = Band-limited white-noise signal corresponding to jth level in wavelet domain

$z_j(t)$ = Band-limited white-noise signal corresponding to jth level in time domain

$z_{j,i}(t)$ = A sample of narrow bandlimited whitenoise with frequency range corresponding to the level j

z = Standard normal variate

$\alpha_j(t)$ = Ratio of instantaneous energy arrival of aftershock to that of main shock

$\alpha_{1,j}$ = Level-wise factor used in GMPE-compatibility algorithm for the matching of median PSV of simulated ensemble with that of target GMPE

$\alpha_{2,j}$ = Level-wise factor used in GMPE-compatibility algorithm for the matching of standard deviation of PSV of simulated ensemble with that of target GMPE

$\hat{\alpha}_j(t)$ = Estimated ratio of energy arrival of aftershock to that of main shock

β_d = Degradation parameter which accounts for the contribution of hysteresis energy to damage index

β_i = Sample-wise stretched/shrunk maximum value of b for all levels

$\beta(T)$ = Ratio of PSV of aftershock to that of main shock

$\widehat{\beta}(T)$ = Estimated ratio of PSV of aftershock to that of main shock

Δ = Representative source-to-site distance

Δ_{Main} = Representative source to site distance of main shock

Δ_{Aft} = Representative source to site distance of aftershock

ΔM = Difference between main shock and aftershock magnitudes

ΔM_1 = Magnitude difference between a main shock and the largest aftershock

Δh = Difference between main shock and aftershock focal depths

$\varepsilon_j(b)$ = Error term in the regression of the energy arrival scaling model

$\varepsilon_{\text{PSV}}(T)$ = Error term in the regression of the PSV scaling model

$\varepsilon_j(t)$ = Error term in the regression of the conditional energy arrival scaling model

$\varepsilon_\beta(T)$ = Error term in the regression of the conditional PSV scaling model

γ_j = Level-dependent constant

γ_j' = Level-dependent constant

$\gamma_{j,i}$ = Value of level-dependent constant for ith sample

$\bar{\gamma}_j$ = Average value of the level-dependent constant $\gamma_{j,i}$

ω = Angular frequency

ω_j^{l} = Lower limit of angular frequency for jth level

ω_j^{u} = Upper limit of angular frequency for jth level

ω_{10}^{l} = Lower limit of angular frequency for the level $j = 10$

ω_{-21}^{u} = Upper limit of angular frequency for the level $j = -21$

π = Pi

ϕ_m = Maximum curvature

ϕ_y = Yield curvature

ϕ_u = Ultimate curvature

$\Phi_F(t,\omega)$ = Evolutionary power spectral density function

$\psi(t)$ = Real wavelet basis function

$\psi_{a,b}(t)$ = $\psi(t)$ dilated and shifted using dilation parameter a and shift parameter b

$\psi_{a_j,b}(t)$ = $\psi_{a,b}(t)$ with discretized a

$\hat{\psi}(\omega)$ = Fourier transform of the wavelet basis function $\psi(t)$

$\hat{\psi}_{a_j,b}(\omega)$ = Fourier transform of the wavelet basis function $\psi_{a_j,b}(t)$

ρ_{axial} = Axial-load ratio

$\sigma_j(b)$ = Standard deviation of error of unconditional scaling model of energy arrivals

$\sigma_{\mathrm{PSV}}(T)$ = Standard deviation of error of unconditional scaling model of PSV

$\sigma_j(t)$ = Standard deviation of error of conditional scaling model of energy arrivals

$\sigma_\beta(T)$ = Standard deviation of error of conditional scaling model of PSV

ABSTRACT

The importance of aftershocks in seismic safety assessment is now widely acknowledged by the scientific community after witnessing several incidents where buildings collapsed during aftershocks after surviving the main shock events. Because of that the recent practice demands a shift from the conventional single-event-based (i.e., the most critical event-based) design to multiple-event-based design, where the adequacy should essentially be checked against a main shock aftershock sequence (MAS). Since an aftershock hits an already degraded structure, it is imperative to carry out nonlinear time-history analysis (THA) to characterize the aftershock-induced additional damage. Such characterization should be statistically significant and should also be specific for the seismological scenarios for the anticipated main shock and its aftershocks. However, it is not possible to have a recorded ensemble of MASs for any given set of seismic scenarios for the main shock and its aftershocks. Further, it is important to develop some simple design solutions for improving the seismic safety of structures against MASs. These issues are addressed in a step-by-step manner in the present study by carrying out extensive analytical and experimental work. An attempt is made first to simulate an ensemble of motions that are specific for a given seismic scenario. The proposed stochastic simulation technique is based on Priestley oscillatory process where the time-frequency characteristics can be controlled via frequency-dependent deterministic amplitude modulations. In order to have the temporal features of the simulated motions be realistic vis-à-vis the ground motion process, a new method is proposed to extract the frequency-dependent modulations from the observed frequency-dependent energy arrival curves of a recorded motion. An empirical scaling model is then proposed for the frequency-dependent energy arrivals with respect to seismological scenarios to finally get a scenario-specific ensemble of motions with realistic variations of time-frequency characteristics among the samples. It is found that the simulated ensembles show expected variations of different ground motion parameters visà-vis seismological scenarios. An attempt is also made to simulate aftershock motions when the main shock event has already taken place and hence known. For this purpose, a new method is proposed for stochastic simulation of aftershock ensemble from the known preceding main shock from the knowledge of the seismic scenario of the anticipated aftershock. This is accomplished via a newly proposed conditional scaling model of frequency-dependent energy arrival and the Priestley process-based simulation of random samples. An approximate version of the conditional scaling model is also proposed for conditional simulation of aftershock ensemble when sufficient aftershock records are not available to carry out regression analysis. It is found that the simulated ground motion ensemble shows better agreement with the recorded aftershock process, especially for larger aftershocks, when the aftershock's dependency on its main shock (via the conditional scaling model) is considered than what it shows when the dependency is not considered. The ground motion simulation is performed using the database of 1999 Chi-Chi earthquake and its aftershocks. With the help of proposed simulation techniques, MASs are simulated to perform a detailed statistical study on the damage during MASs for RC structures. Three reinforced concrete bare frames of different fundamental periods are modelled in OpenSees software with realistic material properties to carry out the numerical study. The damage in the frames is quantified by means of an overall damage index. It is found that for scenarios where the largest aftershock (magnitude-wise) is smaller than the main shock by 0.5 or more, all the three frames are mostly safe against MASs. Design modification in structures for the safety against collapse during any MAS is proposed by applying additional (fictitious) material safety factor. A 10–15% additional material safety factor is found to be able to address the safety against a large class of MASs. Experimental testing of quarter-scale RC bare frames, with different axial load ratios, are also carried out to investigate the additional damaging effect of the aftershocks on already damaged frames. The damage due to main shocks is inflicted in the frames by slow-cyclic test and the damaged frames are tested against aftershocks on the shake table. An exponential trend is observed between the degraded natural frequencies of the frames and the cumulative hysteresis energy dissipated. An empirical predictive model is proposed for degraded natural frequency as a function of cumulative energy dissipation, axial load ratio and size of loading cycle. Finally, based on experimental results, material properties are calibrated in OpenSees to replicate the observed behaviour of RC frames. The calibrated material properties are used to validate the proposed design approach for safety against MAS. It is found that the proposed concept of additional material safety factor can be a viable solution to ensure safety against main shock aftershock sequences, without making a structure too over safe against the conventional single design event.

Chapter 1

INTRODUCTION

1.1 General Introduction

Large earthquakes are in general resulted from plate tectonic activity. The movement of tectonic plates causes stress to build up in the earth's crust and eventually, when a sudden release of stress takes place along a fault, an earthquake occurs. Earthquakes generally happen in clusters (in terms of both time and space) and the largest event among them is called the main shock and the tremors before and after the main shock are called foreshocks and aftershocks, respectively. Structures in seismically active area are subjected to frequent earthquakes during their lifetime. Hence these structures are designed as per design codes to withstand strong earthquakes without collapse. Usually, buildings are designed for a single design earthquake scenario (equivalent to the most critical anticipated main shock) without considering the effects of aftershocks. Past experiences suggest that structures designed for single design earthquakes may collapse during aftershocks while they may all survive the main shocks. Some examples of the fatal effects of the aftershocks on buildings damaged by main shock are mentioned below.

- The Luanhe river bridge collapsed in the aftershock of 7.1 magnitude which took place 15 hours later following the 7.8 magnitude earthquake at Tangshan, China, on July 28, 1976 (Huang et al., 2012).

- The 1997 Umbria-Marche earthquake killed 11 people, of which four were in the Basilica of St. Francis in Assisi at the time of the first aftershock to inspect the damage due to the main shock (Spence and D'Ayala, 1999).

- An aftershock of the 1999 Turkey Kocaeli earthquake killed seven people, injured at least 239 people, and caused several buildings to collapse in three cities near its epicenter (Holzer, 2000).

- Many buildings were severely damaged and collapsed during the aftershock following the main shock of magnitude 8.0 at Wenchuan, China, on May 12, 2008 (Zhao et al., 2009).

- The 2010 Darfield earthquake was followed by two strong aftershocks, which resulted in 185 fatalities and damaged approximately 100,000 buildings in the city of Christchurch (Atzori et al., 2012).
- The five aftershocks with magnitudes over 7.0 that followed the 2011 Tohoku earthquake caused additional damage to infrastructure, liquefaction and loss of lives (Kazama and Noda, 2012).
- The 2011 Sikkim earthquake was followed by several aftershocks of magnitudes greater than 4.0. Several buildings damaged during the main shock later collapsed during the aftershocks on 20th September and 23rd September (Kaushik and Dasgupta, 2013).

1.2 Organization

This work is presented in six chapters following this chapter.

In Chapter 2, a review of past works related to scenario-specific simulation of aftershocks and damage-based analysis of structures subjected to main shock-aftershock sequences are studied.

In Chapter 3, a technique for the simulation of scenario-specific ensemble of ground motions from a newly proposed scaling model of energy arrival curves is developed. A technique is also developed wherein the simulated scenario-specific motions are made fully compatible to any target GMPE(s).

In Chapter 4, a method for the simulation of fully nonstationary aftershock ground motions is developed from known recorded main shock motion and a newly proposed conditional scaling model of energy arrival curves. Also, an approximate conditional scaling model is developed for situations where development of the actual conditional scaling model is not possible due to insufficient or nonavailability of main shock-aftershock data.

In Chapter 5, damage due to aftershocks in structures already damaged by the preceding main shock is investigated. Different main shock ground motions and aftershocks for different scenarios which are simulated by the methods proposed in Chapters 3 and 4 are used for the analytical study by considering three reinforced concrete bare frames. A design modification through additional material safety factor is also attempted in order to make a structure safe against collapse during a MAS.

In Chapter 6, an experimental study of damage during aftershocks in an already damaged RC bare frames is studied. Different levels of main shock damages and gravity loads on the frames are considered in the experiments. A predictive model is also developed for the natural frequency of the degraded frame at the end of each event in a sequence. Further, an analytical model has been developed, with material properties calibrated with the experimental findings, which can be used for various numerical exercises beyond experiments.

A brief summary and conclusions along with the limitations and the future scope of the present study are presented in Chapter 7.

Chapter 2

LITERATURE REVIEW AND OBJECTIVES

2.1 Review of Literature

During large earthquakes, single event-based designed buildings sometimes undergo very high damage where their residual strength and stiffness diminish significantly. Because of this, the main shock-induced damaged buildings are mostly unable to resist even moderate aftershocks that follow the main shock. Hence, consideration of the effects of aftershocks in the seismic design of structures is very important (Zhai et al., 2014; Nazari et al., 2015b; Abdollahzadeh et al., 2019), especially because it is not possible to retrofit a structure (after the main earthquake event) before the next aftershock comes. For both economy and safety, the ideal situation would be where a structure will incur high damage during the design event (i.e. the main shock) but should have enough residual strength to withstand the future aftershocks without collapse.

Aftershocks being smaller events in comparison to their main shock cause additional damage mostly through the additional energy dissipation than through the additional drift (Zhai et al., 2014) and for that the response spectrum-based approaches are not suitable to assess aftershock-induced additional damage (Li and Ellingwood, 2007; Hatzigeorgiou and Beskos, 2009; Goda and Taylor, 2012; Song et al., 2014; Raghunandan et al., 2015; Shokrabadi et al., 2018). Therefore, time-history analysis (THA) is required for the proper assessment of additional damages in damaged buildings (during a main shock) due to aftershocks. The THA can be performed using recorded or simulated aftershock ground motion time-histories. Sufficient number of recorded accelerograms may not be available for a specific seismic scenario in order to perform any statistical analysis for the nonlinear responses of the structures, for which simulated accelerograms can be used (Atkinson and Goda, 2010; Rezaeian and Der Kiureghian, 2012; Galasso et al., 2012). Since the aftershocks are triggered by the parent main shock and usually occur near the same causative fault zone of the main shock, the time-frequency characteristics of the aftershock ground motions depend on those of the parent main shock motion (Das and Gupta, 2010; Hainzl et al., 2016; Papadopoulos et al., 2019). Consideration of this time-frequency dependence, while using main shock-aftershock sequence (MAS) type ground motions for nonlinear THA, is important for correct estimation of damage in the structures (Li and Ellingwood, 2007). Nonlinear responses of the buildings can be quantified by its maximum roof displacement (Lin and Miranda, 2010; Alarcon et al., 2015), maximum inter-storey drift (Neam and Taghikhany, 2016; Yamane et al., 2016), hysteretic energy dissipated (Tso et al., 1993; Miramontes et al., 1996), frequency drop (Zembaty et al., 2006; Di Sarno and Amiri, 2019), damage indices (Williams and Sexsmith, 1995; Stone and Taylor, 1993) etc. Situations may arise where the deformation due to aftershocks may not be significant compared to that due to the main shock, yet the aftershocks induce significant additional damage. For such cases, a displacement-based response parameter alone will not be sufficient for the determination of the damage due to the MAS. The Park & Ang damage index (Williams and Sexsmith, 1995; Stone and Taylor, 1993) that takes both the deformation and hysteretic energy into account is more appropriate for the damage estimation due to MASs (Huang et al., 2012; Zhai et al., 2013, 2014; Wen et al., 2017, 2018).

2.1.1 Ground Motion Simulation

In order to carry out a statistical estimate of aftershock-induced damage, it is necessary to have a suite of MASs for a given seismic scenario for main shock and the aftershocks. Further, the main shock motion (i.e. the design motion) should be consistent with the seismic hazard posed at a site because the site-specific hazard is usually stipulated by some standard via design spectrum or ground motion prediction equation (GMPE) (Atkinson and Boore, 2006; Abrahamson and Silva, 2008; Boore and Atkinson, 2008; Campbell and Bozorgnia, 2010). The GMPEs generally predict spectral quantities, e.g., spectral acceleration (SA), pseudo spectral velocity (PSV) (Campbell and Yousef Bozorgnia, 2008; Abrahamson and Silva, 2008; Atkinson et al., 2014), or sometimes provide other intensity measures like strong motion duration (SMD) (Trifunac and Brady, 1975). Hence, it is imperative that the main shock ground motion ensemble emulates the statistics of the parameter(s) as envisaged by the GMPE(s) (i.e. it should be GMPE compatible) while the aftershock samples should exhibit appropriate dependency on the main shock ground motion characteristics.

Physics-based models for earthquake ground motion simulation are available (Hartzell, 1978; Kamae et al., 1998; Joyner and Boore, 1986; Ordaz et al., 1995), however, these methods of simulation require a thorough knowledge of the seismic parameters, which may be not available in many regions (Rezaeian and Sun, 2014). On the other hand, stochastic simulation methods (Priestley, 1965; Der Kiureghian and Crempien, 1989; Conte and Peng, 1997; Liang, 2005a,b; Liang et al., 2007) have evolved in order to address the amplitude and frequency nonstationarities of a recording process and to generate samples of the process without knowing several seismological parameters. Stochastic method of ground motion simulation provides a way for the generation of ensemble of ground motions for performing any statistical analysis. Der Kiureghian and Crempien (1989) proposed a simple and versatile evolutionary random process model for describing the earthquake ground motion is proposed The model is composed of individually modulated component stationary processes, each component representing the energy in the process in a narrow band of frequencies. Conte and Peng (1997) proposed a versatile, fully nonstationary, analytical stochastic earthquake ground-motion model based on the theory of sigma-oscillatory processes, which can capture very well the temporal variation of both the intensity and the frequency content of real earthquake ground motions. Although, simulation of a scenario-specific ground motion ensemble has not been tried in this work. Iyama and Kuwamura (1999) proposed a method of simulation of earthquake accelerograms by means of wavelet inverse transform, in which the accelerations were simulated according to a given history of instantaneous energy input specified for each frequency component. But the simulated motion is not visually similar to the recorded motion, although its some of its time-frequency parameters match with that of the recorded motion. Liang (2005a,b) proposed a method for simulation of non-stationary ground motion processes having the identical statistical feature, time-dependent power spectrum, with a given ground motion record. Rezaeian and Der Kiureghian (2010) proposed a method for generating a suite of synthetic ground motion time-histories for a specified earthquake as well as for a specified scenario that employs a parameterized stochastic model that is based on a modulated, filtered white-noise process. Yamamoto and Baker (2013) have recently proposed a stochastic simulation method to generate an ensemble of ground motions for a specific scenario that is also comparable with a GMPE developed using the same database. However, their methodology does not guarantee that the underlying earthquake recording process is strictly Gaussian, which is widely accepted (Caughey and Stumpf, 1961; Amin and Ang, 1968; Der Kiureghian and Crempien, 1989; Conte and Peng, 1997; Rezaeian and Der Kiureghian, 2008; Papadrakakis et al., 2011; Takewaki et al., 2012; Deodatis et al., 2014), and the method may not be favourable for modification of the formulation so that the simulated motions become compatible to any stipulated (or target) GMPE.

It is most critical to properly maintain the realistic nature of the amplitude and frequency nonstationarities (i.e. the time-frequency characteristics) of a simulated motion because the nonlinear response is quite sensitive to them. Because of that it has become increasingly popular to get design (or response) spectrum compatible accelerograms that preserve the time-frequency characteristics of an as-recorded motion (usually referred to as seed motion) (Abrahamson, 1992; Karabalis et al., 2000; Mukherjee and Gupta, 2002a,b; Das and Gupta, 2008; Cecini and Palmeri, 2015). Usually, these methods are used when all motions are intended to exhibit a specified nonstationarity, often described by the seed motions, and thus, are not suitable when a realistic variability of nonstationarities is sought after within a scenario-specific ensemble. Priestley process-based simulation techniques are efficient for characterizing the time-frequency properties of a recording process, which can preserve the nonstationarity of the recorded motion by a frequency-dependent deterministic slow varying envelope function (Priestley, 1965; Der Kiureghian and Crempien, 1989; Conte and Peng, 1997). The class of sigma oscillatory process (summation of several elementary Priestley processes) is more realistic than the ordinary Priestley process when a multivariate random process is sought after (Conte and Peng, 1997; Peng et al., 2018). However, for univariate process simulation, Priestley process assumption may be deemed sufficient. Also, Priestley process-based simulation can ensure that the samples strictly obey nonstationary Gaussian process assumption. Such a simulation technique will be very useful for scenario-specific ensemble if the slow varying envelopes can be conveniently estimated for a given seismic scenario along with their variability. It is therefore important that the envelopes should be extracted from a physically meaningful quantity that can be estimated confidently from known seismological parameters. It is further expected that by suitable modification of the frequency-dependent envelopes, GMPE compatible ensembles can be simulated.

Simulation of aftershock ground motions should be done considering the time-frequency dependence of the aftershock motions on that of main shock motions as the nonlinear response of the structures is very sensitive to the time-frequency characteristics of the ground motions. The nonlinear THA for MAS is one step more intricate than that for an individual event scenario. This is because, despite aftershocks being separate earthquake events, aftershock ground motion characteristics are believed to be dependent on those of the preceding main shock (Das and Gupta, 2010; Hainzl et al., 2016; Papadopoulos et al., 2019). In fact, such a dependence can be addressed at the response spectrum and the strong motion duration (SMD) levels with disparities of the seismic scenarios for main shock and aftershock (Das and Gupta, 2010). However, several researchers consider randomized (simulated) main shock-aftershock ground motion sequences where little effort is put in to address such dependence. Das and Gupta (2008) have shown that one sample of aftershock can be simulated conditionally from the recorded motion of the preceding main shock for a given pair of SMD and pseudo spectral acceleration for the aftershock, wherein the frequency-dependent envelopes of the main shock sample are replicated (with uniform shrinking along time) into the aftershock sample. So, this method is not favourable for stochastic simulation of aftershock motions with desired variability of their temporal features. Goda and Taylor (2012) and Goda (2015) have shown that the time-frequency characteristics of the recorded aftershocks are very much critical for proper response statistics (and aftershock-induced vulnerability evaluation therefrom) and a randomized sequence strategy may be faulty. Hu et al. (2018) has also proposed a method for stochastic simulation of aftershock ground motions, but this simulation method does not explicitly use the ground motion properties of the preceding main shock. Papadopoulos et al. (2019) has shown that there exists a significant correlation between spectral acceleration residuals (i.e., probability level of error term in a scaling model) of main shocks and their aftershocks. So it is important to develop a method for stochastic simulation of aftershock motions, given the preceding main shock motion at a site and the seismic scenario of the anticipated aftershock.

2.1.2 Analysis of RC Frames using MAS

The performance of structures against a MAS has become a subject of interest in recent years (Amadio et al., 2003; Lee and Foutch, 2004; Li and Ellingwood, 2007; Hatzigeorgiou and Beskos, 2009; Ryu et al., 2011; Goda, 2012; Zhai et al., 2014). Amadio et al. (2003) investigated the dependence of damage accumulation against repeated earthquake ground motions using a series of SDOF systems and an MDOF system. Oyarzo-Vera and Chouw (2008) analyzed an unreinforced masonry wall as an SDOF system with a sequence of main shock and aftershock ground motions from the 1999 Chi-Chi earthquake. Das (2009) studied the effect of aftershocks (generated conditionally from the preceding main shock ground motion) on additional damage under various situations depending on seismological disparities between main shock and aftershocks, damage state at the end of main shock, main shock ground motion characteristics and structural natural periods, where only one aftershock for each seismic scenario was used. Ryu et al. (2011) developed fragility curves for main shock-damaged structures through incremental dynamic analysis using a nonlinear SDOF system with a sequence of main shock-aftershock ground motions generated from a suite of 30 ground motion records. Goda and Taylor (2012) performed nonlinear dynamic analyses of inelastic SDOF systems using real and artificially generated aftershock sequences to assess the nonlinear damage potential due to aftershocks. Huang et al. (2012) studied the effects of MASs on the cumulative damage of RC frames, using simulated main shock-aftershocks with aftershock as the varying scaled versions of main shock. Ruiz-Garcia (2012) showed that the frequency content of the aftershock has a strong influence on the dynamic post-main shock response (measured by peak and permanent displacement demand) from the dynamic analysis of steel frames using MAS. Zhai et al. (2014) investigated the effect of the relative intensity of aftershock to main shock on inelastic SDOF systems considering four hysteretic models for which the aftershock ground motion in the recorded motion sequence is scaled to have different intensity levels relative to the main shock ground motion. Raghunandan et al. (2015) performed fragility analysis of ductile RC frame buildings against MAS ground motions, wherein main shock ground motions were used as the aftershock ground motions. Shokrabadi et al. (2018) investigated the practice of using repeated MASs versus MASs in the nonlinear response assessment of structures and recommends the practice of using MAS to be discontinued. Di Sarno and Amiri (2019) investigated the lengthening of fundamental periods of nonlinear SDOF systems with deteriorating properties subjected to as-recorded MASs and proposed analytical equations for the estimation of elongated fundamental period from the undamaged time period and structural properties. In some of these studies, the importance of considering aftershock ground motions for the design of structures is felt. However, there is no consensus on how to make a structure safe against the MAS.

Gupta et al. (2001) showed that the design yield force based on conventional seismic design needs to be raised in order to make a structure safe against aftershocks. Nazari et al.

(2015a) performed a study on main shock's and aftershock's effects on a woodframe building and found that 10% increase in stiffness and restoring force is needed to account for the effect of aftershock for a scenario of main shock (of magnitude 8) and aftershock (of magnitude 7). In both the cases, the aftershock ground motions were taken as scaled versions of main shock ground motions without considering the time-frequency dependence of MASs. A detailed statistical analyses of damage of structures using the main shock-aftershock ground motion sequences (with the aftershocks simulated conditional to the main shock motion) considering different seismic scenarios and different buildings are essentially required for the development and proposition of a design strategy considering aftershocks. However, till date no such studies are available in the literature.

2.1.3 Experimental Testing of RC Frames using MAS

From the available literature on dynamic tests of buildings, it is found that most of them are carried out considering single ground motion (Gülkan et al., 1990; Nader and Astaneh-Asl, 1996; Stavridis et al., 2012; Li et al., 2016). The evolution of additional damage, in an already damaged building, due to aftershocks should be investigated by testing building models subjected to main shock-aftershock ground motion sequence. The damage accumulation in a structure due to each aftershock in a sequence depends on the ground motion properties of the aftershock and the damage state of the structure before the application of the aftershock. Žarnić et al. (2001) performed a series of shake table tests on reduced scale models of masonry infilled reinforced concrete frame buildings using horizontal two sine dwell motions with gradually increasing amplitude and at each test stage, the frequency of the input was approximately 10% lower than the model's current first resonant frequency. This was done to simulate the situation when an earthquake is followed by strong aftershocks. Twigden et al. (2010) performed dynamic tests on coir fibre and rope reinforced concrete (CFRRC) columns using a sequence of main and secondary excitations representing main shock and aftershocks, however, each excitation used were harmonic excitations with frequency changing from 10 Hz to 20 Hz in a period of 60 seconds and not ground motion time-histories. Twigden et al. (2011) applied recorded main shock-aftershock ground motion sequence on the CFRRC columns and reinforced columns and studied the damages from the change in fundamental frequency and dissipated energy and fitted a logarithmic curve between the hysteretic energy and normalized frequency (fundamental frequency at each damaged state normalized by the specimen's fundamental frequency at undamaged state). Qin and Chouw (2017) investigated the effects of structure-footing-soil interaction (SFSI) via shake table tests using a model consisting of a laminar box filled with sand and an SDOF-like frame model placed on the sand surface against main shock aftershock sequence motion. The main shock ground motion was simulated based on the Japanese Design Spectrum for a hard soil condition and the aftershock excitations were taken to be same as the main shock excitation. Not much information regarding the experimental tests on RC frames employing aftershock ground motions for the investigation of additional damages are available. However, a few experimental studies are carried out where the specimens are damaged during the main shock motion only and the calibrated structural models are further used for analytical investigation of aftershock-induced additional damage (Jeon et al., 2012; Li et al., 2012; Ruiz-García and Aguilar, 2015; Nazari et al., 2015b). It can be argued that a calibrated model that accounts for the event-by-event degradation observed during an experiment is a better alternative to a single event-based calibrated model, for the purpose of analytical prediction of response during sequence type motions.

2.2 Objectives of the Present Study Based on Identified Gap Areas

Based on the above discussions it is clear that there is a genuine need to have a methodology for stochastic ground motion simulations that is capable of generating earthquake scenario-specific ensembles. Such a simulation technique should also be favourable to generate samples of ground motion consistent with any target GMPE. Further, it is beneficial if, with certain modifications but following the same philosophy, this simulation method can also produce conditional aftershock motions that are time-frequency characteristics-wise dependent on the given (parent) main shock motion, because it will pave the ways to carry out a more realistic statistical assessment of structural damage under MAS. For wider acceptability of analytical results (in a quantitative sense) the analytical model needs to be calibrated by means of experimental findings. Hence, an experimental study on degrading behaviour of RC frames subjected to realistic MASs is also very much required.

In the present study, a method to simulate scenario-specific ensemble of ground motions with realistic variability of time-frequency characteristics is proposed. Also, this method is flexible in the sense that it can be tuned such that the simulated motions become any target GMPE compatible. This is achieved by three new propositions, viz., (1) proposing a Priestley process-based simulation of ground motion samples from the instantaneous energy arrivals of wavelet coefficients of a recorded motion, (2) proposing an empirical scaling model to predict the instantaneous energy arrivals along with their variability for a given seismic scenario, and (3) proposing an effective method to tune the instantaneous energy arrivals such that the scenario-specific simulated ensemble is compatible to any target GMPE. From the knowledge of the developed simulation method for scenario-specific ground motions, an attempt is further made to develop a Priestley process-based methodology for aftershock simulation where the temporal features of the anticipated aftershock motion are characterized (along with its possible variation) from that of the recorded main shock at the same site. For this purpose, a conditional scaling model for the frequency-dependent energy arrival curves for the aftershock is proposed for the first time. A frequency-wise decomposed time-history domain is used here instead of the wavelet domain, as proposed previously, for direct and faster ground motion simulation. For the development of various scaling models of energy arrival curves, the database of main shock and aftershock ground motions recorded during the 1999 Chi-Chi earthquake have been used.

From the proposed methods of ground motions simulation, aftershock motions for different scenarios are simulated corresponding to some simulated main shock motions with different time-frequency characteristics. The simulated MASs corresponding to various hypothetical seismic scenarios are used in the analysis of RC frames (modelled in OpenSees (Mazzoni et al., 2005)) for the investigation of damage due to sequence type motions. Based on the findings a simple design modification is also proposed to enhance structural safety against MASs.

The fundamental frequency of the structure is an excellent indicator of the health of the structure. An estimation of the frequency of the structure when damaged by MASs is needed while designing the structures to control the frequency or the structural properties from degrading beyond some limit so as to avoid the collapse of the structure. In the present study, experimental tests are performed to study the degradation in the structural properties due to aftershocks on an already damaged structure. For this purpose, quarter-scale RC bare frames damaged up to the desired level (vis-à-vis the anticipated main shock) are considered for performing the experimental investigation. Damage due to main shocks are inflicted in the frames by slow-cyclic test using a servo-controlled hydraulic actuator and then the additional damage due to aftershocks are induced by base-excitation on a shake table. The event-by-event degradation of the frames, quantified as a reduction of the natural frequency, is investigated and an empirical prediction law is proposed to predict the reduced natural frequency, as a function of hysteresis energy dissipation, an equivalent deformation, axial load ratio of columns and the natural frequency of the undamaged structure, at the end of each event in a sequence. Analytical models with calibrated material properties (in OpenSees (Mazzoni et al., 2005) platform) are finally developed for the RC frames, which exhibit comparable energy dissipation as observed during experiments under similar conditions.

Chapter 3

WAVELET-BASED SIMULATION OF SCENARIO-SPECIFIC NONSTATIONARY ACCELEROGRAMS AND THEIR GMPE COMPATIBILITY

3.1 Background

In seismic hazard analysis, ground motion prediction equation (GMPE) plays a pivotal role because it provides the statistical distribution of hazard parameter for a chosen seismic scenario. However, GMPEs, in general, do not provide nonlinear response statistics, and the latter should be ideally obtained by time-history analyses of a scenario-specific suite of motions. In the present study, a new wavelet-based method is proposed to simulate scenario-specific ensemble of accelerograms with realistic variability of time-frequency characteristics. Firstly, a methodology is proposed to stochastically characterize the nonstationarity of a recording process from the energy arrival curve of the wavelet coefficients of the recorded ground motion. Then a new empirical scaling model is developed to estimate the instantaneous energy arrival, with model uncertainty. Further, a reconstruction method is formulated to simulate the scenario-specific ensemble of accelerograms from the estimated scenario-specific energy arrival curves. It is found that the simulated ensemble exhibits realistic variation of time-frequency characteristics and hence, it naturally becomes comparable with GMPEs (in terms of median estimates for response spectrum and strong motion duration) developed using the same database. Finally, an algorithm is proposed to tune the estimated energy arrival such that the ensemble of simulated motions can be made compatible with the target GMPEs, both in terms of median estimates and standard deviations. It is found that the GMPE-compatible ensemble, obtained for 5% damping PSV spectra, shows good agreement with respect to PSV scaling models developed for a wide range of damping ratio.

3.2 Priestley Process-Based Characterization of Ground Motion

Wavelet analysis is very useful for the characterization of fully nonstationary ground acceleration process because wavelet coefficients capture adequate information about both time and frequency description of a motion. In the present study, the modified Littlewood-Paley (L-P) wavelet basis as proposed by Basu and Gupta (1998) has been used because these level-wise wavelet basis functions are strictly narrowband-limited in frequency domain – a property that is essential for Priestley process-based simulation. A brief review of the wavelet transform with essential details is provided next for the sake of completeness.

3.2.1 Review of Wavelet Transform

Any finite energy signal, $f(t)$, can be transformed into wavelet domain and reconstructed back from there by using the wavelet transformation and the inverse wavelet transformation, respectively. The continuous wavelet transformation of $f(t)$ is defined with respect to a real wavelet basis, $\psi_{a,b}(t)$, as

$$W_\psi f(a,b) = \langle f, \psi_{a,b} \rangle = \int_{-\infty}^{\infty} f(t)\psi_{a,b}(t)\mathrm{d}t \tag{3.1}$$

where

$$\psi_{a,b}(t) = \frac{1}{a^{1/2}}\psi\left(\frac{t-b}{a}\right) \tag{3.2}$$

and $\psi(t)$ is called the mother wavelet. Here, $a > 0$, the scale parameter, controls the frequency content of the dilated wavelet basis, and $b \in \Re$, the shift parameter, localizes the basis at $t = b$. The function $f(t)$ can be reconstructed back from the wavelet coefficients, $W_\psi f(a,b)$, as

$$f(t) = \frac{1}{2\pi C_\psi}\int_{-\infty}^{\infty}\int_{0}^{\infty}\frac{1}{a^2}W_\psi f(a,b)\psi_{a,b}(t)\mathrm{d}a\,\mathrm{d}b \tag{3.3}$$

with

$$C_\psi = \int_0^\infty \frac{|\hat{\psi}(\omega)|^2}{\omega}\mathrm{d}\omega < \infty \tag{3.4}$$

In Eq. (3.4), $\hat{\psi}(\omega)$ is the Fourier transform of the basis function, $\psi(t)$, defined as

$$\hat{\psi}(\omega) = \frac{1}{\sqrt{2\pi}}\int_{-\infty}^{\infty}\psi(t)e^{-i\omega t}\mathrm{d}t \tag{3.5}$$

In the present study, the modified L-P wavelet basis is used, for which the mother wavelet is defined as

$$\psi(t) = \frac{1}{\pi\sqrt{\sigma-1}}\frac{\sin(\sigma\pi t) - \sin(\pi t)}{t} \tag{3.6}$$

with σ taken as $2^{1/4}$ (Basu and Gupta, 1998). On discretizing and taking $a_j = \sigma^j$, where j is the index of (dilation) level, the wavelet coefficient corresponding to jth level is expressed by

$$W_\psi f(a_j, b) = \langle f, \psi_{a_j,b} \rangle = \int_{-\infty}^{\infty} f(t)\, \psi_{a_j,b}(t) \mathrm{d}t \tag{3.7}$$

Further, $W_\psi f(a_j, b)$ has energy in the period band $(2a_j/\sigma, 2a_j)$s and it can be considered as a narrowband signal in b. Typically $W_\psi f(a_j, b)$ looks like an amplitude modulated signal of pseudo period T_j $(= 0.5(2a_j/\sigma + 2a_j))$. A total number of 32 levels are considered with j = -21 to 10, so that $W_\psi f(a, b)$ $(= \sum_{j=-21}^{10} W_\psi f(a_j, b))$ spans over the period band (0.044–11.32)s which is deemed sufficient for any earthquake signal. Further, for practical purpose of reconstruction, it is sufficient to consider a range for b which will start 12s before the beginning of a signal and end 12s beyond the endpoint of the signal. It may be noted that, any level-specific reconstructed motion, $f_j(t)$ (obtained by inverse transform of $W_\psi f(a_j, b)$ only without summation over j), from any Gaussian white-noise signal becomes a band-limited Gaussian white-noise within the narrow period range $(2a_j/\sigma, 2a_j)$s.

A fully nonstationary process is usually characterized by the evolutionary power spectral density function (EPSDF). The EPSDF, $\Phi_F(t, \omega)$, for a recorded ground motion process, $F(t)$, can be conveniently modelled using the wavelet functional as (Basu and Gupta, 2000)

$$\Phi_F(t, \omega) = \sum_j \frac{K}{2\pi a_j} \mathrm{E}\left[W_\psi^2 f(a_j, b = t) \right] \left| \hat{\Psi}_{a_j, b=t}(\omega) \right|^2 \tag{3.8}$$

where,

$$K = \frac{1}{2C_\psi} \left(\sigma - \frac{1}{\sigma} \right) \tag{3.9}$$

and

$$\hat{\Psi}_{a_j,b}(\omega) = \begin{cases} \sqrt{a_j/(\sigma - 1)}\, e^{-b\omega} & \forall \pi/a_j < |\omega| < \sigma\pi/a_j \\ 0 & \text{Otherwise} \end{cases} \tag{3.10}$$

and $\mathrm{E}[\cdot]$ indicates the statistical expectation.

3.2.2 Modelling of Time-Frequency Characteristics

A random nonstationary process, $F(t)$, like earthquake ground motion process can be modelled as Priestley process (Priestley, 1965):

$$F(t) = \int_{-\infty}^{\infty} A(t, \omega)\, e^{i\omega t}\, \overline{\mathrm{d}Z}(\omega) \tag{3.11}$$

where, $A(t, \omega)$ is a frequency-dependent deterministic slow varying amplitude modulation or envelope and $\overline{\mathrm{d}Z}(\omega)$ is a stationary orthogonal incremental process. Hence, it can be inferred that a nonstationary signal, $f(t)$, for the $F(t)$ process can be simulated by several narrowband-limited white-noise signals and different deterministic slow varying amplitude modulations, specific for the corresponding frequency bands as (Der Kiureghian and Crempien, 1989; Conte and Peng, 1997)

$$f(t) = \sum_j A_j(t) z_j(t) \tag{3.12}$$

where, $A_j(t)$ is the deterministic amplitude modulation specific to the jth frequency band and $z_j(t)$ is the corresponding band-limited white-noise signal. It should be mentioned that all piece-wise frequency bands are disjoint and exhaustive over the entire frequency range of $f(t)$. Since the Priestley process assumption equally holds good in wavelet domain (Spanos and Failla, 2004), Eq. (3.12) is also applicable for the wavelet coefficients. Hence, different samples for the observed $W_\psi f(a_j,b)$ process can be generated as

$$\widehat{W}_\psi f(a_j,b) = V_j(b) z_j(b) \quad ;\forall j \tag{3.13}$$

where, $V_j(b)$ is the hidden deterministic amplitude modulation of the $W_\psi f(a_j,b)$ process and $z_j(b)$ is a random sample of a narrowband-limited Gaussian white-noise with period range $(2a_j/\sigma, 2a_j)$s. In the present study, a simple method of estimating $V_j(b)$ from the energy arrival curve of wavelet coefficients is proposed and is illustrated next.

The energy arrival curve of the recorded wavelet coefficients can be defined as

$$E_j(b) = \int_{-\infty}^{b} [W_\psi f(a_j,\xi)]^2 \mathrm{d}\xi \quad ;\forall j \tag{3.14}$$

Further, $W_\psi f(a_j,b)$ can be idealized as (Basu and Gupta, 1998)

$$W_\psi f(a_j,b) = V_j(b) \sin(\omega_{1,j}(b) - \phi_{1,j}) \sin(\omega_{2,j}(b) - \phi_{2,j}) \quad ;\forall j \tag{3.15}$$

where, $\omega_{1,j} = 0.5\,(\pi/a_j + \sigma\pi/a_j)$ and $\omega_{2,j} = 0.5\,(\sigma\pi/a_j - \pi/a_j)$ are respectively a fast varying and a slow varying frequency and $\phi_{1,j}$, $\phi_{2,j}$ are the phase angles for the jth level. Hence, the energy arrival curve of the wavelet coefficients can be modelled as

$$E_j(b) = \int_{-\infty}^{b} V_j^2(\xi) \sin^2(\omega_{1,j}(\xi) - \phi_{1,j}) \sin^2(\omega_{2,j}(\xi) - \phi_{2,j}) \mathrm{d}\xi \quad ;\forall j \tag{3.16}$$

which can be further split into

$$\begin{aligned} E_j(b) = \frac{1}{4}\int_{-\infty}^{b} V_j^2(\xi)\mathrm{d}\xi - \frac{1}{4}\int_{-\infty}^{b} V_j^2(\xi)(\cos(2\omega_{1,j}(\xi) - \phi_{1,j}) + \cos(2\omega_{2,j}(\xi) - \phi_{2,j}) \\ - \cos(2\omega_{1,j}(\xi) - \phi_{1,j}) \cos(2\omega_{2,j}(\xi) - \phi_{2,j}))\mathrm{d}\xi \quad ;\forall j \end{aligned} \tag{3.17}$$

Since $\omega_{2,j}$ is slow varying with respect to $\omega_{1,j}$ and $V_j(b)$ is slow varying with respect to $2\omega_{2,j}$, the second integration term in Eq. (3.17) is fast oscillatory with respect to the steadily increasing first integration term. This suggests that if $E_j(b)$ is smoothened, denoted by $\bar{E}_j(b)$, it will converge to the first integration term of Eq. (3.17). Hence, it is expected that the hidden modulation, $V_j(b)$, can be extracted from $\bar{E}_j(b)$ as

$$V_j(b) = 2\left[\frac{\mathrm{d}\bar{E}_j(b)}{\mathrm{d}b}\right]^{\frac{1}{2}} \tag{3.18}$$

Since Eq. (3.15) is an idealization for the observed (irregular) beat phenomenon of modified L-P wavelet coefficient, the constant 2 in Eq. (3.18) may not strictly hold good. It is found in the present study that $V_j(b)$ can be reasonably expressed as

$$V_j(b) = \gamma_j\left[\frac{\mathrm{d}\bar{E}_j(b)}{\mathrm{d}b}\right]^{\frac{1}{2}} \tag{3.19}$$

where γ_j is a level-dependent constant. Since only the shape of $V_j(b)$ is extracted from the energy arrival curve, it is assumed that the total energy arrival (corresponding to the maximum value of b) of any simulated wavelet coefficient, $\widehat{W}_{\psi}f(a_j,b)$, will match that of the observed one. Hence, there is no need to calculate γ_j explicitly once $\widehat{W}_{\psi}f(a_j,b)$ (from Eq. (3.13)) is appropriately scaled.

Eq. (3.19) still does not generally produce good results for $j = 7$ to 10. This is because in this range the time period corresponding to the slow varying frequency, ω_{2j}, becomes large enough not to let capture the hidden modulation properly within the total duration of motion (Das and Gupta, 2011). Hence, for the practical purpose $V_j(b)$s for the last four levels are assumed to be constant along b. This is not a serious limitation as the energy associated with each of these levels is usually very small and hence, they will not affect the nonstationarity of the reconstructed motion.

In the present study, $z_j(b)$ in Eq. (3.13) is considered as narrowband-limited Gaussian white-noise signal, which usually exhibits beat-like phenomenon by forming many prominent slow varying loops of varying amplitude (beat-like phenomenon is also exhibited by wavelet coefficients of a recorded motion). For that reason $z_j(b)$ needs to be correctly localized, before using in Eq. (3.13), otherwise, most of the samples will not emulate the observed modulation. By localization, it is meant here that there is a tolerance on either side of the largest peak of $V_j(b)$ where a peak of a slow-varying loop of $z_j(b)$, lying above 2× root-mean-square (r.m.s.) threshold, can randomly lie. In the present study, the tolerance is made equal to T_j arbitrarily to add some desired variability among the random samples. Further, the threshold of 2× r.m.s. is chosen, arbitrarily, to avoid relatively small amplitude loops getting aligned with the peak of the modulation, otherwise, many samples may not capture the observed modulation. A schematic diagram is shown in Figure 3.1 to illustrate the method of sample generation of wavelet coefficients. Figure 3.2 shows the wavelet coefficient of a recorded motion (recorded during the main event at station C087 along north-south direction (Center for Engineering Strong Motion Data) for $j = -7$ (chosen arbitrarily), a simulated sample of wavelet coefficient using the proposed localization and a simulated sample of wavelet coefficient without any localization constraint for the same level. The figure also shows the extracted modulation (suitably scaled) of the wavelet coefficient of the recorded motion by using Eq. (3.19). It is clear from the figure that the proposed methodology of extracting the hidden modulation is quite satisfactory and the simulated sample using the proposed localization fairly preserves the hidden modulation whereas the one without localization restriction fails to capture the amplitude modulation of the recorded wavelet coefficients. Figure 3.3 shows the wavelet coefficients of recorded motions for different earthquakes (motion recorded at Baigao station for the 1988 India-Myanmar Border earthquake along S28W direction (Center for Engineering Strong Motion Data) and at Barstow station for the 1992 Landers earthquake along a horizontal direction (PEER Ground Motion Database) and their extracted modulation, corresponding to $j = -7$. The proposed modulation extraction technique is found to work well for other j's, and for ground motions from different parts of the world. Now a random sample for the recorded motion process can be generated by taking wavelet inverse transform of $\widehat{W}_\psi f(a,b)$ (= $\sum_{j=-21}^{10} \widehat{W}_\psi f(a_j,b)$) using Eq. (3.3). Any simulated ground motion, thus obtained, needs the usual high-pass filter and baseline correction before computing derived quantities from them.

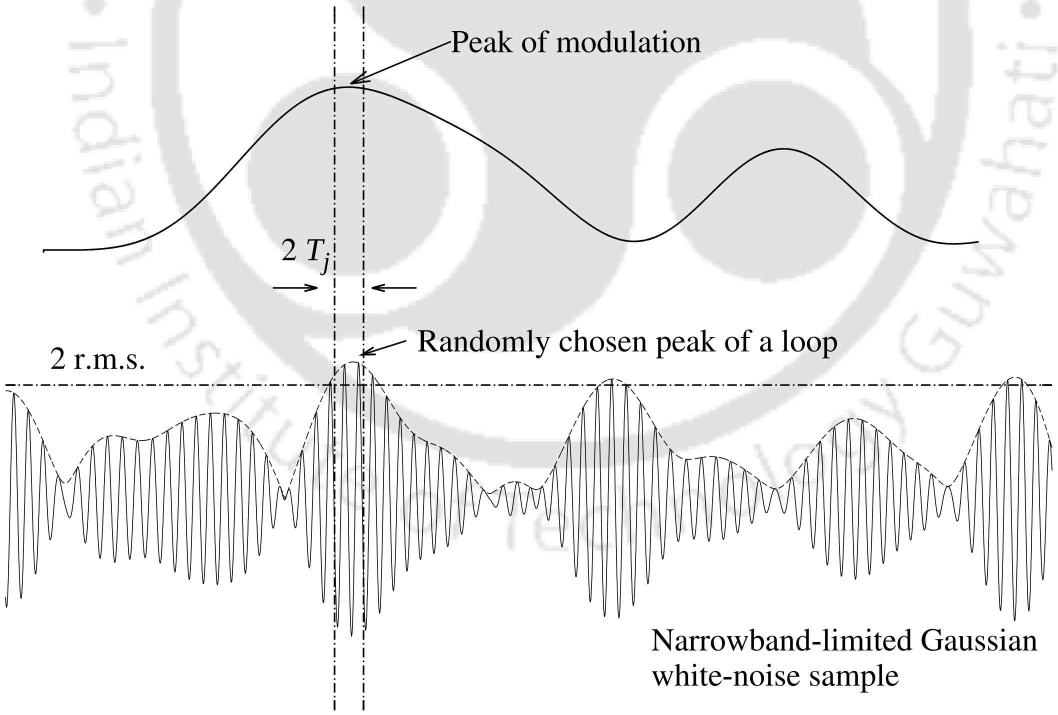

Figure 3.1 Schematic diagram for the proposed localization technique

The proposed process simulation may be considered as a limited Priestley process because (i) the peak of $z_j(b)$ is localized around that of $V_j(b)$ within a tolerance and (ii) no variation of

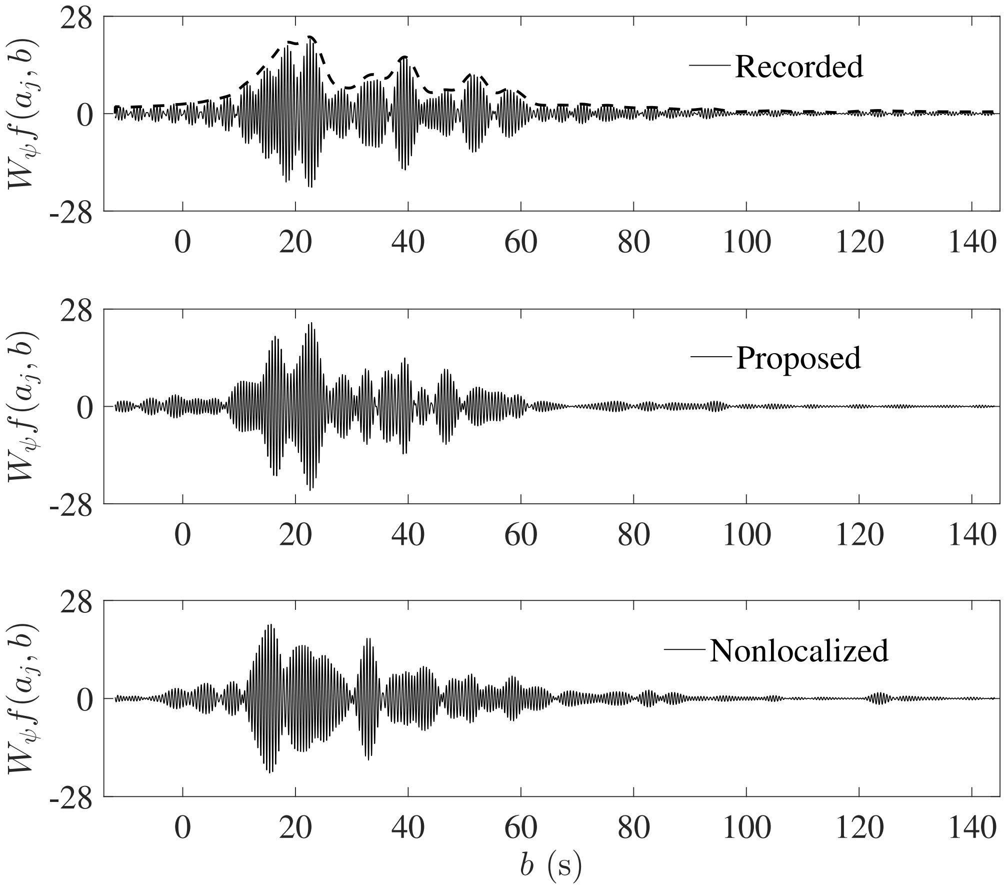

Figure 3.2 The recorded wavelet coefficient (with modulation shown in dotted line) at station C087 for the Chi-Chi earthquake along with simulated wavelet coefficients using different schemes, all for $j = -7$

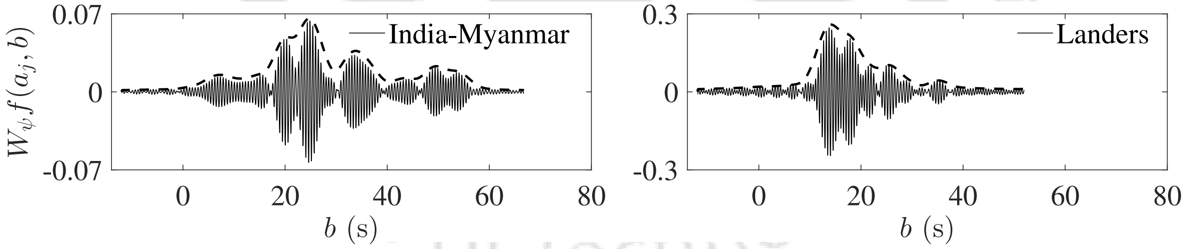

Figure 3.3 The recorded wavelet coefficient along with modulation (shown in dotted line) for $j = -7$ for a motion at (a) Baigao station for the India-Myanmar Border earthquake and (b) Barstow station for the Landers earthquake

total energy of a simulated wavelet coefficient is allowed.

3.2.3 Recording Process-Specific Sample Simulation

The proposed methodology of sample generation is independent of any region of interest and hence to see the performance of the proposed methodologies for the extraction of amplitude modulation and for samples generation, various recorded motions are chosen from different parts of the world. First, the normalized $V_j(b)$s are obtained from Eq. (3.19) and then 500 different samples of ground motions are for each of the considered recorded cases. The EPSDF of the simulated samples is obtained using Eq. (3.8) from the wavelet functionals. But no ground truth for EPSDF is available for the recorded process, however, the normalized shape of EPSDF for the recorded process can be at least idealized using Eq. (3.8) by replacing $\mathrm{E}\left[W_{\psi}^{2}f(a_j,b)\right]$ with the smooth trend of the $W_{\psi}^{2}f(a_j,b)$ of the recorded motion. This approximation is done only to get the shape for EPSDF that is independent of the simulated samples and hence it will provide a basis for qualitative comparison. Figure 3.4 shows the normalized EPSDFs obtained from the recorded motion and from the random samples for the India-Myanmar Border earthquake and the Landers earthquake which have very different time-frequency characteristics as seen from the figure. A reasonably good agreement in terms of distribution of power over time and frequency suggests that the nonstationary characteristics of the simulated samples are satisfactory in statistical sense with respect to the recorded motion. Similar agreements are observed for other recording processes also.

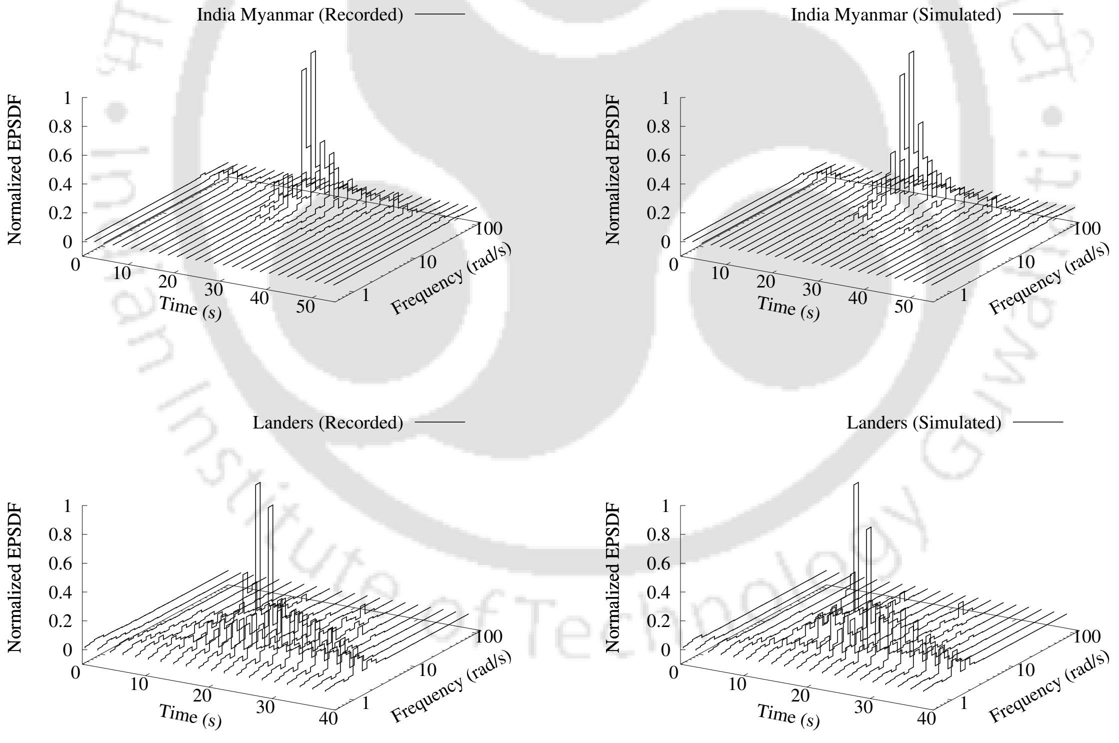

Figure 3.4 Normalized EPSDFs for the recorded (through smoothened wavelet functionals) and simulated ensemble using Eq. (3.8)

It is also necessary to know if the variability at the linear response spectrum level is adequate to have any statistical significance. For that purpose, the 5, 50 and 95 percentiles and minimum and maximum pseudo spectral acceleration spectra, are computed for 5% damping ratio using the 500 simulated samples for recorded motions at C087 station for the Chi-Chi earthquake and at Baigao station for the India-Myanmar Border earthquake and are shown in Figure 3.5. The recorded spectrum is also shown in the same plot for the purpose of comparison. It can be observed that the minimum and maximum levels of response are able to capture the recorded trend quite satisfactorily except in the long period region (beyond 9 seconds) due to inaccurate modulation extraction explained before. However, this has little practical significance because the acceleration response is less by orders beyond this period. More importantly, the variations of spectral response among simulated samples (measured by the separation of confidence bands) along period are very much comparable with what can be expected had the samples been generated using other Priestley process-based simulation (see Conte and Peng (1997)). This indicates that by imposing localization of narrowband-limited white-noise and equality of level-wise total energy arrival the inter-sample variability is not actually compromised at the response level.

In order to see the performance in terms of individual samples, Figure 3.6 shows the same recorded motions as considered for Figure 3.5 along with a simulated sample of the same process. It is apparent from the figure that the temporal features of random samples have adequate variability such that neither they look identical nor they look completely different from the recorded signal. Further, it is also found in the study that the Fourier amplitude spectrum of any random sample conforms with that of the recorded motion because the level-wise total energy is preserved.

The proposed simulation technique follows the Priestley process wherein a nonstationary process is obtained by summation of several zero-mean Gaussian stationary processes each modulated by different envelope functions, which ensures that the simulated ground motion ensembles will also follow zero-mean Gaussian distribution. The goodness of fit can be comprehensively demonstrated by the use of normal probability plots (Tang and Ang, 2007) where a straight line is fitted between the sorted simulated random variables and the corresponding percentile-wise theoretical z-values. The higher the value of R^2 ($0<R^2<1$), the coefficient of determination, better will be the fit. Table 3.1 shows the time instant-wise R^2 values for simulated ensembles for arbitrarily selected five different recorded motions. Newly considered cases are the motions recorded for the 2016 Norcia earthquake at Forca Canapine station along east-west direction (Center for Engineering Strong Motion Data) and for the 1995 Kobe earthquake at TOT station along one of the horizontal directions (PEER Ground Motion Database). Very high R^2 values (all greater than 0.99) indicates that the simulated ensembles follow Gaussian distribution at every time instant. Figure 3.7 shows recorded motions at station C087 for the Chi-Chi earthquake and at Baigao station for the India-Myanmar Border earthquake and the respective ensemble means of their simulated samples. It is clear that the ensemble mean values are negligible compared to the strength of the corresponding records, and for all practical purpose the simulated ensembles are zero-mean.

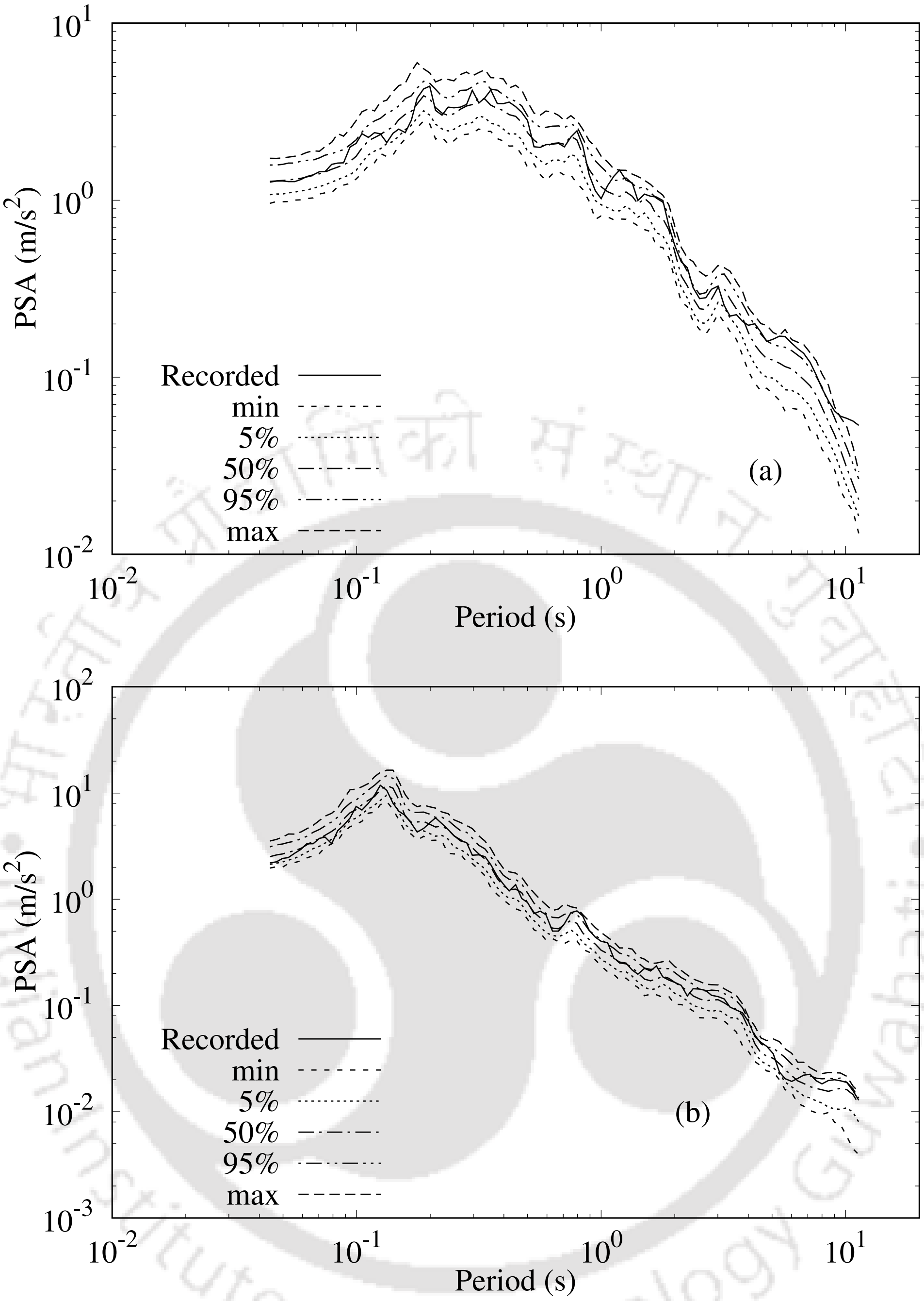

Figure 3.5 Recorded PSA spectrum along with PSA spectra for different levels of confidence from simulation for motion at (a) C087 station for the Chi-Chi earthquake and (b) Baigao station for the India-Myanmar Border earthquake

In order to see various ground motion related statistics Table 3.2 shows peak ground acceleration (PGA), peak ground velocity (PGV), peak ground displacement (PGD), ratio of PGV to PGA (PGV/PGA), ratio of PGD to PGA (PGD/PGA), temporal RMS of acceleration (RMSA), temporal RMS of velocity (RMSV) and temporal RMS of displacement (RMSD) of recorded motions of five earthquakes. Mean, coefficient of variation (CoV), maximum and minimum

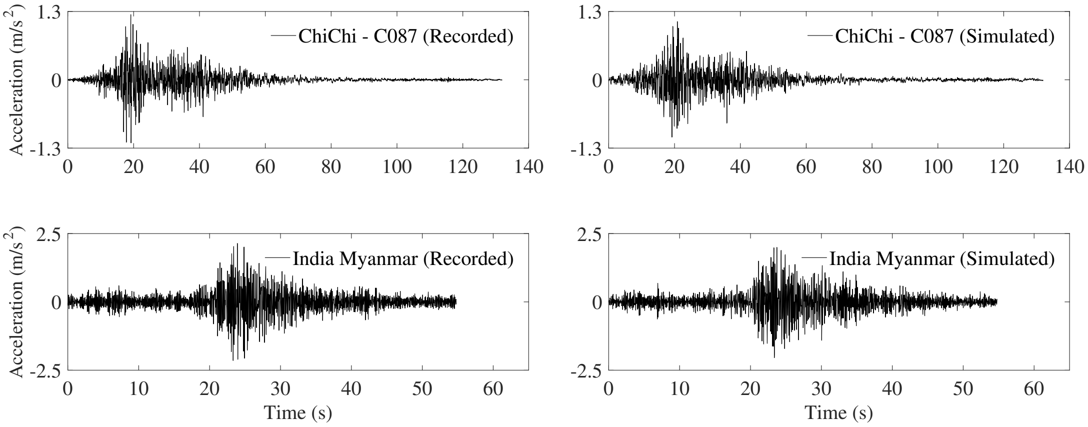

Figure 3.6 Comparison of the recorded motion and a simulated sample at C087 station for the Chi-Chi earthquake and at Baigao station for the India-Myanmar Border earthquake

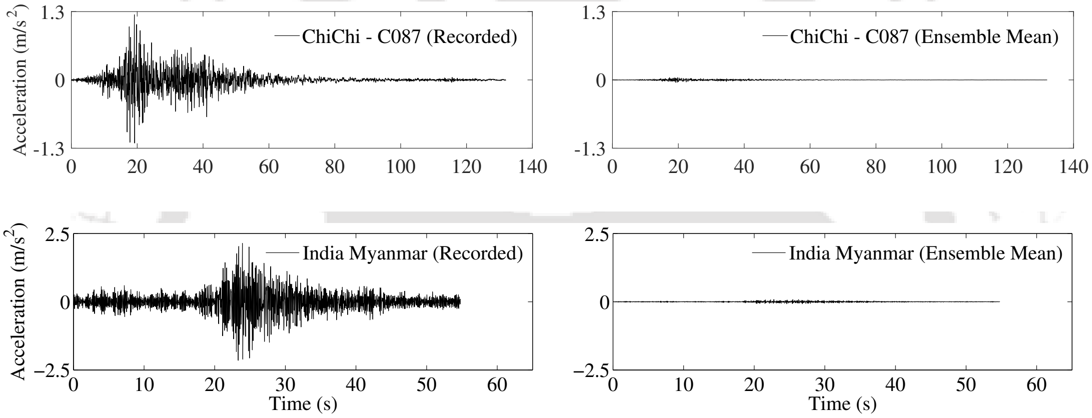

Figure 3.7 Recorded motions along with the ensemble mean of simulated samples at C087 station for the Chi-Chi earthquake and Baigao station for the India-Myanmar Border earthquake

values of the same parameters for simulated ensembles are also shown. The mean of these parameters of the simulated ensemble are close to those of the corresponding recorded motion. The variation of different parameters observed in the present study is of similar order that has been found in previous study (Conte and Peng, 1997).

3.3 Scaling Model of Energy Arrival

It is found in the previous section that the smooth energy arrival of the wavelet coefficients, $\bar{E}_j(b)$, can adequately characterize the time-frequency characteristics of a recorded ground motion process. However, it is not possible practically to define a recording process by specifying several seismological parameters, because neither such parameters are all known nor they are all measurable accurately or quantifiable. On the contrary, it is possible to define a scenario by

Table 3.1 Time instant-wise R^2 values from normal probability plot for simulated ensembles for different recorded motions

Time (s)	Record Details				
	Chi-Chi (C087)	India-Myanmar	Norcia	Landers	Kobe
5	0.996	0.997	0.998	0.998	0.998
10	0.996	0.997	0.995	0.998	0.998
15	0.998	0.997	0.998	0.997	0.996
20	0.997	0.998	0.994	0.997	0.998
25	0.997	0.999	-	0.996	0.996
30	0.998	0.995	-	0.999	0.999
35	0.996	0.997	-	0.997	0.998
40	0.999	0.997	-	0.998	0.991
45	0.995	0.996	-	-	0.997
50	0.998	0.999	-	-	0.996
55	0.996	-	-	-	0.995
60	0.998	-	-	-	0.996
65	0.994	-	-	-	0.996
70	0.998	-	-	-	0.999
75	0.998	-	-	-	-

specifying some easily available seismological parameters, within acceptable tolerance, e.g., magnitude of earthquake event, representative source-to-site distance and local site condition of recording station.

A scenario-specific ensemble of motions can be simulated by estimating $\bar{E}_j(b)$, for the given seismological parameters, along with its aleatory uncertainty. The uncertainty will arise because which particular recording process a scenario might represent is inherently random. A scenario-specific ensemble of motions will, therefore, exhibit varied frequency-dependent amplitude modulations resulting from different underlying recording processes. Hence, an empirical scaling model for $\bar{E}_j(b)$, with model uncertainty, is proposed in terms of some conveniently available seismological parameters.

The PSV scaling models and the Fourier amplitude scaling models consider the logarithm of the corresponding regressed quantity (Trifunac and Lee, 1990). Further, it is a known fact that the energy arrival of a signal and the Fourier amplitudes are directly related through Parseval's identity. So, the scaling relationship for $\bar{E}_j(b)$ is considered as

$$\ln(\bar{E}_j(b)) = a_{1,j}(b)M + a_{2,j}(b)\ln\Delta + a_{3,j}(b)S + a_{4,j}(b) \quad ;\forall j \tag{3.20}$$

where, M is the local magnitude, Δ is the representative source-to-site distance due to Trifunac and Lee (1990, 1989), S is the indicator parameter for local site conditions ($S = 0$, 1 and 2 for soft soil, stiff soil and rock, respectively). The representative distance Δ takes the finite source dimension into account and in general, depends on M, epicentral distance (R), focal depth (h),

Table 3.2 Ground motion parameters for recorded ground motions and their corresponding statistics from the simulated samples

Event	Parameter	PGA (m/s^2)	PGV (m/s)	PGD (m)	$\frac{\text{PGV}}{\text{PGA}}$ (s)	$\frac{\text{PGD}}{\text{PGA}}$ (s^2)	RMSA (m/s^2)	RMSV (m/s)	RMSD (m)
Chi-Chi (C087)	Recorded	1.254	0.138	0.075	0.110	0.060	0.142	0.018	0.013
	Mean	1.275	0.106	0.037	0.084	0.029	0.140	0.017	0.010
	COV (%)	11.480	11.691	14.783	16.033	18.213	0.265	1.092	3.430
	Max.	1.709	0.152	0.057	0.126	0.051	0.141	0.018	0.012
	Min.	0.953	0.075	0.025	0.054	0.017	0.138	0.016	0.009
India - Myanmar	Recorded	2.170	0.066	0.010	0.030	0.005	0.365	0.011	0.003
	Mean	2.477	0.065	0.013	0.026	0.005	0.363	0.010	0.004
	COV (%)	11.721	12.154	14.286	12.500	19.231	0.250	0.932	9.237
	Max.	3.543	0.105	0.019	0.039	0.009	0.364	0.011	0.005
	Min.	1.885	0.047	0.008	0.019	0.003	0.359	0.010	0.003
Norcia	Recorded	8.953	0.767	0.097	0.086	0.011	1.342	0.091	0.026
	Mean	7.548	0.516	0.095	0.069	0.013	1.287	0.111	0.031
	COV (%)	13.004	14.233	24.233	16.498	28.346	0.860	5.888	28.979
	Max.	11.056	0.817	0.181	0.112	0.031	1.317	0.149	0.072
	Min.	5.560	0.355	0.052	0.044	0.006	1.253	0.102	0.020
Landers	Recorded	1.329	0.250	0.175	0.188	0.131	0.185	0.055	0.056
	Mean	0.962	0.141	0.090	0.149	0.095	0.174	0.044	0.035
	COV (%)	13.218	13.759	14.412	18.456	19.182	0.684	4.351	8.198
	Max.	1.473	0.230	0.135	0.277	0.171	0.177	0.053	0.043
	Min.	0.718	0.102	0.058	0.086	0.050	0.170	0.037	0.026
Kobe	Recorded	0.742	0.106	0.043	0.143	0.058	0.114	0.010	0.006
	Mean	0.743	0.080	0.019	0.108	0.025	0.114	0.013	0.005
	COV (%)	12.322	12.422	14.516	13.653	19.291	0.699	1.172	4.620
	Max.	1.055	0.111	0.028	0.155	0.042	0.116	0.014	0.006
	Min.	0.536	0.056	0.013	0.069	0.014	0.109	0.013	0.005

Table 3.3 Details of the events considered for the scaling model

Events	Origin Time			Latitude (°N)	Longitude (°E)	Depth (km)	Magnitude	Number of Records
	Date	Day	Hr:Min:Sec					
Main Shock	09	20	17:47:16.00	23.8603	120.7995	10.33	7.3	93
Aft-1757	09	20	17:57:15.31	23.9255	121.0275	11	6.44	31
Aft-1803	09	20	18:03:41.16	23.8123	120.8590	8.2	6.6	47
Aft-1821	09	20	18:21:28.60	23.9564	121.0630	9.7	5.22	22
Aft-1832	09	20	18:32:55.07	23.8290	120.9912	16.8	5.07	10
Aft-1940	09	20	19:40:32.57	23.5509	120.8759	7.4	5.28	24
Aft-1957	09	20	19:57:52.63	24.0278	120.8134	12	5.19	43
Aft-2002	09	20	20:02:15.90	23.9823	120.7406	12.1	5.35	51
Aft-2021	09	20	20:21:59.67	24.1077	120.9795	11.1	5.22	29
Aft-2127	09	20	21:27:56.71	24.0851	121.0346	11.9	4.99	3
Aft-2146	09	20	21:46:37.49	23.6121	120.8110	1	6.59	28
Aft-2154	09	20	21:54:47.08	23.6230	120.7741	4.3	5.33	30
Aft-2222	09	20	22:22:46.00	23.5510	120.8342	5	5.15	22
Aft-2318	09	20	23:18:13.21	23.4490	120.9052	9.6	5.1	21
Aft-0014	09	22	00:14:40.77	23.8260	121.0470	15.6	6.8	11
Aft-2352	09	25	23:52:49.63	23.8540	121.0020	9.9	6.8	22

time period of seismic wave and shear wave velocity of local site (180 m/s, 270 m/s, 850 m/s for $S = 0$, 1 and 2, respectively).

The database for the regression analysis comprises north-south component of main shock (93 number of recordings) and aftershocks of magnitude 5 and above (394 number of recordings) during the 1999 Chi-Chi earthquake (Lee et al., 2001a,b). The focus of current work is in a methodological development of a new GMPE through a new functional called frequency-dependent energy arrival, so that scenario-specific nonstationary motions can be simulated. Hence, the NS components were selected arbitrarily in the development of energy arrival scaling model to prove the conceptual utility of the proposed approach. Coincidentally, the fault rupture that took place during 1999 Chi-Chi earthquake and its aftershocks was oriented in the NS direction. These aftershock records are chosen such that all recordings are within 50 km of the corresponding epicentral distance (with acceptable signal to noise ratio). The main shock recording at a station is considered only if at least one aftershock recording is chosen for the station, otherwise, the majority of epicentral distances of main shock from the respective recording stations would be higher than 50 km and the distant motion prediction may get biased towards the main shock. Location, time-of-occurrence, seismological details and the number of considered records of the events are given in the Table 3.3. The location details of the recording stations are given in Table 3.4. A map depicting the location of recording stations and epicentres of main shock and aftershocks is shown in Figure 3.8. A table showing the details of the ground motions (event and station) selected for the study is shown in Table 3.5. Different motions are having different length of records and hence to maintain uniformity the maximum value of b is considered as 100 s, which is quite conservative, whereas the minimum value is -12 s. It is understood that smaller records will reach their 100% energy arrival for a smaller value of b than a lengthy record. Further, for estimation of regression coefficients, b is discretized every 0.02 s of interval.

Table 3.4 Details of the stations considered for the scaling model

Station Code	Lat. (ºN)	Long. (ºE)	Station Code	Lat. (ºN)	Long. (ºE)	Station Code	Lat. (ºN)	Long. (ºE)	Station Code	Lat. (ºN)	Long. (ºE)
C002	23.7192	120.4125	C094	23.7935	120.3205	T051	24.1603	120.6518	T089	23.9037	120.8565
C006	23.5815	120.5520	C101	23.6862	120.5622	T052	24.1980	120.7393	T100	24.1858	120.6153
C010	23.4653	120.5440	C104	23.6695	120.4648	T053	24.1935	120.6688	T102	24.2493	120.7208
C014	23.2963	120.5828	H005	23.6608	121.4140	T054	24.1612	120.6750	T103	24.3098	120.7072
C015	23.3550	120.4052	H006	23.6732	121.4173	T056	24.1588	120.6238	T104	24.2455	120.6018
C024	23.7570	120.6062	H020	23.8137	121.4328	T057	24.1732	120.6107	T105	24.2390	120.5590
C025	23.7795	120.5137	H031	23.7653	121.4922	T059	24.2687	120.5637	T106	24.0833	120.5518
C026	23.7987	120.4113	H032	23.7108	121.4120	T060	24.2247	120.6440	T107	24.0727	120.5402
C028	23.6320	120.6052	H033	23.6867	121.4747	T061	24.1355	120.5490	T109	24.0848	120.5713
C029	23.6135	120.5282	H034	23.5905	121.3772	T063	24.1083	120.6158	T111	24.1137	120.4872
C032	23.5799	120.2944	H035	23.7320	121.4362	T065	24.0588	120.6912	T116	23.8568	120.5803
C034	23.5212	120.5443	H037	23.4542	121.3840	T067	24.0912	120.7200	T117	24.1335	120.4598
C035	23.5200	120.5840	H038	23.4615	121.3445	T068	24.2772	120.7658	T118	24.0027	120.4235
C036	23.6073	120.4788	H039	23.3845	121.3523	T070	24.1960	120.5403	T120	23.9803	120.6130
C039	23.5207	120.3440	H056	24.1795	121.5077	T071	23.9855	120.7883	T122	23.8128	120.6097
C041	23.4388	120.5957	K001	23.1618	120.6355	T072	24.0407	120.8488	T129	23.8783	120.6843
C046	23.4765	120.4632	N041	23.1342	121.1177	T074	23.9622	120.9618	T136	24.2603	120.6518
C047	23.4938	120.4468	T036	24.4488	120.6963	T075	23.9827	120.6778	T138	23.9223	120.5955
C052	23.2878	120.5010	T039	24.4917	120.7837	T076	23.9077	120.6757	T140	23.9578	120.3593
C074	23.5103	120.8052	T040	24.4497	120.6455	T078	23.8120	120.8455	T141	23.8338	120.4640
C079	23.1848	120.5280	T046	24.4683	120.8543	T079	23.8395	120.8942	T145	23.9800	120.3368
C081	23.2703	120.4965	T048	24.1800	120.5888	T082	24.1475	120.6760			
C087	23.3845	120.5190	T049	24.1790	120.6902	T087	24.3482	120.7733			
C088	23.3462	120.4293	T050	24.1815	120.6338	T088	24.2533	121.1758			

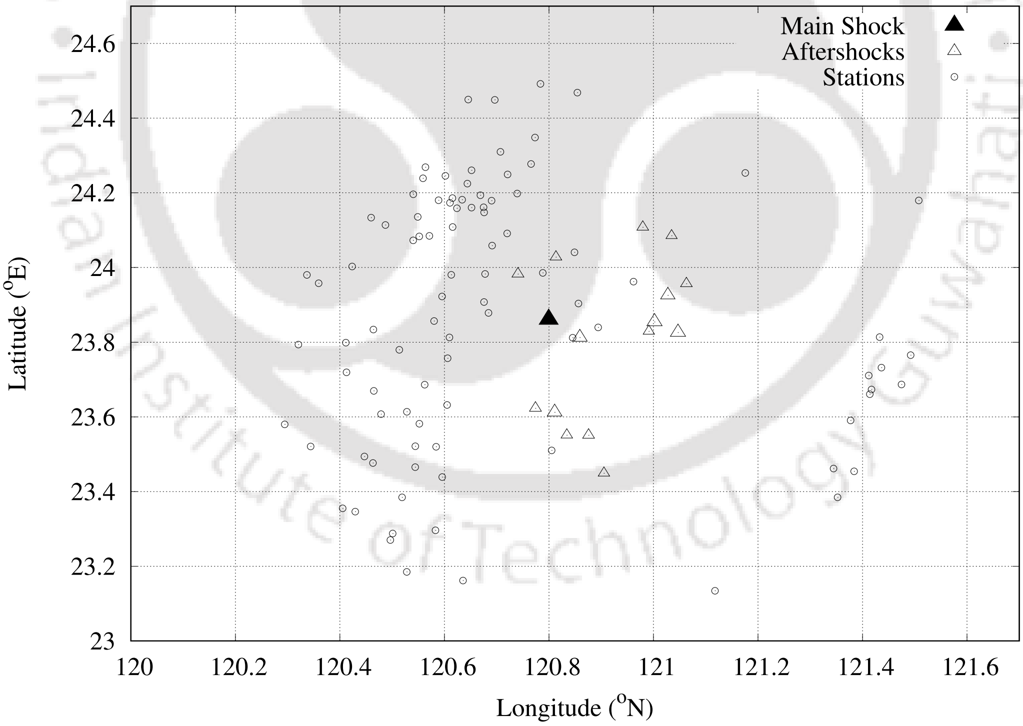

Figure 3.8 Epicentres of main shock and aftershocks and the locations of recording stations considered in the study

The regression analysis is carried out using the maximum likelihood method (Joyner and

Table 3.5 Events and stations of the motions considered in the study (grey box represents considered motion)

Events Stations	Main	1757	1803	1821	1832	1940	1957	2002	2021	2127	2146	2154	2222	2318	0014	2352
C002	■		■					■			■	■	■			
C006	■		■			■		■			■	■	■	■		
C010	■					■					■	■	■	■		
C014	■					■					■	■	■	■		
C015	■											■	■			
C024	■	■	■			■	■	■			■	■	■	■	■	■
C025	■		■			■	■	■			■	■	■			
C026	■		■				■	■			■	■				
C028	■		■			■	■	■			■	■	■			■
C029	■		■			■		■			■	■	■	■		
C032	■											■				
C034	■		■			■					■		■	■		
C035	■		■			■					■	■	■	■		
C036	■		■			■		■			■	■	■	■		
C039	■										■	■				
C041	■		■			■						■	■	■		
C046	■					■					■	■	■	■		
C047	■					■					■	■	■	■		
C052	■					■					■	■		■		
C074	■		■			■					■	■	■	■		■
C079	■													■		
C081	■					■					■	■				
C087	■					■					■	■	■	■		
C088	■										■	■	■	■		
C094	■							■				■				
C101	■		■		■	■	■	■			■					■
C104	■		■			■		■			■	■				
H005	■	■													■	
H006	■	■														
H020	■	■		■											■	■
H031	■														■	
H032	■	■		■											■	
H033	■														■	
H034	■														■	■
H035	■	■		■											■	■
H037	■													■		
H038	■					■										
H039	■													■		
H056	■									■						
K001	■													■		
N041	■													■		
T036	■								■							
T039	■								■							
T040	■						■									
T046	■								■							
T048	■		■				■	■								
T049	■		■				■	■	■							■

Events Stations	Main	1757	1803	1821	1832	1940	1957	2002	2021	2127	2146	2154	2222	2318	0014	2352
T050	■	■	■				■	■	■							
T051	■	■	■	■			■	■	■	■						■
T052	■	■	■	■			■	■	■							■
T053	■	■	■	■			■	■	■							
T054	■	■	■				■	■	■							
T056	■	■	■				■	■	■							
T057	■		■				■	■								
T059	■						■	■	■							
T060	■						■	■								
T061	■		■				■	■								
T063	■	■	■	■			■	■	■	■						
T065	■	■	■	■			■	■								■
T067	■	■	■	■			■	■	■						■	■
T068	■	■					■	■	■							
T070	■						■	■	■							
T071	■	■	■	■	■											
T072	■		■	■	■											■
T074	■	■	■	■	■											
T075	■	■	■	■												■
T076	■	■	■	■	■	■	■	■	■							■
T078	■	■	■	■	■											■
T079	■	■	■	■												■
T082	■	■	■	■			■	■	■							■
T087	■							■	■							
T088	■	■														
T089	■	■	■	■	■	■	■	■	■		■	■	■			
T100	■		■				■	■	■							
T102	■							■	■							
T103	■						■	■	■							
T104	■						■	■	■							
T105	■						■	■	■							
T106	■		■				■	■	■							
T107	■		■				■	■	■							
T109	■	■	■				■	■	■							
T111	■							■								
T116	■	■	■		■	■	■	■			■	■	■			
T117	■						■	■								
T118	■		■				■	■								
T120	■	■	■	■	■		■	■	■		■	■				■
T122	■	■	■	■		■	■	■			■	■	■			■
T129	■	■	■	■	■										■	■
T136	■						■	■								
T138	■	■	■	■			■	■	■		■	■	■		■	■
T140	■						■	■								
T141	■		■				■	■			■	■				
T145	■						■	■								

Boore, 1993) and the error, $\varepsilon_j(b)$, in the scaling model is defined as

$$\varepsilon_j(b) = \ln(\bar{E}_j(b)) - \ln(\hat{E}_j(b)) \quad ;\forall j \tag{3.21}$$

where, $\hat{E}_j(b)$ is the estimated (smooth) energy arrival using Eq. (3.20) via estimated smoothened regression coefficients. Further, $\varepsilon_j(b)$ is a normal variate with mean zero and standard deviation $\sigma_j(b)$. $\varepsilon_j(b)$ is equal to the sum of inter-event and intra-event residuals. The inter-event and intra-event residuals are lumped together and cannot be separated in this regression method. The coefficients are determined via maximization of likelihood of the errors in following a normal distribution with zero mean and some standard deviation.

It is important to investigate the soundness of the estimated regression coefficients before using them. It is found that $a_{1,j}(b)$ is positive for all values of j and b, similarly, $a_{2,j}(b)$ and $a_{3,j}(b)$ are found to be negative throughout. These findings are meaningful because energy arrival at any time should increase with increasing earthquake magnitude and decrease with increasing source-to-site distance and also the energy arrival should increase in presence of soft soil due to local site amplification. All regression coefficients and standard deviation of errors for $j = -10$ and $j = -1$ are shown in Figure 3.9 as an example. Apart from only the nature of coefficients, it is also important to investigate if the observed trend of any coefficient along b is acceptable. However, there is no theory available that can directly explain the trend, hence, an indirect way is adopted for the purpose of justification. The change of shape of the

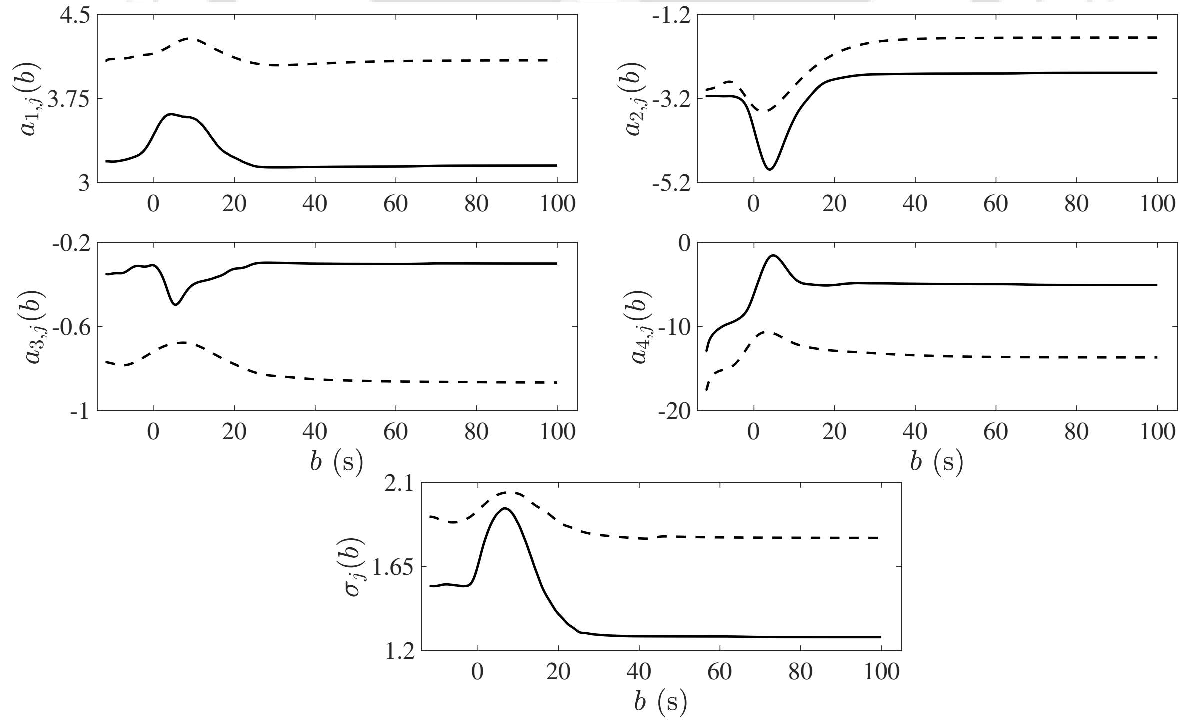

Figure 3.9 Regression coefficients for $\ln(\bar{E}_j(b))$ and the standard deviations of errors in the cases of levels $j = -10$ (solid line) and $j = -1$ (dotted line)

energy arrival pattern is fully governed by the variation of regression coefficients along b and the former affects the level-wise SMD, defined as the duration corresponding to the central 90% energy arrival (Trifunac and Brady, 1975). So, it can be inferred that if the parametric variation of the level-wise SMD obtained from $\hat{E}_j(b)$ is found to be meaningful, the trends of regression coefficients are acceptable.

Figures 3.10(a) to 3.10(c) show the parametric variations of SMD with respect to M, Δ and S , respectively, and for two different levels, $j = -16, -7$, arbitrarily. For Figures 3.10(a) to 3.10(c) the fixed parameters are $\Delta = 50$ km, $S = 1$; $M = 6$, $S = 1$; $M = 6$, $\Delta = 50$ km, respectively. The variation of SMDs for both levels and for all the cases are in general agreement with the facts that SMD is likely to increase with increasing magnitude and distance, and decrease if local site changes from soft soil to rock type. Similar qualitative trends are also observed for other levels. Hence, the regression coefficients are found to be physically sound and so, a scaling model for $\hat{E}_j(b)$ can be considered as a viable proposition to be applied for other region. However, separate regression analysis needs to be carried out for database of other region. For ready reference, the regression coefficients are listed in Table 3.6 for some selected bs and the coefficients can be linearly interpolated for intermediate values of b.

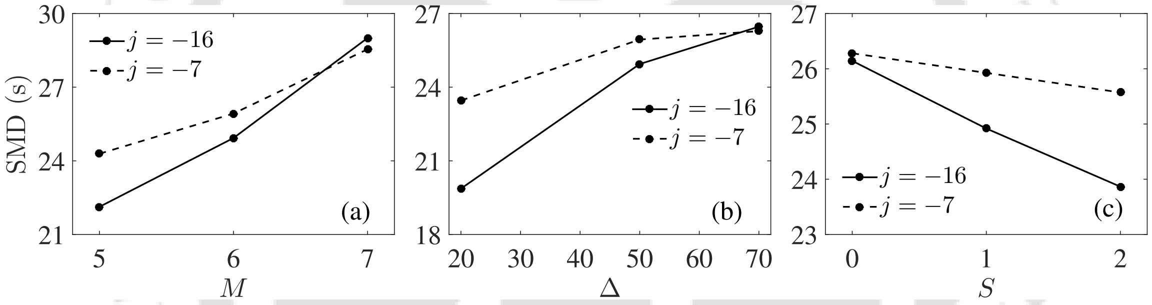

Figure 3.10 Parametric variation of level-wise SMDs with (a) M (b) Δ and (c) S for different levels

3.4 Scenario-Specific Ensemble Generation

It is mentioned earlier that for a given scenario, defined by seismological parameters, the predicted energy arrival pattern for any level j will have some inherent uncertainty. The prediction error has only one parameter, $\sigma_j(b)$, the level-wise standard deviation of $\varepsilon_j(b)$. Hence, the ith sample for the level-wise energy arrival for a given seismic scenario can be modelled as

$$\ln(\hat{E}_{i,j}(b)) = \ln(\hat{E}_j(b)) + k_i \sigma_j(b) \quad ;\forall j \tag{3.22}$$

where, k_i is the sample-specific realization of a standard normal variate. k_i is made level independent so that the time-frequency characteristics of a simulated motion from $\hat{E}_{i,j}(b)$s remain

Table 3.6 Smoothed coefficients and standard deviations of errors of the scaling model for different levels and some instants of b

b (s)	$j=-21$					$j=-20$					$j=-19$					$j=-18$				
	$a_{1,j}$	$a_{2,j}$	$a_{3,j}$	$a_{4,j}$	σ_j	$a_{1,j}$	$a_{2,j}$	$a_{3,j}$	$a_{4,j}$	σ_j	$a_{1,j}$	$a_{2,j}$	$a_{3,j}$	$a_{4,j}$	σ_j	$a_{1,j}$	$a_{2,j}$	$a_{3,j}$	$a_{4,j}$	σ_j
−11.98	1.65	−1.58	−0.34	−14.50	1.65	1.84	−1.86	−0.33	−14.23	1.58	2.09	−2.33	−0.27	−13.66	1.53	2.22	−2.67	−0.18	−12.66	1.49
−8.00	1.68	−1.44	−0.41	−12.00	1.56	1.94	−1.63	−0.39	−12.45	1.49	2.14	−2.02	−0.29	−11.93	1.48	2.31	−2.45	−0.19	−10.97	1.45
−4.00	1.96	−1.75	−0.61	−10.98	1.40	2.23	−1.78	−0.59	−12.09	1.42	2.44	−2.11	−0.52	−11.77	1.40	2.58	−2.51	−0.40	−10.77	1.40
0.00	2.40	−3.50	−0.65	−4.74	1.44	2.56	−3.41	−0.61	−5.51	1.48	2.67	−3.42	−0.59	−5.69	1.51	2.86	−3.84	−0.44	−5.02	1.45
5.00	2.69	−4.13	−0.44	−2.99	1.58	2.82	−4.11	−0.37	−3.2	1.62	2.87	−4.17	−0.38	−2.60	1.67	2.95	−4.52	−0.31	−1.38	1.61
10.00	2.77	−3.86	−0.38	−4.07	1.59	2.85	−3.76	−0.31	−4.22	1.60	2.82	−3.71	−0.31	−3.54	1.65	2.88	−3.90	−0.26	−2.60	1.63
15.00	2.74	−3.68	−0.36	−4.43	1.57	2.79	−3.57	−0.29	−4.46	1.58	2.77	−3.48	−0.27	−3.90	1.61	2.82	−3.60	−0.21	−3.15	1.55
20.00	2.72	−3.65	−0.34	−4.29	1.54	2.76	−3.55	−0.27	−4.24	1.55	2.72	−3.46	−0.24	−3.64	1.58	2.77	−3.56	−0.18	−2.91	1.51
30.00	2.69	−3.58	−0.32	−4.30	1.52	2.74	−3.51	−0.25	−4.20	1.54	2.70	−3.41	−0.23	−3.62	1.57	2.75	−3.51	−0.17	−2.88	1.49
40.00	2.68	−3.54	−0.32	−4.35	1.52	2.73	−3.48	−0.25	−4.24	1.53	2.70	−3.38	−0.23	−3.68	1.56	2.74	−3.49	−0.17	−2.95	1.49
55.00	2.68	−3.53	−0.32	−4.39	1.51	2.73	−3.48	−0.25	−4.25	1.53	2.70	−3.38	−0.23	−3.68	1.56	2.75	−3.49	−0.17	−2.96	1.48
75.00	2.69	−3.52	−0.32	−4.51	1.50	2.74	−3.46	−0.25	−4.35	1.52	2.71	−3.38	−0.23	−3.74	1.56	2.76	−3.48	−0.17	−3.03	1.48
100.00	2.69	−3.51	−0.32	−4.57	1.50	2.74	−3.46	−0.25	−4.38	1.52	2.71	−3.38	−0.23	−3.76	1.56	2.76	−3.48	−0.17	−3.05	1.48

b (s)	$j=-17$					$j=-16$					$j=-15$					$j=-14$				
	$a_{1,j}$	$a_{2,j}$	$a_{3,j}$	$a_{4,j}$	σ_j	$a_{1,j}$	$a_{2,j}$	$a_{3,j}$	$a_{4,j}$	σ_j	$a_{1,j}$	$a_{2,j}$	$a_{3,j}$	$a_{4,j}$	σ_j	$a_{1,j}$	$a_{2,j}$	$a_{3,j}$	$a_{4,j}$	σ_j
−11.98	2.41	−3.05	−0.15	−11.87	1.49	2.54	−3.12	−0.16	−11.89	1.51	2.69	−3.53	−0.19	−10.69	1.48	2.68	−3.44	−0.11	−10.62	1.53
−8.00	2.46	−2.66	−0.15	−10.54	1.44	2.58	−2.96	−0.17	−9.70	1.49	2.72	−3.41	−0.21	−8.32	1.47	2.72	−3.33	−0.10	−8.30	1.52
−4.00	2.67	−2.7	−0.34	−10.15	1.42	2.77	−2.99	−0.29	−9.38	1.45	2.85	−3.30	−0.27	−8.25	1.45	2.84	−3.29	−0.21	−7.90	1.48
0.00	2.91	−3.57	−0.42	−5.96	1.44	3.06	−3.67	−0.39	−6.36	1.44	2.94	−3.69	−0.37	−5.38	1.45	3.04	−3.83	−0.29	−5.23	1.48
5.00	2.99	−4.62	−0.35	−0.62	1.62	3.13	−5.05	−0.32	0.51	1.65	3.13	−5.04	−0.41	0.93	1.70	3.18	−5.12	−0.36	1.16	1.77
10.00	2.87	−3.96	−0.28	−1.61	1.64	3.00	−4.20	−0.25	−0.95	1.70	3.00	−4.21	−0.31	−0.34	1.72	3.11	−4.25	−0.30	−0.42	1.78
15.00	2.79	−3.63	−0.25	−2.05	1.55	2.92	−3.81	−0.20	−1.68	1.57	2.91	−3.76	−0.27	−1.17	1.55	2.98	−3.76	−0.25	−1.16	1.59
20.00	2.72	−3.55	−0.20	−1.86	1.49	2.84	−3.68	−0.15	−1.58	1.48	2.83	−3.66	−0.20	−0.97	1.43	2.88	−3.66	−0.20	−0.85	1.44
30.00	2.71	−3.51	−0.19	−1.86	1.47	2.81	−3.63	−0.13	−1.53	1.45	2.80	−3.63	−0.17	−0.89	1.38	2.83	−3.61	−0.18	−0.63	1.39
40.00	2.71	−3.49	−0.19	−1.94	1.46	2.82	−3.61	−0.13	−1.60	1.44	2.80	−3.61	−0.18	−0.96	1.38	2.83	−3.59	−0.18	−0.70	1.39
55.00	2.71	−3.49	−0.19	−1.96	1.46	2.82	−3.61	−0.13	−1.62	1.44	2.81	−3.61	−0.18	−0.99	1.38	2.84	−3.59	−0.18	−0.73	1.39
75.00	2.72	−3.48	−0.19	−2.03	1.46	2.83	−3.6	−0.13	−1.69	1.44	2.82	−3.59	−0.18	−1.10	1.37	2.85	−3.57	−0.19	−0.87	1.38
100.00	2.72	−3.48	−0.19	−2.05	1.46	2.83	−3.6	−0.13	−1.71	1.44	2.82	−3.59	−0.18	−1.11	1.37	2.85	−3.57	−0.19	−0.88	1.37

b (s)	$j=-13$					$j=-12$					$j=-11$					$j=-10$				
	$a_{1,j}$	$a_{2,j}$	$a_{3,j}$	$a_{4,j}$	σ_j	$a_{1,j}$	$a_{2,j}$	$a_{3,j}$	$a_{4,j}$	σ_j	$a_{1,j}$	$a_{2,j}$	$a_{3,j}$	$a_{4,j}$	σ_j	$a_{1,j}$	$a_{2,j}$	$a_{3,j}$	$a_{4,j}$	σ_j
−11.98	2.75	−3.38	−0.12	−10.78	1.60	2.89	−3.51	−0.21	−10.57	1.63	3.00	−3.36	−0.34	−11.36	1.59	3.19	−3.14	−0.35	−12.97	1.55
−8.00	2.77	−3.31	−0.15	−8.12	1.58	2.92	−3.37	−0.22	−8.27	1.61	3.03	−3.34	−0.36	−8.61	1.59	3.20	−3.15	−0.35	−10.05	1.55
−4.00	2.88	−3.33	−0.23	−7.48	1.56	2.96	−3.39	−0.25	−7.30	1.63	3.06	−3.40	−0.37	−7.51	1.60	3.24	−3.18	−0.31	−9.15	1.55
0.00	3.07	−3.89	−0.34	−4.83	1.63	3.12	−3.95	−0.27	−4.73	1.63	3.23	−4.13	−0.32	−4.35	1.66	3.43	−3.93	−0.31	−6.12	1.66
5.00	3.22	−5.25	−0.38	1.75	1.88	3.29	−4.91	−0.43	0.30	1.92	3.36	−4.85	−0.38	−0.10	1.90	3.61	−4.80	−0.49	−1.55	1.94
10.00	3.11	−4.25	−0.35	−0.01	1.88	3.19	−3.69	−0.40	−2.27	1.90	3.30	−3.81	−0.35	−2.32	1.88	3.57	−3.68	−0.40	−4.25	1.88
15.00	3.00	−3.65	−0.29	−1.32	1.66	3.05	−3.14	−0.37	−3.03	1.64	3.15	−3.21	−0.35	−3.24	1.62	3.37	−3.02	−0.37	−5.04	1.59
20.00	2.89	−3.43	−0.19	−1.36	1.45	2.93	−2.87	−0.28	−3.23	1.42	3.03	−2.96	−0.29	−3.31	1.41	3.22	−2.74	−0.33	−5.06	1.40
30.00	2.83	−3.40	−0.18	−1.02	1.38	2.88	−2.83	−0.24	−3.04	1.32	2.96	−2.83	−0.25	−3.28	1.31	3.14	−2.63	−0.30	−4.86	1.28
40.00	2.84	−3.39	−0.19	−1.09	1.37	2.89	−2.82	−0.24	−3.12	1.32	2.97	−2.81	−0.25	−3.37	1.31	3.14	−2.61	−0.30	−4.91	1.28
55.00	2.84	−3.38	−0.19	−1.13	1.37	2.90	−2.81	−0.24	−3.15	1.32	2.97	−2.80	−0.25	−3.40	1.31	3.14	−2.61	−0.30	−4.95	1.28
75.00	2.86	−3.36	−0.19	−1.25	1.37	2.91	−2.79	−0.25	−3.28	1.31	2.98	−2.77	−0.25	−3.58	1.29	3.15	−2.59	−0.30	−5.05	1.27
100.00	2.86	−3.36	−0.20	−1.26	1.37	2.91	−2.79	−0.25	−3.29	1.31	2.98	−2.77	−0.25	−3.60	1.29	3.15	−2.59	−0.30	−5.06	1.27

b (s)	$j=-9$					$j=-8$					$j=-7$					$j=-6$				
	$a_{1,j}$	$a_{2,j}$	$a_{3,j}$	$a_{4,j}$	σ_j	$a_{1,j}$	$a_{2,j}$	$a_{3,j}$	$a_{4,j}$	σ_j	$a_{1,j}$	$a_{2,j}$	$a_{3,j}$	$a_{4,j}$	σ_j	$a_{1,j}$	$a_{2,j}$	$a_{3,j}$	$a_{4,j}$	σ_j
−11.98	3.27	−3.07	−0.27	−13.47	1.63	3.33	−3.02	−0.31	−13.75	1.70	3.42	−2.89	−0.4	−14.42	1.76	3.63	−3.09	−0.65	−14.59	1.82
−8.00	3.27	−3.11	−0.29	−10.38	1.63	3.33	−3.05	−0.30	−10.71	1.70	3.46	−2.95	−0.41	−11.48	1.77	3.65	−3.12	−0.66	−11.64	1.83
−4.00	3.30	−3.21	−0.27	−9.15	1.62	3.34	−3.13	−0.30	−9.44	1.70	3.51	−3.09	−0.41	−10.26	1.78	3.71	−3.32	−0.65	−10.21	1.85
0.00	3.44	−4.05	−0.25	−5.59	1.74	3.53	−3.90	−0.31	−6.35	1.79	3.63	−3.67	−0.45	−7.60	1.90	3.85	−4.07	−0.68	−7.05	1.95
5.00	3.59	−4.73	−0.33	−1.77	1.97	3.65	−4.40	−0.40	−3.12	2.05	3.79	−4.13	−0.56	−4.88	2.16	3.93	−4.15	−0.70	−5.45	2.08
10.00	3.58	−3.74	−0.27	−4.19	1.92	3.60	−3.34	−0.33	−5.61	2.00	3.84	−3.42	−0.50	−6.66	2.07	3.88	−3.40	−0.60	−6.93	2.02
15.00	3.40	−3.06	−0.28	−5.15	1.70	3.46	−2.79	−0.33	−6.29	1.77	3.63	−2.87	−0.54	−6.88	1.84	3.72	−2.80	−0.61	−7.68	1.84
20.00	3.31	−2.82	−0.27	−5.28	1.53	3.33	−2.61	−0.31	−5.97	1.60	3.48	−2.58	−0.53	−6.78	1.66	3.62	−2.52	−0.62	−7.84	1.70
30.00	3.20	−2.68	−0.24	−5.00	1.40	3.24	−2.48	−0.31	−5.76	1.48	3.38	−2.45	−0.52	−6.49	1.56	3.50	−2.36	−0.62	−7.55	1.59
40.00	3.20	−2.66	−0.24	−5.07	1.39	3.24	−2.46	−0.32	−5.82	1.47	3.37	−2.43	−0.53	−6.55	1.55	3.50	−2.31	−0.62	−7.64	1.58
55.00	3.20	−2.66	−0.24	−5.10	1.39	3.24	−2.45	−0.32	−5.86	1.47	3.38	−2.42	−0.53	−6.59	1.54	3.50	−2.31	−0.62	−7.7	1.58
75.00	3.21	−2.64	−0.24	−5.21	1.38	3.25	−2.44	−0.31	−5.98	1.47	3.38	−2.41	−0.53	−6.66	1.54	3.51	−2.30	−0.62	−7.74	1.58
100.00	3.21	−2.64	−0.24	−5.22	1.38	3.25	−2.43	−0.32	−5.99	1.47	3.39	−2.41	−0.53	−6.67	1.54	3.51	−2.30	−0.62	−7.75	1.58

b (s)	$j=-5$					$j=-4$					$j=-3$					$j=-2$				
	$a_{1,j}$	$a_{2,j}$	$a_{3,j}$	$a_{4,j}$	σ_j	$a_{1,j}$	$a_{2,j}$	$a_{3,j}$	$a_{4,j}$	σ_j	$a_{1,j}$	$a_{2,j}$	$a_{3,j}$	$a_{4,j}$	σ_j	$a_{1,j}$	$a_{2,j}$	$a_{3,j}$	$a_{4,j}$	σ_j
−11.98	3.75	−2.90	−0.7	−15.91	1.90	3.82	−2.67	−0.65	−17.18	1.81	3.93	−2.79	−0.71	−17.33	1.84	4.08	−2.50	−0.77	−19.25	1.83
−8.00	3.76	−2.97	−0.71	−12.77	1.87	3.84	−2.68	−0.64	−14.31	1.80	3.94	−2.81	−0.71	−14.35	1.83	4.08	−2.58	−0.76	−16.03	1.80
−4.00	3.79	−3.16	−0.71	−11.13	1.88	3.87	−2.87	−0.63	−12.71	1.84	3.94	−2.98	−0.70	−12.69	1.85	4.08	−2.80	−0.73	−14.20	1.81
0.00	3.89	−3.81	−0.76	−8.08	1.99	3.97	−3.52	−0.65	−9.75	1.94	4.02	−3.54	−0.67	−10.03	1.95	4.13	−3.29	−0.65	−11.76	1.90
5.00	3.96	−3.91	−0.79	−6.44	2.08	4.09	−3.72	−0.70	−8.10	2.07	4.16	−3.78	−0.65	−8.58	2.05	4.20	−3.52	−0.55	−10.11	1.97
10.00	3.94	−3.33	−0.79	−7.50	2.02	4.12	−3.21	−0.77	−9.10	2.05	4.16	−3.24	−0.68	−9.52	1.97	4.23	−3.09	−0.59	−10.85	1.93
15.00	3.81	−2.79	−0.82	−8.16	1.88	3.99	−2.68	−0.81	−9.70	1.90	4.02	−2.67	−0.72	−10.18	1.82	4.13	−2.59	−0.70	−11.43	1.84
20.00	3.68	−2.49	−0.80	−8.23	1.76	3.86	−2.41	−0.82	−9.61	1.76	3.92	−2.38	−0.73	−10.34	1.73	4.02	−2.30	−0.77	−11.44	1.77
30.00	3.54	−2.23	−0.79	−8.14	1.65	3.74	−2.12	−0.83	−9.75	1.66	3.81	−2.13	−0.74	−10.35	1.65	3.91	−1.98	−0.82	−11.62	1.70
40.00	3.54	−2.17	−0.79	−8.30	1.63	3.73	−2.03	−0.84	−9.92	1.64	3.81	−2.04	−0.75	−10.60	1.64	3.91	−1.86	−0.83	−11.99	1.70
55.00	3.54	−2.16	−0.80	−8.36	1.62	3.74	−2.02	−0.85	−10.02	1.65	3.82	−2.02	−0.76	−10.74	1.64	3.92	−1.82	−0.84	−12.19	1.70
75.00	3.55	−2.16	−0.80	−8.39	1.62	3.74	−2.01	−0.85	−10.06	1.65	3.83	−2.01	−0.76	−10.79	1.63	3.93	−1.81	−0.84	−12.26	1.69
100.00	3.55	−2.16	−0.80	−8.41	1.62	3.74	−2.01	−0.85	−10.07	1.65	3.83	−2.01	−0.76	−10.80	1.63	3.93	−1.81	−0.85	−12.28	1.69

b (s)	$j=-1$					$j=0$					$j=1$					$j=2$				
	$a_{1,j}$	$a_{2,j}$	$a_{3,j}$	$a_{4,j}$	σ_j	$a_{1,j}$	$a_{2,j}$	$a_{3,j}$	$a_{4,j}$	σ_j	$a_{1,j}$	$a_{2,j}$	$a_{3,j}$	$a_{4,j}$	σ_j	$a_{1,j}$	$a_{2,j}$	$a_{3,j}$	$a_{4,j}$	σ_j
−11.98	4.09	−3.00	−0.77	−17.58	1.92	4.24	−2.81	−0.88	−19.11	2.07	4.49	−2.24	−0.88	−22.80	2.02	4.50	−1.93	−0.81	−24.26	1.99
−8.00	4.10	−2.86	−0.78	−15.21	1.89	4.25	−2.67	−0.85	−16.78	2.01	4.50	−2.34	−0.84	−19.60	1.98	4.52	−2.16	−0.79	−20.64	1.95
−4.00	4.13	−2.91	−0.76	−14.12	1.89	4.28	−2.85	−0.79	−15.34	1.98	4.50	−2.65	−0.79	−17.43	1.98	4.56	−2.49	−0.76	−18.59	1.94
0.00	4.15	−3.40	−0.72	−11.48	1.95	4.30	−3.32	−0.75	−12.81	2.02	4.54	−2.95	−0.77	−15.69	2.04	4.63	−2.68	−0.73	−17.47	2.00
5.00	4.24	−3.40	−0.68	−10.83	2.04	4.27	−3.35	−0.72	−11.41	2.08	4.61	−2.95	−0.77	−15.02	2.11	4.69	−2.60	−0.73	−17.14	2.05
10.00	4.28	−2.91	−0.69	−12.01	2.04	4.23	−2.97	−0.72	−11.77	2.09	4.59	−2.70	−0.83	−14.98	2.11	4.69	−2.31	−0.76	−17.46	2.06
15.00	4.19	−2.45	−0.73	−12.59	1.97	4.20	−2.59	−0.76	−12.45	2.05	4.53	−2.42	−0.90	−15.10	2.07	4.66	−2.02	−0.77	−17.84	2.07
20.00	4.12	−2.14	−0.78	−12.89	1.89	4.15	−2.29	−0.82	−12.88	1.97	4.49	−2.18	−0.95	−15.40	2.02	4.63	−1.77	−0.78	−18.27	2.07
30.00	4.05	−1.85	−0.84	−13.19	1.82	4.09	−1.99	−0.87	−13.24	1.91	4.45	−1.86	−1.02	−15.91	1.96	4.62	−1.48	−0.82	−18.87	2.06
40.00	4.06	−1.78	−0.85	−13.42	1.80	4.13	−1.90	−0.90	−13.64	1.90	4.47	−1.74	−1.05	−16.30	1.93	4.64	−1.38	−0.86	−19.23	2.06
55.00	4.08	−1.76	−0.86	−13.60	1.81	4.17	−1.85	−0.92	−13.98	1.88	4.50	−1.67	−1.05	−16.71	1.94	4.67	−1.32	−0.89	−19.57	2.06
75.00	4.09	−1.75	−0.86	−13.66	1.80	4.18	−1.84	−0.92	−14.10	1.89	4.51	−1.65	−1.05	−16.85	1.93	4.69	−1.31	−0.89	−19.71	2.05
100.00	4.09	−1.75	−0.87	−13.68	1.80	4.18	−1.83	−0.93	−14.13	1.89	4.52	−1.65	−1.05	−16.88	1.93	4.70	−1.30	−0.90	−19.76	2.07

b (s)	$j=3$					$j=4$					$j=5$					$j=6$				
	$a_{1,j}$	$a_{2,j}$	$a_{3,j}$	$a_{4,j}$	σ_j	$a_{1,j}$	$a_{2,j}$	$a_{3,j}$	$a_{4,j}$	σ_j	$a_{1,j}$	$a_{2,j}$	$a_{3,j}$	$a_{4,j}$	σ_j	$a_{1,j}$	$a_{2,j}$	$a_{3,j}$	$a_{4,j}$	σ_j
−11.98	4.55	−2.40	−0.76	−23.35	2.23	4.63	−2.39	−0.65	−24.09	2.22	5.00	−2.62	−0.47	−25.55	2.14	4.87	−3.02	−0.62	−22.94	2.38
−8.00	4.63	−2.56	−0.74	−20.26	2.17	4.71	−2.41	−0.60	−21.48	2.14	5.01	−2.64	−0.48	−22.54	2.12	4.91	−2.88	−0.58	−20.8	2.38
−4.00	4.74	−2.77	−0.69	−19.10	2.13	4.82	−2.49	−0.54	−20.84	2.08	5.00	−2.63	−0.49	−21.42	2.14	4.95	−2.69	−0.52	−20.83	2.41
0.00	4.80	−2.84	−0.64	−18.39	2.11	4.90	−2.52	−0.52	−20.41	2.07	5.01	−2.54	−0.50	−21.06	2.21	4.98	−2.50	−0.47	−21.06	2.44
5.00	4.84	−2.74	−0.64	−18.13	2.13	4.96	−2.43	−0.51	−20.34	2.11	5.03	−2.31	−0.51	−21.27	2.27	5.00	−2.26	−0.45	−21.44	2.46
10.00	4.85	−2.51	−0.67	−18.36	2.16	4.97	−2.18	−0.51	−20.75	2.08	5.04	−2.02	−0.53	−21.89	2.29	5.01	−2.03	−0.46	−21.89	2.47
15.00	4.84	−2.19	−0.70	−18.92	2.20	4.96	−1.87	−0.53	−21.35	2.08	5.05	−1.74	−0.55	−22.55	2.30	5.02	−1.81	−0.50	−22.35	2.46
20.00	4.82	−1.86	−0.73	−19.67	2.23	4.95	−1.60	−0.57	−21.93	2.11	5.04	−1.50	−0.59	−23.09	2.30	5.02	−1.62	−0.55	−22.76	2.46
30.00	4.80	−1.39	−0.78	−20.88	2.24	4.92	−1.22	−0.64	−22.71	2.14	5.03	−1.18	−0.68	−23.75	2.29	5.02	−1.34	−0.65	−23.32	2.46
40.00	4.80	−1.20	−0.82	−21.42	2.21	4.92	−1.06	−0.71	−23.10	2.15	5.04	−1.06	−0.75	−24.04	2.30	5.02	−1.23	−0.73	−23.55	2.46
55.00	4.84	−1.13	−0.86	−21.76	2.20	4.95	−0.98	−0.76	−23.50	2.14	5.07	−1.01	−0.81	−24.29	2.29	5.05	−1.20	−0.79	−23.76	2.45
75.00	4.86	−1.10	−0.88	−21.98	2.18	4.98	−0.95	−0.78	−23.69	2.13	5.10	−1.00	−0.84	−24.44	2.28	5.08	−1.19	−0.81	−23.89	2.44
100.00	4.86	−1.09	−0.88	−22.03	2.17	4.98	−0.94	−0.79	−23.76	2.12	5.11	−0.99	−0.85	−24.51	2.28	5.09	−1.16	−0.82	−24.01	2.43

b (s)	$j=7$					$j=8$					$j=9$					$j=10$				
	$a_{1,j}$	$a_{2,j}$	$a_{3,j}$	$a_{4,j}$	σ_j	$a_{1,j}$	$a_{2,j}$	$a_{3,j}$	$a_{4,j}$	σ_j	$a_{1,j}$	$a_{2,j}$	$a_{3,j}$	$a_{4,j}$	σ_j	$a_{1,j}$	$a_{2,j}$	$a_{3,j}$	$a_{4,j}$	σ_j
−11.98	Regression analyses not performed for this range of b and j																			
−8.00																				
−4.00																				
0.00																				
5.00																				
10.00																				
15.00																				
20.00																				
30.00																				
40.00																				
55.00																				
75.00																				
100.00	5.29	−1.12	−0.86	−25.62	2.46	5.22	−0.85	−0.62	−26.94	2.36	5.36	−0.46	−0.52	−29.89	2.13	5.09	−0.47	−0.64	−28.69	2.05

realistic, otherwise only one or a few narrowband waves can dominate the simulated motion – a phenomenon that has never been observed in the recorded data set. Further, the standard deviation of $\varepsilon_j(b)$ is smoothened along b before applying in Eq. (3.22) so that the estimated energy arrival remains smooth and the extracted $V_j(b)$ remains slow varying. It is further understood that $\hat{E}_{i,j}(b)$ for all j actually define the hidden level-wise amplitude modulations for the ith recording process included in the scenario. It should be noted that, in principle, $\hat{E}_{i,j}(b)$ is a non-decreasing function of b, however, some local anomaly may arise occasionally where the energy arrival curve is expected to be quite flat. To rectify this local anomaly, $\hat{E}_{i,j}(b)$ is forcefully made non-decreasing by replacing any local depression by horizontal trend (see Figure 3.11). From $\hat{E}_{i,j}(b)$s the corresponding sample of motion is computed in similar manner as a sample is computed from $\bar{E}_j(b)$ in Section 3.2.2. Hence, a sample of a given scenario will have inherent uncertainties arising from (i) which process the scenario may represent and (ii) which random realization it takes for that process.

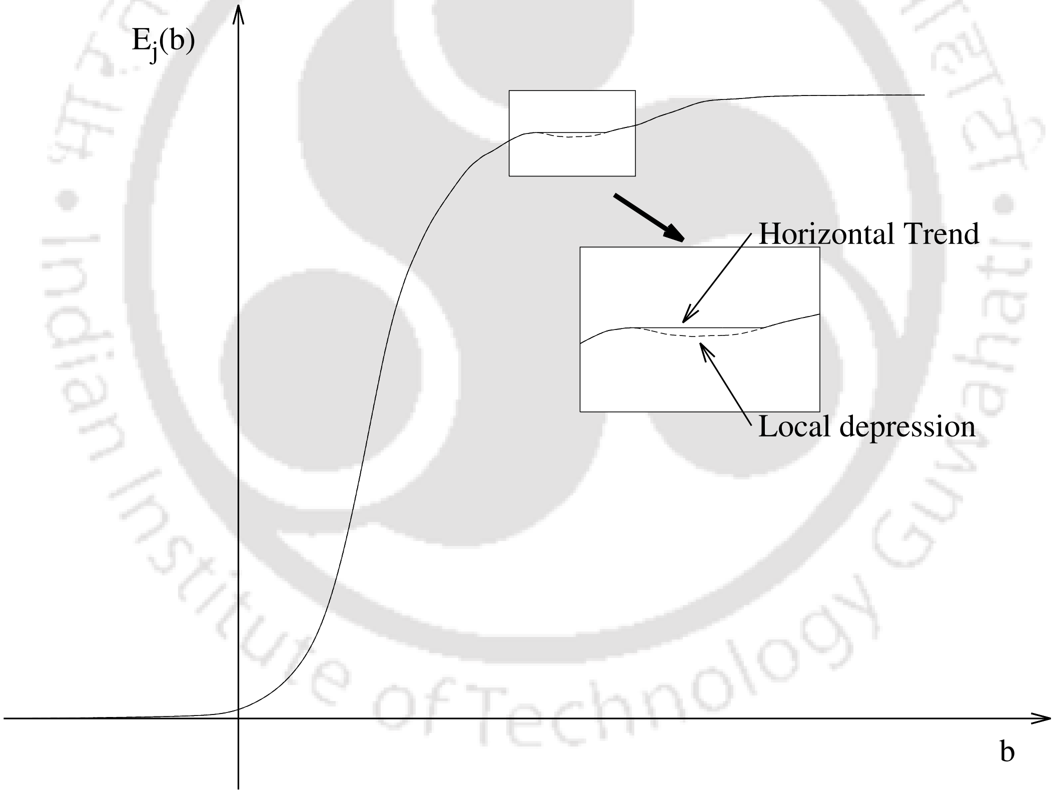

Figure 3.11 Schematic diagram for the proposed correction to ensure non-decreasing energy arrival curve

It is interesting to see if the samples generated by the above method can represent the expected trend. For this purpose, the median trend of response spectra, obtained from different scenario-specific ensembles, have been compared with those obtained directly from a GMPE developed using the same database. The regression coefficients of a PSV scaling model is obtained using the maximum likelihood method (Joyner and Boore, 1993), and the mathematical form of the scaling model is chosen as

$$\ln(PSV(T)) = b_1(T)M + b_2(T)\ln\Delta + b_3(T)S + b_4(T) \tag{3.23}$$

through the same independent parameters as considered for modelling $\bar{E}_j(b)$. The error in the estimation of the scaling model is defined as

$$\varepsilon_{\mathrm{PSV}}(T) = \ln(PSV(T)) - \ln(\widehat{PSV}(T)) \tag{3.24}$$

where, $\ln(\widehat{PSV}(T))$ is the estimated PSV using Eq (3.23) through estimated smooth regression coefficients. Further, $\varepsilon_{\mathrm{PSV}}(T)$ is normal variate with mean zero and standard deviation $\sigma_{\mathrm{PSV}}(T)$.

For the numerical comparison, two hypothetical seismic scenarios are considered for generating 500 samples for each of them. In the first case $M = 5.0$, $R = 40$ km, $h = 8$ km, $S = 1$ (Scenario 1) and for the second case $M = 7.0$, $R = 50$ km, $h = 10$ km, $S = 0$ (Scenario 2) are considered. In either case the values for Δ are computed accordingly (Trifunac and Lee, 1990, 1989). Figures 3.12 shows the median estimates of the derived spectra from samples for the two scenarios. The same figure also shows the median estimates, $\ln(\widehat{PSV}(T))$s, obtained from the PSV scaling model for the two scenarios. It is clear that the median estimates of the PSV spectra from simulated ensemble are in reasonable agreement with those obtained directly from the PSV scaling model. This finding carries significance because the frequency-dependent smooth energy arrival curve is very low level information, which speaks for the hidden normalized amplitude modulation.

Now to see the variability of temporal features, two random samples are arbitrarily selected for Scenario 1 and Scenario 2 and are shown in Figures 3.13 and 3.14. Apart from the varied visual characteristics, the strengths of different records are also varying as any scenario may represent different recording processes with different sample uncertainties. Moreover, it is found that the median SMD of 500 samples for Scenario 1 is 22.3 s and that for Scenario 2 is 36.77 s. This also suggests that the median SMD of an ensemble is following the expected trend with respect to seismic scenario, because SMD for a smaller and nearer event (like Scenario 1) is likely to be smaller than that for a larger and farther event (like Scenario 2). An SMD model is developed using the same database with the same mathematical form as proposed by Trifunac and Brady (1975), which is given as

$$SMD = c_1S + c_2M + c_3R \tag{3.25}$$

The error in the estimation of the scaling model is defined as

$$\varepsilon_{\mathrm{SMD}} = SMD - \widehat{SMD} \tag{3.26}$$

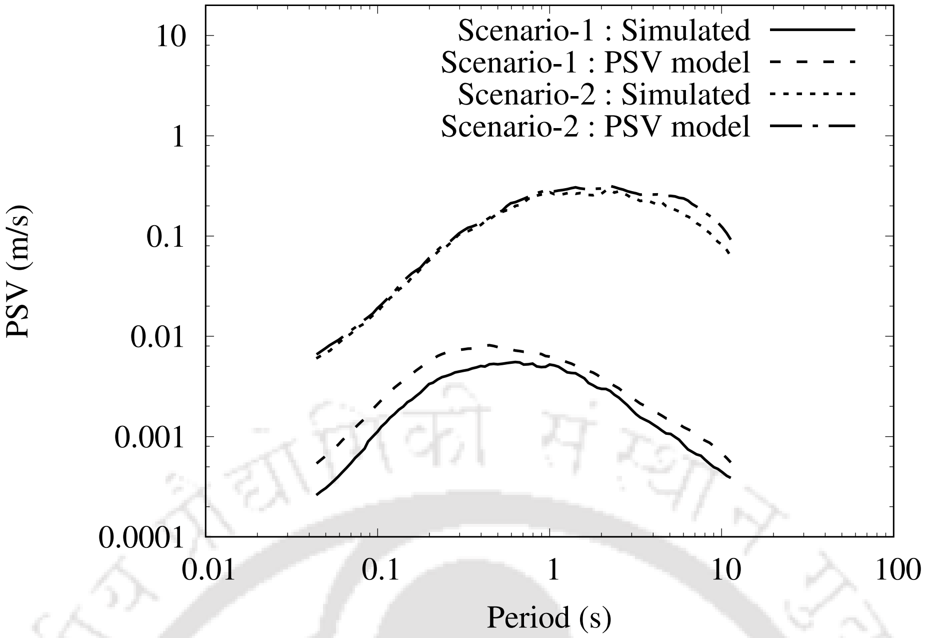

Figure 3.12 Comparison of median spectra obtained from the simulated ensembles and from the PSV scaling model for two different scenarios

where, $\widehat{SMD}$ is the estimated SMD using Eq (3.25) through estimated regression coefficients (obtained via least-square method). The median SMDs calculated from the scaling model for Scenario 1 and Scenario 2 are 18.0 s and 34.16 s, respectively, which are close to the corresponding values obtained from the scenario-specific ensembles.

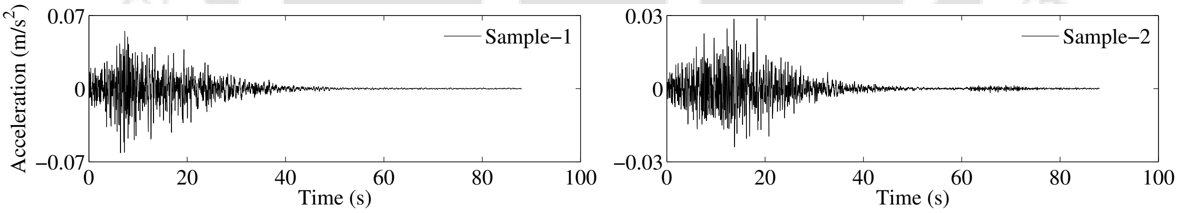

Figure 3.13 Two arbitrarily selected random samples for Scenario 1

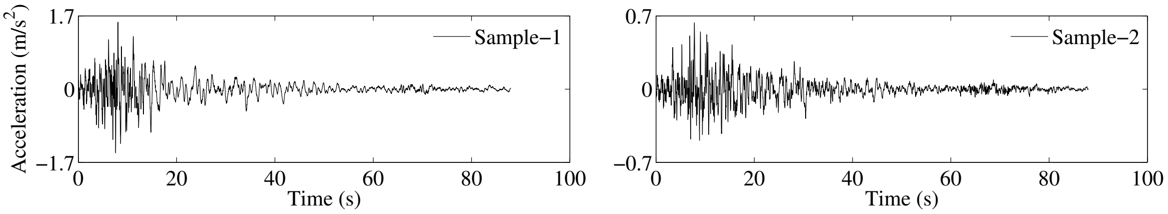

Figure 3.14 Two arbitrarily selected random samples for Scenario 2

The uncertainties of PSV spectra separately obtained from a PSV scaling model and from a scenario-specific ensemble are not compatible with each other. The PSV model is regressed using one data per seismic scenario, and hence, the inherent uncertainty is computed considering all scenarios. For the same reason, the aleatory uncertainty of such a GMPE is essentially scenario independent. On the other hand, for the scenario-specific ensemble, there are two types of uncertainty; (i) recording process represented by the scenario is uncertain, (ii) level-wise sample of a given recording process is uncertain. Apart from them, there is additional variability in the composite ground motion due to positive or negative interference of different decomposed waves (corresponding to different levels, j). These all make the variability of PSV spectra among an ensemble not only scenario-dependent but also higher than that obtained directly from the PSV model.

The standard deviation of $\ln PSV(T)$ for the simulated ensemble is obtained (from 500 samples for each scenario) so that it can be compared with $\sigma_{\mathrm{PSV}}(T)$ of PSV scaling model. This comparison is shown in Figure 3.15. It is clear that the trends of standard deviations along the period are quite similar in all the cases, though their values corresponding to the ensembles are different for different scenarios and they are also individually higher than that for the PSV scaling model.

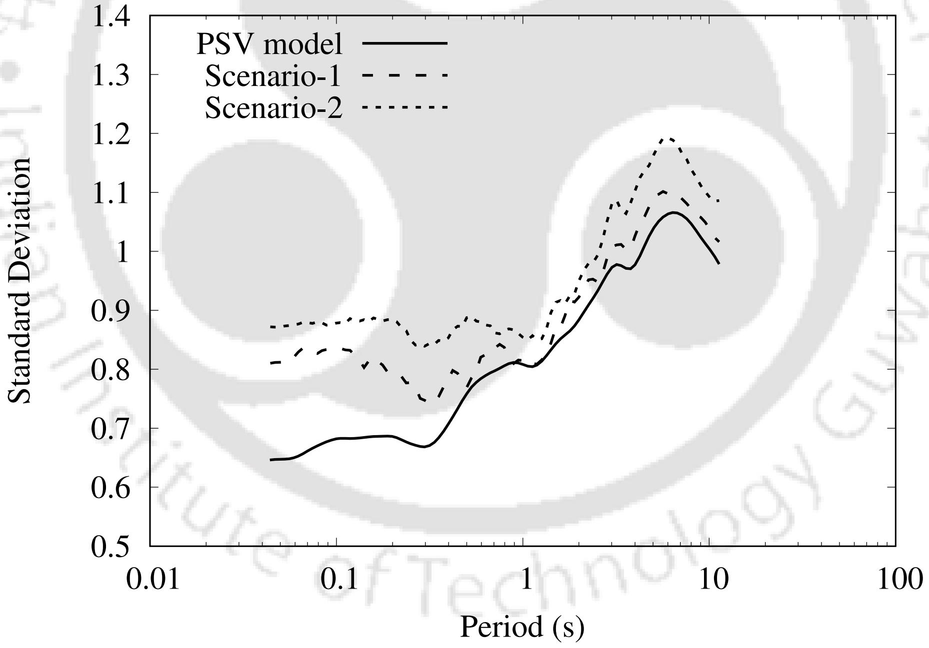

Figure 3.15 Comparison of standard deviations of PSV spectra from different simulated ensembles and the PSV scaling model

The standard deviation of the SMD obtained from the SMD scaling model (Eq. (3.25)) is found to be 11.29 s. But the standard deviations of SMD from both the ensembles are less than 3 s, which indicates that unlike higher variability in spectral estimates the variability in SMD is significantly less. This is due to the fact that by applying different levels of $\sigma_j(b)$ in Eq. (3.22), sufficient variation in the total energy arrival is achieved but sufficient variation is not achieved in the level-wise SMD that governs the SMD of the composite motion (Das and Gupta, 2010). The nonlinear response is affected both by spectral and temporal characteristics, where SMD is only one of the aspects of temporal features. Moreover, spectral variability is in exponential scale and hence, its variability will primarily control the response statistics. Therefore, it can be argued that the scenario-dependent ensemble, thus obtained, can be used to study the region-specific nonlinear response statistics for any structure.

3.5 GMPE-Compatible Ensemble Generation

The scenario-specific nonlinear response statistics will further become a stipulated hazard consistent if the simulated ensemble becomes compatible to one or more GMPEs. Hence, a new algorithm is needed to further modify the estimated energy arrival $\hat{E}_j(b)$ and the model uncertainty $\sigma_j(b)\ \forall j$ so that a scenario-specific ensemble becomes compatible to any target GMPE, both in terms of median estimate and variability.

In the present study, an algorithm is developed next such that the simulated ensemble becomes compatible to both the PSV scaling model and the SMD scaling model. The energy arrival curve of Eq. (3.22) is modified as follows to facilitate the generation of GMPE-compatible ground motions:

$$\ln(\hat{E}_{i,j}(\overline{b_i})) = \ln(\hat{E}_j(b)) + \ln(\alpha_{1,j}) + \alpha_{2,j} k_i \sigma_j(b) \quad ;\forall j \tag{3.27}$$

where,

$$\overline{b_i} = p_{1,i}\, b + p_{2,i}\,, \tag{3.28}$$

$$p_{1,i} = \frac{\beta_i - b_{min}}{b_{max} - b_{min}}\,, \tag{3.29}$$

and

$$p_{2,i} = \beta_i - b_{max}\frac{\beta_i - b_{min}}{b_{max} - b_{min}}\,. \tag{3.30}$$

Here, $\alpha_{1,j}$ is a level-wise factor used to scale up/down the energy arrival such that the median PSV of the simulated motions matches with that of the target PSV model (see Figure 3.16) and $\alpha_{2,j}$ is another level-wise factor (similar to $\alpha_{1,j}$) used to scale up/down $\sigma_j(b)$ such that standard deviation of the PSV from the simulated motions matches that of the target one. Duration of a ground motion can be changed by stretching/shrinking the energy arrival curve along b. Hence, β_i, the sample-wise stretched/shrunk maximum value of b for all levels, is introduced to transform b into $\overline{b_i}$, using Eqs. (3.28) to (3.30) (see Figure 3.17), in order to control the mean and variance of SMD. b_{max} and b_{min} are the maximum and minimum values of b of the energy arrival obtained from Eq. (3.22), which are as mentioned before 100 s and -12 s, respectively. It may be observed that for $\beta_i = b_{max}$, $\alpha_{1,j} = 1.0$ and for $\alpha_{2,j} = 1.0$ Eq. (3.27) reduces to Eq. (3.22). It is now possible to generate an ensemble of energy arrival patterns for simulating GMPE-compatible ground motions by iteratively estimating β_i, $\alpha_{1,j}$ and $\alpha_{2,j}$ by achieving some reasonable tolerance in the quality of match. In the present study, for the purpose of GMPE-compatibility, 200 motions are simulated using Eq. (3.22) and the same PSV and SMD scaling models as in Eqs. (3.23) and (3.25) are used as the target ones. It should be mentioned here that the tuning algorithm will work for any target PSV and SMD models other than the ones developed using the same database. Further, the compatible ensemble, thus obtained, will reflect the scenario-dependent temporal features corresponding to the database using which the energy arrival pattern is regressed and not those corresponding to the database using which any target GMPE is developed.

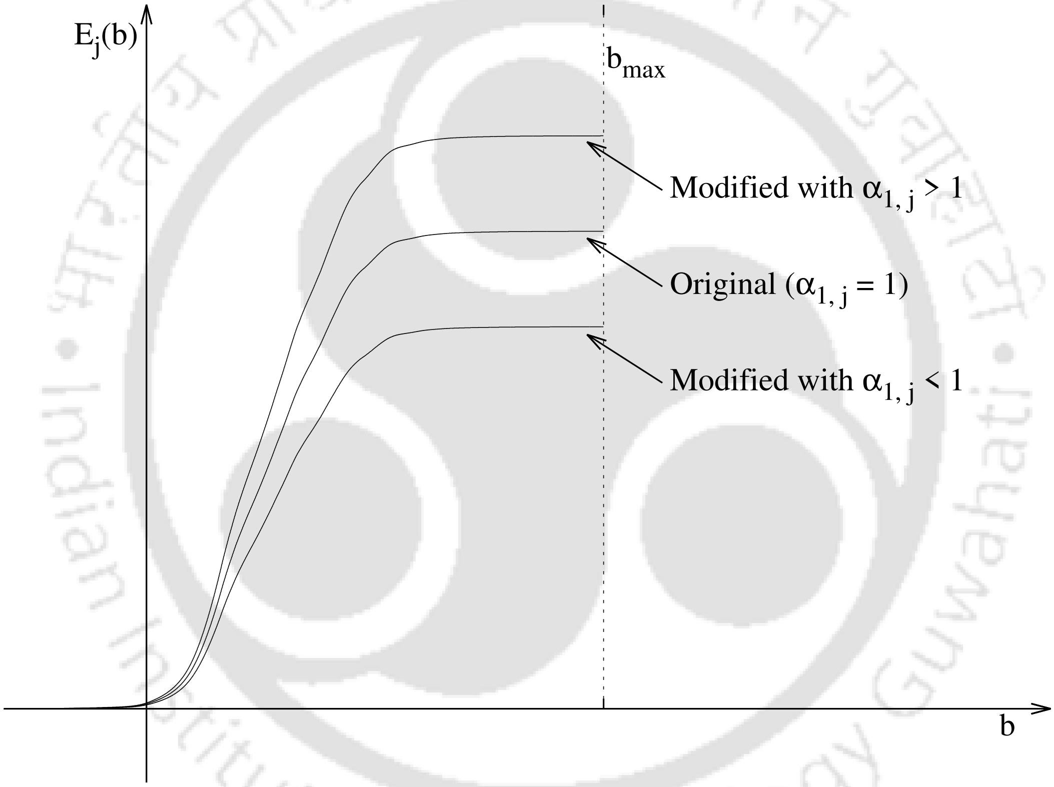

Figure 3.16 Schematic diagram for uniform scaling of energy arrival curve by $\alpha_{1,j}$

Figures 3.18 and 3.19 show the results for the same quantities as shown in Figures 3.12 and 3.15, respectively, with the only exception that the GMPE-compatible case is added to them. It is obvious from the figures that the ensembles are compatible with the target PSV in terms of median and standard deviation. Also, it is found that the median and standard deviation of SMD from the GMPE compatible motions are 34.38 s ($\widehat{SMD} = 34.16$ s) and 10.90 s ($\sigma_{\mathrm{SMD}} = 11.29$ s), respectively. Further, Figure 3.20 shows the PSV values corresponding to different confidence levels from the ensembles for Scenario 2 along with the theoretical estimates from the PSV scaling model (from $\widehat{PSV}(T)$ and $\sigma_{\mathrm{PSV}}(T)$). It can be inferred that, via the proposed simulation technique, the distribution of PSV from GMPE-compatible ensemble is

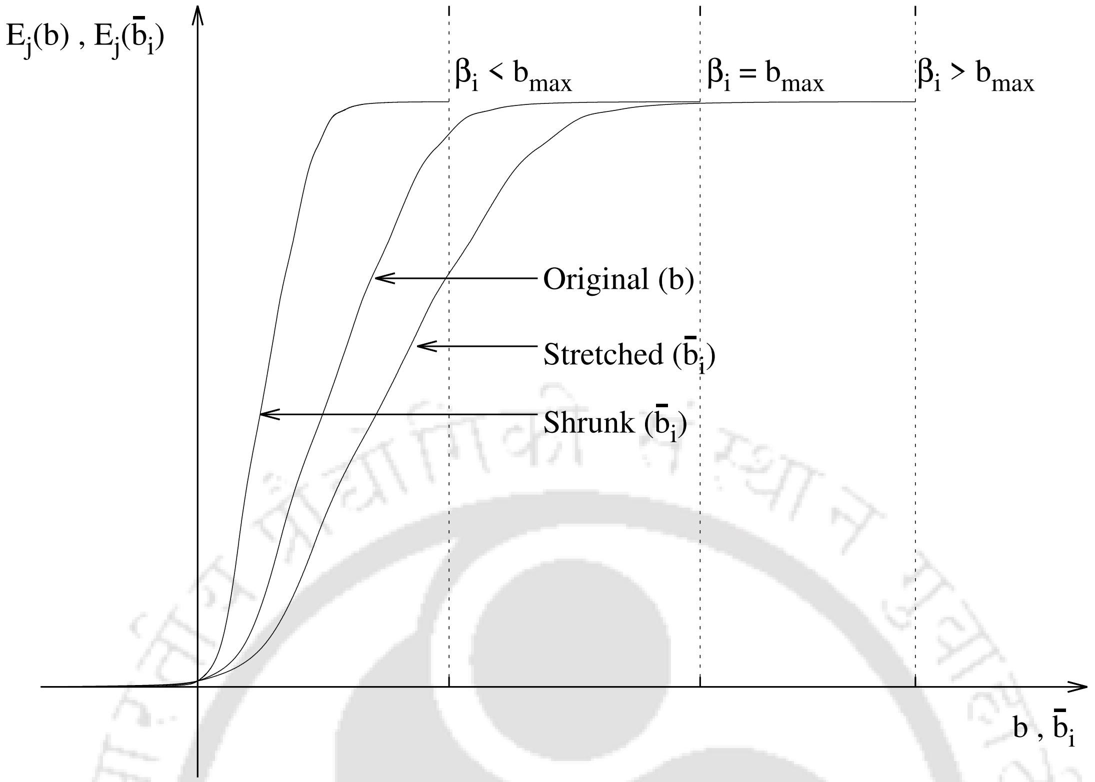

Figure 3.17 Schematic diagram for uniform stretching or shrinking of energy arrival curve by β_i

naturally matching with that of the target PSV model when only median and standard deviation are targeted. This is because both the regression models for PSV and energy arrival curves follow Gaussian distribution (in logarithmic scale) for aleatory uncertainties. Such an acceptable match of distribution (which is more stringent than only median and standard deviation matching) is also achieved, from the same ensemble, when PSV models are developed for damping ratios ranging from 2% to 10%.

3.6 Summary

In the present chapter, a new methodology has been proposed to simulate seismic scenario-specific ensemble of fully nonstationary ground motions. Additionally, the proposed formulation is flexible towards tuning with any target GMPE such that the simulated motions become fully compatible to the GMPE. The current study has been accomplished by the following major steps:

- For any recording process the instantaneous energy arrival of the wavelet coefficients of the recorded motion has been obtained. A new method has been proposed to obtain the frequency-dependent process-specific amplitude modulations from the frequency-

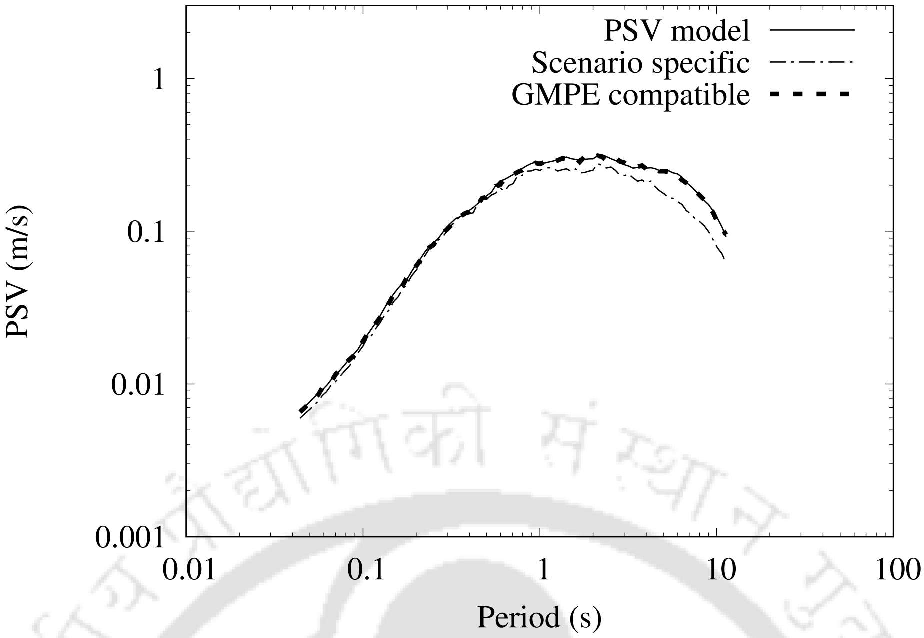

Figure 3.18 Comparison of median PSV spectra obtained from scenario-specific and GMPE-compatible ensembles for Scenario 2

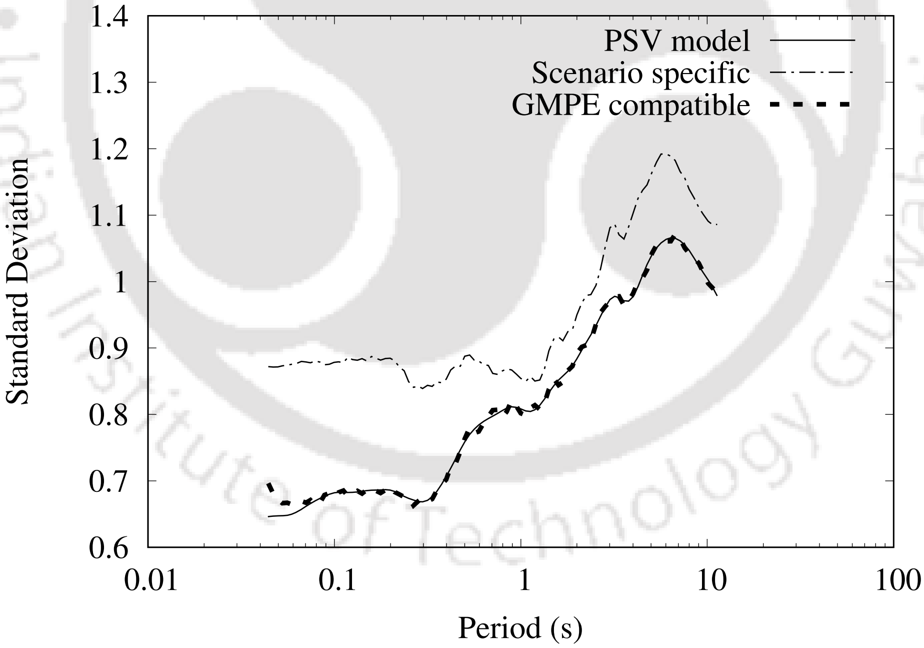

Figure 3.19 Comparison of standard deviations obtained from scenario-specific and GMPE-compatible ensembles for Scenario 2

dependent instantaneous energy arrivals and to simulate several samples of motion from them using the Priestley process assumption. The proposed method is validated by considering various recorded motions from different regions.

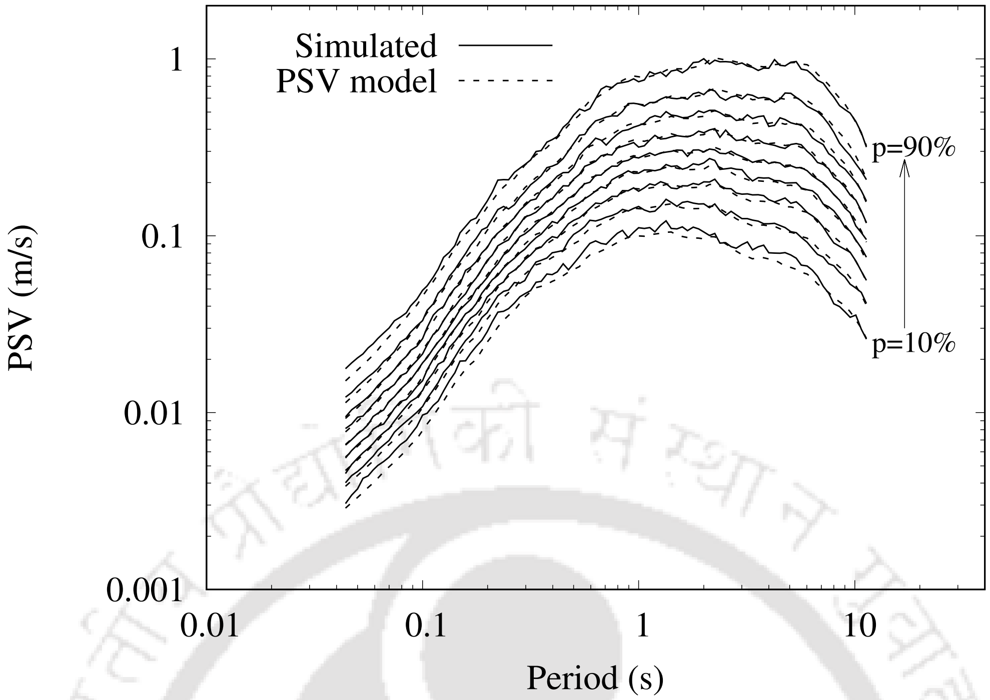

Figure 3.20 Comparison of different percentile PSV spectra obtained from GMPE-compatible ensemble and PSV scaling model for Scenario 2

- An empirical scaling model has been developed for the frequency-dependent instantaneous energy arrival in terms of different seismological parameters so that the energy arrival can be estimated (along with its variation) for a given seismic scenario. The scaling model is developed using the database of the 1999 Chi-Chi earthquake and its major aftershocks.

- A new technique has been developed for simulating scenario-specific ensemble of ground motions from the estimated (scenario-specific) instantaneous energy arrival by combining the currently proposed recording process-based simulation.

- A procedure has been further devised to modify the frequency-dependent estimated energy arrival, using the proposed scaling model, so that the simulated ensembles become fully compatible, in terms of both median and standard deviation, to any target GMPE. In the present study, a PSV and SMD scaling models have been considered in order to demonstrate the effectiveness of the proposed GMPE compatibility. The GMPEs have been developed using the data of the 1999 Chi-Chi earthquake and its major aftershocks.

It has been found that the process-specific simulated ensembles of ground motions capture the time-frequency characteristics of the corresponding recorded motions for different earthquakes from various parts of the world. Also, the simulated samples exhibit nonstationary Gaussian process. The scenario-specific ensembles have been found to exhibit expected trends of the median PSV and median SMD with respect to different seismological parameters. Further, the median quantities obtained from the simulated ensembles have been found to be quite close to those obtained directly from the respective GMPEs (when developed using the same database). The proposed GMPE compatibility algorithm has successfully produced ensembles of ground motions that are fully compatible with both PSV and SMD scaling models simultaneously. Moreover, the GMPE compatibility algorithm has been found to be capable of producing lognormal distribution of derived PSV spectra, which is desirable when the GMPE for PSV yields lognormal distribution. When GMPE compatible ensemble is simulated for 5% damping PSV spectrum, it is found to be compatible with PSV spectra for damping ratios ranging from 2% to 10%.

Chapter 4

STOCHASTIC SIMULATION OF FULLY NONSTATIONARY AFTERSHOCK GROUND MOTIONS FROM KNOWN PRECEDING MAIN SHOCK

4.1 Background

In this chapter, a modification of the process-specific simulation (as proposed in Chapter 3) is proposed where the wavelet-domain is replaced by decomposed time-history domain. Also, an improvement in the extraction of amplitude modulation is attempted where both the normalized shape and the amplitude are characterized. This is done because the amplitude modulations of decomposed time-histories are similar to those of the corresponding wavelet coefficients within the total duration of the motion, decomposed time-histories can be computed much faster than wavelet-coefficients, and the decomposed time-histories provide the ground motion by direct summation. A conditional scaling model for the frequency-dependent energy arrival curve for aftershocks are also proposed that is conditional to the preceding main shock characteristics depending on the seismological parameters for aftershocks and the main shock. Together this conditional scaling model and the proposed process-specific ground motion simulation will enable one to simulate nonstationary aftershock ground motion ensemble from known main shock motion.

4.2 Stochastic Process-Specific Ground Motion Simulation

4.2.1 Proposed Methodology for Process-Specific Simulation

In the present study, any recorded sample, $f(t)$, of a ground motion process, $\mathbf{F}(t)$, is decomposed into 32 different disjoint frequency bands (as in Table 4.1) in accordance with the 32 levels of wavelet coefficients discussed above. Each decomposed time-history, denoted by $f_j(t)$, has very similar nonstationary behaviour as exhibited by the corresponding $W_\psi f(a_j, b)$. E.g., Figure 4.1 shows the decomposed time-histories and the wavelet coefficients for $j = -16$

Table 4.1 Level-wise lower and upper limits of angular frequency, ω_j, and time period, T_j (*the superscripts* l *and* u *indicate the lower and upper limits, respectively*)

Level, j	ω_j^{l} (rad/s)	ω_j^{u} (rad/s)	T_j^{l} (s)	T_j^{u} (s)
−21	119.552	142.172	0.044	0.053
−20	100.531	119.552	0.053	0.063
−19	84.536	100.531	0.063	0.074
−18	71.086	84.536	0.074	0.088
−17	59.776	71.086	0.088	0.105
−16	50.265	59.776	0.105	0.125
−15	42.268	50.265	0.125	0.149
−14	35.543	42.268	0.149	0.177
−13	29.888	35.543	0.177	0.210
−12	25.133	29.888	0.210	0.250
−11	21.134	25.133	0.250	0.297
−10	17.772	21.134	0.297	0.354
−9	14.944	17.772	0.354	0.420
−8	12.566	14.944	0.420	0.500
−7	10.567	12.566	0.500	0.595
−6	8.886	10.567	0.595	0.707
−5	7.472	8.886	0.707	0.841
−4	6.283	7.472	0.841	1.000
−3	5.284	6.283	1.000	1.189
−2	4.443	5.284	1.189	1.414
−1	3.736	4.443	1.414	1.682
0	3.142	3.736	1.682	2.000
1	2.642	3.142	2.000	2.378
2	2.221	2.642	2.378	2.828
3	1.868	2.221	2.828	3.364
4	1.571	1.868	3.364	4.000
5	1.321	1.571	4.000	4.757
6	1.111	1.321	4.757	5.657
7	0.934	1.111	5.657	6.727
8	0.785	0.934	6.727	8.000
9	0.660	0.785	8.000	9.514
10	0.555	0.660	9.514	11.314

and -6 for Barstow station record (090 direction during the 1992 Landers Earthquake). It is evident from the figure that the nature of the amplitude modulation of a decomposed time-history is same as that of the corresponding wavelet coefficients within the total duration of the motion. Further, the decomposed motions can be fast obtained by Fourier analysis as (Das and Hazra, 2018)

$$f_j(t) = \frac{1}{2\pi}\int_{-\sigma\pi/a_j}^{-\pi/a_j} F(\omega)e^{i\omega t}\mathrm{d}\omega + \frac{1}{2\pi}\int_{\pi/a_j}^{\sigma\pi/a_j} F(\omega)e^{i\omega t}\mathrm{d}\omega \tag{4.1}$$

where, $F(\omega) = \int_{-\infty}^{\infty} f(t)e^{-i\omega t}dt$ is the Fourier transform of the recorded signal $f(t)$. In the present work, the process-specific simulation method as in Chapter 3 is shifted verbatim to the decomposed time-history (i.e. $f_j(t)$) from the wavelet coefficients (i.e. $W_\psi f(a_j, b)$). Hence, the deterministic frequency-dependent slow varying modulation is obtained from the smoothed frequency-dependent energy arrival curves for $f(t)$ as

$$V_j(t) = \gamma_j \left[\left(\frac{\mathrm{d}\bar{E}_j(t)}{\mathrm{d}t}\right)_{\mathrm{N}}\right]^{\frac{1}{2}} \tag{4.2}$$

where,

$$E_j(t) = \int_0^t [f_j(\xi)]^2 \mathrm{d}\xi \quad \forall j \tag{4.3}$$

is the frequency-dependent instantaneous cumulative energy arrival, $\bar{E}_j(t)$ is the smooth trend of $E_j(t)$. For the levels $j = 7, 8, 9, 10$, $V_j(t)$ is assumed to be

$$V_j(t) = \gamma_j \tag{4.4}$$

This is because at these levels the dominant periods are large enough not to allow proper extraction of the modulations within the recorded duration of the motion (Das and Gupta, 2011), so it is assumed to be constant. The contribution of the combined energy from these levels to the total energy of the ground motion is usually very less and hence, this assumption will not affect the nonstationarity of the reconstructed motion. $V_j(t)$s are used to modulate samples of a random Gaussian bandlimited process of specific stationary PSDF in order to get random samples of $\mathbf{F}(t)$. In the method in Chapter 3, the values of γ_js are not required because every generated random sample of $\mathbf{F}(t)$ is scaled such that its total energy is same as that of $f(t)$. The proposed simulation technique has been modified such that a single set of 32 γ_js are used for the simulation of all ground motions for a process, which is in general agreement with the Priestley process philosophy. So, the present simulation technique consists of two steps, in which γ_js are determined in the first step and all samples are simulated using this single set of γ_j in the second step.

In the first step, adequate number of trial samples are simulated by matching the energy of each sample (frequency band-wise) with that of $f_j(t)$. These samples are called trial samples because they are not the final ones and are simulated for calculating γ_js only. The value of γ_j

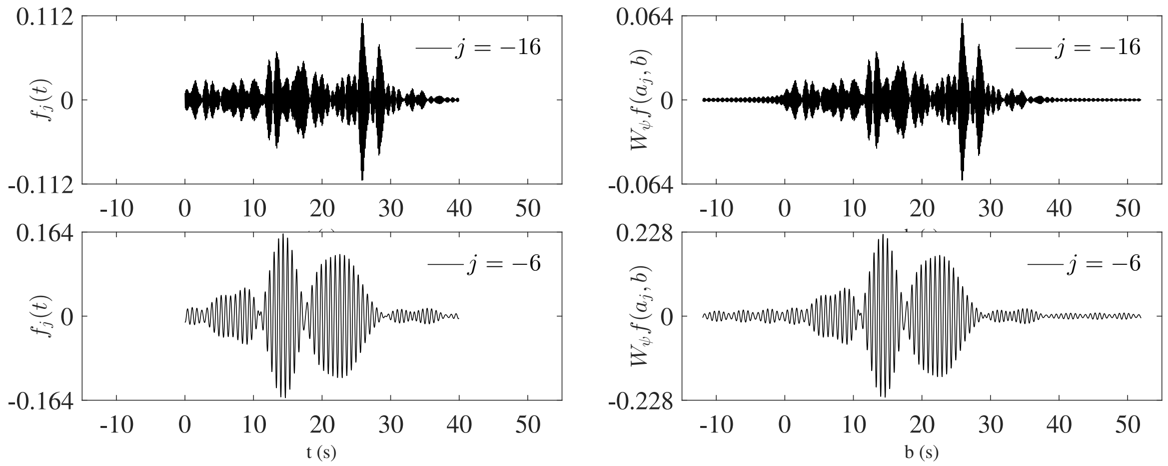

Figure 4.1 Decomposed time-histories $f_j(t)$ and wavelet coefficients $W_\psi f(a_j,b)$ in the case of Barstow station record during the 1992 Landers earthquake for different levels, j

of the ith sample, $\gamma_{j,i}$, is obtained as

$$\gamma_{j,i}=\sqrt{\frac{E_j(T)}{E_{j,i}(T)}} \tag{4.5}$$

where,

$$E_{j,i}(t)=\int_0^t [y_{j,i}(\xi)]^2 \mathrm{d}\xi\,, \tag{4.6}$$

$$y_{j,i}(t)=\bar{V}_j(t)z_{j,i}(t)\,, \tag{4.7}$$

$$\bar{V}_j(t)=\begin{cases}\left[\left(\frac{\mathrm{d}\bar{E}_j(t)}{\mathrm{d}t}\right)_{\mathrm{N}}\right]^{\frac{1}{2}}, & \forall -21\le j\le 6\\ 1.0, & \forall 7\le j\le 10\end{cases} \tag{4.8}$$

T is the total duration of the ground motion, $z_{j,i}(t)$ is a sample of narrow bandlimited white-noise with frequency range corresponding to the level j. Narrow bandlimited white-noise samples were obtained by fourier decomposition (using Eq.(4.1)) of zero-mean Gaussian bandlimited white-noise samples conforming to a stationary PSDF of any specified value, S_0. A narrowband white-noise sample corresponding to jth level is then modulated by $\bar{V}_j(t)$ satisfying the localization criterion as in Chapter 3 to generate $y_{j,i}(t)$. Finally the average value of $\gamma_{j,i}$ is calculated as

$$\bar{\gamma}_j=\frac{\sum_{i=1}^{30}\gamma_{j,i}}{30} \quad \forall j \tag{4.9}$$

Here, the number of trial samples has been taken as 30, since it has been found that $\bar{\gamma}_j$ from 30 trial samples lies within ±2.5% bound with respect to $\bar{\gamma}_j$ from 500 of them. In the second step of simulation, $\bar{\gamma}_j$ is used along with $\bar{V}_j(t)$ for the simulation of as many ground motion samples as intended. Any particular sample generated is specific to the random sample of the bandlimited white-noise of magnitude S_0, thus, the ith sample for $\mathbf{F}(t)$ is obtained as

$$x_i(t) = \sum_{j=-21}^{10} \bar{\gamma}_j \bar{V}_j(t) z_{j,i}(t) \quad \forall j \tag{4.10}$$

It should be mentioned that the product of $\bar{\gamma}_j$ and $z_{j,i}(t)$ is independent of S_0. Any ground motion simulated this way is finally filtered through high-pass Butterworth filter with a cutoff frequency of 0.10 Hz for further use.

The efficacy of the ground motion process-specific simulation technique using wavelet coefficients has been demonstrated in Chapter 3 and as expected, for the present case also the same method works satisfactorily with the decomposed time-histories. Since the time-frequency characteristics are the most important aspects of any (nonstationary) simulated motion, two figures are shown to assess the performance of the proposed process-specific simulation. Figure 4.2 shows three random ground motion samples for the Barstow record along with the recorded motion. It is clear that the temporal features of all the samples are by and large similar to the recorded one though the waveforms are not identical due to randomness. To check whether the time-frequency characteristics of the simulated samples are similar to that of the recorded motion in stochastic sense, evolutionary power spectral density functions (EPSDFs) are calculated for the simulated samples and for the recorded motion in the case of the Barstow recording process. The idealized EPSDF $\Phi_F(t,\omega)$ given a ground motion record can be obtained using the identified (frequency-dependent) deterministic modulation and the theoretical stationary white-noise S_0 as

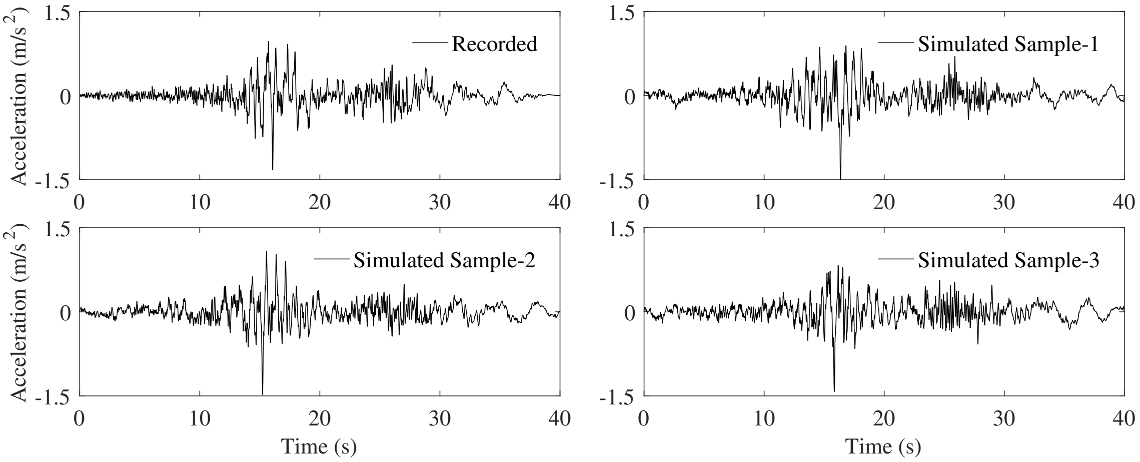

Figure 4.2 Barstow record during the 1992 Landers earthquake along with three random samples of simulated ground motions

$$\Phi_F(t,\omega) = \sum_{j=-21}^{10} V_j^2(t) S_0 \quad \forall\, \omega_{10}^{\mathrm{l}} < \omega < \omega_{-21}^{\mathrm{u}} \tag{4.11}$$

where, $V_j(t) = \bar{\gamma}_j \bar{V}_j(t)$ is the identified deterministic amplitude modulation for the jth frequency band (the product $\bar{\gamma}_j^2 S_0$ is independent of S_0). For the EPSDF of the simulated motions, 500 samples (obtained from Eq. (4.10)) are considered. First the level-(or frequency-)dependent energy arrival curves from each sample is computed and normalized with respect to the maximum value and then the statistical average is taken level-wise. Since these average energy arrival curves are not smooth enough (because of only 500 samples are considered) for its time-derivative to be slow varying, they are further smoothed before taking time-derivative to find the normalized amplitude modulations (see Eq. (4.8)). Let us denote these normalized amplitude modulations by $\tilde{V}_j(t)$. Now the EPSDF of the simulated ensemble $X(t)$ can be expressed being consistent with Eq. (4.11) by

$$\Phi_X(t,\omega) = \sum_{j=-21}^{10} \bar{\gamma}_j^2 \tilde{V}_j^2(t) \frac{1}{2\pi} \int_{-\infty}^{\infty} R_{Z,j}(\tau) e^{-i\omega\tau} d\tau \tag{4.12}$$

where, $R_{Z,j}(\tau)$ is the autocorrelation function of the narrow bandlimited Gaussian white-noise samples corresponding to level j. Since the white-noise process is ergodic, $R_{Z,j}$ is obtained from the temporal autocorrelation of any ith sample $z_{j,i}(t)$ as in Eq. (4.10). Figure 4.3 shows the idealized EPSDF calculated from Eq. (4.11) and the simulated EPSDF from Eq. (4.12), for the Barstow record. It is clear that the simulated EPSDF is quite similar to the idealized EPSDF, which indicates that the deterministic frequency-dependent amplitude modulations, $V_j(t)$s, extracted from the recorded motion are maintained within the samples statistically and the time-frequency characteristics of the recorded motion is replicated into the ensemble. Similar exercise has been carried out with various other recorded motions and the results are found satisfactory. It should be noted that the proposed methodology is based on Priestley process assumption wherein a nonstationary process is obtained by frequency-dependent amplitude modulation of a zero-mean Gaussian stationary process, which ensures that any simulated ground motion ensemble will obey zero-mean Gaussian distribution quite well (see in Chapter 3). The Priestley process-based simulation technique developed here is applicable for any univariate ground motion process, in general.

4.3 Scenario-Specific Aftershock Ground Motion Ensemble

4.3.1 Overview

In Chapter 3 it is shown that from the basic theory of process-specific simulation via frequency-dependent energy arrival curves an earthquake scenario-specific ensemble of ground motions can be simulated through a scaling model of the energy arrival curves with respect to different seismological parameters that define the scenario. In an earlier study, Das and Gupta (2010) showed that the scaling models for response spectrum and strong motion duration can

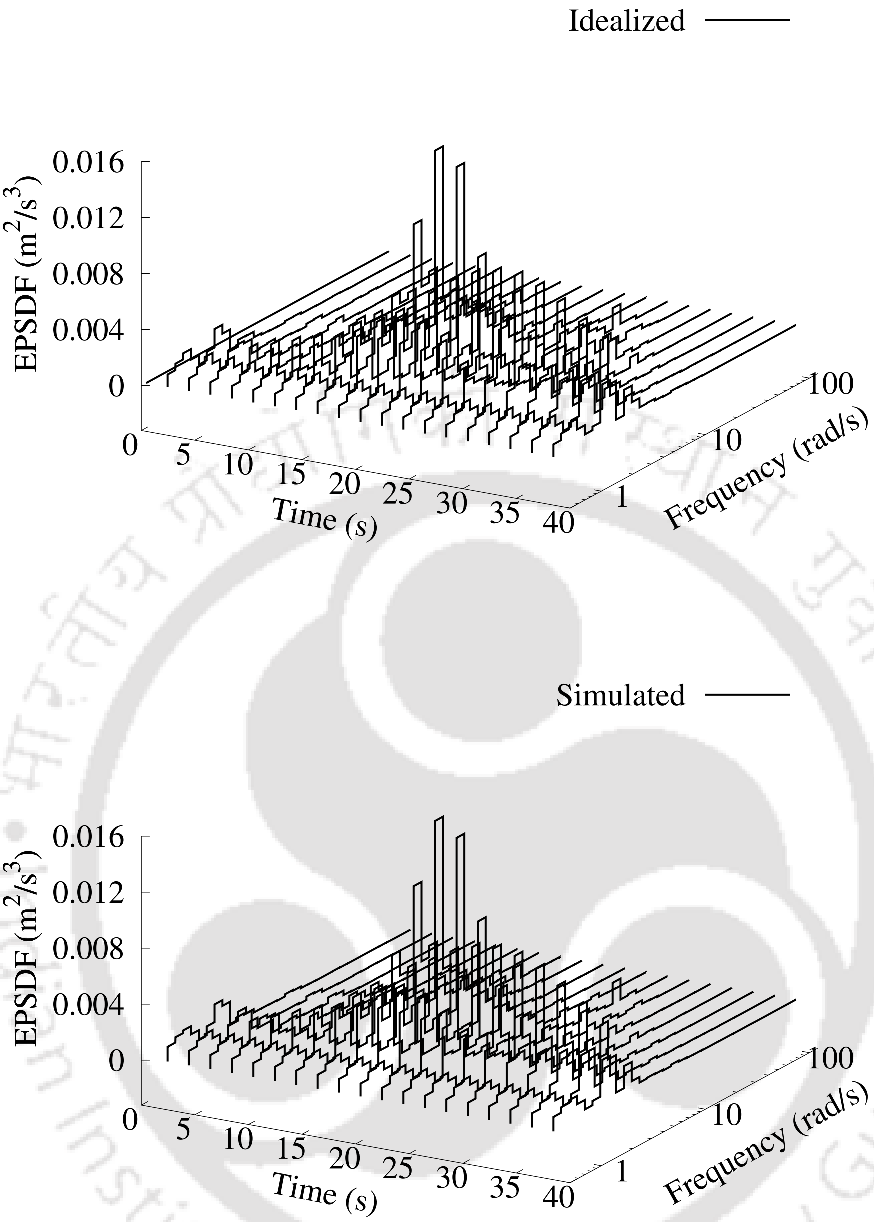

Figure 4.3 Idealized and simulated EPSDFs for Barstow record during the 1992 Landers earthquake

be modified to develop conditional scaling models for the respective quantities exclusively for the aftershocks. Such scaling models use the actual information of the preceding main shock to predict target quantities for the future aftershocks for an anticipated aftershock scenario. Since frequency-dependent energy arrival curves carry the whole information (temporal and spectral) of the ground motion, it is highly opportune to develop a conditional scaling model from the unconditional scaling model of the energy arrival curves. This will enable an analyst to simulate realistic samples of aftershock ground motions with desired variability from the knowledge of the preceding main shock motion for an assumed seismic scenario for the aftershock.

4.3.2 Scaling Model for Aftershocks

It is possible to finally arrive at a conditional scaling model for a quantity from an acceptable form of unconditional scaling model for that quantity (Das and Gupta, 2010). From the knowledge of the basic form of a scaling model for the energy arrival curves (as in Chapter 3), a conditional scaling model for the smoothed instantaneous cumulative energy arrival of aftershocks, $\bar{E}_{\text{Aft},j}(t)$, in terms of $\alpha_j(t)$ (ratio of cumulative energy of aftershock to that of main shock up to time t for level j) is considered as

$$\begin{aligned}\ln(\alpha_j(t)) = \ln\left(\frac{\bar{E}_{\text{Aft},j}(t)}{\bar{E}_{\text{Main},j}(t)}\right) &= a_{1,j}(t)\Delta M + a_{2,j}(t)\Delta M^2 \\ &+ a_{3,j}(t)\ln\left(\frac{\Delta_{\text{Main}}}{\Delta_{\text{Aft}}}\right) + a_{4,j}(t)\left(\Delta_{\text{Main}} - \Delta_{\text{Aft}}\right) \\ &+ a_{5,j}(t)\Delta h + a_{6,j}(t)\Delta MS \quad ;\forall j\end{aligned} \tag{4.13}$$

where, $\bar{E}_{\text{Main},j}(t)$ is the smoothed energy arrival of decomposed motions of main shock, ΔM $(= M_{\text{Main}} - M_{\text{Aft}})$ is the difference between main shock and aftershock magnitudes, , Δ_{Main} and Δ_{Aft} are representative source-to-site distances (due to Trifunac and Lee (1990, 1989)) of main shock and aftershock, respectively, Δh $(= h_{\text{Main}} - h_{\text{Aft}})$ is the difference between main shock and aftershock focal depths and S is the indicator parameter for the local site conditions (S = 0, 1 and 2 for soft soil, stiff soil and rock, respectively). The representative distance Δ takes the finite source dimension into account and in general, depends on M, epicentral distance (R), focal depth (h), time period of seismic wave and shear wave velocity of local site (180 m/s, 270 m/s, 850 m/s for $S = 0$, 1 and 2, respectively). $a_{1,j}(t)$ and $a_{2,j}(t)$ together account for the change in energy arrival due to the magnitude difference while $a_{2,j}(t)$ reflects the saturation of energy arrival for large magnitudes. $a_{3,j}(t)$ and $a_{4,j}(t)$ reflect the change in energy arrival because of different geometrical spreading and inelastic attenuation, respectively, of seismic waves due to difference in representative distances of main shock and aftershock. $a_{5,j}(t)$ and $a_{6,j}(t)$ account for the change in energy arrival due to difference in focal depths and nonlinear site response (with stronger motion having less amplification), respectively.

Same database of ground motions used in Chapter 3 is considered here. Since different motions are having different lengths of record, in order to maintain uniformity the maximum value of t for evaluation of energy arrival is considered as 70 s. It is understood that any shorter record will reach its 100% energy arrival for a smaller value of t than a longer record. Further, for estimation of regression coefficients t is discretized every 0.02 s of interval.

Maximum likehood method (Joyner and Boore, 1993) is used to carry out the regression

Table 4.2 Smoothed coefficients and standard deviations of errors of the conditonal scaling model for different levels and some time-instants

t (s)	$j=-21$					$j=-20$					$j=-19$					$j=-18$					$j=-17$					$j=-16$					$j=-15$					$j=-14$				
	$a_{1,j}$	$a_{3,j}$	$a_{5,j}$	$a_{6,j}$	σ_j	$a_{1,j}$	$a_{3,j}$	$a_{5,j}$	$a_{6,j}$	σ_j	$a_{1,j}$	$a_{3,j}$	$a_{5,j}$	$a_{6,j}$	σ_j	$a_{1,j}$	$a_{3,j}$	$a_{5,j}$	$a_{6,j}$	σ_j	$a_{1,j}$	$a_{3,j}$	$a_{5,j}$	$a_{6,j}$	σ_j	$a_{1,j}$	$a_{3,j}$	$a_{5,j}$	$a_{6,j}$	σ_j	$a_{1,j}$	$a_{3,j}$	$a_{5,j}$	$a_{6,j}$	σ_j	$a_{1,j}$	$a_{3,j}$	$a_{5,j}$	$a_{6,j}$	σ_j
0.02	−1.79	4.93	−0.06	−0.29	1.85	−1.88	5.08	−0.01	−0.36	1.90	−2.10	4.93	0.00	−0.35	1.86	−2.19	4.44	0.07	−0.39	1.77	−2.34	4.07	0.02	−0.27	1.86	−2.59	3.94	0.04	−0.35	2.04	−2.49	3.09	0.03	−0.33	2.13	−3.02	3.35	0.00	−0.16	2.08
1.26	−1.90	4.79	−0.07	−0.26	1.80	−1.96	4.81	−0.01	−0.33	1.81	−2.17	4.67	0.01	−0.28	1.82	−2.19	4.56	0.05	−0.43	1.68	−2.4	4.22	0.01	−0.25	1.80	−2.64	4.07	0.04	−0.30	1.96	−2.51	3.44	0.03	−0.34	2.08	−3.00	3.53	0.00	−0.19	1.97
2.50	−2.05	4.39	−0.07	−0.22	1.76	−2.09	4.56	−0.03	−0.30	1.73	−2.25	4.38	0.01	−0.23	1.75	−2.19	4.48	0.04	−0.43	1.62	−2.51	4.41	0.01	−0.21	1.72	−2.70	4.21	0.04	−0.24	1.87	−2.54	3.79	0.03	−0.33	1.99	−2.95	3.77	0.00	−0.20	1.93
3.76	−2.16	4.04	−0.08	−0.19	1.71	−2.19	4.33	−0.04	−0.26	1.67	−2.30	4.16	0.01	−0.22	1.69	−2.18	4.25	0.03	−0.43	1.62	−2.55	4.37	0.01	−0.19	1.66	−2.66	4.23	0.04	−0.24	1.81	−2.49	3.78	0.03	−0.35	1.93	−2.87	3.86	0.01	−0.20	1.96
5.00	−2.24	3.72	−0.09	−0.17	1.69	−2.24	4.02	−0.05	−0.24	1.64	−2.31	3.81	0.00	−0.23	1.67	−2.16	4.02	0.02	−0.43	1.63	−2.46	4.05	0.00	−0.22	1.65	−2.53	4.01	0.02	−0.28	1.80	−2.37	3.52	0.01	−0.41	1.92	−2.72	3.57	0.01	−0.25	1.99
7.50	−2.39	3.16	−0.10	−0.13	1.72	−2.36	3.42	−0.07	−0.23	1.68	−2.33	3.11	−0.04	−0.24	1.71	−2.17	3.50	−0.03	−0.43	1.63	−2.33	3.23	−0.05	−0.28	1.67	−2.36	3.10	−0.03	−0.33	1.87	−2.23	2.75	−0.07	−0.47	2.00	−2.51	2.67	−0.08	−0.30	2.13
10.00	−2.54	2.94	−0.11	−0.10	1.75	−2.44	3.04	−0.08	−0.22	1.74	−2.38	2.75	−0.06	−0.24	1.71	−2.21	3.07	−0.06	−0.42	1.62	−2.32	2.78	−0.08	−0.28	1.60	−2.30	2.68	−0.06	−0.37	1.75	−2.21	2.19	−0.08	−0.44	1.84	−2.45	2.25	−0.12	−0.32	2.04
15.00	−2.61	2.84	−0.11	−0.08	1.67	−2.50	2.93	−0.09	−0.21	1.65	−2.42	2.71	−0.08	−0.25	1.61	−2.3	2.91	−0.07	−0.37	1.45	−2.36	2.55	−0.08	−0.26	1.40	−2.33	2.49	−0.05	−0.37	1.51	−2.26	2.07	−0.06	−0.40	1.50	−2.45	2.13	−0.09	−0.31	1.64
20.00	−2.64	3.01	−0.12	−0.09	1.66	−2.53	3.03	−0.11	−0.20	1.62	−2.46	2.85	−0.09	−0.23	1.53	−2.32	3.15	−0.08	−0.37	1.36	−2.38	2.70	−0.08	−0.24	1.28	−2.36	2.63	−0.05	−0.34	1.38	−2.28	2.31	−0.06	−0.40	1.33	−2.42	2.33	−0.08	−0.33	1.42
25.00	−2.69	3.00	−0.13	−0.05	1.66	−2.59	3.03	−0.11	−0.16	1.62	−2.50	2.80	−0.10	−0.20	1.52	−2.37	3.07	−0.09	−0.34	1.34	−2.42	2.63	−0.09	−0.22	1.25	−2.39	2.58	−0.06	−0.32	1.34	−2.32	2.36	−0.07	−0.39	1.29	−2.44	2.36	−0.09	−0.34	1.38
35.00	−2.68	2.99	−0.13	−0.04	1.63	−2.6	3.01	−0.12	−0.15	1.59	−2.52	2.78	−0.10	−0.19	1.49	−2.4	3.05	−0.09	−0.32	1.31	−2.45	2.60	−0.10	−0.21	1.24	−2.43	2.56	−0.07	−0.31	1.33	−2.37	2.35	−0.08	−0.38	1.27	−2.49	2.35	−0.10	−0.32	1.36
50.00	−2.67	3.00	−0.13	−0.05	1.62	−2.6	3.02	−0.11	−0.15	1.59	−2.52	2.79	−0.10	−0.19	1.49	−2.41	3.05	−0.10	−0.32	1.31	−2.46	2.60	−0.10	−0.21	1.24	−2.45	2.56	−0.07	−0.30	1.32	−2.38	2.35	−0.08	−0.38	1.26	−2.50	2.35	−0.11	−0.32	1.35
70.00	−2.67	2.99	−0.12	−0.06	1.59	−2.59	3.01	−0.11	−0.15	1.58	−2.52	2.79	−0.10	−0.19	1.48	−2.42	3.05	−0.09	−0.32	1.30	−2.46	2.60	−0.10	−0.21	1.23	−2.45	2.56	−0.07	−0.30	1.32	−2.39	2.35	−0.08	−0.38	1.26	−2.51	2.34	−0.10	−0.32	1.34

t (s)	$j=-13$					$j=-12$					$j=-11$					$j=-10$					$j=-9$					$j=-8$					$j=-7$					$j=-6$				
	$a_{1,j}$	$a_{3,j}$	$a_{5,j}$	$a_{6,j}$	σ_j	$a_{1,j}$	$a_{3,j}$	$a_{5,j}$	$a_{6,j}$	σ_j	$a_{1,j}$	$a_{3,j}$	$a_{5,j}$	$a_{6,j}$	σ_j	$a_{1,j}$	$a_{3,j}$	$a_{5,j}$	$a_{6,j}$	σ_j	$a_{1,j}$	$a_{3,j}$	$a_{5,j}$	$a_{6,j}$	σ_j	$a_{1,j}$	$a_{3,j}$	$a_{5,j}$	$a_{6,j}$	σ_j	$a_{1,j}$	$a_{3,j}$	$a_{5,j}$	$a_{6,j}$	σ_j	$a_{1,j}$	$a_{3,j}$	$a_{5,j}$	$a_{6,j}$	σ_j
0.02	−3.03	3.95	−0.02	−0.31	2.10	−3.34	4.10	−0.01	−0.11	2.18	−3.36	3.01	0.06	−0.06	2.22	−3.54	2.90	0.02	−0.15	2.27	−3.39	2.87	0.07	−0.15	2.24	−3.56	3.35	0.07	−0.17	2.40	−3.20	2.33	0.10	−0.44	2.37	−3.34	2.83	0.09	−0.51	2.43
1.26	−3.06	3.96	−0.01	−0.29	2.10	−3.28	4.01	−0.01	−0.16	2.13	−3.32	3.16	0.06	−0.09	2.17	−3.50	2.98	0.02	−0.16	2.24	−3.39	2.95	0.07	−0.15	2.20	−3.53	3.29	0.07	−0.17	2.36	−3.18	2.37	0.10	−0.44	2.33	−3.32	2.78	0.09	−0.51	2.40
2.50	−3.02	3.96	0.01	−0.28	2.10	−3.18	3.84	0.01	−0.20	2.09	−3.22	3.46	0.06	−0.17	2.08	−3.41	3.11	0.03	−0.17	2.21	−3.36	3.10	0.07	−0.15	2.16	−3.46	3.21	0.08	−0.19	2.32	−3.13	2.42	0.10	−0.45	2.31	−3.26	2.73	0.08	−0.54	2.38
3.76	−2.85	3.87	0.03	−0.30	2.09	−3.01	3.68	0.02	−0.26	2.07	−3.08	3.57	0.06	−0.25	2.01	−3.30	3.16	0.03	−0.18	2.16	−3.29	3.17	0.07	−0.18	2.14	−3.35	3.06	0.08	−0.22	2.29	−3.07	2.42	0.11	−0.47	2.29	−3.19	2.61	0.08	−0.57	2.35
5.00	−2.66	3.51	0.04	−0.36	2.07	−2.78	3.54	0.02	−0.37	2.07	−2.92	3.41	0.06	−0.31	2.00	−3.15	3.02	0.03	−0.21	2.13	−3.20	3.08	0.06	−0.23	2.13	−3.25	2.82	0.08	−0.23	2.27	−3.03	2.33	0.11	−0.49	2.26	−3.15	2.43	0.07	−0.57	2.33
7.50	−2.42	2.69	0.00	−0.44	2.05	−2.44	2.84	0.00	−0.49	2.09	−2.75	2.62	0.04	−0.36	2.01	−2.91	2.42	0.00	−0.31	2.10	−3.07	2.56	0.03	−0.31	2.09	−3.13	2.19	0.07	−0.25	2.24	−3.03	2.04	0.10	−0.52	2.23	−3.16	1.95	0.05	−0.52	2.30
10.00	−2.32	2.10	−0.04	−0.46	1.95	−2.43	2.26	−0.03	−0.48	2.00	−2.74	2.09	0.03	−0.33	1.92	−2.86	1.81	−0.01	−0.35	2.01	−3.01	2.11	0.02	−0.35	1.98	−3.10	1.71	0.06	−0.25	2.15	−3.09	1.74	0.07	−0.51	2.15	−3.20	1.45	0.04	−0.46	2.23
15.00	−2.37	1.89	−0.04	−0.43	1.67	−2.52	1.97	−0.03	−0.39	1.64	−2.73	1.92	0.01	−0.32	1.61	−2.78	1.61	0.00	−0.36	1.62	−2.97	1.84	0.01	−0.34	1.71	−3.11	1.21	0.03	−0.22	1.87	−3.08	1.39	0.05	−0.48	1.87	−3.18	0.93	0.04	−0.42	1.96
20.00	−2.44	1.99	−0.05	−0.35	1.42	−2.56	2.08	−0.03	−0.34	1.37	−2.77	2.01	0.01	−0.28	1.39	−2.77	1.68	0.01	−0.34	1.39	−3.03	1.81	0.01	−0.30	1.52	−3.09	1.27	0.02	−0.22	1.69	−3.07	1.27	0.03	−0.46	1.68	−3.17	0.86	0.03	−0.43	1.78
25.00	−2.48	2.00	−0.06	−0.33	1.38	−2.58	2.21	−0.04	−0.36	1.32	−2.81	1.98	0.00	−0.26	1.33	−2.78	1.74	0.01	−0.35	1.32	−3.05	1.80	0.00	−0.29	1.44	−3.11	1.33	0.01	−0.23	1.61	−3.09	1.27	0.02	−0.45	1.62	−3.15	0.89	0.01	−0.46	1.71
35.00	−2.55	2.04	−0.07	−0.31	1.35	−2.66	2.27	−0.05	−0.34	1.30	−2.86	1.96	−0.01	−0.25	1.31	−2.84	1.76	0.00	−0.33	1.31	−3.11	1.84	−0.01	−0.28	1.41	−3.15	1.37	0.00	−0.23	1.57	−3.12	1.32	0.02	−0.45	1.56	−3.16	1.01	0.01	−0.48	1.65
50.00	−2.57	2.03	−0.07	−0.31	1.35	−2.67	2.26	−0.05	−0.34	1.30	−2.88	1.95	−0.01	−0.25	1.30	−2.86	1.77	0.00	−0.32	1.30	−3.13	1.85	−0.01	−0.27	1.40	−3.18	1.37	−0.01	−0.22	1.55	−3.14	1.33	0.01	−0.45	1.55	−3.18	1.02	0.01	−0.47	1.64
70.00	−2.57	2.03	−0.07	−0.31	1.34	−2.67	2.26	−0.05	−0.34	1.29	−2.88	1.94	−0.01	−0.24	1.29	−2.87	1.76	0.00	−0.32	1.30	−3.14	1.84	−0.01	−0.27	1.39	−3.18	1.37	−0.01	−0.22	1.54	−3.15	1.33	0.01	−0.45	1.55	−3.19	1.01	0.00	−0.47	1.64

t (s)	$j=-5$					$j=-4$					$j=-3$					$j=-2$					$j=-1$					$j=0$					$j=1$					$j=2$				
	$a_{1,j}$	$a_{3,j}$	$a_{5,j}$	$a_{6,j}$	σ_j	$a_{1,j}$	$a_{3,j}$	$a_{5,j}$	$a_{6,j}$	σ_j	$a_{1,j}$	$a_{3,j}$	$a_{5,j}$	$a_{6,j}$	σ_j	$a_{1,j}$	$a_{3,j}$	$a_{5,j}$	$a_{6,j}$	σ_j	$a_{1,j}$	$a_{3,j}$	$a_{5,j}$	$a_{6,j}$	σ_j	$a_{1,j}$	$a_{3,j}$	$a_{5,j}$	$a_{6,j}$	σ_j	$a_{1,j}$	$a_{3,j}$	$a_{5,j}$	$a_{6,j}$	σ_j	$a_{1,j}$	$a_{3,j}$	$a_{5,j}$	$a_{6,j}$	σ_j
0.02	−3.50	2.89	0.13	−0.48	2.42	−3.85	2.80	0.20	−0.23	2.47	−3.55	3.31	0.20	−0.45	2.49	−3.75	2.16	0.21	−0.32	2.40	−4.02	2.59	0.21	−0.39	2.44	−4.18	3.90	0.20	−0.30	2.21	−4.40	3.30	0.21	−0.26	2.36	−4.27	2.20	0.26	−0.27	2.37
1.26	−3.47	2.83	0.13	−0.48	2.39	−3.85	2.75	0.20	−0.22	2.46	−3.58	3.25	0.20	−0.44	2.47	−3.75	2.14	0.21	−0.31	2.38	−4.01	2.58	0.21	−0.39	2.42	−4.17	3.88	0.20	−0.31	2.19	−4.41	3.26	0.21	−0.25	2.35	−4.28	2.17	0.26	−0.26	2.34
2.50	−3.42	2.78	0.13	−0.50	2.37	−3.83	2.69	0.19	−0.21	2.43	−3.60	3.25	0.19	−0.43	2.44	−3.76	2.06	0.20	−0.30	2.36	−4.00	2.46	0.21	−0.39	2.40	−4.18	3.81	0.19	−0.30	2.16	−4.40	3.21	0.21	−0.26	2.33	−4.26	2.17	0.26	−0.28	2.30
3.76	−3.35	2.70	0.12	−0.53	2.35	−3.82	2.58	0.18	−0.21	2.39	−3.62	3.23	0.18	−0.42	2.38	−3.76	1.95	0.19	−0.29	2.34	−3.99	2.29	0.21	−0.40	2.38	−4.20	3.69	0.19	−0.28	2.13	−4.40	3.15	0.21	−0.26	2.31	−4.24	2.15	0.25	−0.30	2.26
5.00	−3.28	2.61	0.12	−0.56	2.33	−3.81	2.43	0.18	−0.20	2.34	−3.64	3.14	0.17	−0.41	2.33	−3.77	1.82	0.18	−0.28	2.31	−3.98	2.10	0.21	−0.40	2.36	−4.21	3.57	0.19	−0.26	2.12	−4.40	3.08	0.22	−0.27	2.30	−4.23	2.13	0.25	−0.32	2.21
7.50	−3.21	2.40	0.11	−0.59	2.29	−3.80	2.08	0.16	−0.21	2.25	−3.67	2.81	0.15	−0.39	2.22	−3.78	1.55	0.16	−0.28	2.26	−3.93	1.70	0.21	−0.40	2.31	−4.24	3.34	0.19	−0.23	2.08	−4.42	2.94	0.22	−0.26	2.26	−4.24	2.06	0.25	−0.32	2.13
10.00	−3.27	2.14	0.11	−0.53	2.19	−3.78	1.70	0.15	−0.23	2.17	−3.65	2.40	0.14	−0.38	2.12	−3.76	1.27	0.16	−0.28	2.18	−3.90	1.35	0.20	−0.38	2.24	−4.27	3.14	0.19	−0.22	2.04	−4.44	2.77	0.22	−0.26	2.20	−4.25	1.99	0.24	−0.31	2.08
15.00	−3.38	1.62	0.10	−0.41	2.00	−3.68	1.17	0.11	−0.25	1.99	−3.56	1.81	0.11	−0.41	1.92	−3.67	0.92	0.15	−0.32	2.03	−3.88	0.96	0.18	−0.34	2.12	−4.26	2.78	0.21	−0.23	1.92	−4.46	2.36	0.20	−0.24	2.09	−4.31	1.92	0.24	−0.27	2.00
20.00	−3.34	1.41	0.09	−0.41	1.88	−3.59	1.01	0.09	−0.27	1.86	−3.55	1.55	0.10	−0.39	1.82	−3.58	0.82	0.14	−0.36	1.94	−3.90	0.82	0.16	−0.31	2.00	−4.21	2.49	0.20	−0.26	1.82	−4.46	2.08	0.19	−0.23	1.98	−4.37	1.87	0.25	−0.22	1.94
25.00	−3.32	1.40	0.09	−0.43	1.83	−3.56	0.99	0.08	−0.29	1.81	−3.59	1.49	0.09	−0.37	1.80	−3.53	0.77	0.14	−0.39	1.90	−3.94	0.86	0.16	−0.29	1.89	−4.16	2.33	0.19	−0.30	1.80	−4.44	2.02	0.18	−0.25	1.90	−4.44	1.87	0.25	−0.19	1.89
35.00	−3.34	1.39	0.07	−0.43	1.77	−3.57	0.95	0.08	−0.30	1.75	−3.64	1.46	0.08	−0.35	1.73	−3.57	0.71	0.13	−0.39	1.84	−4.01	0.97	0.14	−0.28	1.80	−4.23	2.20	0.19	−0.27	1.73	−4.45	2.06	0.18	−0.27	1.80	−4.51	2.06	0.24	−0.22	1.79
50.00	−3.37	1.39	0.07	−0.41	1.75	−3.60	0.93	0.07	−0.29	1.74	−3.69	1.43	0.08	−0.33	1.70	−3.62	0.66	0.12	−0.38	1.81	−4.04	1.02	0.13	−0.29	1.76	−4.33	2.07	0.19	−0.22	1.67	−4.50	1.94	0.17	−0.27	1.76	−4.54	2.09	0.23	−0.27	1.74
70.00	−3.38	1.39	0.07	−0.41	1.74	−3.60	0.92	0.07	−0.29	1.74	−3.70	1.41	0.08	−0.32	1.70	−3.64	0.66	0.12	−0.37	1.78	−4.06	1.01	0.13	−0.28	1.75	−4.35	2.02	0.19	−0.22	1.65	−4.52	1.91	0.16	−0.27	1.75	−4.56	2.05	0.23	−0.27	1.73

t (s)	$j=3$					$j=4$					$j=5$					$j=6$					$j=7$					$j=8$					$j=9$					$j=10$				
	$a_{1,j}$	$a_{3,j}$	$a_{5,j}$	$a_{6,j}$	σ_j	$a_{1,j}$	$a_{3,j}$	$a_{5,j}$	$a_{6,j}$	σ_j	$a_{1,j}$	$a_{3,j}$	$a_{5,j}$	$a_{6,j}$	σ_j	$a_{1,j}$	$a_{3,j}$	$a_{5,j}$	$a_{6,j}$	σ_j	$a_{1,j}$	$a_{3,j}$	$a_{5,j}$	$a_{6,j}$	σ_j	$a_{1,j}$	$a_{3,j}$	$a_{5,j}$	$a_{6,j}$	σ_j	$a_{1,j}$	$a_{3,j}$	$a_{5,j}$	$a_{6,j}$	σ_j	$a_{1,j}$	$a_{3,j}$	$a_{5,j}$	$a_{6,j}$	σ_j
0.02	−4.51	3.69	0.19	−0.49	2.38	−5.13	2.72	0.24	−0.10	2.43	−4.73	2.12	0.33	−0.42	2.39	−5.26	2.42	0.32	−0.28	2.57	Regression analyses not performed for this range of t and j																			
1.26	−4.53	3.67	0.19	−0.47	2.36	−5.14	2.71	0.23	−0.09	2.43	−4.75	2.18	0.34	−0.42	2.38	−5.24	2.43	0.32	−0.30	2.58																				
2.50	−4.55	3.63	0.19	−0.47	2.33	−5.15	2.67	0.23	−0.09	2.43	−4.76	2.13	0.34	−0.42	2.37	−5.23	2.41	0.32	−0.31	2.58																				
3.76	−4.56	3.57	0.19	−0.47	2.30	−5.17	2.61	0.23	−0.08	2.43	−4.77	2.06	0.34	−0.41	2.36	−5.22	2.38	0.32	−0.33	2.57																				
5.00	−4.57	3.52	0.19	−0.47	2.28	−5.20	2.53	0.23	−0.06	2.44	−4.79	1.98	0.34	−0.41	2.36	−5.21	2.34	0.32	−0.34	2.57																				
7.50	−4.59	3.39	0.19	−0.48	2.24	−5.26	2.37	0.23	−0.03	2.45	−4.82	1.84	0.35	−0.40	2.34	−5.19	2.24	0.33	−0.37	2.57																				
10.00	−4.61	3.23	0.20	−0.48	2.21	−5.30	2.22	0.24	−0.02	2.47	−4.85	1.76	0.35	−0.41	2.32	−5.18	2.12	0.33	−0.40	2.56																				
15.00	−4.64	2.86	0.22	−0.49	2.16	−5.31	2.04	0.24	−0.04	2.47	−4.90	1.72	0.35	−0.42	2.26	−5.17	1.90	0.34	−0.43	2.51																				
20.00	−4.68	2.57	0.23	−0.49	2.11	−5.29	1.90	0.25	−0.08	2.40	−4.96	1.68	0.34	−0.41	2.22	−5.18	1.73	0.35	−0.44	2.48																				
25.00	−4.69	2.36	0.23	−0.48	2.06	−5.26	1.74	0.24	−0.12	2.33	−5.01	1.66	0.34	−0.40	2.18	−5.20	1.63	0.35	−0.43	2.44																				
35.00	−4.73	2.12	0.23	−0.47	1.99	−5.24	1.52	0.23	−0.14	2.23	−5.11	1.67	0.33	−0.37	2.12	−5.29	1.64	0.36	−0.40	2.39																				
50.00	−4.82	2.00	0.22	−0.42	1.93	−5.28	1.42	0.23	−0.13	2.18	−5.23	1.74	0.31	−0.31	2.09	−5.40	1.87	0.34	−0.36	2.35																				
70.00	−4.87	1.93	0.22	−0.39	1.90	−5.34	1.42	0.23	−0.10	2.13	−5.32	1.73	0.30	−0.27	2.06	−5.49	1.95	0.33	−0.32	2.31	−6.09	2.12	0.38	0.04	2.36	−5.97	1.30	0.42	−0.04	2.33	−5.95	0.56	0.30	0.13	2.18	−5.67	1.19	0.38	−0.10	2.74

analysis and the error, $\varepsilon_j(t)$, in the scaling model is defined as

$$\varepsilon_j(t) = \ln(\bar{\alpha}_j(t)) - \ln(\hat{\alpha}_j(t)) \quad ;\forall j \tag{4.14}$$

where, $\hat{\alpha}_j(t)$ is the estimated ratio of energy arrival of aftershock to that of main shock using Eq. (4.15) via estimated smoothened regression coefficients. Further, $\varepsilon_j(t)$ is a normal variate with mean zero and standard deviation $\sigma_j(t)$. $\varepsilon_j(t)$ is equal to the sum of inter-event and intra-event residuals. The inter-event and intra-event residuals are lumped together and cannot be separated in this regression method. The coefficients are determined via maximization of likelihood of the errors in following a normal distribution with zero mean and some standard deviation. It should be mentioned here that for $j = 7$ to 10 the regression analysis has been performed only for $t = 70$ s, i.e. only for the 100% energy arrival because the normalized shape for those levels are constant (see Eq. (4.8)). After performing the regression analysis the coefficients $a_{2,j}(t)$ and $a_{4,j}(t)$ are not found to be physically meaningful to properly reflect the saturation and inelastic attenuation. So, the two corresponding terms were dropped and the proposed conditional scaling model becomes

$$\begin{aligned} \ln(\alpha_j(t)) = \ln\left(\frac{\bar{E}_{\mathrm{Aft},j}(t)}{\bar{E}_{\mathrm{Main},j}(t)}\right) &= a_{1,j}(t)\Delta M + a_{3,j}(t)\ln\left(\frac{\Delta_{Main}}{\Delta_{Aft}}\right) \\ &+ a_{5,j}(t)\Delta h + a_{6,j}(t)\Delta MS \quad ;\forall j \end{aligned} \tag{4.15}$$

All regression coefficients and standard deviation of errors for $j = -10$ and $j = -1$ are shown in Figure 4.4 as an example. To understand the variation of the coefficients with respect to different levels, the maximum and minimum values of all the coefficients along time are shown in Figure 4.5 for different levels, j. It can be seen from the figure that $a_{1,j}(t)$ is negative for all values of j and t. Negative values of $a_{1,j}(t)$ indicate that smaller aftershocks will have smaller energy arrival as compared to larger aftershocks, which is meaningful. The magnitude of $a_{1,j}(t)$ is higher at longer periods (higher js) as larger earthquake event has relatively stronger long period waves compared to smaller event. $a_{3,j}(t)$ is found to be positive throughout since nearer aftershocks will be stronger than farther aftershocks. Also, magnitude of $a_{3,j}(t)$ increases towards shorter periods (smaller js) as high-frequency waves attenuate faster with distance than the low-frequency waves. $a_{5,j}(t)$ is found to be positive for most of the levels since shallower events appear to be stronger. But, $a_{5,j}(t)$ follows a decreasing trend from higher to lower levels because deeper events are expected to have a relatively higher proportion of higher frequency waves. Since the Chi-Chi earthquake was a crustal event, the effect of focal depth was not so prominent but still the coefficient $a_{5,j}(t)$ is retained as it reflects the proper trend. $a_{6,j}(t)$ is negative for all j except at $j = 7$ to $j = 9$. Negative values of $a_{6,j}(t)$ indicate that a higher site response due to soft soil subsides during larger aftershocks due to nonlinear site response. It is not a serious limitation if the coefficients do not sound meaningful in the last few large values of

j, not only because the contribution of energy of signal from these bands to the total energy is very less but also because these long-period waves may have higher noise-to-signal ratio (Das and Gupta, 2008, 2011) and for that, the subtle nonlinear site response is not captured properly. For ready reference, the regression coefficients are listed in Table 4.2 for some selected ts and the coefficients can be linearly interpolated for intermediate values of t.

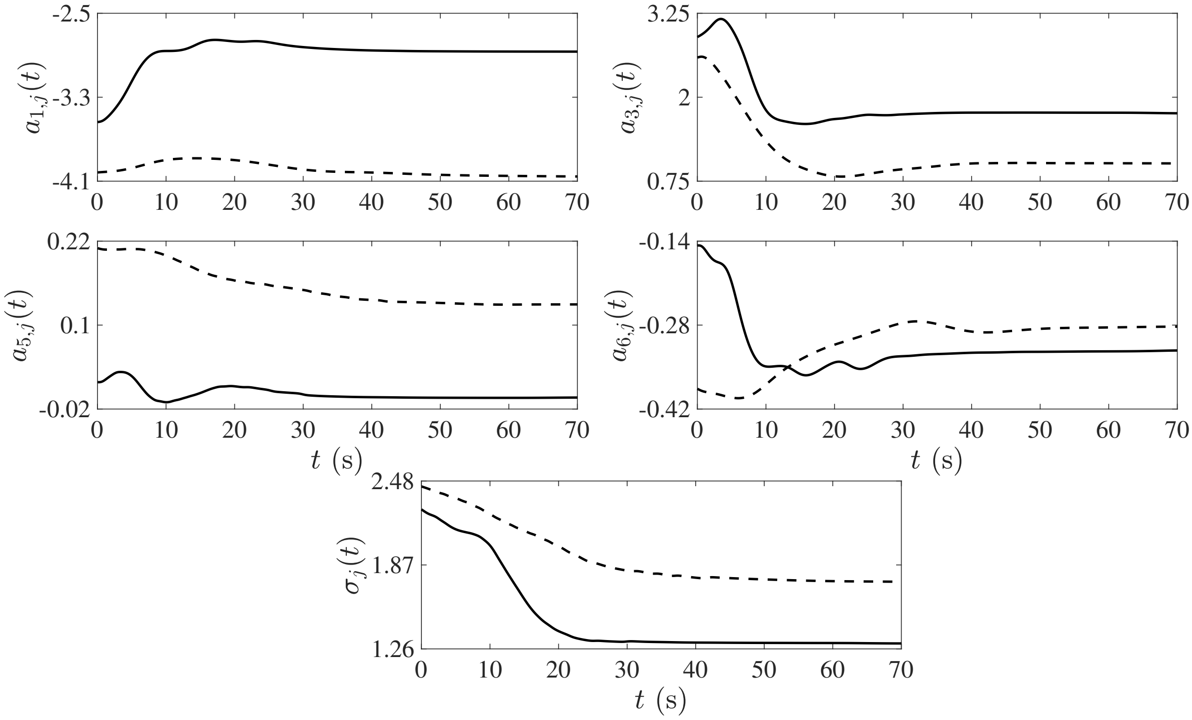

Figure 4.4 Regression coefficients for $\ln(\bar{E}_{\text{Aft},j}(t))$ and the standard deviations of errors in the cases of levels $j = -10$ (solid line) and $j = -1$ (dotted line)

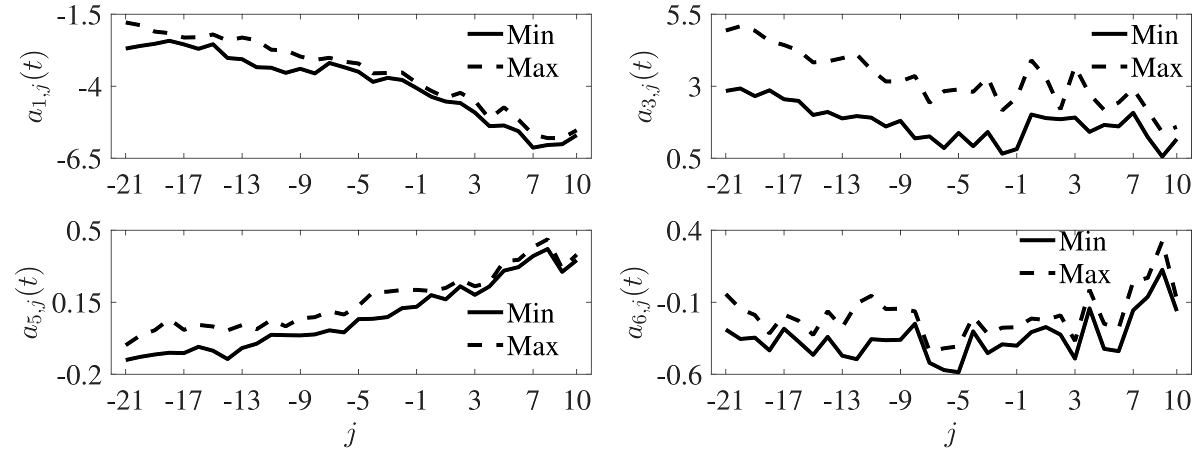

Figure 4.5 Minimum and maximum values of regression coefficients for $\ln(\bar{E}_{\text{Aft},j}(t))$ as in Eq. (4.15) for different levels, j

4.3.3 Ensemble Generation of Aftershocks

The proposed conditional scaling model gives the conditional estimate for the frequency-dependent energy arrival curves for the aftershock, using which samples of aftershock can be simulated. The statistical description of error in the energy arrival estimation is characterized by a single parameter, $\sigma_j(t)$, the level-wise standard deviation of $\varepsilon_j(t)$. The p th sample for the level-wise energy arrival for a given recorded main shock and scenario of the aftershock can be modelled as (as in Chapter 3)

$$\ln(\hat{E}_{\text{Aft},p,j}(t)) = \ln(\hat{E}_{\text{Aft},j}(t)) + k_p\,\sigma_j(t) \quad ;\forall j \tag{4.16}$$

where $\hat{E}_{\text{Aft},j}(t)$ is the estimated (median) energy arrival curve for aftershock corresponding to $\hat{\alpha}_j(t)$ and k_p is a standard normal variate to account for the aleatory uncertainty. For the purpose of scenario-specific ensemble, only one aftershock ground motion is generated randomly from the pth estimated energy arrival curves ($\hat{E}_{\text{Aft},p,j}(t)$) using the process-specific simulation technique as in Section 4.2.1. It may be noted that for the purpose of computing $\bar{\gamma}_j$, $E_j(T)$ in Eq.(4.5) will be the estimated 100% energy from the conditional scaling model (Eq.(4.15)).

This is done because the variation of ground motion samples resulting from different k_ps is much more than the variation of samples within a process (specific to p). It will be interesting to see if the samples generated by the above method can represent the expected trend with variation in the seismological parameters in terms of pseudo spectral velocity (PSV) spectra obtained from the simulated motions. For this purpose, a main shock recording of the ChiChi earthquake at C087 station is considered arbitrarily and aftershock ensembles (500 motions for each scenario) are generated for different hypothetical scenarios - Scenario-1 ($M = 5.5$, $R = 30.0$ km, $h = 5.0$ km, $S = 0$), Scenario-2 ($M = 6.0$, $R = 30.0$ km, $h = 5.0$ km, $S = 0$), Scenario-3 ($M = 6.5$, $R = 30.0$ km, $h = 5.0$ km, $S = 0$), Scenario-4 ($M = 6.0$, $R = 15.0$ km, $h = 5.0$ km, $S = 0$), Scenario-5 ($M = 6.0$, $R = 50.0$ km, $h = 5.0$ km, $S = 0$), Scenario-6 ($M = 6.0$, $R = 30.0$ km, $h = 10.0$ km, $S = 0$), Scenario-7 ($M = 6.0$, $R = 30.0$ km, $h = 15.0$ km, $S = 0$), Scenario-8 ($M = 6.0$, $R = 30.0$ km, $h = 5.0$ km, $S = 1$) and Scenario-9 ($M = 6.0$, $R = 30.0$ km, $h = 5.0$ km, $S = 2$). The values of seismological parameters considered for the different seismic scenarios are within the range of values of the seismological parameters of recorded data used for regression analysis. From the simulated ensemble of aftershocks, median PSV spectra are calculated for the different scenarios. Figure 4.6 shows a comparative plot of the median PSV spectra with a single seismological parameter varying while keeping others constant. Figure 4.6(a) shows the median PSV spectra for varying magnitudes (Scenario-1, 2 and 3). The spectral ordinates of larger aftershocks are greater than that of smaller aftershocks, which is observed in Figure 4.6(a). The difference between spectral ordinates of larger aftershock and smaller aftershock is more in the longer period since a larger aftershock (or any event) has stronger long period waves compared with a smaller aftershock. Figure 4.6(b) shows the median PSV spectra for varying epicentral distances (Scenario-4, 2 and 5). The strength of ground motions decreases with an increase in source to site distance which is observed in Figure 4.6(b). Figure 4.6(c) shows the median PSV spectra for varying focal depths (Scenario-2, 6 and 7). It is clear from the figure that deeper events generate weaker long period waves as the source to site distance increases, however, this effect is neutralized at the high frequency side because relatively deeper events likely to produce stronger high frequency waves than shallower events. Figure 4.6(d) shows the median PSV spectra for varying soil types (Scenario-2, 8 and 9). It can be seen that the strength of aftershock increases from rock to soft soil due to nonlinear site amplification - a phenomenon due to which the main shock has less amplification on soft soil than a smaller aftershock at the same site.

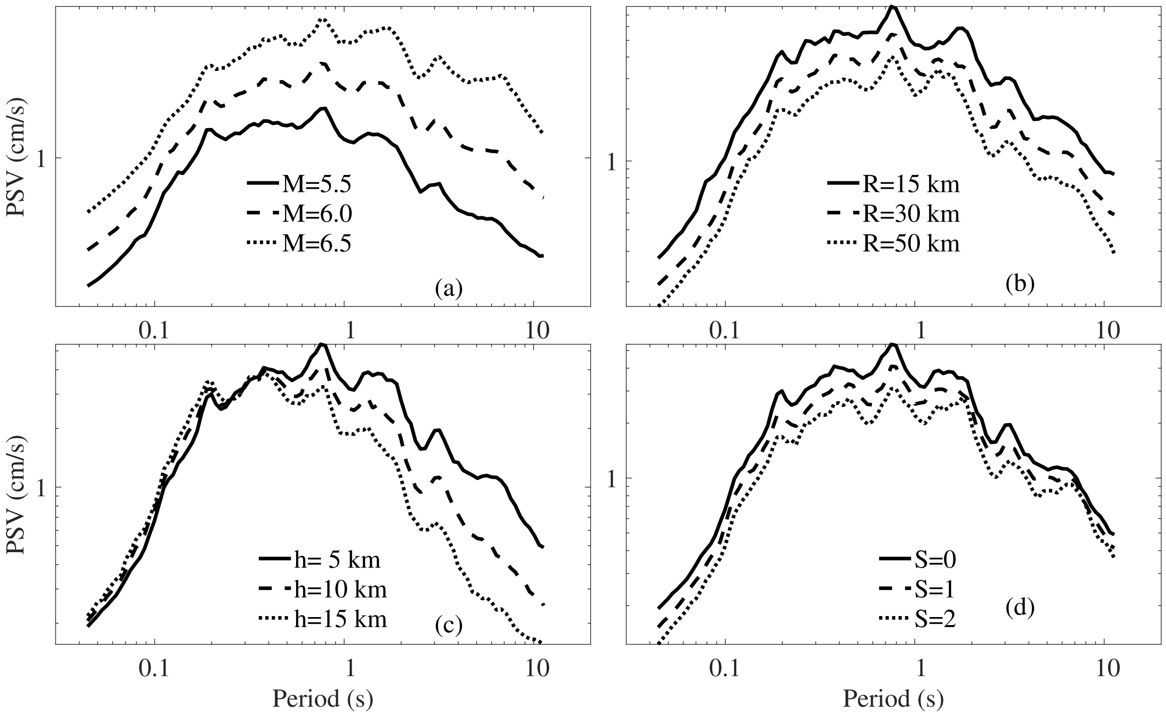

Figure 4.6 Median PSV spectra of simulated aftershocks for different values of (a) magnitude, (b) distance, (c) depth and (d) local soil conditions when the the main shock time-history is same as the recorded Chi-Chi main event at C087 station

To see the performance of aftershocks simulation with respect to recorded aftershocks, ground motions are generated for some recorded scenarios and the median PSV spectrum is compared with that of the recorded aftershock PSV spectrum. Two recorded aftershock scenarios are arbitrarily considered for this purpose. Figure 4.7 shows Aft-1757 (aftershock of $M_L = 6.44$ that occurred at 17:57 hours on September 20) recorded at station H032 and Aft-1832 (aftershock of $M_L = 5.07$ that occurred at 18:32 hours on September 20) recorded at station T116 for the ChiChi earthquake. In each of these figures, PSV spectrum of the main shock ground motion whose energy arrival curves have been used to simulate the aftershocks is also shown. The median PSV spectrum of the simulated aftershock ensemble is closer to the recorded aftershock PSV spectrum. It will also be interesting to see whether a conditional PSV scaling model obtained from the same database will yield similar results as envisaged by the conditional energy arrival scaling model because the latter is a very different quantity from the PSV. The regression coefficients of the PSV scaling model is obtained using the maximum

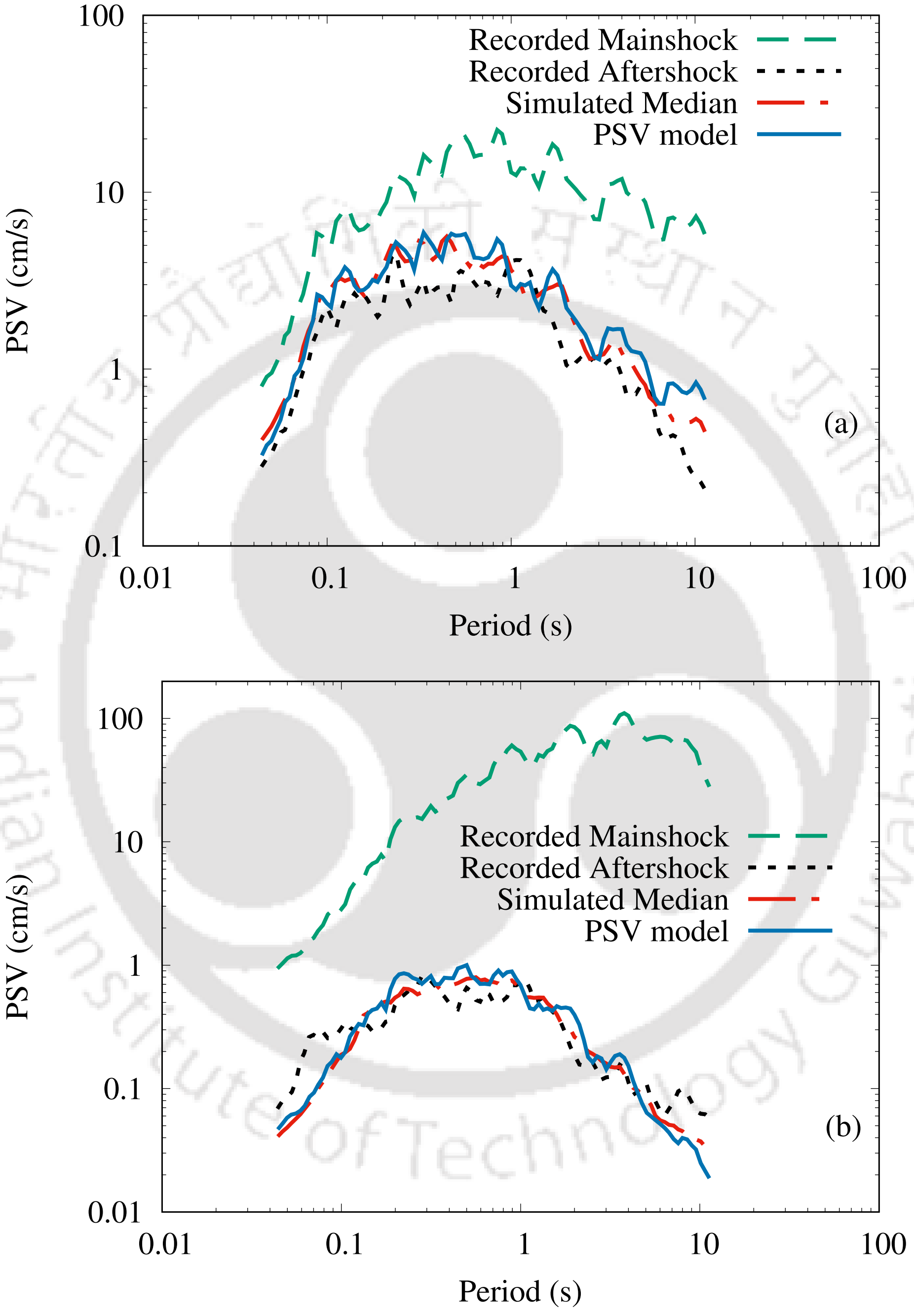

Figure 4.7 Comparison of the observed (from the recorded motion) and the median aftershock spectra obtained from both simulated ensemble and the conditional PSV scaling model in the cases of (a) Aft-1757 recorded at station H032 ($M_L = 6.44$, $R = 45.81$ km, $h = 11.04$ km, $S = 1$), (b) Aft-1832 recorded at station T116 ($M_L = 5.07$, $R = 41.93$ km, $h = 16.83$ km, $S = 0$)

likelihood method (Joyner and Boore, 1993), and the mathematical form of the scaling model is chosen as

$$\ln(\beta(T)) = \ln\left(\frac{PSV_{\text{Aft}}(T)}{PSV_{\text{Main}}(T)}\right) = c_1(T)\Delta M + c_2(T)\ln\left(\frac{\Delta_{\text{Main}}}{\Delta_{\text{Aft}}}\right) \\ + c_3(T)\Delta h + c_4(T)\Delta MS \tag{4.17}$$

through the same independent parameters as considered for modelling $\bar{\alpha}_j(t)$. The error in estimation of the scaling model is defined as

$$\varepsilon_\beta(T) = \ln(\beta(T)) - \ln(\widehat{\beta}(T)) \tag{4.18}$$

where, $\ln(\widehat{\beta}(T))$ is the estimated ratio of PSV using Eq (4.17) through estimated smooth regression coefficients. Further, $\varepsilon_\beta(T)$ is normal variate with mean zero and standard deviation $\sigma_\beta(T)$. In Figure 4.7, the median PSV spectrum of the PSV scaling model is found to be similar to that of the median PSV spectrum of the simulated aftershock ensemble for two different recorded scenarios. The variation in the temporal features of simulated ground motions is shown by three arbitrarily selected random samples for Aft-2146 (aftershock of $M_L = 6.59$ that occurred at 21:46 hours on September 20) recorded at station C010 in Figure 4.8. The variations of the time-frequency characteristics among samples are coming from two facts, viz., a sample represents any random process from the entire pool of random processes the scenario might represent and there is sample to sample variation within a process. The recorded ground motion is also shown in order to show that the recorded motion might very well be a member of the sample space. The scaling model of energy arrival curves developed in Chapter 3 (hereafter, referred as unconditional scaling model) can be used for the simulation of ground motions for any aftershock scenario but it cannot adequately address the main shock aftershock dependence

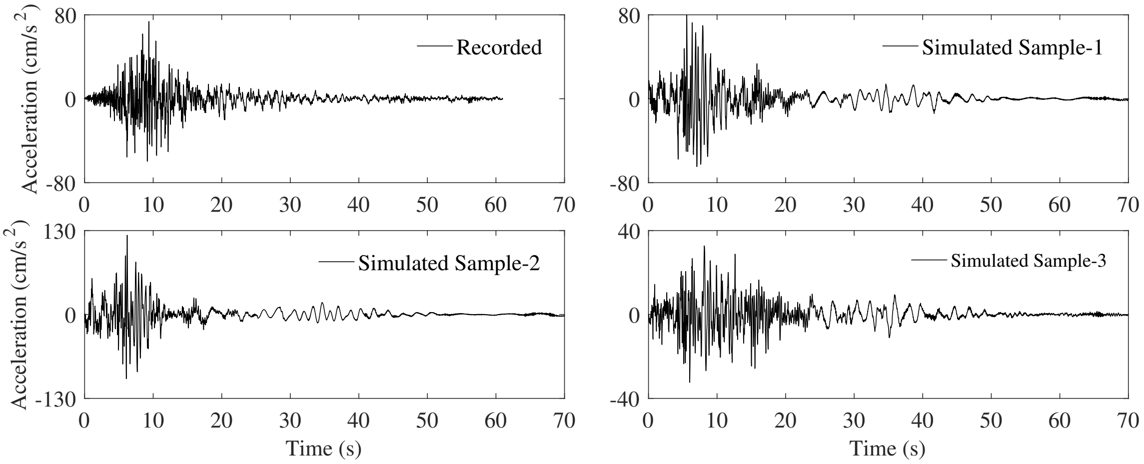

Figure 4.8 Recorded ground motion and some arbitrarily selected random simulated ground motion samples for Aft-2146 at station C010 ($M_L = 6.59$, $R = 31.73$ km, $h = 1.05$ km, $S = 1$)

once the main shock is given. A comparative study of conditional and unconditional simulation is done to clearly demonstrate the necessity for a conditional scaling model for aftershocks. To make the comparison between conditional and unconditional scaling models fair enough a new form for unconditional scaling model is developed. For this purpose, we consider a form with all the seismological parameters considered while developing the conditional scaling model. Hence, the unconditional model considered is

$$\begin{aligned}\ln(\bar{E}_j(t)) =& b_{1,j}(t)M + b_{2,j}(t)\ln\Delta + b_{3,j}(t)h + b_{4,j}(t)S + b_{5,j}(t)MS + \\ & b_{6,j}(t) \quad ;\forall j\end{aligned} \tag{4.19}$$

Using the currently developed unconditional and conditional scaling models, ground motions are simulated for some arbitrarily selected scenarios of recorded aftershocks – Aft-1757 recorded at station T065, Aft-2352 (aftershock of $M_L = 6.80$ that occurred at 23:52 hours on September 25) recorded at station H020 and Aft-0014 (aftershock of $M_L = 6.80$ that occurred at 00:14 hours on September 22) recorded at station H031. 500 numbers of ground motions for each case are simulated for the comparative study. Figure 4.9 shows 10 percentile and 90 percentile PSV spectra of ground motions simulated using conditional and unconditional scaling models and the recorded PSV spectrum. The 10 percentile and 90 percentile spectra of the ground motions simulated by the conditional scaling model are able to capture the recorded PSV spectrum and follow the trend of the recorded PSV spectrum very well along different time-periods. But the unconditional scaling model are not able to capture the trend of the recorded PSV spectrum along different time-periods and the recorded PSV spectrum lies outside the bound of 10 percentile and 90 percentile for some time-periods, this observation is for other various scenarios especially for larger aftershocks. Figure 4.10 shows the percentage of records for which the recorded PSV spectral ordinates lie within 10 and 90 percentile PSV spectra (from 500 samples every case) of motions simulated by conditional and unconditional scaling models separately for larger and smaller aftershocks. For $M_L >= 6.0$, the performance of conditional model is similar to that of the unconditional model till time-period of 1.0s and afterwards, conditional model performs much better than the unconditional model. Since time-period of a damaged structure (during main shock) increases, better estimation towards longer period improves accuracy in larger aftershock-induced additional vulnerability. For $M_L < 6.0$, the improvement of conditional scaling model is relatively less as compared to the improvement seen for the larger aftershocks at longer periods, but the same level of improvement is seen along all periods. The improvement even in the shorter period range for smaller aftershocks (not seen in the case of larger aftershocks) may arise from the fact that smaller aftershocks are relatively rich in high frequency content so the conditional model helps to improve upon in that range, on the other hand for the same reason the improvement in the longer period range is somewhat offset.

Other than the response spectrum the SMD also plays important role in cumulative damage during any aftershock event. For that purpose, the statistics of SMD obtained from simulated

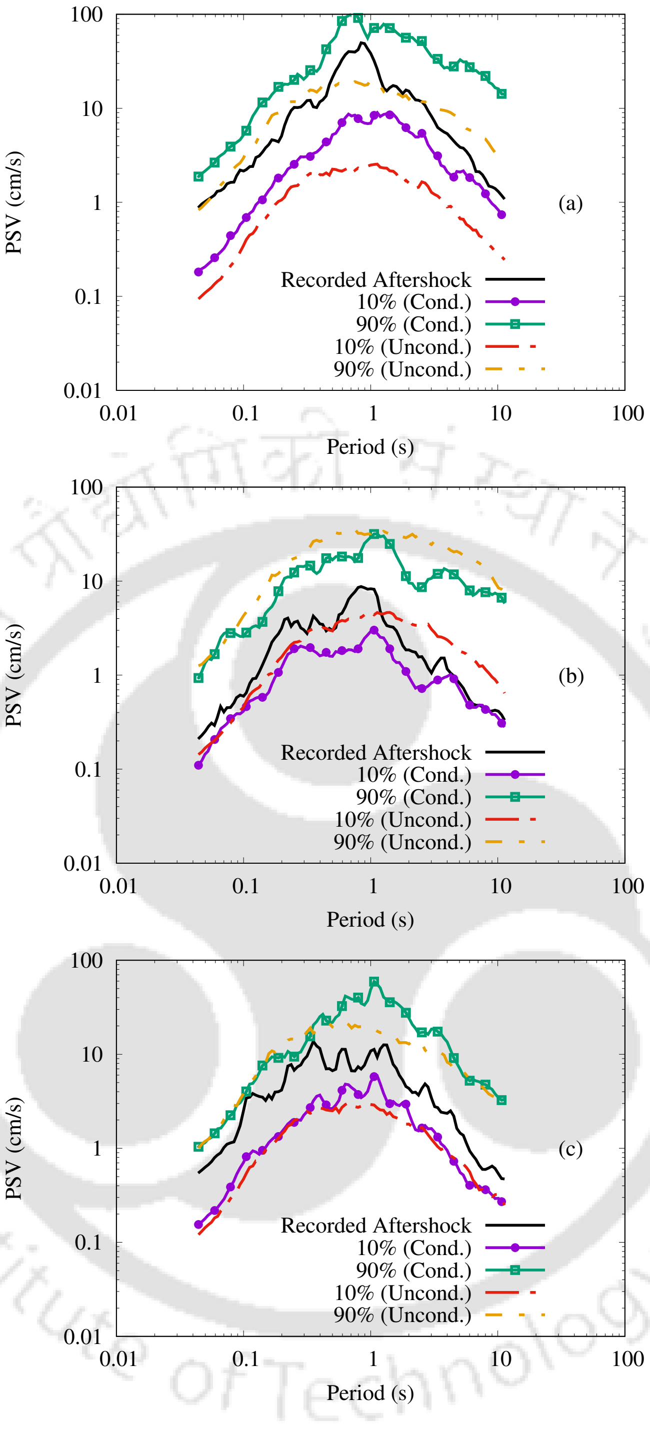

Figure 4.9 Observed PSV spectrum from the recorded motion and 10 and 90 percentile PSV spectra of ground motions simulated using conditional and unconditional scaling models in the cases of (a) Aft-1757 at station T065 ($M_L = 6.44$, $R = 37.24$ km, $h = 11.04$ km, $S = 1$), (b) Aft-2352 at station H020 ($M_L = 6.80$, $R = 44.07$ km, $h = 9.89$ km, $S = 1$), (c) Aft-0014 at station H031 ($M_L = 6.80$, $R = 45.82$ km, $h = 15.59$ km, $S = 1$)

ground motions from both conditional and unconditional scaling models are presented for two records arbitrarily chosen. Table 4.3 shows the comparison in the cases of Aft-2146 recorded at station C028 and Aft-2002 (aftershock of $M_L = 5.35$ that occurred at 20:02 hours on September 20) recorded at station T140. It is clear that the conditional scaling model can predict the SMD better than the unconditional one. The results in Figures 4.7 to 4.9 and Table 4.3 collectively demonstrate the effectiveness of the conditional scaling model in capturing the trends of recording scenarios.

Table 4.3 Comparison of the observed SMD with statistical estimates of SMD from the simulated samples generated using the conditional and unconditional scaling models

Event Name	Station Name	Observed	Confidence Probability Levels					
			Conditional			Unconditional		
			Median	10%	90%	Median	10%	90%
Aft-2146	C028	12.47	10.60	8.04	14.40	17.19	12.84	22.62
Aft-2002	T140	32.21	29.60	27.70	30.59	19.82	15.03	21.56

4.3.4 Approximate Conditional Scaling Model

From the discussions in the previous section, it is clear that it is important to have a conditional scaling model for aftershocks for their prediction given the preceding main shock motion. However, sometimes it is not possible to develop a conditional scaling model for a region if sufficient aftershock sequences are not available for carrying out regression analysis despite sufficient earthquake recordings are available to obtain an unconditional scaling model. In such a case, it can be inferred from the study carried out by Das and Gupta (2010) that an approximate conditional scaling model may be obtained from the unconditional scaling model with the assumption that the energy arrival curves for both main shock and aftershock at a given site will show similar dependence on different seismological parameters. Thus, the approximate conditional scaling model is formed from the unconditional scaling model of energy arrival as

$$\begin{aligned}\ln(\alpha_j(t)) = \ln\left(\frac{\bar{E}_{\text{Aft},j}(t)}{\bar{E}_{\text{Main},j}(t)}\right) &= -b_{1,j}(t)\Delta M - b_{2,j}(t)\ln\left(\frac{\Delta_{\text{Main}}}{\Delta_{\text{Aft}}}\right) \\ &- b_{3,j}(t)\Delta h - b_{5,j}(t)\Delta MS \quad ;\forall j\end{aligned} \tag{4.20}$$

where no further regression analysis is needed because the coefficients for various seismological disparities are negatives of the corresponding coefficients of the unconditional model. Hence, for the development of approximate conditional model, it is necessary to have an unconditional scaling model. Using this approximate conditional scaling model along with conditional and unconditional ones, aftershock ground motions are simulated in the case of Aft-1757 recorded at station H032 and Aft-2352 recorded at station H034, arbitrarily. Figure 4.11 shows the comparison of recorded spectrum and median spectrum for ground motions simulated separately using conditional, approximate conditional and unconditional scaling models. The median spectra from both conditional and approximate conditional simulations are able to capture the trend of the recorded spectrum and hence just the form of approximate conditional model

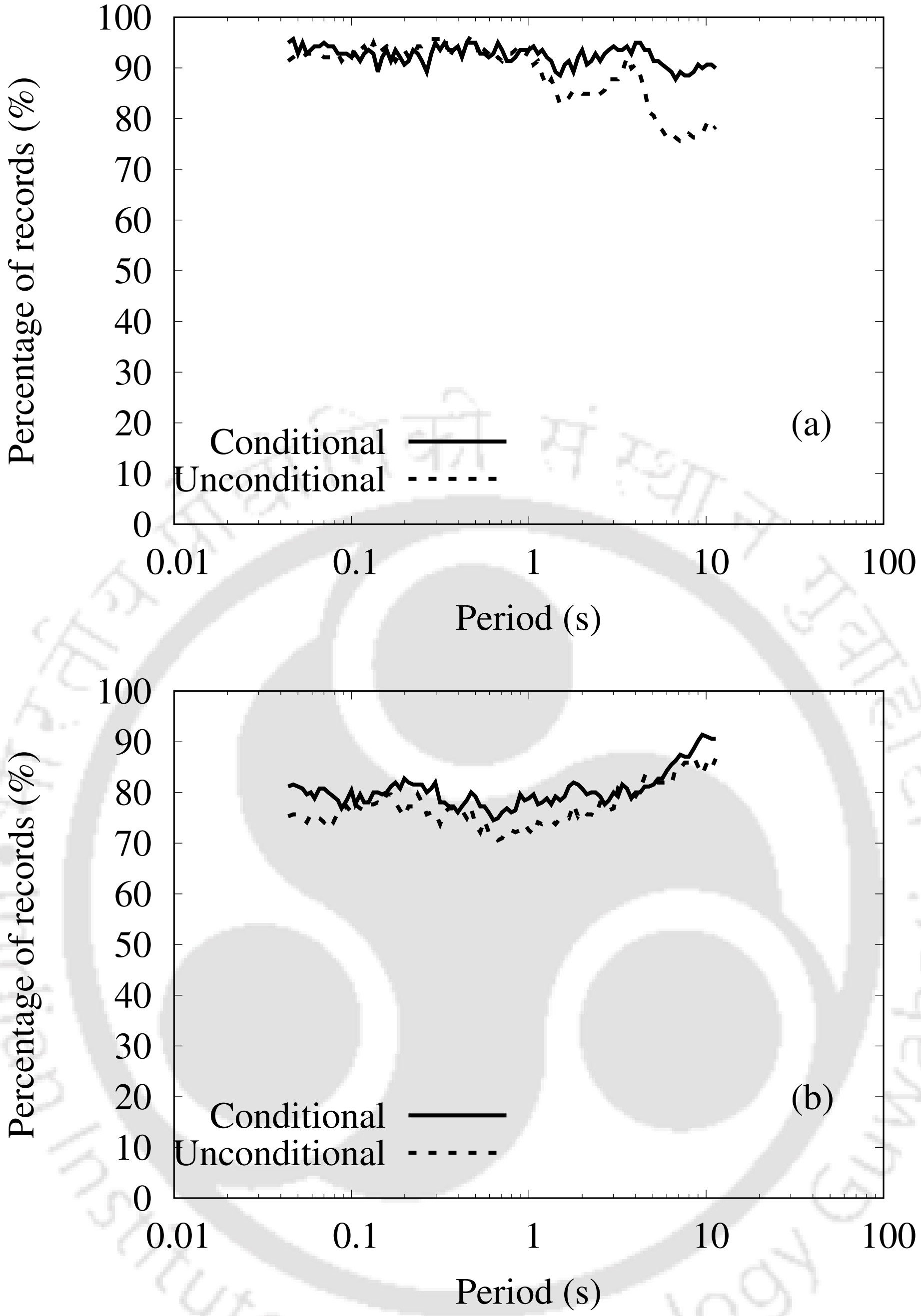

Figure 4.10 Spectra of percentage of cases wherein the recorded PSV spectral ordinates lie within the 10 and 90 percentile PSV spectra obtained from the simulated motions in the cases of recorded scenarios (a) with $M_L >= 6.0$, (b) with $M_L < 6.0$

can improve the prediction by unconditional scaling model. It must be mentioned that the standard deviation of error for approximate conditional model is always higher than that for the conditional model and so whenever data is available a conditional model should be developed for better accuracy in prediction. The approximate conditional model gives satisfactory results from SMD as well. The median SMDs for the two cases considered before (as in Table 4.3) are found to be 9.07 s and 29.87 s, respectively for Aft-2146 and Aft-2002.

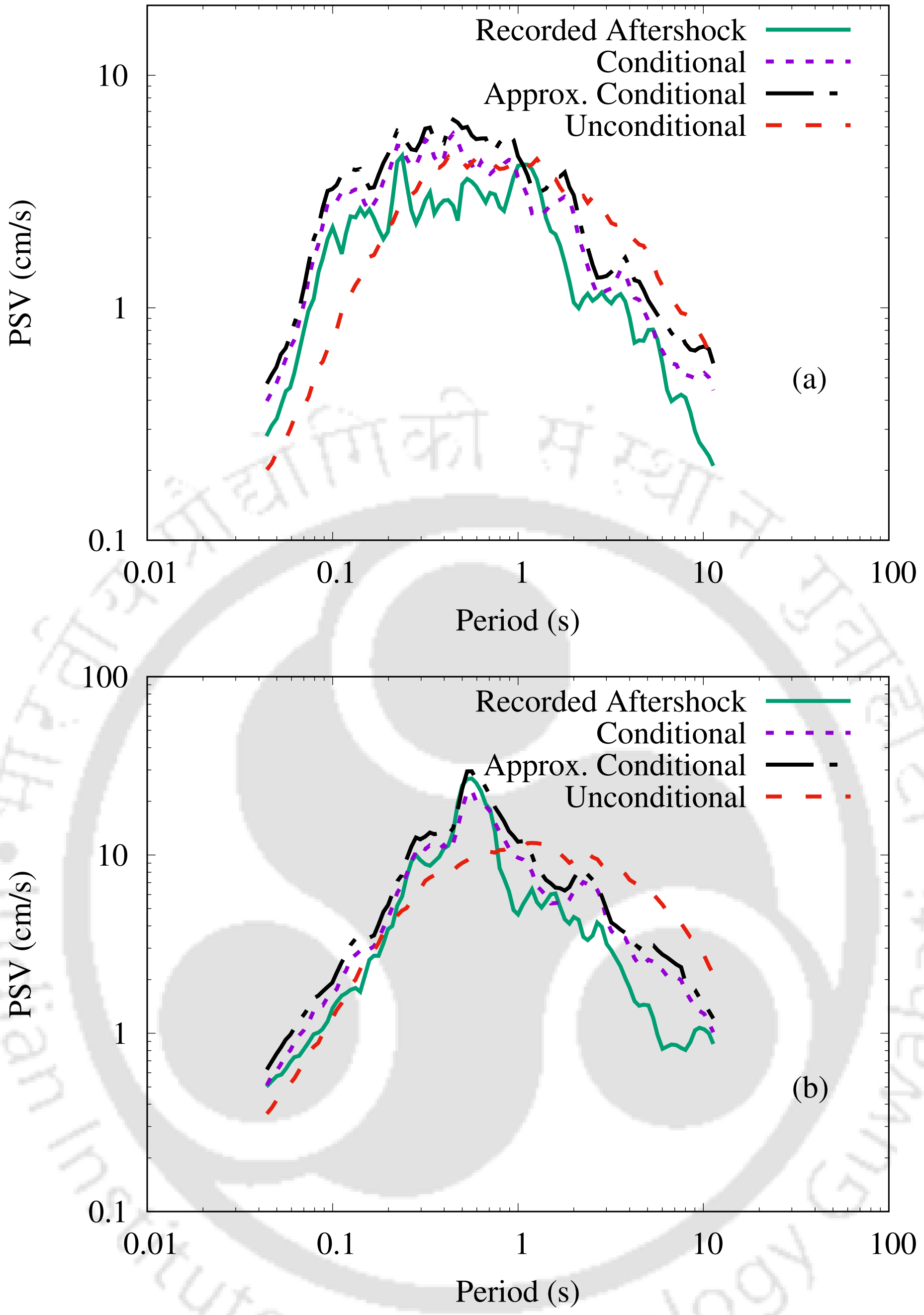

Figure 4.11 Observed PSV spectrum (from the recorded motion) and median PSV spectra of ground motions simulated using conditional, approximate conditional and unconditional scaling models in the cases of (a) Aft-1757 at station H032 ($M_L = 6.44$, $R = 45.81$ km, $h = 11.04$ km, $S = 1$), (b) Aft-2352 at station H034 ($M_L = 6.80$, $R = 48.12$ km, $h = 9.89$ km, $S = 1$)

4.4 Summary

In the present study, an improved method has been proposed for generating process-specific random samples of fully nonstationary earthquake ground motions from a known recorded accelerogram. The ground motion simulation is based on the Priestley process assumption where the amplitude and frequency nonstationarities are characterized through slow-varying deterministic frequency-dependent amplitude modulations that are extracted from the instantaneous frequency-dependent cumulative energy arrival of a recorded motion. A conditional scaling model for aftershocks has been proposed where the energy arrival curves of an aftershock are predicted conditionally from those of the preceding main shock motion with known seismic scenarios for both main shock and the aftershock. Finally the scenario-specific and conditional ground motion samples of the aftershock have been simulated from the frequency-dependent modulations (obtained from the predicted energy arrival curves), which are fully nonstationary by nature. The major contributions and conclusions of the current study are listed below.

- An earthquake recording process-specific simulation technique proposed in Chapter 3 has been improved and the characterization of the deterministic frequency-dependent amplitude modulations is shifted from the wavelet domain to the decomposed time-history domain for more efficient reconstruction. The proposed technique for process-specific simulation is found to yield similar simulated motions as obtained from the previous wavelet-based approach.

- A conditional scaling model for aftershock has been proposed to predict the instantaneous cumulative energy arrival from that of the preceding main shock in terms of the disparities of various seismological parameters while taking into account the possible nonlinear site response in presence of soil. The simulated ground motions using the conditional scaling model show expected trend vis-à-vis the seismological scenarios in terms of the PSV spectra obtained from them.

- The conditional scaling model has been found to perform better than the unconditional scaling model in capturing the recorded response spectra through the 10 and 90 percentile PSV spectra and SMD of simulated motions.

- An approximate version of conditional scaling model for aftershock has also been proposed when aftershock data are inadequate for carrying out fresh regression analysis for the conditional scaling model in a particular region. It is found that the approximate conditional model produces comparable results in regard to the (freshly regressed) conditional scaling model and it can be used in lieu of the unconditional one for better prediction.

Chapter 5

SEISMIC SAFETY OF RC FRAMES AGAINST MAIN SHOCK-AFTERSHOCK SEQUENCES

5.1 Background

In the previous chapter, a method has been proposed to simulate an aftershock ensemble that is consistent with the preceding main shock motion. When a structure is designed for the most critical event (e.g., MCE level of main shock) it is expected that the structure will undergo into irreparable damage regime. It is imperative to investigate, depending on the seismological scenario, how much additional damage can be inflicted by aftershocks to an already damaged structure during the preceding main shock. Further, it is also important to find a favourable way to modify the existing design so that a structure does not collapse during a MAS. Three different ductile RC bare frames are considered as the bases for the present study.

5.2 Modelling of RC Frames

Three numbers of 2D RC frames, viz., 1-storey, 2-storey and 5-storey, have been designed following the provisions of Indian design codes; IS 456 (2000), IS 1893 (2002), IS 13920 (1993), IS 875 (Part I) (1987) and IS 875 (Part II) (1987). IS 875 (Part I) (1987) specifies the unit weights of materials for dead load calculation and IS 875 (Part II) (1987) specifies the live load to be used in the design. Provisions of IS 456 were used for the design of the RC members (beams and columns). IS 1893 (2002) specifies the lateral forces corresponding to earthquake forces and the load combinations (considering dead load, imposed load and earthquake load) to be considered in the design. IS 13920 (1993) deals with the ductile detailing of beams and columns of the structures. The design philosophy ensures that every flexural member will undergo plastic deformation through flexural plastic hinge only, which is ductile by nature as opposed to shear hinge, which is brittle by nature. This philosophy is adopted because most of the existing RC frames in India are built in that fashion. The structure has not been designed following the strong column-weak beam mechanism as it is not specified in IS 13920:1993, whereas it is specified in the recent revision of the code. Concrete grade of M25 (characteristic cube strength of 25 MPa) and steel grade of Fe500 (yield strength of the steel is 500 MPa) have been used in the design of these frames. Further, the loading on the 2D frames was reasonably estimated considering the dead and live loads from the floor slab system of the underlying 3D structure. The geometric details of the frames along with the section details of the members are shown in Figures 5.1 to 5.3. The 2D frames are modelled in the software OpenSees

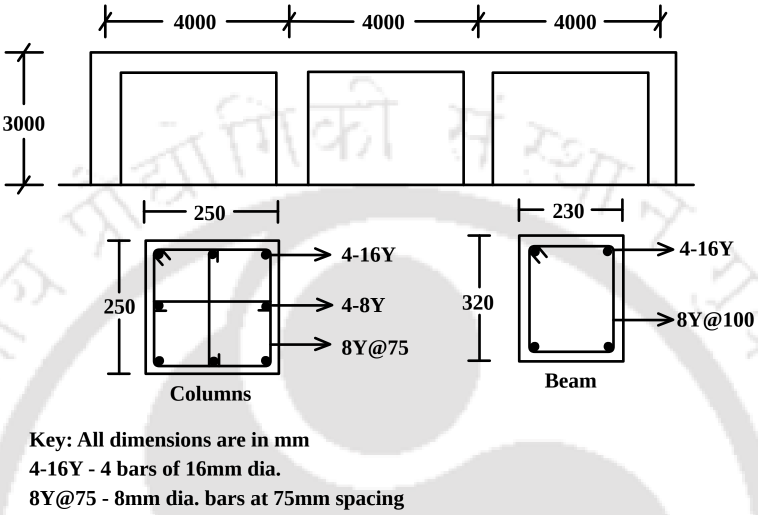

Figure 5.1 Geometry (not to scale) and sectional details of the 1-storey frame

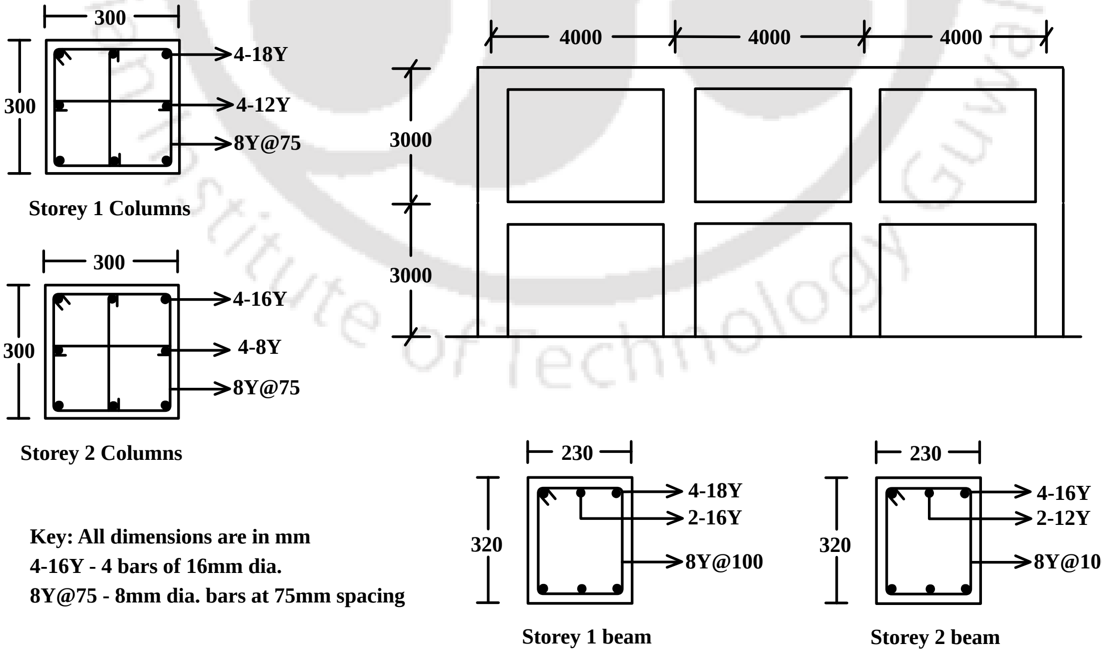

Figure 5.2 Geometry (not to scale) and sectional details of the 2-storey frame

(Mazzoni et al., 2005). `Concrete07` material and `ReinforcingSteel` material available in

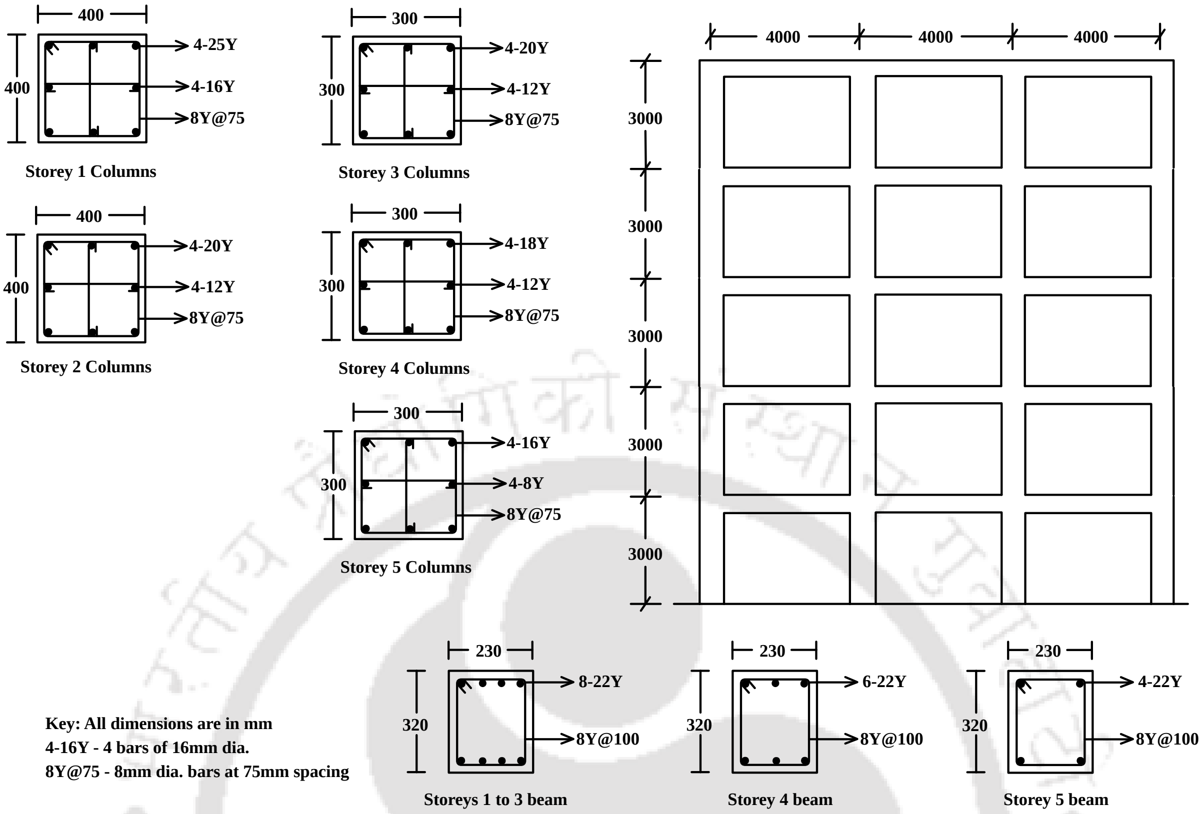

Figure 5.3 Geometry (not to scale) and sectional details of the 5-storey frame

OpenSees are used to model concrete and steel, respectively. Cover concrete and core concrete are modelled separately using `Concrete07` with different parameters since their stress-strain behaviours are different due to the confinement of core concrete. Additional details of the parameter used in various material models are shown in Tables 5.1 and 5.2. The frame members are modelled using `beamWithHinges` element recommended for lateral load analysis (as in the case of earthquake-induced loads) where the flexural members predominantly exhibit double curvature profile. The plastic hinge length that needs to be assigned in a hinge location of a `beamWithHinges` element is computed in accordance with Paulay and Priestly (2009) as

$$l_p = 0.08L + 0.022 f_y d_b \tag{5.1}$$

where, l_p is the plastic-hinge length in metre, L is the shear-span of the member in metre, f_y is the yield strength of reinforcement in MPa and d_b is the diameter of the longitudinal reinforcement in metre. The mass converted from the dead load and the factored live load as recommended by IS 1893 (2002) is considered for the dynamic analysis. Thus, the fundamental periods of 1-storey, 2-storey and 5-storey frames are found to be 0.329 s, 0.460 s and 0.960 s, respectively. The linear damping of the frames are modelled as Rayleigh damping where the proportionality constants are obtained from 5% of the critical damping for the first two modes.

Table 5.1 Details of parameters used in `ReinforcingSteel` material

Reinforcing Steel	
Parameters	Values
fy (MPa)	500.0
fu (MPa)	550.0
Es (MPa)	200000.0
Esh (MPa)	10000.0
esh	0.020
eult	0.120

Table 5.2 Details of parameters used in `Concrete07` material

	`Concrete07` Type														
	Cover Concrete	Core Concrete													
	All Frames	1-Storey Frame		2-Storey Frame				5-Storey Frame							
Member / Parameters	All	Column	Beam	1-Storey Column	2-Storey Column	1-Storey Beam	2-Storey Beam	1-Storey Column	2-Storey Column	3-Storey Column	4-Storey Column	5-Storey Column	1, 2 & 3-Storey Beam	4-Storey Beam	5-Storey Beam
fc (MPa) (Cyl. Str.)	20.0	37.2	24.9	35.0	34.6	25.8	25.6	31.9	31.5	35.2	35.0	34.6	26.6	26.3	25.6
ec	0.0020	0.0106	0.0045	0.0095	0.0093	0.0049	0.0048	0.0080	0.0078	0.0096	0.0095	0.0093	0.0053	0.0051	0.0048
Ec (MPa)	25217.4	25217.4	25217.4	25217.4	25217.4	25217.4	25217.4	25217.4	25217.4	25217.4	25217.4	25217.4	25217.4	25217.4	25217.4
ft (MPa)	2.8	2.8	2.8	2.8	2.8	2.8	2.8	3.5	3.5	3.7	3.7	3.6	3.2	3.2	3.1
et	0.0002	0.0002	0.0002	0.0002	0.0002	0.0002	0.0002	0.0002	0.0002	0.0002	0.0002	0.0002	0.0002	0.0002	0.0002
xp	2.0	2.0	2.0	2.0	2.0	2.0	2.0	2.0	2.0	2.0	2.0	2.0	2.0	2.0	2.0
xn	2.3	30.0	30.0	30.0	30.0	30.0	30.0	30.0	30.0	30.0	30.0	30.0	30.0	30.0	30.0
r	1.95	1.16	1.28	1.17	1.17	1.26	1.27	1.19	1.19	1.17	1.17	1.17	1.25	1.26	1.27

The damage at a plastic hinge location is quantified via the modified Park & Ang damage index (Williams and Sexsmith, 1995; Stone and Taylor, 1993), where the local damage index (DI) as a function of the sectional demand and capacity is expressed as

$$DI = \frac{\phi'_m - \phi_y}{\phi_u - \phi_y} + \beta_d \frac{E_H}{M_y \phi_u} \tag{5.2}$$

where,

$$\phi'_m = \max(\phi_m, \phi_y) \tag{5.3}$$

where ϕ_m, ϕ_y and ϕ_u are the maximum, yield and ultimate curvatures, respectively. E_H is the (dissipated) hysteretic energy of the moment-rotation curves at the plastic hinge location and β_d is a degradation parameter, which accounts for the contribution of E_H to the total damage. In the present study, β_d is considered as 0.15, which is generally applicable for ductile RC sections. The moment-rotation relationships at various plastic hinge locations in the cases of three different frames are listed in Tables 5.3 to 5.5. The overall damage index (ODI) at the structure level for any frame is calculated as a weighted average of all local damage indices, expressed as (Kunnath et al., 1992; Williams and Sexsmith, 1995)

Table 5.3 Moment-rotation relationships at plastic hinge locations of the 1-storey frame

Location	Yield Rotation (rad)	Yield Moment (kN.m)	Ultimate Rotation (rad)	Ultimate Moment (kN.m)
Beam	0.0043	46.8	0.1718	53.6
Exterior Column	0.0065	43.4	0.2628	47.6
Interior Column	0.0069	47.5	0.2483	51.4

Table 5.4 Moment-rotation relationships at plastic hinge locations of the 2-storey frame

Location	Yield Rotation (rad)	Yield Moment (kN.m)	Ultimate Rotation (rad)	Ultimate Moment (kN.m)
1-Storey Beam	0.0048	79.1	0.1796	91.1
2-Storey Beam	0.0041	59.1	0.1608	67.7
1-Storey Exterior Column	0.0050	81.7	0.1225	92.5
1-Storey Interior Column	0.0054	91.1	0.1044	101.7
2-Storey Exterior Column	0.0046	57.6	0.1860	64.1
2-Storey Interior Column	0.0048	63.3	0.2057	69.7

$$ODI = \frac{\sum\limits_{i=1}^{n} (DI_i) E_i}{\sum\limits_{i=1}^{n} E_i} \tag{5.4}$$

Table 5.5 Moment-rotation relationships at plastic hinge locations of the 5-storey frame

Location	Yield Rotation (rad)	Yield Moment (kN.m)	Ultimate Rotation (rad)	Ultimate Moment (kN.m)
1, 2 & 3-Storey Beams	0.0065	159.9	0.2130	187.5
4-Storey Beam	0.0062	121.7	0.2126	141.5
5-Storey Beam	0.0057	83.2	0.2120	95.6
1-Storey Exterior Column	0.0044	227.9	0.0735	267.9
1-Storey Interior Column	0.0048	258.2	0.0631	293.5
2-Storey Exterior Column	0.0034	160.7	0.0744	185.3
2-Storey Interior Column	0.0037	187.6	0.0601	208.7
3-Storey Exterior Column	0.0064	98.1	0.1268	109.3
3-Storey Interior Column	0.0070	110.4	0.1138	122.1
4-Storey Exterior Column	0.0057	81.8	0.1388	92.7
4-Storey Interior Column	0.0061	90.9	0.1195	101.5
5-Storey Exterior Column	0.0046	57.7	0.1836	64.2
5-Storey Interior Column	0.0047	63.2	0.2086	69.6

where, DI_i and E_i are the local DI and E_H, respectively, for the ith hinge and n is the total number of plastic hinges in the frame.

5.3 Generation of Main Shock-Aftershock Sequences

A total six numbers of main shock motions are considered such that they are characteristically different from each other. For each of such main shock several aftershock motions are simulated using the proposed conditional scaling relationship for some assumed seismic scenarios for the main shock and the aftershocks. Firstly, a single sample of main shock motion is simulated randomly from an arbitrarily chosen scenario of $M = 7.0$, $R = 20$ km, $h = 10$ km and $S = 0$ using the unconditional scaling model and sample generation as described in Chapter 4, (Section 4.3.3). This particular main shock is referred to as MS1 from now onward. The PGA normalized time-history of MS1 and its PSA spectrum are shown in Figures 5.4 and 5.5, respectively. Here, MS1 depends on $\bar{\gamma}_j$ and the normalized frequency-dependent modulations as described in Section 4.3.3 of Chapter 4.

In order to investigate the effects of the normalized shape of the main shock modulations (i.e., the time-frequency characteristics) five different recorded main shock motions are considered to borrow their normalized frequency-dependent amplitude modulations. Each recorded motion's modulations are then modified by multiplying the normalized modulations by $\bar{\gamma}_j$ of MS1 correspondingly and one random modified sample is obtained for each of them (see Chapter 4, Section 4.2.1). The considered recorded motions are for (i) the 1940 Imperial Valley earthquake recorded at El Centro Site Imperial Valley Irrigation District along S00E,

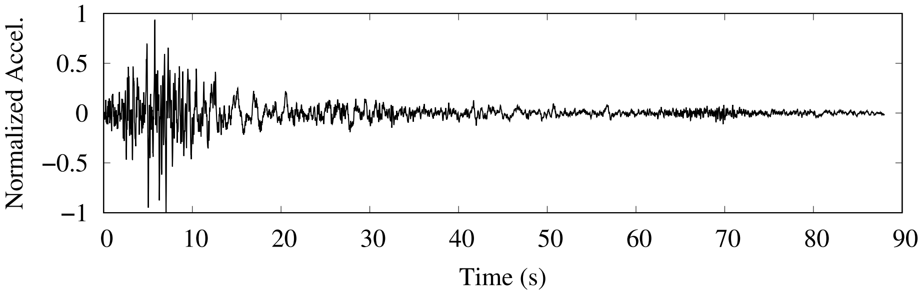

Figure 5.4 A sample of main shock ground motion simulated for $M = 7$, $R = 20$ km, $h = 10$ km and $S = 0$ from the unconditional scaling model

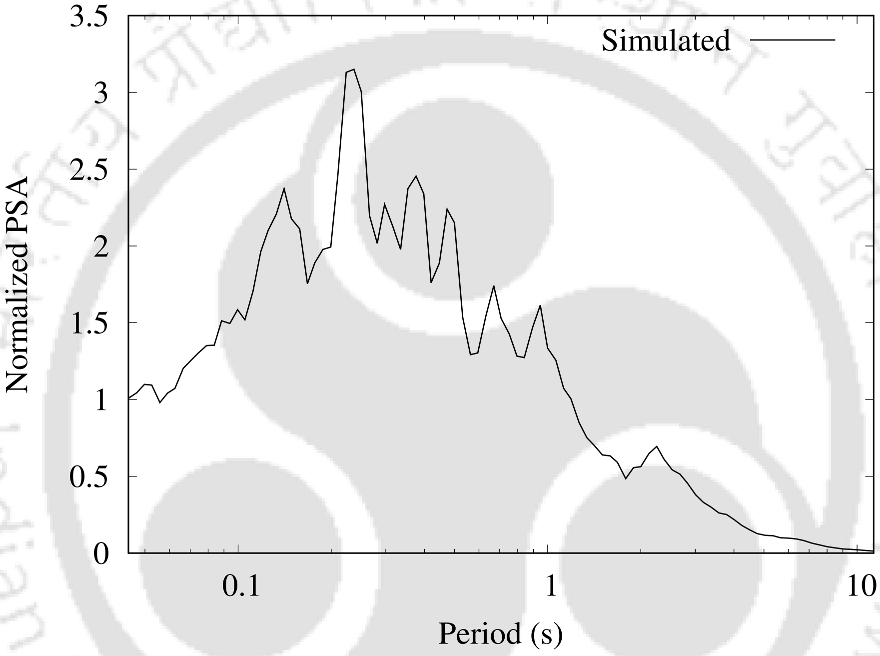

Figure 5.5 Normalized 5% damping PSA spectra of MS1

(ii) the 1952 Kern County earthquake recorded at Taft Lincoln School Tunnel along N21E, (iii) the 1966 Parkfield Earthquake recorded at Cholame, Shandon, California Array No. 5 along N05W, (iv) the 1971 San Fernando Earthquake recorded at 215 West Broadway, Utilities Building, Long Beach, California along N90E and (v) the 1968 Borrego Mountain Earthquake recorded at Engineering Building, Santa Ana, Orange County, California along S04E. These motions are considered because they altogether exhibit a varied range of time-frequency characteristics (Mukhopadhyay et al., 2019). The modified samples corresponding to the Imperial Valley, Kern County, Parkfield, San Fernando and Borrego Mountain events are hereafter referred to as MS2, MS3, MS4, MS5 and MS6, respectively. The five main shock motions (MS2 to MS6), all PGA normalized, are shown in Figure 5.6 and their PSA spectra are shown in Figure 5.7. From the figures of time-histories and response spectra for MS1 to MS6 it is clear that the main shocks have significant variations of ground motion characteristics (given a choice of $\bar{\gamma}_j$ for a closer event from the site) and hence they can form a sound basis for investigating the aftershock-induced damage when additionally the seismic scenarios of aftershocks will be varied vis-à-vis the main shock.

For the purpose of generating aftershock sequences, four aftershocks are considered for each main shock arbitrarily. Further, the magnitude difference between a main shock and the largest aftershock (ΔM_1) is varied and three values of ΔM_1, viz., 0.3, 0.5 and 0.8 are considered. In order to get some estimate for the other three aftershocks' magnitudes, for every chosen value of ΔM_1, an ordered statistics method is applied (Das et al. (2007)) where the b value for the aftershock sequence is assumed to be 0.85 (Chan and Wu (2013)) and the minimum magnitude is taken as 4. The upper bound of the aftershock magnitude is chosen such that the largest aftershock magnitude comes out to be in accordance with the assumed ΔM_1. It should be mentioned here that the choice of b and the minimum magnitude of the aftershocks are arbitrary because the main purpose is to get some plausible aftershock sequences with decreasing magnitudes to investigate the effects of single (the largest) and multiple aftershocks on additional damage. Further, it is assumed that the epicentral distances from a site for any aftershock is same as that for the preceding main shock at that site. In a particular ensemble of sequences, the first, second, third and fourth aftershock ensembles (of motions) are denoted by AS1, AS2, AS3 and AS4, respectively. For each ordered aftershock's (say, of AS1) seismic scenario and for every main shock 30 numbers of random samples for the aftershock ensemble are generated using the proposed simulation technique described in Chapter 4. Finally, 15 samples of sequences are formed for any particular sequence ensemble by randomly choosing one motion from each of the aftershock ensembles, AS1 to AS4. The details of various ensembles of sequences and the seismological scenarios for AS1 to AS4 are provided in Table 5.6. The aftershock ensemble-wise median spectra for each sequence case are shown in Figures 5.8 to 5.12 for ready reference. While forming a sequence, the aftershock events are arranged in decreasing order of their magnitudes. This is done because at the expectation level aftershocks are getting weaker with decreasing magnitudes so the first aftershock is expected to cause maximum damage and then the second largest aftershock is subjected to the maximum damaged structure to cause further expected maximum additional damage and so on. A set of random samples where each sample corresponds to a particular ensemble of sequences are shown in Figures 5.13 to 5.17. At a sample level, the decreasing trend of aftershock motion intensity from AS1 to AS4 cannot be maintained because the random selection of aftershock samples (for AS1 to AS4) should be independent of each other.

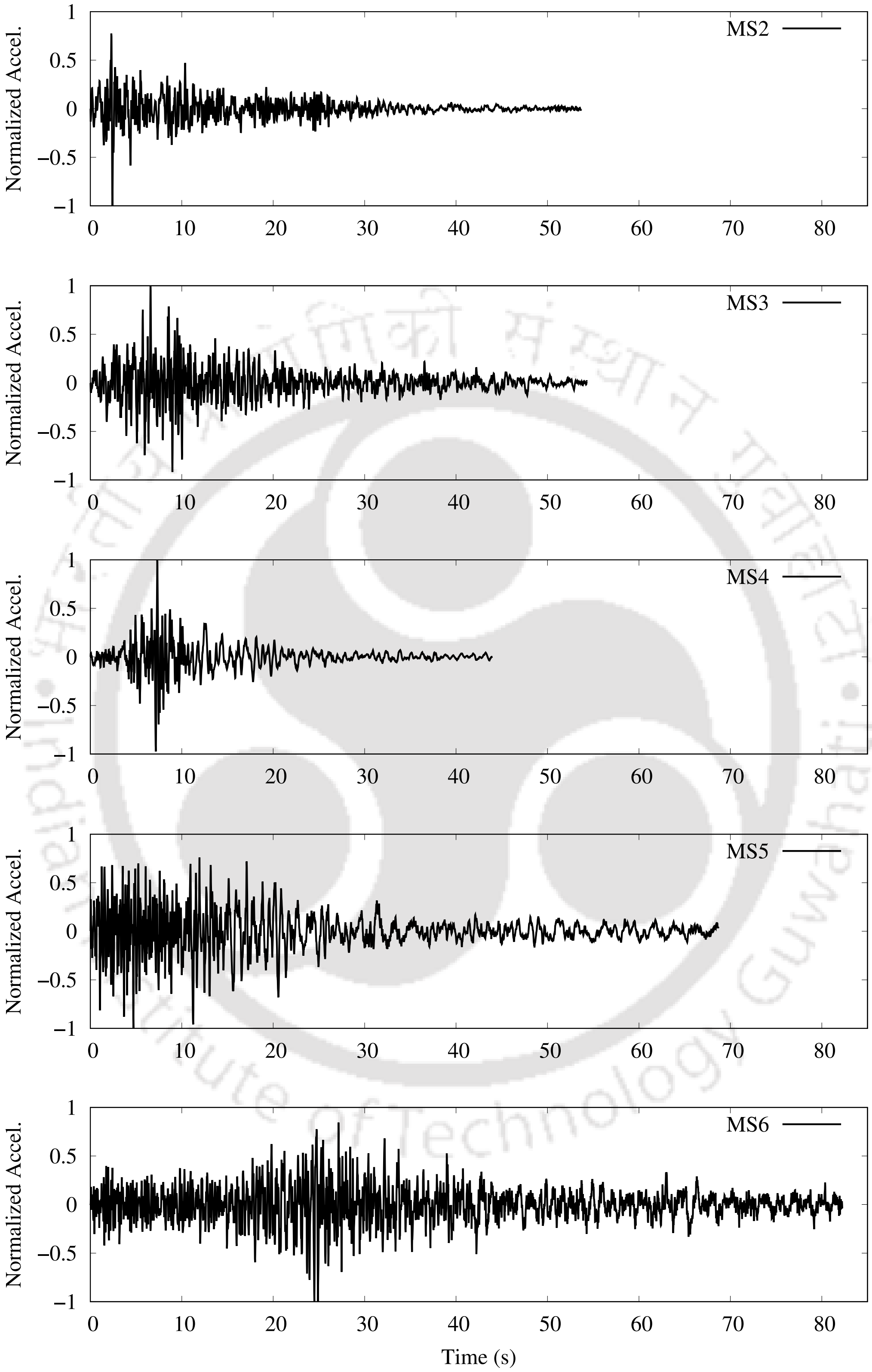

Figure 5.6 Normalized main shock motions in the cases of MS2, MS3, MS4, MS5 and MS6

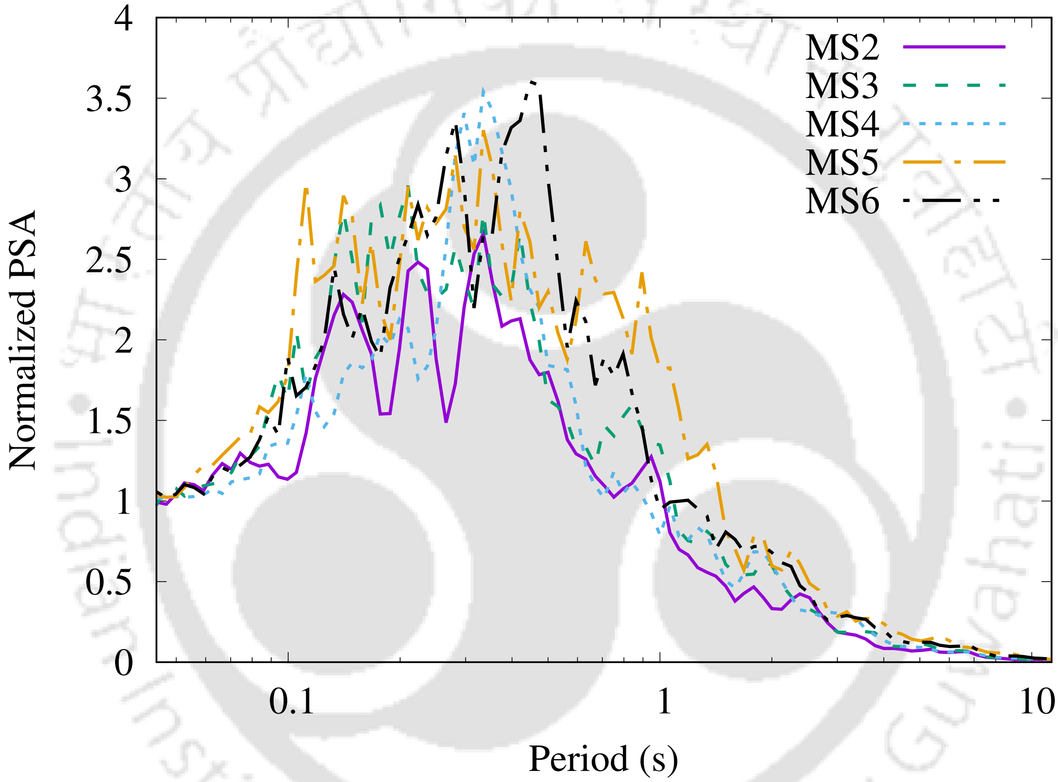

Figure 5.7 PGA Normalized 5% damping PSA spectra for the cases of MS2, MS3, MS4, MS5 and MS6

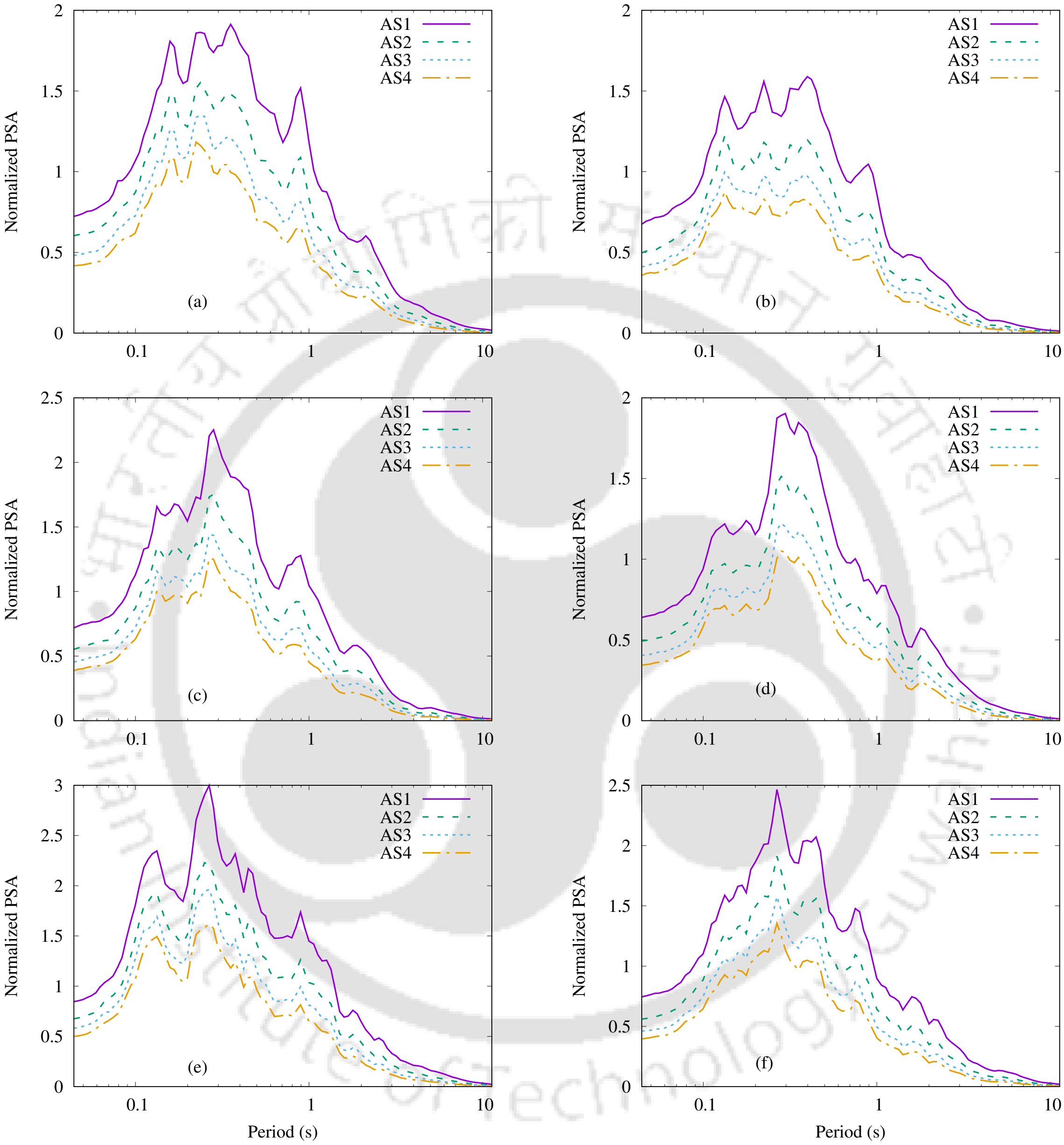

Figure 5.8 Median 5% damping PSA spectra of aftershocks for the corresponding PGA normalized main shock in the cases of (a) SEQ01, (b) SEQ02, (c) SEQ03, (d) SEQ04, (e) SEQ05 and (f) SEQ06

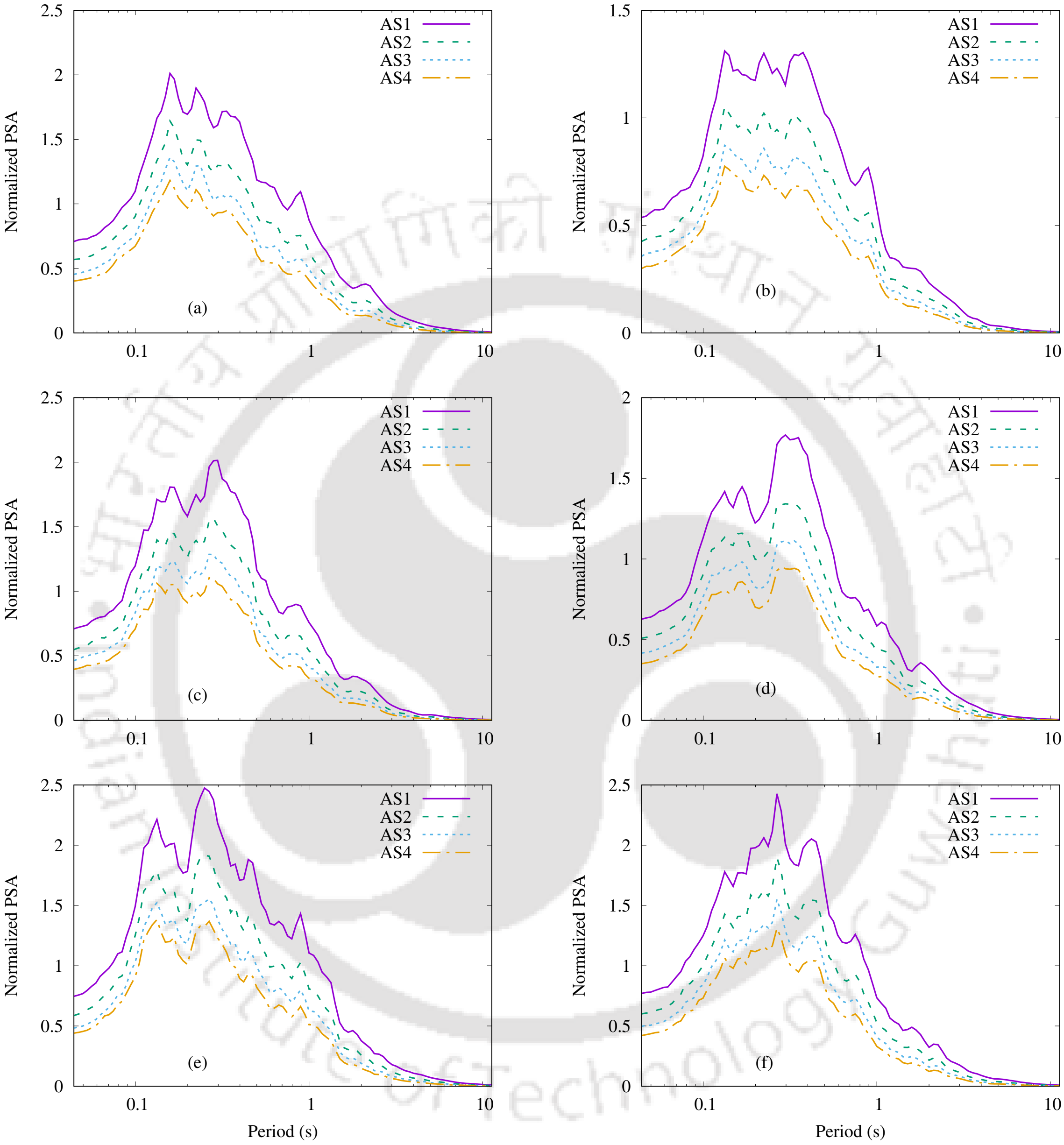

Figure 5.9 Median 5% damping PSA spectra of aftershocks for the corresponding PGA normalized main shock in the cases of (a) SEQ07, (b) SEQ08, (c) SEQ09, (d) SEQ10, (e) SEQ11 and (f) SEQ12

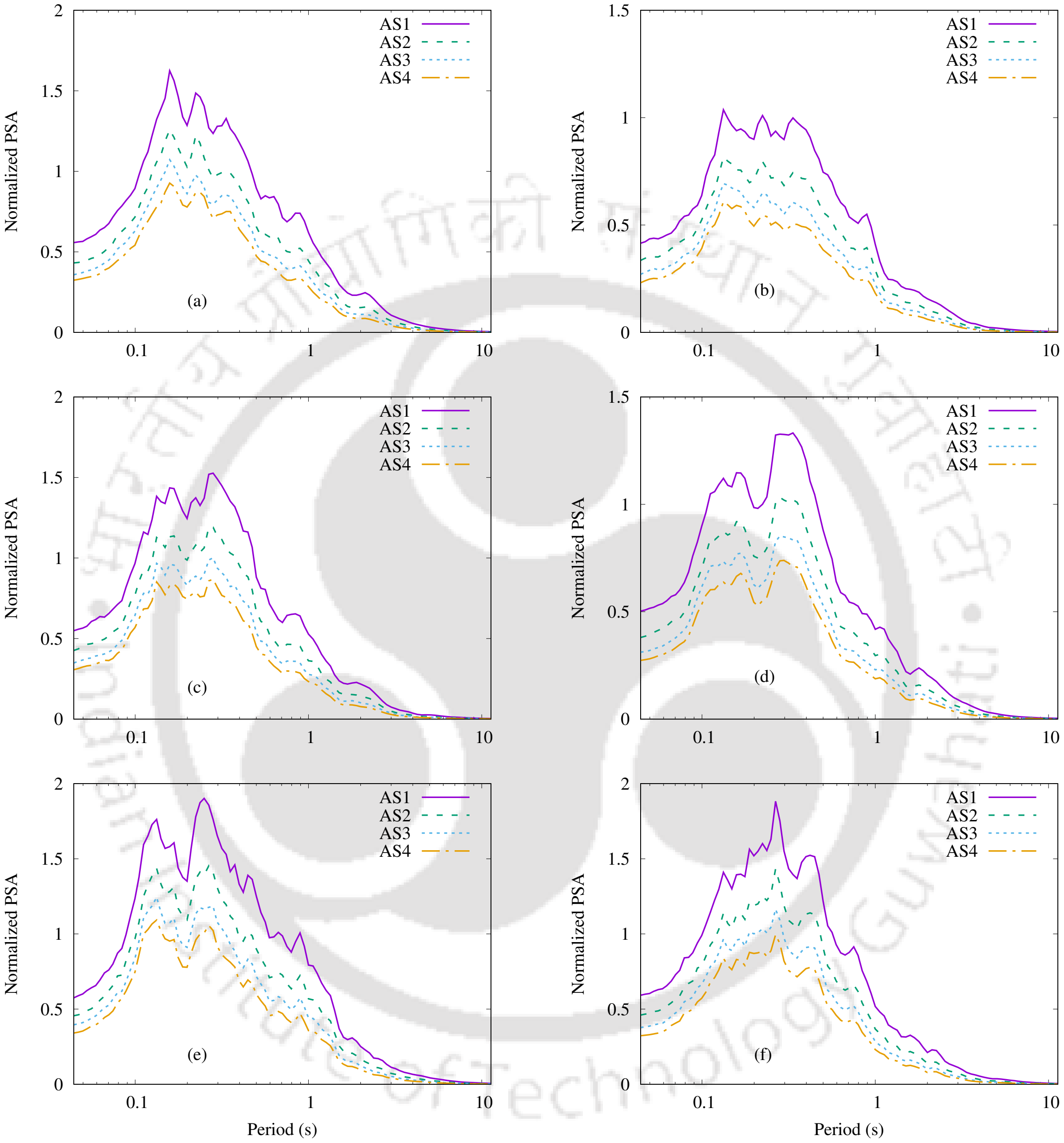

Figure 5.10 Median 5% damping PSA spectra of aftershocks for the corresponding PGA normalized main shock in the cases of (a) SEQ13, (b) SEQ14, (c) SEQ15, (d) SEQ16, (e) SEQ17 and (f) SEQ18

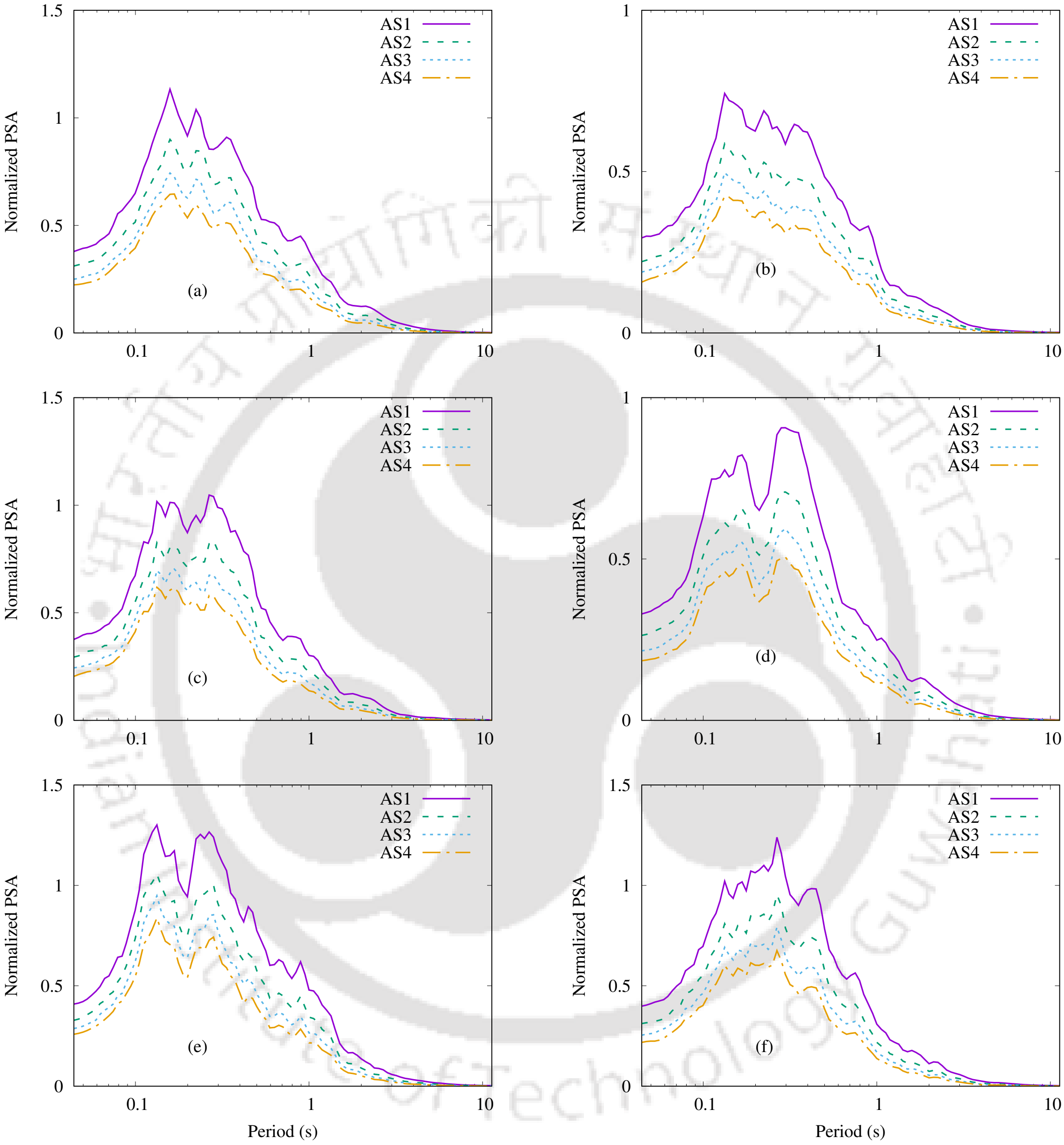

Figure 5.11 Median 5% damping PSA spectra of aftershocks for the corresponding PGA normalized main shock in the cases of (a) SEQ19, (b) SEQ20, (c) SEQ21, (d) SEQ22, (e) SEQ23 and (f) SEQ24

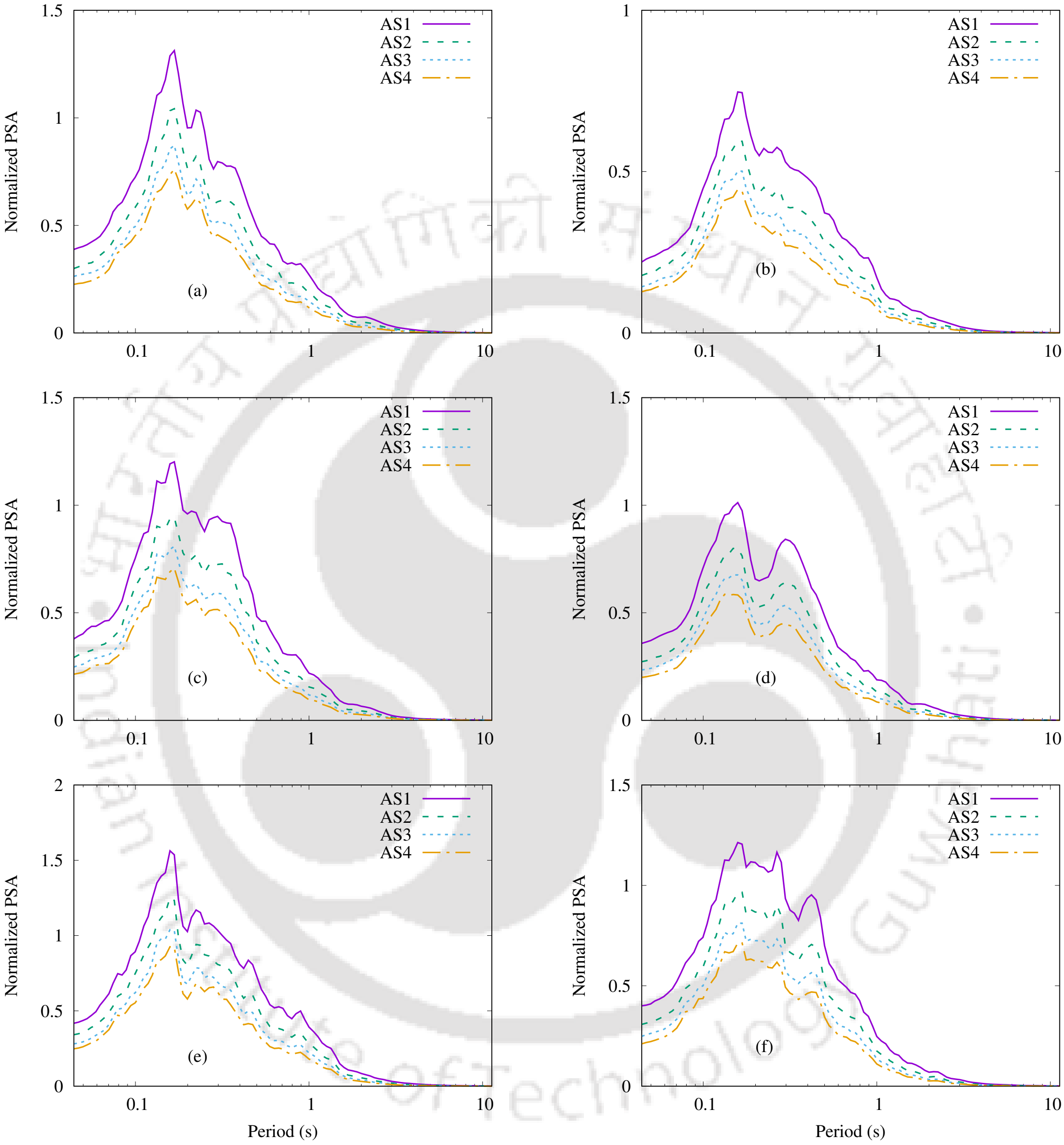

Figure 5.12 Median 5% damping PSA spectra of aftershocks for the corresponding PGA normalized main shock in the cases of (a) SEQ25, (b) SEQ26, (c) SEQ27, (d) SEQ28, (e) SEQ29 and (f) SEQ30

Table 5.6 Nomenclature and details of the MAS ensembles

Sequence Ensemble	Main shock	Seismological Parameters	
SEQ01	MS1	$M_{\text{Main}} = 7.00$ $M_{\text{AS1}} = 6.70$ $M_{\text{AS2}} = 6.51$ $M_{\text{AS3}} = 6.36$ $M_{\text{AS4}} = 6.24$	$h_{\text{Main}} = 10.0$ km $h_{\text{AS1}} = 5.0$ km $h_{\text{AS2}} = 5.0$ km $h_{\text{AS3}} = 5.0$ km $h_{\text{AS4}} = 5.0$ km
SEQ02	MS2		
SEQ03	MS3		
SEQ04	MS4		
SEQ05	MS5		
SEQ06	MS6		
SEQ07	MS1		$h_{\text{Main}} = 10.0$ km $h_{\text{AS1}} = 10.0$ km $h_{\text{AS2}} = 10.0$ km $h_{\text{AS3}} = 10.0$ km $h_{\text{AS4}} = 10.0$ km
SEQ08	MS2		
SEQ09	MS3		
SEQ10	MS4		
SEQ11	MS5		
SEQ12	MS6		
SEQ13	MS1	$M_{\text{Main}} = 7.00$ $M_{\text{AS1}} = 6.50$ $M_{\text{AS2}} = 6.30$ $M_{\text{AS3}} = 6.15$ $M_{\text{AS4}} = 6.03$	
SEQ14	MS2		
SEQ15	MS3		
SEQ16	MS4		
SEQ17	MS5		
SEQ18	MS6		
SEQ19	MS1	$M_{\text{Main}} = 7.00$ $M_{\text{AS1}} = 6.20$ $M_{\text{AS2}} = 6.00$ $M_{\text{AS3}} = 5.85$ $M_{\text{AS4}} = 5.73$	
SEQ20	MS2		
SEQ21	MS3		
SEQ22	MS4		
SEQ23	MS5		
SEQ24	MS6		
SEQ25	MS1		$h_{\text{Main}} = 10.0$ km $h_{\text{AS1}} = 15.0$ km $h_{\text{AS2}} = 15.0$ km $h_{\text{AS3}} = 15.0$ km $h_{\text{AS4}} = 15.0$ km
SEQ26	MS2		
SEQ27	MS3		
SEQ28	MS4		
SEQ29	MS5		
SEQ30	MS6		

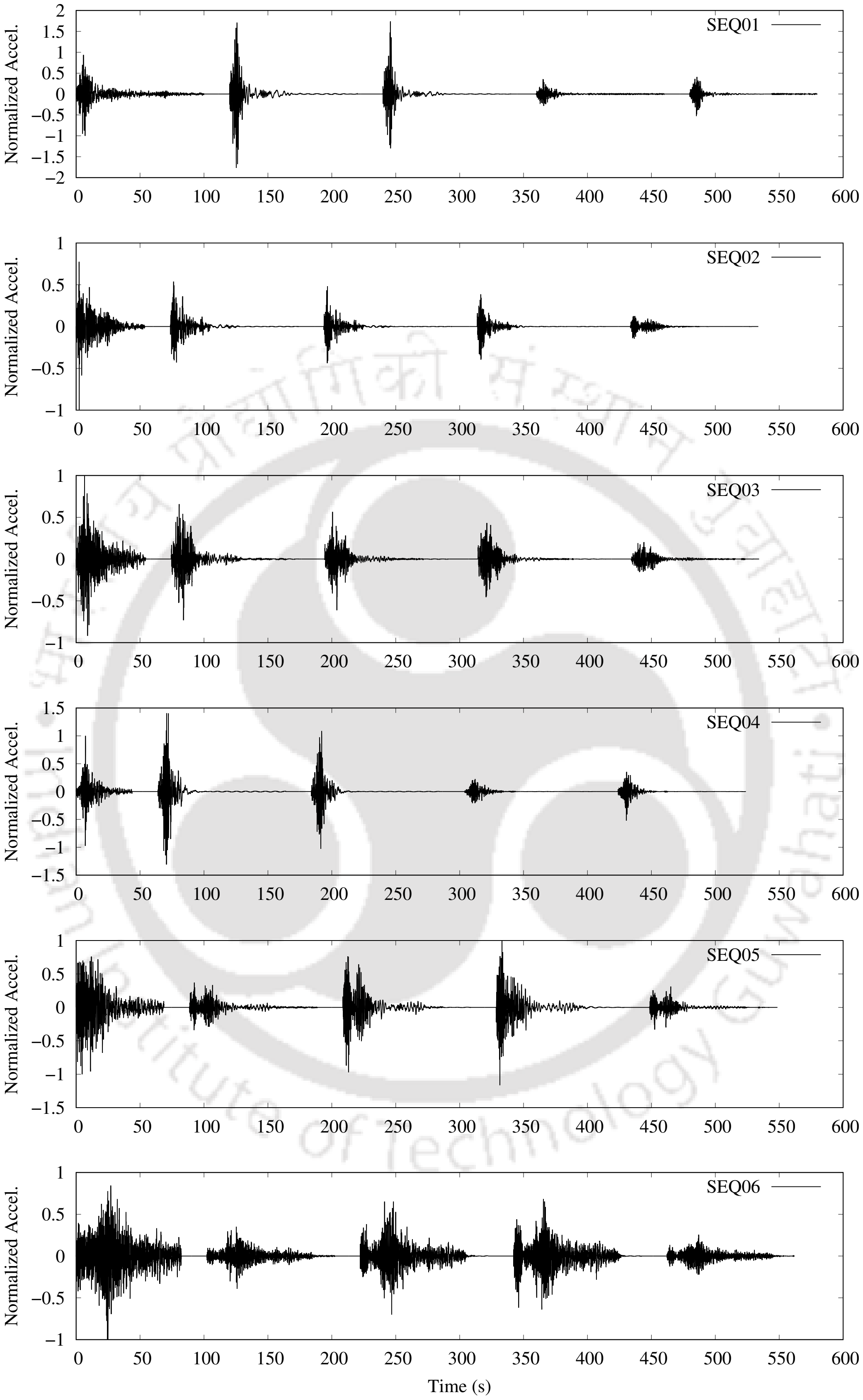

Figure 5.13 Normalized random samples, one each from every ensemble, in the cases of SEQ01, SEQ02, SEQ03, SEQ04, SEQ05 and SEQ06

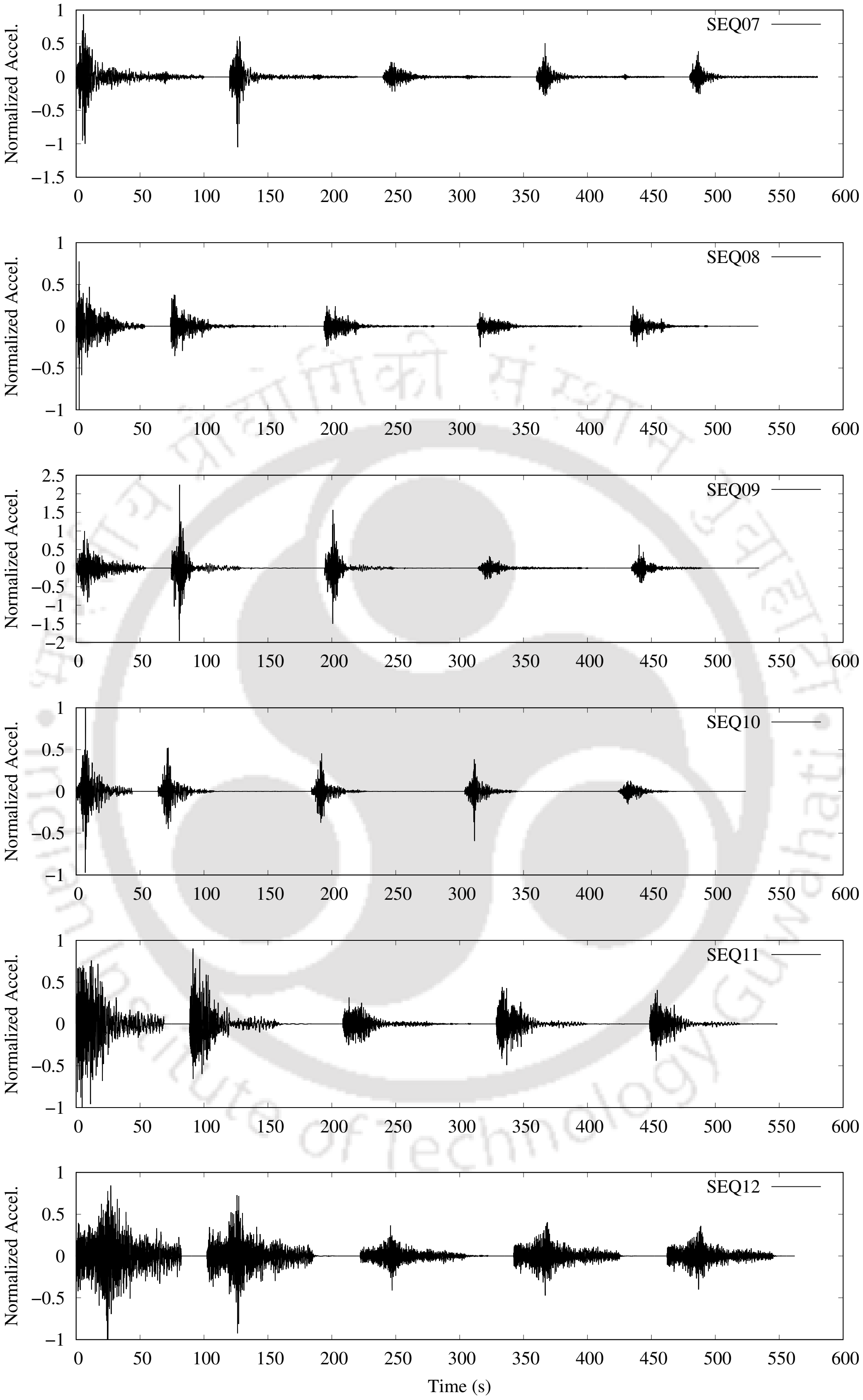

Figure 5.14 Normalized random samples, one each from every ensemble, in the cases of SEQ07, SEQ08, SEQ09, SEQ10, SEQ11 and SEQ12

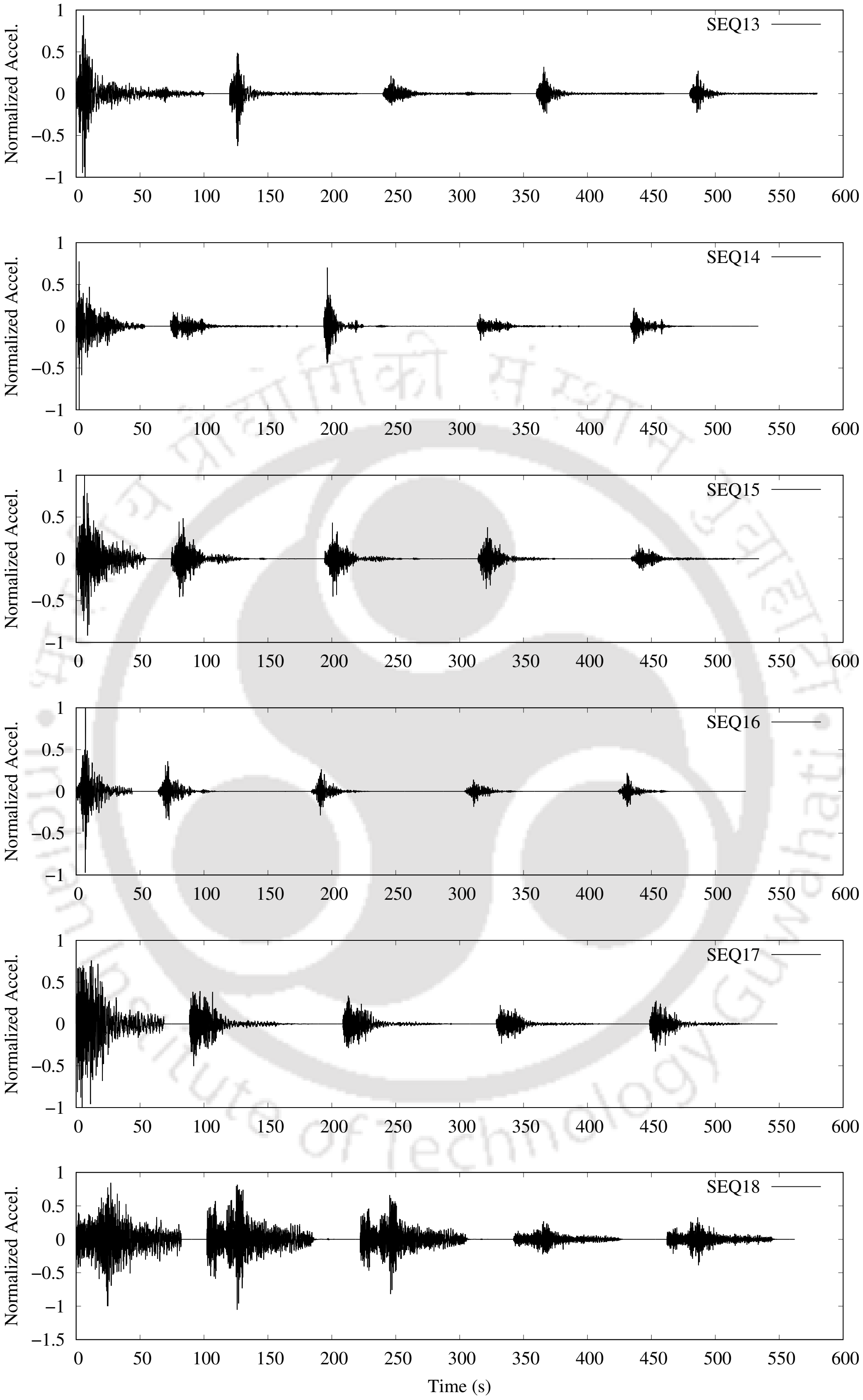

Figure 5.15 Normalized random samples, one each from every ensemble, in the cases of SEQ13, SEQ14, SEQ15, SEQ16, SEQ17 and SEQ18

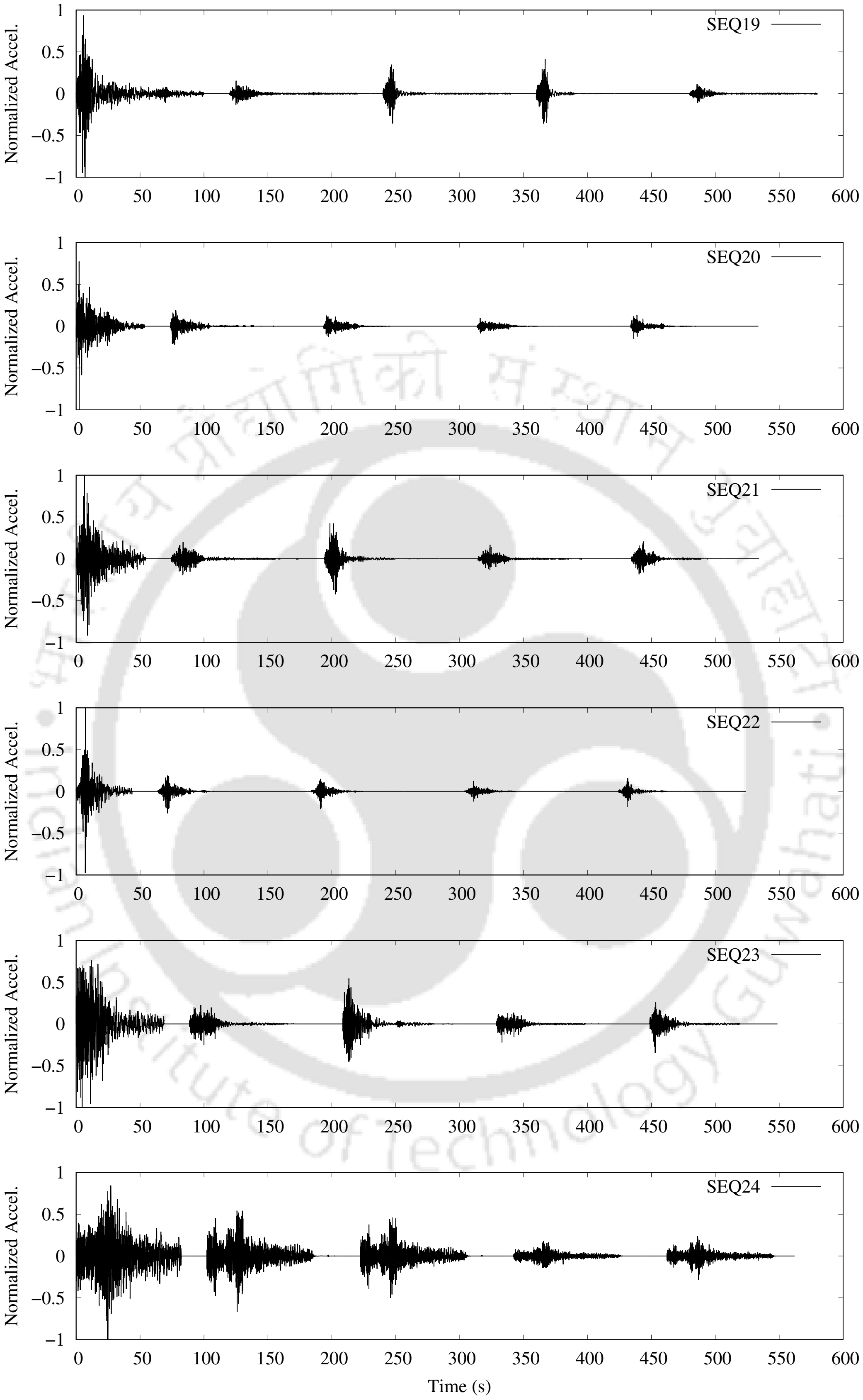

Figure 5.16 Normalized random samples, one each from every ensemble, in the cases of SEQ19, SEQ20, SEQ21, SEQ22, SEQ23 and SEQ24

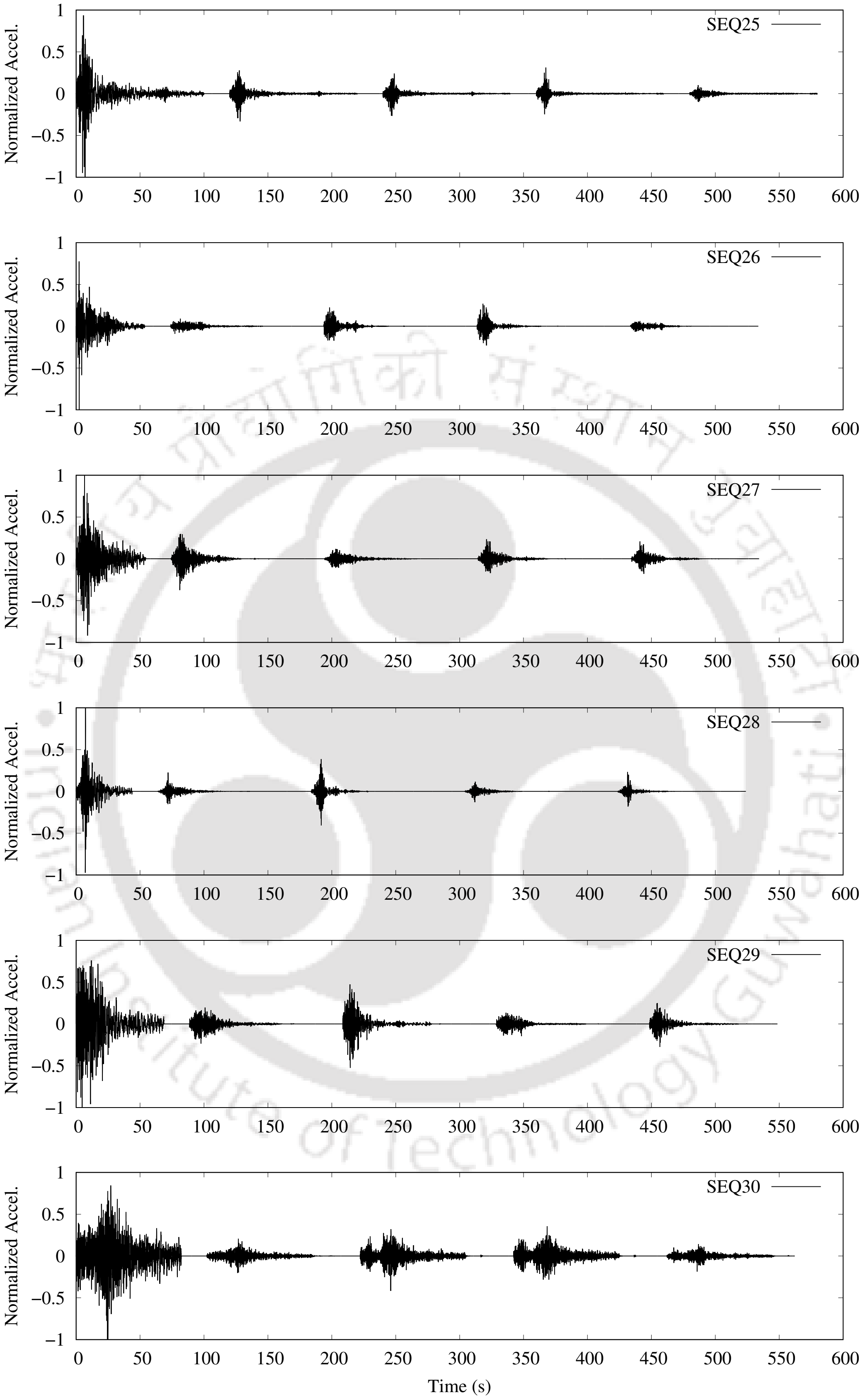

Figure 5.17 Normalized random samples, one each from every ensemble, in the cases of SEQ25, SEQ26, SEQ27, SEQ28, SEQ29 and SEQ30

5.4 Analysis of RC Frames and Safety Enhancement Strategy

As per the existing philosophy, a structure is designed to undergo into irreparable damage zone when it experiences a rare (large) event and the latter might lead to strong aftershocks causing additional damage. The modified Park & Ang type damage models quantified by damage index are broadly correlated with the physical extent of structural damage (Ang (1988); De Guzman and Ishiyama (2004); Kim et al. (2005)), where *ODI* of 0.4, 0.6 and 0.8 may be considered as the onset of irreparable damage, severe damage with some reserved strength and very severe damage with little reserved strength, respectively. On the other hand, $ODI \geq 1$ indicates collapse. So it is rational to assume that the physical damage state, a structure is targeted to attain during a major earthquake, would correspond to an *ODI* of 0.6, and in no case, it should be less than 0.4 (making it too conservative) or more than 0.8 (too unsafe for imminent aftershocks).

The main shock motions MS1 to MS6 are intended to be used for designing the structures (i.e., the frames) separately for any target damage levels defined by *ODI*. However, instead of designing the structure every time to achieve a target *ODI* for a particular main shock by changing the reinforcement details or section dimensions, the ground motions are scaled uniformly to make the structure reach the target *ODI*. The scaling factor, thus obtained for a particular combination of main shock, structure and target *ODI*, is applied to each simulated aftershock sample (for AS1 to AS4) to maintain the consistency between the main shock and its aftershocks. The ground motion scaling factor approach is adopted because in that case it can be made sure that a particular structure will have the same fundamental period (and modal properties) for different main shocks and for any target *ODI*. Otherwise, if the fundamental period changes every time, it will not be possible to identify the sole effects of the ground motion characteristics and the target *ODI* on the aftershock-induced additional damage. For the purpose of nonlinear time-history analysis (NTHA) the three frames as shown in Section 5.2 have been considered to see the effects of various MASs on the additional damage. The NTHA is carried out in OpenSees (Mazzoni et al., 2005) by Newmark-Beta method with $\gamma = 0.5$ and $\beta = 0.25$. The geometric nonlinearity has been accounted for through P-Delta option available in OpenSees.

The main objective is to propose some simple modification in the existing design philosophy in an attempt to make a structure safe against the MAS when the structure corresponds to $ODI = 0.6$ at the end of the main shock. To limit the damage of a structure during a MAS to $ODI = 1$ (i.e. collapse) the sectional capacities of the structure are modified by simultaneously increasing the strength of reinforcing steel and concrete by 10%, 15% and 20%, and the MAS (uniformly scaled as per the original structure) are applied on the modified structure to assess the adequacy. This exercise has been performed so that one can find a possible way to ensure structural safety against MASs by applying additional material safety factor (albeit fictitious) while sticking to the conventional design methodology for single event scenario.

The modified sectional capacities at various plastic hinge locations for the three example frames and for different levels of material strength enhancement are shown in Tables 5.7 to 5.15. It should be noted that in the present case the fundamental periods of the original and the modified structures are same, so for all practical purposes, the fundamental period of a structure designed based on the enhanced material safety factor (i.e. with reduced permissible strength) should be referred to whenever needed.

Table 5.7 Moment-rotation relationships at plastic hinge locations of the 1-storey frame in the case of 10% increase in material strength

Location	Yield Rotation (rad)	Yield Moment (kN.m)	Ultimate Rotation (rad)	Ultimate Moment (kN.m)
Beam	0.0047	51.3	0.1721	58.3
Exterior Column	0.0071	47.1	0.2633	51.5
Interior Column	0.0074	51.3	0.2633	55.1

Table 5.8 Moment-rotation relationships at plastic hinge locations of the 2-storey frame in the case of 10% increase in material strength

Location	Yield Rotation (rad)	Yield Moment (kN.m)	Ultimate Rotation (rad)	Ultimate Moment (kN.m)
1-Storey Beam	0.0053	86.9	0.1800	99.2
2-Storey Beam	0.0045	64.8	0.1611	73.7
1-Storey Exterior Column	0.0054	88.4	0.1578	99.2
1-Storey Interior Column	0.0058	98.1	0.1105	108.3
2-Storey Exterior Column	0.0050	62.4	0.1864	69.6
2-Storey Interior Column	0.0052	68.3	0.1935	75.1

Table 5.9 Moment-rotation relationships at plastic hinge locations of the 5-storey frame in the case of 10% increase in material strength

Location	Yield Rotation (rad)	Yield Moment (kN.m)	Ultimate Rotation (rad)	Ultimate Moment (kN.m)
1, 2 & 3-Storey Beams	0.0072	175.8	0.2136	205.0
4-Storey Beam	0.0068	133.7	0.2130	154.3
5-Storey Beam	0.0063	91.3	0.2125	104.0
1-Storey Exterior Column	0.0047	246.2	0.0828	283.4
1-Storey Interior Column	0.0052	276.9	0.0731	312.2
2-Storey Exterior Column	0.0037	172.3	0.0883	195.9
2-Storey Interior Column	0.0040	199.8	0.0581	220.7
3-Storey Exterior Column	0.0069	105.9	0.1359	116.9
3-Storey Interior Column	0.0076	118.3	0.1153	129.1
4-Storey Exterior Column	0.0062	88.6	0.1778	99.4
4-Storey Interior Column	0.0066	97.8	0.1161	108.1
5-Storey Exterior Column	0.0050	62.5	0.1840	69.7
5-Storey Interior Column	0.0051	68.2	0.1908	75.1

Table 5.10 Moment-rotation relationships at plastic hinge locations of the 1-storey frame in the case of 15% increase in material strength

Location	Yield Rotation (rad)	Yield Moment (kN.m)	Ultimate Rotation (rad)	Ultimate Moment (kN.m)
Beam	0.0049	53.6	0.1723	60.6
Exterior Column	0.0073	49.0	0.2632	53.3
Interior Column	0.0077	53.2	0.2808	56.8

Table 5.11 Moment-rotation relationships at plastic hinge locations of the 2-storey frame in the case of 15% increase in material strength

Location	Yield Rotation (rad)	Yield Moment (kN.m)	Ultimate Rotation (rad)	Ultimate Moment (kN.m)
1-Storey Beam	0.0055	90.9	0.1802	103.1
2-Storey Beam	0.0047	67.7	0.1612	76.6
1-Storey Exterior Column	0.0056	91.9	0.1574	102.6
1-Storey Interior Column	0.0060	101.5	0.1129	111.4
2-Storey Exterior Column	0.0052	64.9	0.1866	72.4
2-Storey Interior Column	0.0054	70.7	0.1934	77.9

Table 5.12 Moment-rotation relationships at plastic hinge locations of the 5-storey frame in the case of 15% increase in material strength

Location	Yield Rotation (rad)	Yield Moment (kN.m)	Ultimate Rotation (rad)	Ultimate Moment (kN.m)
1, 2 & 3-Storey Beams	0.0075	183.7	0.2138	214.3
4-Storey Beam	0.0071	139.8	0.2133	160.9
5-Storey Beam	0.0066	95.6	0.2127	108.0
1-Storey Exterior Column	0.0049	255.1	0.0862	292.3
1-Storey Interior Column	0.0053	285.9	0.0775	321.1
2-Storey Exterior Column	0.0038	178.3	0.0916	200.8
2-Storey Interior Column	0.0041	205.9	0.0595	226.7
3-Storey Exterior Column	0.0071	109.8	0.1368	120.5
3-Storey Interior Column	0.0078	122.2	0.1173	132.3
4-Storey Exterior Column	0.0064	92.1	0.1772	102.8
4-Storey Interior Column	0.0068	101.3	0.1309	111.2
5-Storey Exterior Column	0.0052	64.9	0.1841	72.4
5-Storey Interior Column	0.0053	70.6	0.1908	77.8

Table 5.13 Moment-rotation relationships at plastic hinge locations of the 1-storey frame in the case of 20% increase in material strength

Location	Yield Rotation (rad)	Yield Moment (kN.m)	Ultimate Rotation (rad)	Ultimate Moment (kN.m)
Beam	0.0051	55.8	0.1725	62.8
Exterior Column	0.0076	50.9	0.2631	55.2
Interior Column	0.0080	55.1	0.2807	58.6

Table 5.14 Moment-rotation relationships at plastic hinge locations of the 2-storey frame in the case of 20% increase in material strength

Location	Yield Rotation (rad)	Yield Moment (kN.m)	Ultimate Rotation (rad)	Ultimate Moment (kN.m)
1-Storey Beam	0.0058	94.8	0.1804	107.0
2-Storey Beam	0.0049	70.7	0.1614	79.4
1-Storey Exterior Column	0.0058	95.3	0.2016	105.9
1-Storey Interior Column	0.0062	105.0	0.1621	114.3
2-Storey Exterior Column	0.0054	67.4	0.1868	75.1
2-Storey Interior Column	0.0056	73.2	0.1934	80.5

Table 5.15 Moment-rotation relationships at plastic hinge locations of the 5-storey frame in the case of 20% increase in material strength

Location	Yield Rotation (rad)	Yield Moment (kN.m)	Ultimate Rotation (rad)	Ultimate Moment (kN.m)
1, 2 & 3-Storey Beams	0.0078	191.6	0.2141	223.5
4-Storey Beam	0.0074	145.9	0.2136	167.9
5-Storey Beam	0.0068	99.7	0.2129	112.2
1-Storey Exterior Column	0.0051	264.1	0.0900	302.9
1-Storey Interior Column	0.0055	295.2	0.0824	329.6
2-Storey Exterior Column	0.0040	184.1	0.1334	205.9
2-Storey Interior Column	0.0043	212.2	0.0911	232.6
3-Storey Exterior Column	0.0074	113.7	0.1959	124.0
3-Storey Interior Column	0.0081	126.1	0.1520	135.2
4-Storey Exterior Column	0.0067	95.5	0.2304	106.1
4-Storey Interior Column	0.0071	104.8	0.1348	114.2
5-Storey Exterior Column	0.0054	67.5	0.1843	75.1
5-Storey Interior Column	0.0055	73.1	0.1907	80.5

5.5 Results and Discussions

Table 5.16 shows the average and maximum *ODI*s at the end of different aftershocks in a sequence for different sequence ensembles for the original 1-storey frame (designed for $ODI = 0.6$ against the main shock). Tables 5.17 to 5.19 show the same quantities along with the main shock *ODI* when the original 1-storey frame is modified, respectively by 10%, 15% and 20% increase in the material strength (both for steel and concrete). Similar results are shown for 2-storey frame in Tables 5.20 to 5.23 and for 5-storey frame in Tables 5.24 to 5.27. In any table, the collapse cases ($ODI \geq 1$) are emphasized in *italic*, whereas the safe cases ($ODI < 1$) owing to the latest modification are emphasized in bold. The already safe cases before any further modification (i.e. increased material strength) are not reported because further modification is not relevant for those cases. For better clarity, such cases are represented by different shades to indicate at what levels of modification the unsafe cases in the original structure have become safe.

It is clear from Table 5.16, 5.20 and 5.24 that when the largest aftershock is smaller than the main shock by 0.5 or more (magnitude-wise), the 1-storey 2-storey and 5-storey frames are safe against collapse for almost all the cases when the maximum *ODI* is considered except for SEQ13 for 1-storey and 2-storey frames (AS2 onward for 1-storey and AS4 for 2-storey). On the other hand, for $\Delta M_1 = 0.3$ almost all cases indicate collapse when the maximum *ODI* is considered, even for a single (largest) aftershock. However, from the average *ODI* point of view, all cases are safe against the first (largest) aftershock for $\Delta M_1 = 0.3$ in the cases of 1-storey and 2-storey frames but failure happens onward. 1-storey, 2-storey and 5-storey frames are safe against collapse for all the aftershocks (AS1 to AS4) from the average *ODI* point of view in the cases of SEQ07 to SEQ12, except for SEQ09 (AS3 onward) for 1-storey and 2-storey frames.

For 5-storey frame, the effects of geometrical nonlinearity (i.e. P-Delta effect) are significant during the response due to aftershocks and due to this, for some sequences, the 5-storey frame undergoes excessively large deformation resulting in unrealistically high damage indices. Since such high values do not have any numerical relevance other than indicating catastrophic failure, the numerical values for these sequence cases are not reported. Hence for such sequences, *ODI*s are marked by “X” in Tables 5.24 to 5.27. This is observed for larger and shallower aftershocks (SEQ01 to SEQ06) only, which are very extreme cases for aftershock severity. It is found that if the P-Delta effect is ignored, the 5-storey frame does not exhibit the above-mentioned excessive large displacement (though $ODI > 1$), which indicates that for response due to aftershocks the consideration of the P-Delta effect is crucial.

Other than identifying the safe and unsafe cases from collapse point of view, it is important to identify any trend in the variation of *ODI* in order to draw any general inference. The average *ODI* shows some saturation in increase with the number of aftershocks because aftershocks are arranged in descending order of their magnitudes. Also, the difference between

Table 5.16 Average and maximum *ODI*s at the end of each aftershock for different sequence ensembles for 1-storey frame when *ODI* at the end of main shock is 0.6

Sequence Ensemble	Main shock Name	Average *ODI*				Maximum *ODI*			
		AS1	AS2	AS3	AS4	AS1	AS2	AS3	AS4
SEQ01	MS1	0.81	0.98	*1.09*	*1.14*	*1.42*	*1.46*	*1.46*	*1.59*
SEQ02	MS2	0.85	*1.13*	*1.34*	*1.38*	*1.89*	*2.60*	*2.64*	*2.71*
SEQ03	MS3	0.79	*1.10*	*1.32*	*1.38*	*1.55*	*1.57*	*1.83*	*1.99*
SEQ04	MS4	0.85	*1.01*	*1.09*	*1.18*	*1.45*	*1.52*	*1.55*	*2.55*
SEQ05	MS5	0.84	0.98	*1.08*	*1.13*	*1.56*	*1.57*	*1.65*	*1.70*
SEQ06	MS6	0.89	*1.07*	*1.18*	*1.23*	*1.88*	*1.90*	*1.97*	*2.02*
SEQ07	MS1	0.73	0.79	0.84	0.86	*1.18*	*1.21*	*1.21*	*1.24*
SEQ08	MS2	0.75	0.81	0.87	0.91	*1.08*	*1.19*	*1.22*	*1.25*
SEQ09	MS3	0.84	0.96	*1.04*	*1.08*	*1.31*	*1.47*	*1.49*	*1.54*
SEQ10	MS4	0.71	0.77	0.83	0.86	0.97	*1.00*	*1.07*	*1.07*
SEQ11	MS5	0.72	0.81	0.87	0.90	0.97	0.99	*1.03*	*1.09*
SEQ12	MS6	0.73	0.83	0.90	0.92	*1.08*	*1.09*	*1.13*	*1.16*
SEQ13	MS1	0.67	0.72	0.74	0.75	0.89	*1.05*	*1.05*	*1.08*
SEQ14	MS2	0.66	0.69	0.73	0.74	0.84	0.84	0.86	0.88
SEQ15	MS3	0.67	0.72	0.76	0.77	0.87	0.88	0.88	0.90
SEQ16	MS4	0.65	0.68	0.70	0.71	0.76	0.77	0.77	0.78
SEQ17	MS5	0.66	0.70	0.73	0.74	0.79	0.80	0.82	0.84
SEQ18	MS6	0.66	0.69	0.72	0.73	0.80	0.80	0.82	0.83
SEQ19	MS1	0.62	0.63	0.64	0.64	0.67	0.67	0.67	0.68
SEQ20	MS2	0.62	0.64	0.65	0.65	0.70	0.75	0.75	0.76
SEQ21	MS3	0.63	0.65	0.66	0.66	0.72	0.77	0.77	0.78
SEQ22	MS4	0.62	0.62	0.63	0.63	0.66	0.66	0.66	0.66
SEQ23	MS5	0.62	0.64	0.64	0.64	0.70	0.74	0.74	0.74
SEQ24	MS6	0.61	0.62	0.63	0.63	0.65	0.65	0.66	0.66
SEQ25	MS1	0.61	0.62	0.62	0.62	0.64	0.64	0.64	0.64
SEQ26	MS2	0.61	0.62	0.62	0.62	0.65	0.68	0.68	0.68
SEQ27	MS3	0.62	0.62	0.63	0.63	0.67	0.71	0.71	0.71
SEQ28	MS4	0.61	0.61	0.62	0.62	0.64	0.64	0.64	0.64
SEQ29	MS5	0.61	0.62	0.62	0.62	0.65	0.67	0.67	0.68
SEQ30	MS6	0.61	0.62	0.62	0.62	0.65	0.67	0.67	0.67

Italic shows collapse case ($ODI \geq 1$)

the average initial *ODI* (i.e. at the end of main shock) and the average final *ODI* (i.e. at the end of AS4) are varied across the different main shock cases for a specific seismological scenario. The variations are to be attributed to both the time-frequency characteristics of the main shocks and those of the simulated aftershocks. Hence, the time-frequency characteristics of the preceding main shock may play an important role in the future aftershock-induced damage. It can be further observed that the motions with longer SMD (like MS6) are likely to have higher final *ODI* in comparison with a motion having smaller SMD (like MS4). Observations for the average *ODI* are trend-wise true for the maximum *ODI* as well by and large. However, there may be some aberrations in the trend of maximum *ODI* due to the presence of some individual aftershock motion samples in some sequences that are either associated with a very low probability of exceedance (for the given seismic scenario) or the motion is very well-tuned with

Table 5.17 Average and maximum *ODI*s at the end of each aftershock for different sequence ensembles for 1-storey frame with 10% increase in material strength

Sequence Ensemble	Main shock Name	Main shock *ODI*	Average *ODI*				Maximum *ODI*			
			AS1	AS2	AS3	AS4	AS1	AS2	AS3	AS4
SEQ01	MS1	0.52			**0.99**	*1.04*	*1.23*	*1.26*	*1.38*	*1.50*
SEQ02	MS2	0.55		*1.04*	*1.22*	*1.26*	*1.79*	*2.45*	*2.48*	*2.55*
SEQ03	MS3	0.55		*1.00*	*1.20*	*1.25*	*1.44*	*1.45*	*1.70*	*1.84*
SEQ04	MS4	0.55		**0.91**	**0.97**	*1.01*	*1.29*	*1.35*	*1.37*	*1.58*
SEQ05	MS5	0.55			**0.97**	*1.02*	*1.37*	*1.38*	*1.45*	*1.49*
SEQ06	MS6	0.53		**0.93**	*1.03*	*1.07*	*1.53*	*1.54*	*1.60*	*1.64*
SEQ07	MS1	0.52					*1.05*	*1.07*	*1.07*	*1.10*
SEQ08	MS2	0.55					**0.90**	**0.98**	*1.00*	*1.07*
SEQ09	MS3	0.55			**0.94**	**0.97**	*1.18*	*1.35*	*1.37*	*1.42*
SEQ10	MS4	0.55						**0.89**	**0.95**	**0.95**
SEQ11	MS5	0.55							**0.94**	**0.99**
SEQ12	MS6	0.53					**0.97**	**0.98**	*1.02*	*1.04*
SEQ13	MS1	0.52						**0.93**	**0.94**	**0.96**
SEQ14	MS2									
SEQ15	MS3									
SEQ16	MS4									
SEQ17	MS5									
SEQ18	MS6									
SEQ19	MS1									
SEQ20	MS2									
SEQ21	MS3									
SEQ22	MS4									
SEQ23	MS5									
SEQ24	MS6									
SEQ25	MS1									
SEQ26	MS2									
SEQ27	MS3									
SEQ28	MS4									
SEQ29	MS5									
SEQ30	MS6									

Italic shows collapse case ($ODI \geq 1$)
Bold shows safe cases ($ODI < 1$) due to 10% increase in material strength
Blank spaces show safe cases ($ODI < 1$) in original structure

the degraded structure causing large residual displacement. E.g., in the case of AS4 in SEQ04 for 1-storey frame (see Table 5.16) the maximum *ODI* has increased by unity because in that case, the residual displacement caused by one of the samples of AS4 is around 0.7 m (at the roof level) in the direction of previously incurred residual displacement. Such cases are, though plausible, unlikely to arise.

As mentioned earlier it is highly intriguing to see if the enhanced material safety factor can commute some failure cases to success, in terms of collapse during MAS. For 10% increase in strength, in terms of average *ODI*, 1-storey and 2-storey frames have become safe against aftershocks of all cases as seen in Tables 5.17 and 5.21, respectively except for SEQ01 to SEQ06 (Bigger and shallower aftershocks) for 1-storey and SEQ02 to SEQ06 for 2-storey. 5-

Table 5.18 Average and maximum *ODI*s at the end of each aftershock for different sequence ensembles for 1-storey frame with 15% increase in material strength

Sequence Ensemble	Main shock Name	Main shock *ODI*	Average *ODI*				Maximum *ODI*			
			AS1	AS2	AS3	AS4	AS1	AS2	AS3	AS4
SEQ01	MS1	0.48			▨	**0.98**	*1.18*	*1.21*	*1.32*	*1.41*
SEQ02	MS2	0.52		**0.99**	*1.15*	*1.19*	*1.71*	*2.34*	*2.37*	*2.43*
SEQ03	MS3	0.52		**0.94**	*1.13*	*1.17*	*1.37*	*1.38*	*1.61*	*1.74*
SEQ04	MS4	0.52		▨	▨	**0.93**	*1.19*	*1.24*	*1.26*	*1.40*
SEQ05	MS5	0.52			▨	**0.95**	*1.26*	*1.27*	*1.33*	*1.37*
SEQ06	MS6	0.49		▨	**0.94**	**0.98**	*1.43*	*1.43*	*1.49*	*1.52*
SEQ07	MS1	0.48					**0.97**	**0.99**	**0.99**	*1.02*
SEQ08	MS2	0.52					▨	▨	**0.91**	*1.01*
SEQ09	MS3	0.52			▨	▨	*1.12*	*1.28*	*1.30*	*1.34*
SEQ10	MS4	▨						▨	▨	▨
SEQ11	MS5	▨							▨	▨
SEQ12	MS6	0.49					▨	▨	**0.94**	**0.97**
SEQ13	MS1	▨						▨	▨	▨
SEQ14	MS2									
SEQ15	MS3									
SEQ16	MS4									
SEQ17	MS5									
SEQ18	MS6									
SEQ19	MS1									
SEQ20	MS2									
SEQ21	MS3									
SEQ22	MS4									
SEQ23	MS5									
SEQ24	MS6									
SEQ25	MS1									
SEQ26	MS2									
SEQ27	MS3									
SEQ28	MS4									
SEQ29	MS5									
SEQ30	MS6									

Italic shows collapse case ($ODI \geq 1$)
Bold shows safe cases ($ODI < 1$) due to 15% increase in material strength
Blank spaces show safe cases ($ODI < 1$) in original structure

▨ Safe with 10% increase in material strength

storey frame is already safe for all cases except for SEQ01 to SEQ06 without any increase in strength in terms of average *ODI*. For SEQ01 to SEQ06, up to AS2 (second aftershock), 1-storey and 2-storey have become safe in terms of average *ODI*, except for SEQ02 and SEQ03 for 1-storey frame. For SEQ01 to SEQ06, 1-storey frame has become safe till AS3 except for SEQ02, SEQ03 and SEQ06. For SEQ01, 2-storey frame has become safe for all aftershocks in terms of average *ODI*. 5-storey frame is not safe against collapse for any aftershocks of SEQ01 to SEQ06 in terms of average *ODI* as seen in Table 5.25 except for AS1 for SEQ02 and SEQ03, where for AS1 of SEQ03, the original frame was already safe. Also for 5-storey frame, large displacements observed for the original frame have been arrested till AS1 for

Table 5.19 Average and maximum *ODI*s at the end of each aftershock for different sequence ensembles for 1-storey frame with 20% increase in material strength

Sequence Ensemble	Main shock Name	Main shock *ODI*	Average *ODI*				Maximum *ODI*			
			AS1	AS2	AS3	AS4	AS1	AS2	AS3	AS4
SEQ01	MS1	0.45			░	▓	*1.17*	*1.20*	*1.30*	*1.39*
SEQ02	MS2	0.51		▓	*1.11*	*1.15*	*1.68*	*2.27*	*2.29*	*2.35*
SEQ03	MS3	0.51		▓	*1.10*	*1.14*	*1.34*	*1.35*	*1.57*	*1.70*
SEQ04	MS4	0.50		░	░	▓	*1.13*	*1.18*	*1.20*	*1.33*
SEQ05	MS5	0.51			░	▓	*1.20*	*1.21*	*1.27*	*1.31*
SEQ06	MS6	0.47		░	▓	▓	*1.36*	*1.37*	*1.42*	*1.46*
SEQ07	MS1	0.45					▓	▓	▓	**0.98**
SEQ08	MS2	0.51					░	░	▓	**0.97**
SEQ09	MS3	0.51			░	░	*1.09*	*1.25*	*1.26*	*1.31*
SEQ10	MS4	░						░	░	░
SEQ11	MS5	░							░	░
SEQ12	MS6	▓					░	░	▓	▓
SEQ13	MS1	░						░	░	░
SEQ14	MS2									
SEQ15	MS3									
SEQ16	MS4									
SEQ17	MS5									
SEQ18	MS6									
SEQ19	MS1									
SEQ20	MS2									
SEQ21	MS3									
SEQ22	MS4									
SEQ23	MS5									
SEQ24	MS6									
SEQ25	MS1									
SEQ26	MS2									
SEQ27	MS3									
SEQ28	MS4									
SEQ29	MS5									
SEQ30	MS6									

Italic shows collapse case ($ODI \geq 1$)
Bold shows safe cases ($ODI < 1$) due to 20% increase in material strength
Blank spaces show safe cases ($ODI < 1$) in original structure

░ Safe with 10% increase in material strength
▓ Safe with 15% increase in material strength

SEQ02, although not safe against collapse. It is more important to see the performance of 10% increase in strength in terms of the maximum *ODI* for different cases. 1-storey frame has become safe against all aftershocks of SEQ10, SEQ11 and SEQ13 and 2-storey frame against all aftershocks of SEQ07, SEQ08, SEQ10, SEQ12 and SEQ13. For SEQ07 to SEQ12, 1-storey and 2-storey frames have become safe upto AS2 except for SEQ07 and SEQ09 for 1-storey and SEQ09 for 2-storey.

It is interesting to see how many failure cases for 10% increase in material strength have been converted in safe when material strength has been increased by 15% for all the frames. The failure cases for SEQ01, SEQ04, SEQ05 and SEQ06 have now become safe against all

Table 5.20 Average and maximum *ODI*s at the end of each aftershock for different sequence ensembles for 2-storey frame when *ODI* at the end of main shock is 0.6

Sequence Ensemble	Main shock Name	Average *ODI*				Maximum *ODI*			
		AS1	AS2	AS3	AS4	AS1	AS2	AS3	AS4
SEQ01	MS1	0.80	0.93	*1.03*	*1.07*	*1.33*	*1.37*	*1.37*	*1.44*
SEQ02	MS2	0.83	*1.08*	*1.23*	*1.28*	*1.77*	*2.34*	*2.36*	*2.42*
SEQ03	MS3	0.80	*1.12*	*1.36*	*1.42*	*1.56*	*1.63*	*2.00*	*2.09*
SEQ04	MS4	0.92	*1.11*	*1.21*	*1.26*	*1.52*	*1.65*	*1.72*	*1.78*
SEQ05	MS5	0.91	*1.08*	*1.20*	*1.27*	*1.97*	*2.00*	*2.10*	*2.16*
SEQ06	MS6	0.89	*1.08*	*1.19*	*1.24*	*1.72*	*1.74*	*1.82*	*1.86*
SEQ07	MS1	0.71	0.76	0.80	0.82	*1.05*	*1.06*	*1.06*	*1.09*
SEQ08	MS2	0.71	0.76	0.81	0.84	0.89	0.95	0.99	*1.08*
SEQ09	MS3	0.83	0.95	*1.02*	*1.06*	*1.29*	*1.57*	*1.59*	*1.64*
SEQ10	MS4	0.72	0.80	0.87	0.90	0.99	*1.00*	*1.07*	*1.11*
SEQ11	MS5	0.75	0.84	0.92	0.95	*1.06*	*1.09*	*1.11*	*1.19*
SEQ12	MS6	0.73	0.82	0.89	0.92	*1.07*	*1.08*	*1.12*	*1.14*
SEQ13	MS1	0.66	0.70	0.72	0.73	0.83	0.98	0.98	*1.00*
SEQ14	MS2	0.65	0.68	0.71	0.72	0.85	0.85	0.87	0.88
SEQ15	MS3	0.67	0.71	0.75	0.77	0.86	0.87	0.87	0.90
SEQ16	MS4	0.65	0.69	0.72	0.74	0.78	0.79	0.81	0.82
SEQ17	MS5	0.67	0.72	0.75	0.77	0.83	0.84	0.86	0.88
SEQ18	MS6	0.66	0.70	0.73	0.73	0.83	0.83	0.84	0.85
SEQ19	MS1	0.62	0.63	0.64	0.64	0.67	0.67	0.68	0.68
SEQ20	MS2	0.62	0.63	0.63	0.64	0.68	0.72	0.72	0.73
SEQ21	MS3	0.63	0.65	0.66	0.67	0.71	0.77	0.77	0.78
SEQ22	MS4	0.62	0.63	0.64	0.64	0.67	0.67	0.68	0.68
SEQ23	MS5	0.62	0.64	0.65	0.65	0.72	0.77	0.77	0.78
SEQ24	MS6	0.61	0.62	0.62	0.63	0.65	0.65	0.66	0.66
SEQ25	MS1	0.61	0.61	0.62	0.62	0.64	0.64	0.64	0.65
SEQ26	MS2	0.61	0.61	0.61	0.61	0.64	0.65	0.65	0.66
SEQ27	MS3	0.62	0.62	0.63	0.63	0.67	0.71	0.71	0.72
SEQ28	MS4	0.61	0.61	0.62	0.62	0.65	0.65	0.65	0.65
SEQ29	MS5	0.61	0.62	0.62	0.62	0.66	0.68	0.68	0.68
SEQ30	MS6	0.61	0.61	0.61	0.61	0.64	0.65	0.65	0.66

Italic shows collapse case (*ODI* ≥ 1)

aftershocks for 1-storey in terms of average *ODI* as seen from Table 5.18 and failure cases for SEQ02 and SEQ03 have become safe up to AS2 making 1-storey safe against AS2 for all cases in terms of average *ODI*. From Table 5.22 it is clear that 2-storey frame for SEQ01 and SEQ06 have become safe against all aftershocks from average *ODI* point of view. Further, for 5-storey frame the large displacements observed for the original frame have been arrested for AS2 for SEQ03 and has become safe till AS2 for SEQ03 as seen in Table 5.26 in terms of average *ODI*. However, in none of the cases for SEQ01 to SEQ06, the structures are safe from the maximum *ODI* point of view because the aftershocks are bigger ($\Delta M_1 = 0.3$) and shallower (with respect to the main shock) for these cases. But even for similarly bigger aftershocks with focal depths equal to that of the main shock (i.e. SEQ07 to SEQ12), it is found that several cases are safe based on the maximum *ODI* not only against a few larger aftershocks but also against the entire

Table 5.21 Average and maximum *ODI*s at the end of each aftershock for different sequence ensembles for 2-storey frame with 10% increase in material strength

Sequence Ensemble	Main shock Name	Main shock *ODI*	Average *ODI*				Maximum *ODI*			
			AS1	AS2	AS3	AS4	AS1	AS2	AS3	AS4
SEQ01	MS1	0.50			**0.89**	**0.93**	*1.18*	*1.20*	*1.23*	*1.26*
SEQ02	MS2	0.53		**0.95**	*1.08*	*1.11*	*1.59*	*2.08*	*2.10*	*2.15*
SEQ03	MS3	0.51		**0.96**	*1.16*	*1.21*	*1.34*	*1.43*	*1.75*	*1.83*
SEQ04	MS4	0.54		**0.98**	*1.06*	*1.10*	*1.33*	*1.44*	*1.50*	*1.54*
SEQ05	MS5	0.55		**0.96**	*1.07*	*1.12*	*1.70*	*1.72*	*1.81*	*1.86*
SEQ06	MS6	0.52		**0.92**	*1.01*	*1.06*	*1.50*	*1.52*	*1.58*	*1.61*
SEQ07	MS1	0.50					**0.93**	**0.94**	**0.94**	**0.97**
SEQ08	MS2	0.53								**0.91**
SEQ09	MS3	0.51			**0.87**	**0.90**	*1.11*	*1.36*	*1.37*	*1.41*
SEQ10	MS4	0.54						**0.89**	**0.95**	**0.98**
SEQ11	MS5	0.55					**0.95**	**0.97**	*1.00*	*1.06*
SEQ12	MS6	0.52					**0.78**	**0.81**	**0.92**	**0.97**
SEQ13	MS1	0.50								**0.86**
SEQ14	MS2									
SEQ15	MS3									
SEQ16	MS4									
SEQ17	MS5									
SEQ18	MS6									
SEQ19	MS1									
SEQ20	MS2									
SEQ21	MS3									
SEQ22	MS4									
SEQ23	MS5									
SEQ24	MS6									
SEQ25	MS1									
SEQ26	MS2									
SEQ27	MS3									
SEQ28	MS4									
SEQ29	MS5									
SEQ30	MS6									

Italic shows collapse case ($ODI \geq 1$)
Bold shows safe cases ($ODI < 1$) due to 10% increase in material strength
Blank spaces show safe cases ($ODI < 1$) in original structure

sequence at the end of 15% increase in material strength. E.g., the modified 1-storey frame for SEQ10, SEQ11 and SEQ12, the modified 2-storey frame for SEQ07, SEQ08, SEQ10 and the modified 5-storey frame for SEQ12 are all safe against the entire sequence of aftershocks in terms of the maximum *ODI*. On the other hand, the modified 1-storey and 2-storey frames for SEQ07 to SEQ12 except SEQ09 and the modified 5-storey frame for SEQ08 and SEQ12 are safe up to AS3. In none of the above cases (with modification up to 15% strength increase) the *ODI* at the end of the main shock is less than 0.4, which indicates the damage during the main shock is still in the irreparable zone – a well-accepted philosophy in seismic design against critical events.

Since not all structures are safe against the entire sequence at the end of 15% increase of

Table 5.22 Average and maximum *ODI*s at the end of each aftershock for different sequence ensembles for 2-storey frame with 15% increase in material strength

Sequence Ensemble	Main shock Name	Main shock *ODI*	Average *ODI*				Maximum *ODI*			
			AS1	AS2	AS3	AS4	AS1	AS2	AS3	AS4
SEQ01	MS1	0.47			▨	▨	*1.15*	*1.18*	*1.21*	*1.23*
SEQ02	MS2	0.51		▨	*1.04*	*1.07*	*1.56*	*2.04*	*2.06*	*2.11*
SEQ03	MS3	0.50		▨	*1.12*	*1.16*	*1.30*	*1.40*	*1.69*	*1.79*
SEQ04	MS4	0.53		▨	*1.02*	*1.06*	*1.29*	*1.39*	*1.44*	*1.49*
SEQ05	MS5	0.55		▨	*1.04*	*1.09*	*1.63*	*1.65*	*1.73*	*1.78*
SEQ06	MS6	0.50		▨	**0.96**	**0.99**	*1.43*	*1.45*	*1.50*	*1.53*
SEQ07	MS1	▨					▨	▨	▨	▨
SEQ08	MS2	▨								▨
SEQ09	MS3	0.50			▨	▨	*1.07*	*1.31*	*1.33*	*1.36*
SEQ10	MS4	▨						▨	▨	▨
SEQ11	MS5	0.55					▨	▨	**0.98**	*1.03*
SEQ12	MS6	▨					▨	▨	▨	▨
SEQ13	MS1	▨								▨
SEQ14	MS2									
SEQ15	MS3									
SEQ16	MS4									
SEQ17	MS5									
SEQ18	MS6									
SEQ19	MS1									
SEQ20	MS2									
SEQ21	MS3									
SEQ22	MS4									
SEQ23	MS5									
SEQ24	MS6									
SEQ25	MS1									
SEQ26	MS2									
SEQ27	MS3									
SEQ28	MS4									
SEQ29	MS5									
SEQ30	MS6									

Italic shows collapse case (*ODI* ≥1)
Bold shows safe cases (*ODI* <1) due to 15% increase in material strength
Blank spaces show safe cases (*ODI* <1) in original structure

▨ Safe with 10% increase in material strength

material strength and the *ODI*s at the end of main shocks are all greater than 0.4, 20% increase in strength is attempted to see further improvement in seismic safety of structures and some salient observations are discussed next. The 1-storey and 2-storey frames (see Tables 5.19 and 5.23) have now become safe for all cases in terms of average *ODI* except beyond AS3 in the cases of SEQ02 and SEQ03 for 1-storey frame. With 20% increase in strength, 5-storey frame is safe till AS2 for all cases except for SEQ02, SEQ04 and SEQ06 in terms of average *ODI*. In terms of the maximum *ODI*, all sequence cases except SEQ01 to SEQ06 and SEQ09 for 1-storey frame and SEQ02 to SEQ06 and SEQ09 for 2-storey are now safe. For 5-storey frame (see Table 5.27), all the cases except SEQ01 to SEQ06 are safe when the maximum *ODI* is

Table 5.23 Average and maximum *ODI*s at the end of each aftershock for different sequence ensembles for 2-storey frame with 20% increase in material strength

Sequence Ensemble	Main shock Name	Main shock *ODI*	Average *ODI*				Maximum *ODI*			
			AS1	AS2	AS3	AS4	AS1	AS2	AS3	AS4
SEQ01	MS1	0.35			░	░	**0.89**	**0.91**	**0.95**	**0.96**
SEQ02	MS2	0.38		░	**0.79**	**0.81**	*1.21*	*1.57*	*1.58*	*1.62*
SEQ03	MS3	0.39		░	**0.87**	**0.90**	*1.00*	*1.08*	*1.31*	*1.37*
SEQ04	MS4	0.42		░	**0.79**	**0.82**	*1.00*	*1.06*	*1.10*	*1.14*
SEQ05	MS5	0.44		░	**0.82**	**0.85**	*1.25*	*1.26*	*1.32*	*1.35*
SEQ06	MS6	0.39		░	▓	▓	*1.12*	*1.13*	*1.17*	*1.19*
SEQ07	MS1	░					░	░	░	░
SEQ08	MS2	░								░
SEQ09	MS3	0.39			░	░	**0.82**	*1.00*	*1.01*	*1.04*
SEQ10	MS4	░						░	░	░
SEQ11	MS5	0.44					░	░	▓	**0.81**
SEQ12	MS6	░					░	░	░	░
SEQ13	MS1	░								░
SEQ14	MS2									
SEQ15	MS3									
SEQ16	MS4									
SEQ17	MS5									
SEQ18	MS6									
SEQ19	MS1									
SEQ20	MS2									
SEQ21	MS3									
SEQ22	MS4									
SEQ23	MS5									
SEQ24	MS6									
SEQ25	MS1									
SEQ26	MS2									
SEQ27	MS3									
SEQ28	MS4									
SEQ29	MS5									
SEQ30	MS6									

Italic shows collapse case ($ODI \geq 1$)
Bold shows safe cases ($ODI < 1$) due to 20% increase in material strength
Blank spaces show safe cases ($ODI < 1$) in original structure

░ Safe with 10% increase in material strength
▓ Safe with 15% increase in material strength

considered and many of the large displacement cases have been arrested though $ODI > 1$. Also with 20% increase in strength, 5-storey frame is safe for AS1 of SEQ03 in terms of maximum *ODI*. More importantly, in majority of the commuted cases (due to 20% increase in material strength), the *ODI* at the end of the main shock is more than 0.4 except for a few cases. This observation is very significant because this indicates that a solution is available through the proposed additional material safety where the design against the main shock will not be too conservative according to the current seismic design philosophy, even for a critical scenario for aftershocks. Further to mention that for the only failure case observed for $\Delta M_1 \geq 0.5$ in Tables 5.16 and 5.20 (see SEQ13) is safe against the entire sequence for just 10% increase in

Table 5.24 Average and maximum *ODI*s at the end of each aftershock for different sequence ensembles for 5-storey frame when *ODI* at the end of main shock is 0.6

Sequence Ensemble	Main shock Name	Average *ODI*				Maximum *ODI*			
		AS1	AS2	AS3	AS4	AS1	AS2	AS3	AS4
SEQ01	MS1	X	X	X	X	X	X	X	X
SEQ02	MS2	X	X	X	X	X	X	X	X
SEQ03	MS3	0.75	X	X	X	1.15	X	X	X
SEQ04	MS4	X	X	X	X	X	X	X	X
SEQ05	MS5	X	X	X	X	X	X	X	X
SEQ06	MS6	X	X	X	X	X	X	X	X
SEQ07	MS1	0.74	0.79	0.85	0.85	*1.20*	*1.30*	*1.71*	*1.71*
SEQ08	MS2	0.73	0.78	0.84	0.87	0.93	0.99	*1.15*	*1.16*
SEQ09	MS3	0.73	0.80	0.84	0.86	*1.05*	*1.15*	*1.15*	*1.16*
SEQ10	MS4	0.72	0.80	0.87	0.89	*1.15*	*1.15*	*1.29*	*1.44*
SEQ11	MS5	0.75	0.82	0.87	0.88	*1.30*	*1.31*	*1.31*	*1.32*
SEQ12	MS6	0.71	0.78	0.82	0.83	*1.13*	*1.13*	*1.16*	*1.17*
SEQ13	MS1	0.64	0.66	0.67	0.67	0.77	0.85	0.85	0.85
SEQ14	MS2	0.66	0.68	0.71	0.72	0.91	0.95	0.97	0.98
SEQ15	MS3	0.64	0.66	0.67	0.68	0.80	0.80	0.80	0.80
SEQ16	MS4	0.65	0.68	0.70	0.70	0.88	0.89	0.89	0.89
SEQ17	MS5	0.65	0.67	0.68	0.68	0.83	0.83	0.83	0.83
SEQ18	MS6	0.63	0.65	0.66	0.66	0.79	0.79	0.79	0.79
SEQ19	MS1	0.61	0.61	0.61	0.61	0.64	0.64	0.64	0.64
SEQ20	MS2	0.61	0.62	0.62	0.62	0.70	0.74	0.74	0.74
SEQ21	MS3	0.61	0.61	0.61	0.61	0.66	0.68	0.68	0.68
SEQ22	MS4	0.61	0.61	0.62	0.62	0.66	0.66	0.66	0.66
SEQ23	MS5	0.61	0.61	0.61	0.61	0.67	0.68	0.68	0.68
SEQ24	MS6	0.60	0.60	0.60	0.60	0.62	0.62	0.62	0.62
SEQ25	MS1	0.60	0.60	0.60	0.60	0.61	0.61	0.61	0.61
SEQ26	MS2	0.60	0.60	0.60	0.60	0.63	0.63	0.63	0.63
SEQ27	MS3	0.60	0.60	0.60	0.60	0.61	0.62	0.62	0.62
SEQ28	MS4	0.60	0.60	0.60	0.60	0.62	0.62	0.62	0.62
SEQ29	MS5	0.60	0.60	0.60	0.60	0.61	0.61	0.61	0.61
SEQ30	MS6	0.60	0.60	0.60	0.60	0.60	0.60	0.60	0.60

Italic shows collapse case ($ODI \geq 1$)

X	Drift to Large Displacement

strength (Table 5.17 and 5.21). Since the past earthquake records suggest that in majority of the cases the largest aftershocks are at least smaller by 0.5 magnitude scale than the main shock, the 10% additional material safety factor can address the safety against a large class of MASs.

5.6 Summary

In the current chapter, an investigative study of additional damage caused by aftershocks to an already damaged structure (by the preceding main shock) has been performed. The main shock-aftershock ground motions required for the study are simulated using the simulation methods and scaling models developed in the previous chapters. To consider the effects of

Table 5.25 Average and maximum *ODI*s at the end of each aftershock for different sequence ensembles for 5-storey frame with 10% increase in material strength

Sequence Ensemble	Main shock Name	Main shock *ODI*	Average *ODI*				Maximum *ODI*			
			AS1	AS2	AS3	AS4	AS1	AS2	AS3	AS4
SEQ01	MS1	0.56	X	X	X	X	X	X	X	X
SEQ02	MS2	0.57	**0.86**	X	X	X	*1.67*	X	X	X
SEQ03	MS3	0.56		X	X	X	*1.10*	X	X	X
SEQ04	MS4	0.55	X	X	X	X	X	X	X	X
SEQ05	MS5	0.54	X	X	X	X	X	X	X	X
SEQ06	MS6	0.53	X	X	X	X	X	X	X	X
SEQ07	MS1	0.56					*1.09*	*1.09*	*1.09*	*1.09*
SEQ08	MS2	0.57							*1.05*	*1.07*
SEQ09	MS3	0.56					*1.00*	*1.11*	*1.11*	*1.12*
SEQ10	MS4	0.55					*1.06*	*1.06*	*1.11*	*1.14*
SEQ11	MS5	0.54					*1.20*	*1.20*	*1.20*	*1.21*
SEQ12	MS6	0.53					*1.00*	*1.01*	*1.03*	*1.03*
SEQ13	MS1									
SEQ14	MS2									
SEQ15	MS3									
SEQ16	MS4									
SEQ17	MS5									
SEQ18	MS6									
SEQ19	MS1									
SEQ20	MS2									
SEQ21	MS3									
SEQ22	MS4									
SEQ23	MS5									
SEQ24	MS6									
SEQ25	MS1									
SEQ26	MS2									
SEQ27	MS3									
SEQ28	MS4									
SEQ29	MS5									
SEQ30	MS6									

Italic shows collapse case (*ODI* $\geq$1)
Bold shows safe cases (*ODI* <1) due to 10% increase in material strength
Blank spaces show safe cases (*ODI* <1) in original structure

X Drift to Large Displacement

time-frequency characteristics of the main shock ground motion on the aftershock-induced damage, several main shock ground motions have been simulated with predefined temporal features. Apart from this, different hypothetical seismic scenarios have been considered for the main shock events for the purpose of investigation.

The entire analytical exercise has been performed with the help of three RC bare frames in OpenSees (Mazzoni et al., 2005) platform. The damage state is quantified by *ODI* and both average and maximum *ODI*s for any aftershock ensemble are considered separately. Moreover, the additional damage due to aftershocks has been studied against $ODI = 0.6$ at the end of the main shock. Based on the thorough investigation performed, a new design strategy has been

Table 5.26 Average and maximum *ODI*s at the end of each aftershock for different sequence ensembles for 5-storey frame with 15% increase in material strength

Sequence Ensemble	Main shock Name	Main shock *ODI*	Average *ODI*				Maximum *ODI*			
			AS1	AS2	AS3	AS4	AS1	AS2	AS3	AS4
SEQ01	MS1	0.53	X	X	X	X	X	X	X	X
SEQ02	MS2	0.54	▨	X	X	X	*1.28*	X	X	X
SEQ03	MS3	0.54		**0.96**	X	X	*1.06*	*1.71*	X	X
SEQ04	MS4	0.51	X	X	X	X	X	X	X	X
SEQ05	MS5	0.50	X	X	X	X	X	X	X	X
SEQ06	MS6	0.48	X	X	X	X	X	X	X	X
SEQ07	MS1	0.53					*1.06*	*1.06*	*1.06*	*1.06*
SEQ08	MS2	0.54							**0.98**	*1.01*
SEQ09	MS3	0.54					**0.96**	*1.08*	*1.08*	*1.08*
SEQ10	MS4	0.51					**0.98**	**0.98**	*1.03*	*1.05*
SEQ11	MS5	0.50					*1.11*	*1.11*	*1.11*	*1.12*
SEQ12	MS6	0.48					**0.92**	**0.92**	**0.94**	**0.94**
SEQ13	MS1									
SEQ14	MS2									
SEQ15	MS3									
SEQ16	MS4									
SEQ17	MS5									
SEQ18	MS6									
SEQ19	MS1									
SEQ20	MS2									
SEQ21	MS3									
SEQ22	MS4									
SEQ23	MS5									
SEQ24	MS6									
SEQ25	MS1									
SEQ26	MS2									
SEQ27	MS3									
SEQ28	MS4									
SEQ29	MS5									
SEQ30	MS6									

Italic shows collapse case (*ODI* ≥1)
Bold shows safe cases (*ODI* <1) due to 15% increase in material strength
Blank spaces show safe cases (*ODI* <1) in original structure

X Drift to Large Displacement
▨ Safe with 10% increase in material strength

proposed to make structures safe against collapse during a MAS through additional material safety factor for both steel and concrete. The modified frames (with enhanced material strength) are analyzed with the same main shock-aftershock ground motion sequences that were applied on the original frames, to see the effectiveness of the proposed design modification. Major conclusions of the present study are summarized as follows.

- The time-frequency characteristics of the main shock play an important role in the aftershock-induced damage and the longer the SMD of a main shock the higher is the final *ODI*.
- When largest aftershock in a sequence is smaller than the main shock by 0.5 or more

Table 5.27 Average and maximum *ODI*s at the end of each aftershock for different sequence ensembles for 5-storey frame with 20% increase in material strength

Sequence Ensemble	Main shock Name	Main shock *ODI*	Average *ODI*				Maximum *ODI*			
			AS1	AS2	AS3	AS4	AS1	AS2	AS3	AS4
SEQ01	MS1	0.41	**0.56**	**0.74**	X	X	*1.11*	*1.37*	X	X
SEQ02	MS2	0.43	░	X	X	X	*1.02*	X	X	X
SEQ03	MS3	0.41		▓	X	X	**0.81**	*1.22*	X	X
SEQ04	MS4	0.39	X	X	X	X	X	X	X	X
SEQ05	MS5	0.40	**0.72**	**0.92**	*1.03*	*1.04*	*1.43*	*1.44*	*1.51*	*1.54*
SEQ06	MS6	0.37	X	X	X	X	X	X	X	X
SEQ07	MS1	0.41					**0.81**	**0.81**	**0.81**	**0.81**
SEQ08	MS2	0.43							▓	**0.78**
SEQ09	MS3	0.41					▓	**0.84**	**0.84**	**0.84**
SEQ10	MS4	0.39					▓	▓	**0.79**	**0.81**
SEQ11	MS5	0.40					**0.86**	**0.86**	**0.86**	**0.86**
SEQ12	MS6	▓					▓	▓	▓	▓
SEQ13	MS1									
SEQ14	MS2									
SEQ15	MS3									
SEQ16	MS4									
SEQ17	MS5									
SEQ18	MS6									
SEQ19	MS1									
SEQ20	MS2									
SEQ21	MS3									
SEQ22	MS4									
SEQ23	MS5									
SEQ24	MS6									
SEQ25	MS1									
SEQ26	MS2									
SEQ27	MS3									
SEQ28	MS4									
SEQ29	MS5									
SEQ30	MS6									

Italic shows collapse case (*ODI*≥1)
Bold shows safe cases (*ODI*<1) due to 20% increase in material strength
Blank spaces show safe cases (*ODI*<1) in original structure

X Drift to Large Displacement
░ Safe with 10% increase in material strength
▓ Safe with 15% increase in material strength

(magnitude-wise), flexible (taller) frames are likely to be safe against collapse in terms of the maximum *ODI*.

- Structures are less likely to survive against a sequence when the first (largest) aftershock is smaller than the main shock by 0.3, especially if the aftershocks are shallower in comparison with the main shock.

- The effect of the geometric nonlinearity in the assessment of additional damage due to aftershocks is found to be significant for 5-storey frame, hence it should not be ignored for tall structures.

- It has been found that 10% to 15% additional material safety factor can arrest the collapse of all the RC frames against a large proportion of MASs, where the damage states of the redesigned structures at the end of main shocks are all desirably in the irreparable zone.

Chapter 6

EXPERIMENTAL STUDY OF DAMAGES IN RC FRAMES DUE TO MAIN SHOCK-AFTERSHOCK SEQUENCES

6.1 Background

Experimental testing of RC frames under the action of MASs provides an insight on their realistic behaviour against MASs. The fundamental frequency of the structure is very well related to its structural properties and decrease in the frequency is a good measure of the damage incurred in the structure. Hence, the degradation of the frequency of the already damaged structure by the aftershocks can be investigated to study the additional damages due to the aftershocks. The knowledge of the decrease in the frequency of the structures due to aftershocks can be useful in considering the effects of the aftershocks in the design of the structures against MASs. In this chapter, experimental testing of RC frames is performed to investigate the degradation in the structural properties due to aftershocks. For performing the experimental testing, quarter scale RC bare frames with ductile detailing are used. Analytical models can be calibrated with the experimental results which can be used for extensive analysis for the validation of design modification proposed in the previous chapter.

6.2 Description of RC Frames

In the current study, quarter-scale models of an exterior ground-storey frame of a two-storey office building in Assam, which is one of the most seismically active regions in India, are used. Quarter-scale frames are tested due to limitations of the load capacity of the shake table. The longitudinal reinforcement steel ratio in the column section of the prototype section is maintained in that of the scaled frame. The average compressive strength of the concrete cubes tested at 28 days is found to be about 34 MPa. The yield strength of the longitudinal reinforcement and shear reinforcement is found to be 570.0 MPa based on tensile testing of steel samples. Shear reinforcement in the columns of the scaled frame has been designed following the special confinement reinforcement provisions as per IS 13920 (1993), from which 2-legged

6 mm diameter bars at 50 mm spacing has been found to be sufficient. The dimensions of the frame along with its RC detailing are shown in Figure 6.1. The influence of RC slab in the structural response of the scaled frame is considered by constructing a 65 mm thick RC slab along with the beam (extending to a width of 250mm on both sides of the beam). The slab also provided a means to support the gravity loads over the frame. The columns of the frame are constructed on a bottom RC beam of size 400 mm × 190 mm, which provides a means of fixing the frame firmly to the strong floor during testing. Quarter-bridge, four-wired, linear strain gauges (HBM make) are fixed on the longitudinal reinforcement to measure the strains during testing. The strain gauges are fixed at locations of the columns where the plastic hinging is most likely to occur. No strain gauges have been fixed on the longitudinal reinforcements of the beam as no damages are expected to occur in the beam due to the rigid diaphragm action of the slab. A strain gauge is fixed at each main reinforcement bar in a column section at each plastic hinge location. The experiments on the RC frames are conducted for 10 kN (1.5% axial load ratio) and 20 kN (3.0% axial load ratio) gravity loading to understand the influence of axial load ratio on behavior of the frame under MAS. The gravity loadings of 10 kN and 20 kN are provided on the top of the RC slab by using steel plates (each of 500 kg).

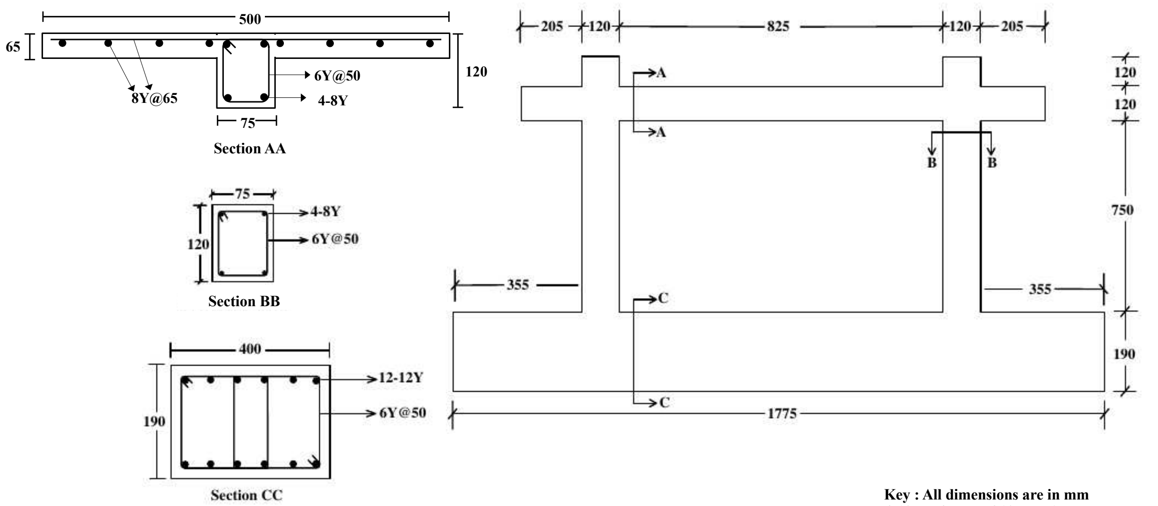

Key : All dimensions are in mm
4-12Y – 4 bars of 12mm dia.
6Y@50 - 6mm dia. bars at 50mm spacing

Figure 6.1 Detailing of RC frames

6.3 Experimental Setup Details

Two types of tests are carried out on RC frames in the present study: slow-cyclic, pseudo-static tests using servo-controlled hydraulic actuators (MTS make), and dynamic tests using servo-controlled hydraulic shake table (BISS make). The hydraulic actuator has a load capacity of 250 kN and a stroke length of ±125 mm. The shake table has an acceleration capacity of ±2.0g and a stroke length of ±500 mm. Experimental setup for slow-cyclic testing and dynamic testing is shown in Figure 6.2. Frames are fixed rigidly to the strong floor via steel beams and bolts during slow-cyclic testing. The head of the actuator is tightly locked with the top of the frame at the slab level by steel plates and bolts to avoid any slippage between the actuator and the frame. Gravity loadings (steel plates) are placed over concrete cubes placed on top of the slab to allow the placement of bolts (which pass along the length of the slab) used to fix the actuator head tightly with top of the frame. For dynamic testing of the frames, they are fixed on the shake table by means of steel channels and bolts. Four steel channels are used for fixing the frame on the shake table, out of which two are fixed in between the columns and other the two outside the bay area. Each channel is fixed on the shake table using three bolts, wherein one bolt passes through the base beam of the frame. Four holes are provided in the base beam (which passes through the full depth of the beam) of the RC frame for inserting bolts through the base beam for fixing on top of the shake table. To prevent out-of-plane movement of the frame during testing, lateral restraints are provided as shown in Figure 6.3. L-shaped steel plates are fixed on the side of the slab of the frame to provide contact between the frame and lateral restraint setup, wherein the contact is established by means of rollers as seen in Figure 6.3. The lateral displacements of frame are measured by LVDTs (linear varying displacement transducers) and laser displacement sensors (Micro-Epsilon make). The base and top accelerations of the frames during dynamic testing are recorded using accelerometers (Episensor accelerometers of Kinematrics make).

Figure 6.2 Experimental setup shown for (a) slow-cyclic, pseudo-static tests and (b) dynamic tests

Figure 6.3 Lateral restraint setup to prevent out of plane movement of RC frames during testing

6.4 Experimental Procedure

The testing of the RC frames involves the study of the damage of the frames due to the main shock-aftershock ground motion sequence. Since it is difficult to damage an undamaged frame by the main shock on the shake table due to the limitation of the shake table, the frame is given initial damage, due to the main shock, via slow-cyclic testing. The slow-cyclic testing is performed to impart the main shock damage, since the deformation of the frame for imparting target damage is well controlled than dynamic testing. Imparting this initial damage via slow-cyclic testing in place of dynamic testing is not a serious limitation as it is the damage at the end of the main shock that affects the additional damage due to succeeding aftershocks. The frames damaged via slow-cyclic test are then subjected to aftershock ground motions by dynamic testing. The present shake table testing setup is such that it does not provide the input loading data. Therefore, an alternate method is attempted to obtain the lateral loads imparted to the frame at different displacements during the dynamic testing. This method of testing involves considering two frames for testing, wherein the relative displacements recorded on the top of the first frame during dynamic testing due to aftershocks are applied on the second frame tested via pseudo-static testing. The loads corresponding to the lateral displacement applied on the frame are then recorded using the load cell of the actuator. Initially, both the frames are damaged by the slow-cyclic test by deforming it to the same displacement level to represent a main shock damage level. One of the frames (named as Frame-1) is then tested dynamically and the relative displacements recorded at the top of Frame-1 corresponding to each aftershock are applied on the second frame (named as Frame-2) via pseudo-static test. The fundamental frequency of the frame at each stage of testing is measured by white-noise testing or by impact testing, to study the degradation of the structural properties. Figure 6.4 shows a flowchart of the procedure of the experiment. It can be seen in Figure 6.4, that frequencies of Frame-1 are measured by white-noise test only and that of Frame-2 are measured by impact testing. Frame-

1 is fixed on the shake table for all testings except during slow-cyclic testing for imparting initial damage and Frame-2 is fixed with the actuator for all the testings. For easy testing and to avoid frequent shifting of the frame, frequencies of Frame-2 have been measured by impact testing. Also, the frequencies measured from impact testing and white-noise testing are very close. The cyclic testing to inflict main shock damage is done by applying cyclically increasing displacements on the frame following the displacement pattern as shown in Figure 6.5. Based on the target initial damage level to be applied, the cyclic testing is done up to some pre-decided displacement level.

The aftershock ground motions for dynamic testing are simulated using an approximate conditional scaling model developed using earthquake data for North East India region for a main shock scenario of $M = 7.2$, $R = 30.0$ km and $h = 15$ km. The aftershocks are simulated for $M = 6.7$, 6.5 & 6.3 with distance and depth same as that of the main shock. The aftershock ground motions corresponding to $M = 6.7$, 6.5 & 6.3 will be referred to as Aft1, Aft2 and Aft3 from here onwards. Figure 6.6 shows Aft1, Aft2 and Aft3 with their PGA normalized.

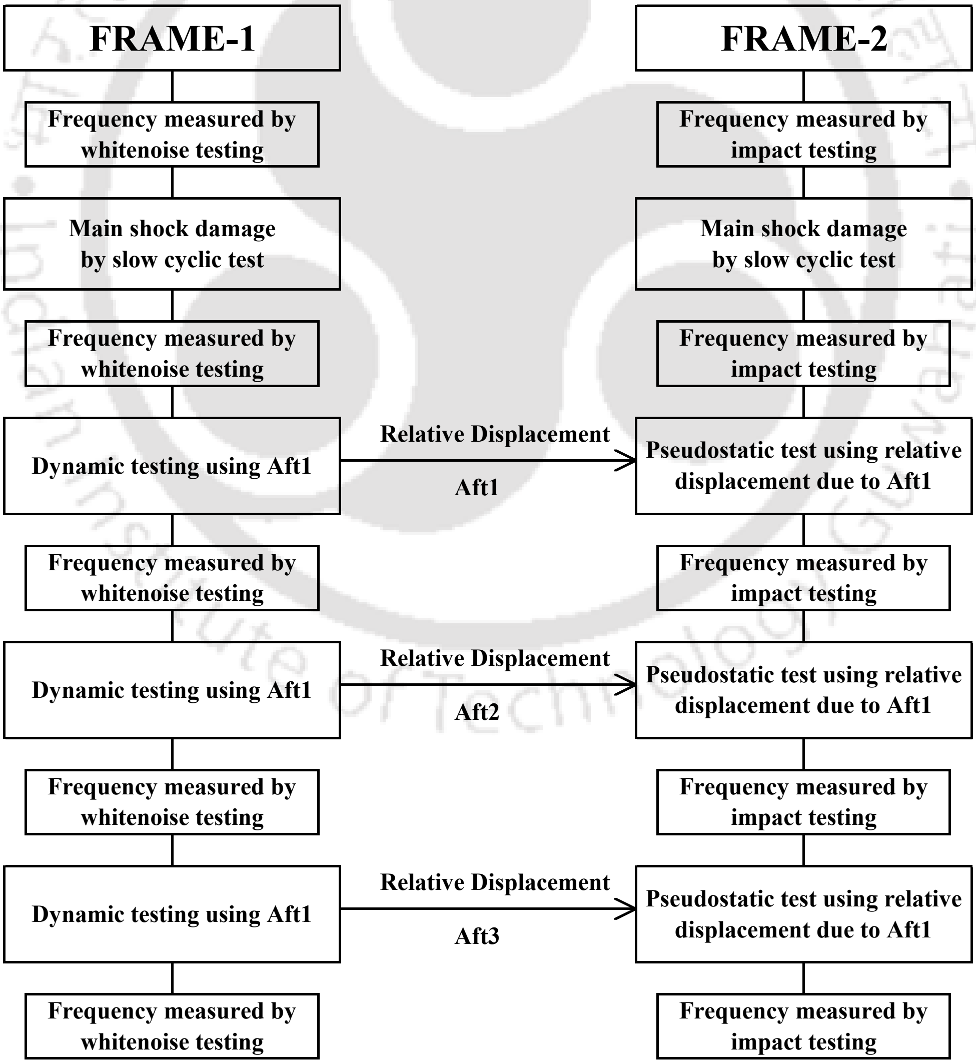

Figure 6.4 Flowchart of the experimental procedure

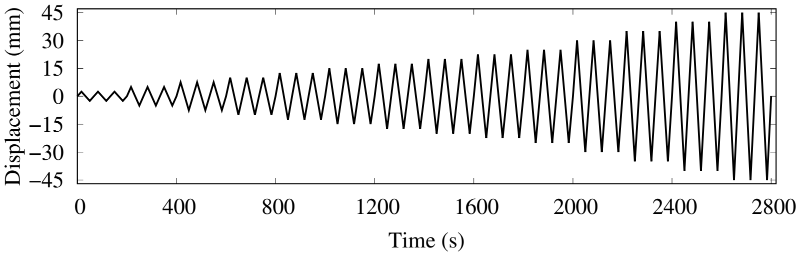

Figure 6.5 Displacement profile applied during slow-cyclic testing of frames

Based on some finite element analysis of the frame, the final displacement level corresponding to a target main shock damage level is calculated. For this purpose, an analytical model of the quarter-scale RC frame has been modelled in the software OpenSees (Mazzoni et al., 2005). A schematic diagram of the analytical model is shown in Figure 6.7. The frame has been modelled using an `elasticBeamColumn element` for beam and `beamWithHinges` element for the column. In `beamWithHinges` element, nonlinearity is concentrated over some length, specified as plastic hinge length, at the ends and the middle portion is elastic. The length of the plastic hinge (L_p) is specified by Equation 5.1 mentioned in Chapter 5. In the plastic hinge

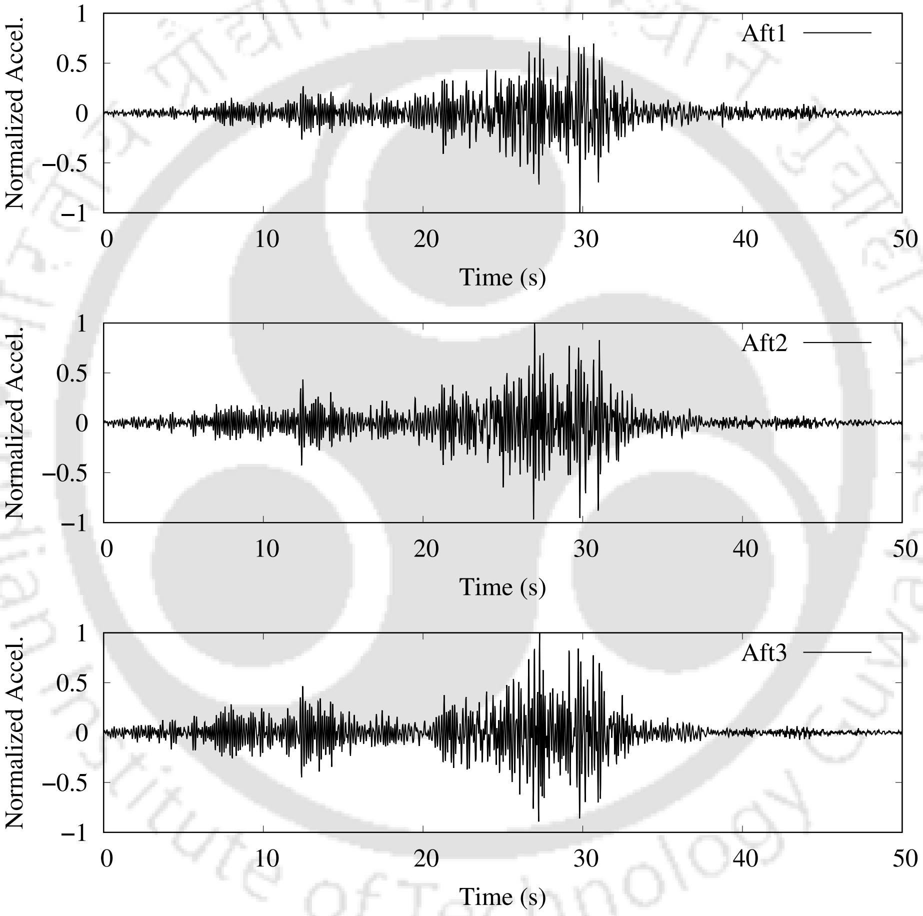

Figure 6.6 Normalized aftershock motion for Aft1, Aft2 and Aft3

region, nonlinear behaviour is defined by specifying the section details. The section is divided into many small fibres in which `Pinching4` material model has been assigned. Damages in the frames during the tests were observed only at the column ends and not anywhere else. Hence, nonlinearity in the frame has been only modelled in the column using the `beamWithHinges` element.

The capacity (load as well as displacement) of the RC frames are determined by monotonic load tests for 10 kN and 20 kN gravity loading. The analytical models are then calibrated separately with the force-displacement data from monotonic load tests for 10 kN and 20 kN gravity loading. Figure 6.8 shows the comparison of monotonic pushover curves of the calibrated analytical models against the force-displacement curves from monotonic load tests for 10 kN and 20 kN gravity loading. `Pinching4` material model contains parameters that define the stress-strain envelope and parameters which define the unloading-reloading pathway of the stress-strain. The analytical RC frame models for 10 kN and 20 kN loadings have been calibrated by inputting appropriate values only to the parameters of `Pinching4` material model

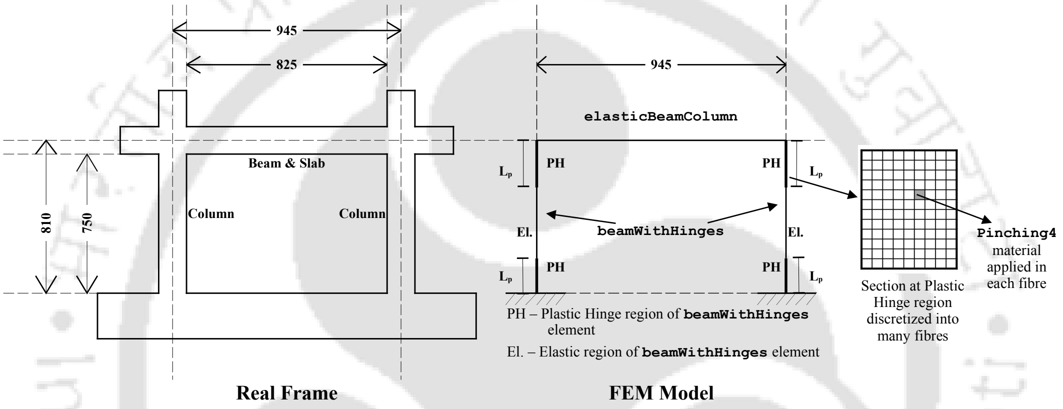

Figure 6.7 Analytical model of the quarter-scale RC frame

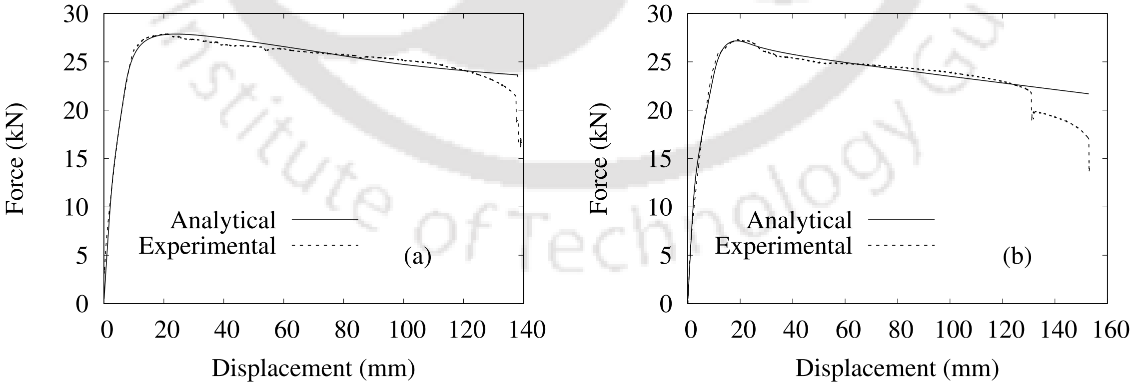

Figure 6.8 Comparison of experimental and analytical monotonic pushover curves for (a) 10 kN and (b) 20 kN gravity loading

which define the stress-strain envelope. The main shock damage is inflicted in the frame by the slow-cyclic testing and to inflict some specific damage in the frame, the displacement up to which the frame is to be loaded should be known beforehand. The damage (*ODI*) in the frame can be quantified by the Park & Ang damage index as mentioned in Chapter 5. *ODI* is calculated from the damage index of each hinge which are calculated from the moment-curvature output data of the hinges. For the calculation of the damage index at the hinges, the values of yield rotation, yield moment and ultimate rotation of the hinges are required. The yield curvature and yield moment of a section are calculated from the monotonic moment-curvature curve of a section using the method by Park (1988). The ultimate curvature is calculated as the curvature corresponding to the first failure of the top or bottom layer of material in the section (the section is discretized as explained before). The yield and ultimate rotations are calculated by multiplying the yield and ultimate curvatures with the plastic hinge length.

An analysis of a calibrated analytical model can provide a reasonable estimate of the displacement to be applied on the frame to inflict the target main shock damage. Since the analytical model made here has not been calibrated with respect to force-displacement data from some cyclic tests, it cannot be used to perform analysis to estimate the displacement corresponding to some target damage level. Hence, the analytical models are required to be calibrated at their hysteretic behaviour level also. Since the force-displacement data of cyclic test of the quarter-scale RC frame in the present study is not available initially, the parameters of `Pinching4` material model which define the unloading-reloading pathway of the stress-strain are borrowed from an analytical model calibrated with respect to some past experimental cyclic pushover data. For this purpose, slow-cyclic test data for a half-scale RC frame has been taken from an earlier study by Basha and Kaushik (2016) and an analytical RC frame is modelled for the half-scale RC frame and calibrated with respect to the slow-cyclic test data. Figure 6.9 shows the comparison of the experimentally obtained hysteresis curve with the hysteresis curve obtained from the calibrated model. The calibration is performed such that the visual matching between the hysteresis curves from experimental testing and an analytical model is good and the area under both the curves match. From this calibrated model, the parameters which define the unloading-reloading pathway of the stress-strain are incorporated in the analytical quarter-scale model which has been already calibrated with respect to monotonic load test data. Cyclic pushover analysis of this quarter-scale frame is then performed to determine a trial estimate of displacement level corresponding to some target main shock damage level (Here, *ODI*=0.6). The force-displacement curve of the pushover analysis is shown in Figure 6.10. Although the hysteresis behaviour of the quarter-scale frame in the present study will be different from the half-scale frame from which the hysteresis parameters are borrowed, this has been done just to obtain some realistic but not exact estimate of the target displacement level to be applied on the frame during the testing to impart sufficient main shock damage. These borrowed parameters are used only once due to the initial unavailability of force-displacement data from cyclic tests of the present frame. Once the slow-cyclic test data from imparting main shock damage are obtained, the analytical frame model will be again calibrated with this data to further improve the prediction for successive tests.

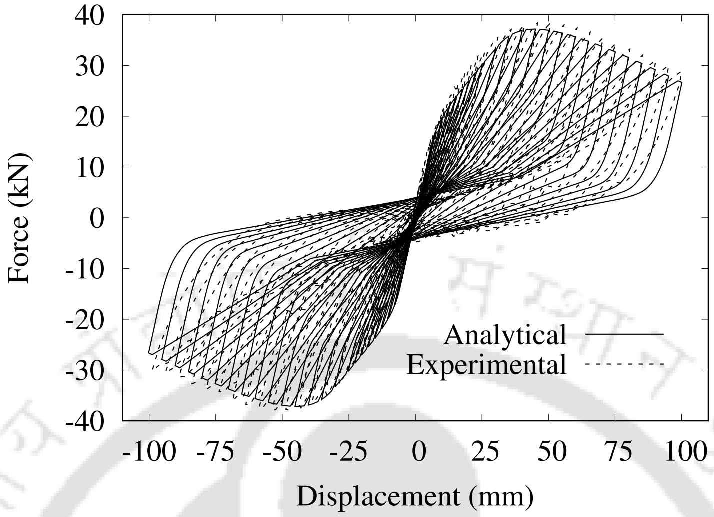

Figure 6.9 Comparison of experimental and analytical pushover curves for slow-cyclic testing of half-scale frame

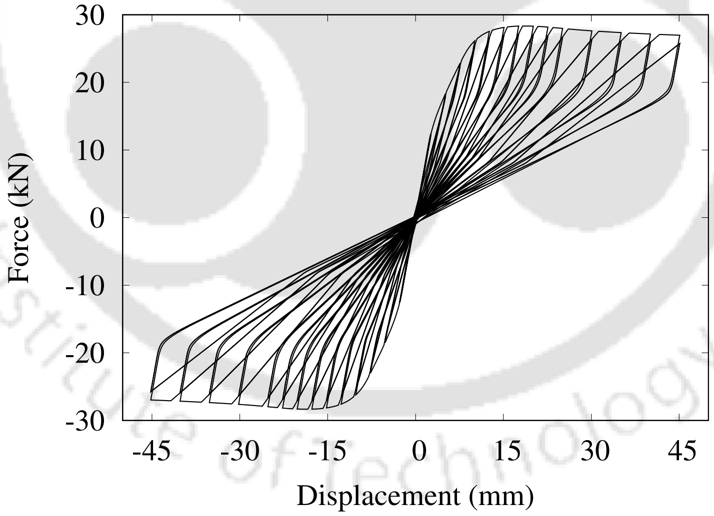

Figure 6.10 Analytical pushover curve of quarter-scale frame with 10 kN gravity loading subjected to cyclic lateral displacement upto 45 mm corresponding to an *ODI* of 0.6

6.5 Experimental Results

From the cyclic pushover analysis of the analytical frame model for 10 kN gravity loading, it has been determined that cyclic test upto 45 mm displacement gives a damage level corresponding to an *ODI* of about 0.6. For 10 kN gravity loading, two frames, named A1 and A2, are considered for testing. These two frames are given initial main shock damage via slow-cyclic testing with displacement pattern as shown in Figure 6.5 upto 45mm. The experimentally obtained hysteresis curves of Frame A1 and A2 are shown in Figure 6.11. Frames A1 and A2 inflicted with main shock damage by the slow-cyclic test are shown in Figures 6.12 and 6.13, respectively. The damaged regions in the frames are marked and they have been shown separately in the same figure. It can be seen that similar physical damages are present between both frames. From the force-displacement data obtained for the slow-cyclic testing of frames A1 and A2, the analytical model is calibrated again. Cyclic pushover analysis up to 45 mm displacement is performed on the newly calibrated frame to calculate the damage in the frame, from which an *ODI* of 0.9 is obtained. The obtained *ODI* is different from the targeted one, due to the hysteresis behaviour of the analytical model being different from that of the actual frame owing to the usage of borrowed parameters from a different analytical model. As mentioned earlier, this has been done just to obtain an initial trial displacement. *ODI* of 0.9 corresponds to a high damage state close to collapse (*ODI* >1.0) which closely matches with the high damages observed in Figures 6.12 and 6.13 for frames A1 and A2, respectively. The damaged frames A1 and A2 are then subjected to aftershocks to study the additional damages due to them. The calibrated analytical model is analyzed with the three aftershock ground motions Aft1, Aft2 and Aft3 to determine the PGA to be applied for dynamic testing to produce significant damage on the frame. From the analysis, the PGA intensity of Aft1, Aft2 and Aft3 are decided at 0.4g, 0.6g and 0.25g to inflict significant damage on the frame. These PGAs of the aftershocks are kept constant for all the tests, to avoid the influence of intensity of the ground motions from affecting the results. Before testing, the shake table is tuned with dummy loads equal to the mass of the frame with the gravity loads to obtain an acceptable response from the shake table. Even after tuning, the intensity and time-frequency characteristics of the actual ground motion cannot be exactly reproduced by the shake table. The damaged frame A1 is dynamically tested against aftershock ground motions Aft1, Aft2 and Aft3. The acceleration data recorded from the accelerometers fixed on the shake table and the frame will contain noise and hence they should be filtered to remove the noise. The frequency range for filtering has been chosen as 0.1-10.0 Hz. This frequency range has been decided such that the displacement-history calculated from the filtered acceleration time-history matches well with that of the recorded displacement time-history. The acceleration time-histories recorded on the shake table when tested with Aft1, Aft2 and Aft3 after filtering are shown in Figure 6.14. From the displacements measured on top and base of the frame A1 when subjected to Aft1, Aft2 and Aft3, the relative displacements are obtained which are shown in Figure 6.15. The relative displacements obtained corresponding to Aft1, Aft2 and Aft3 for frame A1 are applied on frame A2 via pseudo-static, slow-cyclic testing of frame A2. Figure 6.16 shows the hysteresis curves obtained for frame A2 due to lateral load testing using the relative displacements of frame A1

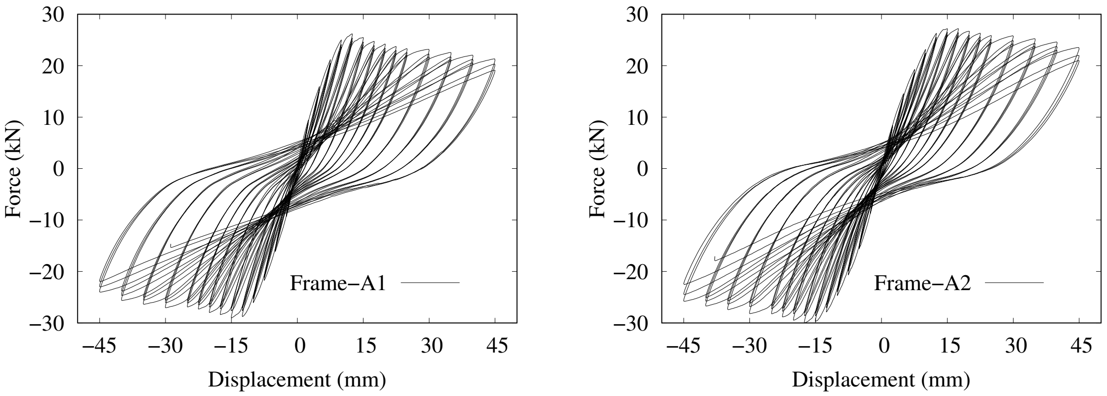

Figure 6.11 Hysteresis curves of frames-A1 and A2 for slow-cyclic testing to inflict main shock damage corresponding to 45 mm lateral displacement (10 kN Gravity Loading)

due to Aft1, Aft2 and Aft3.

Similar testing sequence is carried out on the scaled RC frame with 20 kN gravity loading. To determine the displacement level to be applied on the frame to give initial main shock damage, an analytical model for 20 kN loading is developed and is calibrated with force-displacement data from monotonic testing of RC frame for 20-kN gravity loading. Since the cyclic test data for 20 kN loading is not available to calibrate the hysteresis behaviour of the analytical model, the approach adopted earlier is used here, wherein the hysteresis parameters from the calibrated frame model for 10 kN loading is taken and applied in the analytical model of 20 kN loading. This is reasonable since the axial load ratios corresponding to 10 kN and 20 kN are not significant to affect the sectional properties very much. From the cyclic pushover analysis of the analytical model with 20 kN loading, it is calculated that a displacement level of 35 mm can inflict an initial damage level in the RC columns with an *ODI* of 0.6. Based on this estimate, slow-cyclic testing upto 35 mm displacement has been performed on the frame, but the frame suffered significant damage that it became unsafe for dynamic testing. Hence the testing sequence has been repeated lower initial damages corresponding to lower displacement levels of 15 mm and 25 mm. For the initial damage state corresponding to 15mm displacement, two frames, named B1 and B2, are considered for testing. For the initial damage state corresponding to 25mm displacement, two frames, named C1 and C2, are considered for testing. The hysteresis curves obtained experimentally for frames B1 and B2 corresponding to 15mm displacement are shown in Figure 6.17. Frames B1 and B2 inflicted with main shock damage by slow-cyclic test corresponding to 15 mm displacement level are shown in Figures 6.18 and 6.19, respectively. Significant damages are not observed for this level of the initial damage and only very minor cracks are observed. The damaged frame B1 is tested against aftershock ground motions Aft1, Aft2 and Aft3 via dynamic testing. The filtered acceleration time-histories recorded on the shake table for Aft1, Aft2 and Aft3 are shown in Figure 6.20. From the measured top and base displacements, the relative displacements of frame B1 are calculated which is shown

Figure 6.12 Damaged frame-A1 due to main shock damage corresponding to 45 mm displacement by slow-cyclic testing (10 kN gravity loading)

in Figure 6.21. The relative displacements corresponding to Aft1, Aft2 and Aft3 for frame B1 are applied on frame B2 via pseudo-static testing of frame B2 to determine the hysteresis response. Figure 6.22 shows the hysteresis curves of frame B2 due to pseudo-static testing using the relative displacements of frame B1 due to Aft1, Aft2 and Aft3.

Similarly frames C1 and C2 are tested for main shock damage corresponding to the lateral displacement level of 25 mm applied cyclically using the actuator. The experimentally obtained hysteresis curves of frames C1 and C2 corresponding to 25 mm displacement are shown in Figure 6.23. Frames C1 and C2 inflicted with main shock damage by the slow-cyclic test are shown in Figures 6.24 and 6.25. The damaged frame C1 is tested against aftershock ground

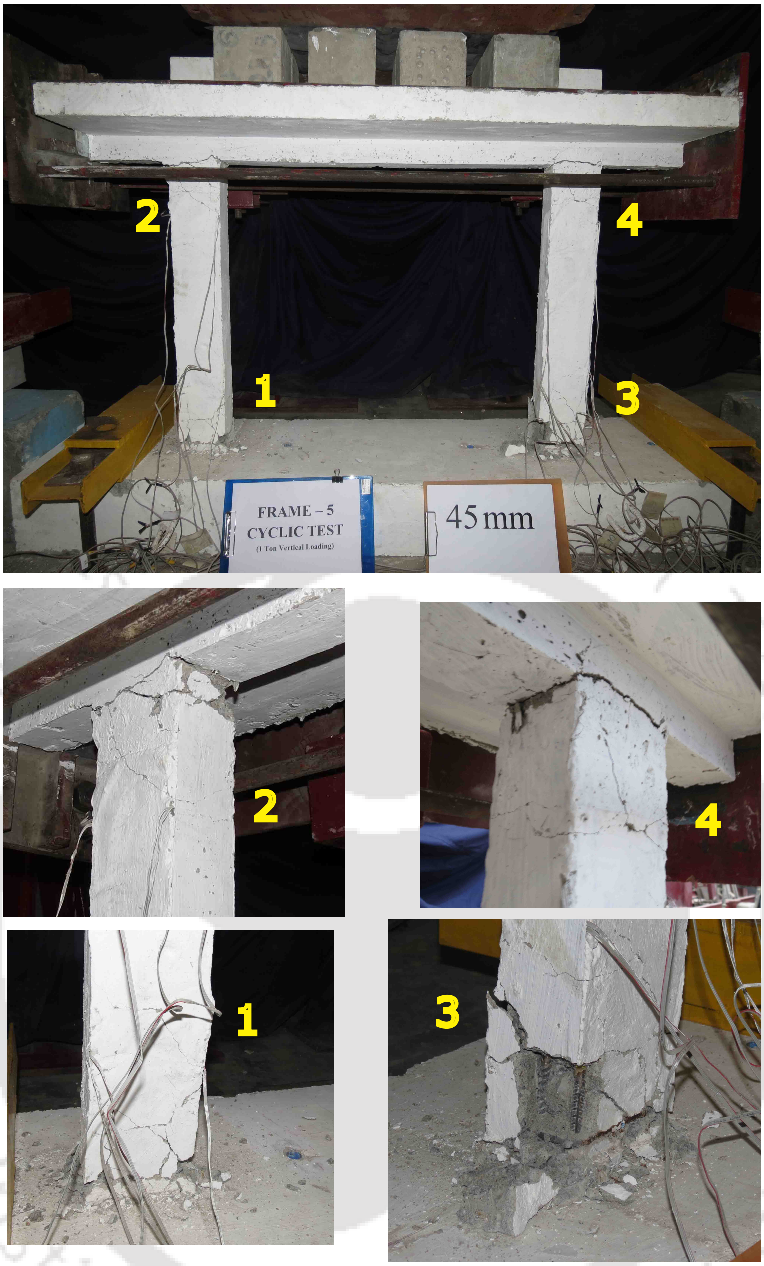

Figure 6.13 Damaged frame-A2 due to main shock damage corresponding to 45 mm displacement by slow-cyclic testing (10 kN gravity loading)

motions Aft1, Aft2 and Aft3 via dynamic testing. The acceleration time-histories recorded on the shake table for Aft1, Aft2 and Aft3 are shown in Figure 6.26. From the top and base displacements measured, the relative displacements of frame C1 are calculated which is shown in Figures 6.27. The relative displacements corresponding to Aft1, Aft2 and Aft3 for frame C1 are applied on frame C2 via pseudo-static testing of frame C2 to determine the hysteresis response. Figures 6.28 shows the hysteresis curves obtained for frame C2 by carrying out pseudo-static testing using the relative displacements of frame C1 due to Aft1, Aft2 and Aft3.

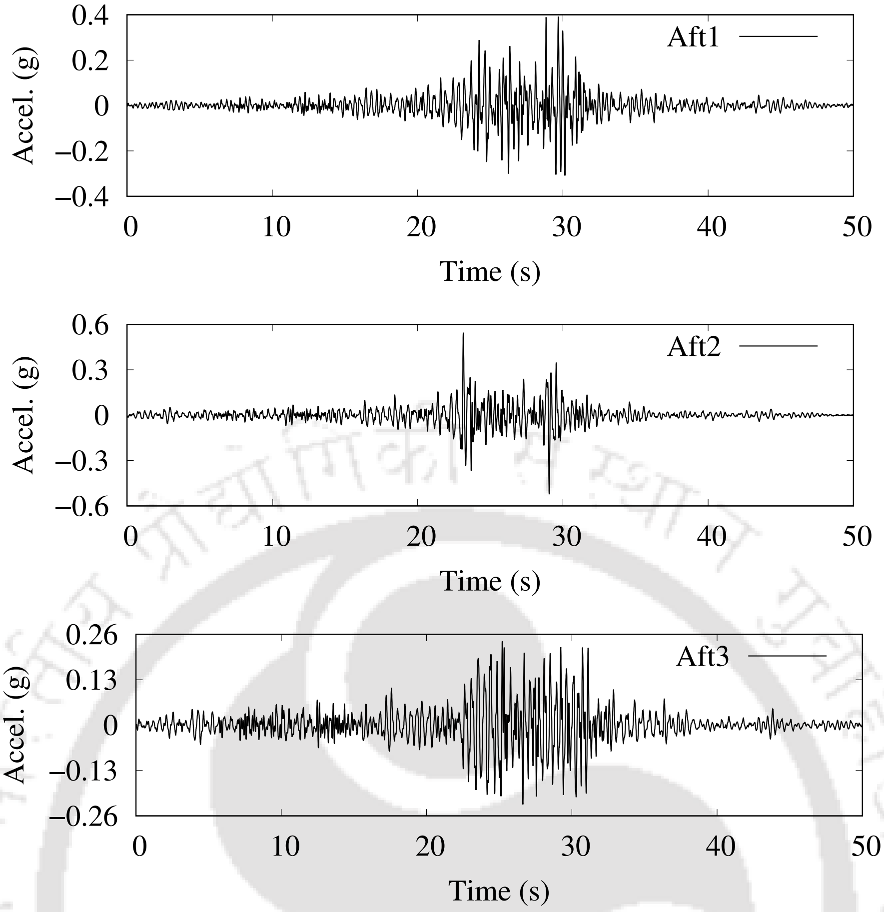

Figure 6.14 Acceleration recorded on the shake table when the damaged frame-A1 is tested with Aft1, Aft2 and Aft3 (10 kN gravity loading)

From the structural frequency data measured at each stage of the testing, it has been observed that the frequencies of both the frames (corresponding to the same initial damage) are similar at each stage of testing. It has also been constrained that the deformation in the second frame is the same as that of the first frame at each stage of damage due to main shock and aftershocks. From this, it can be inferred that the hysteresis data for a frame tested on the shake table can be reasonably obtained by applying its relative displacement via pseudo-static test on a second frame with similar properties as that of the first frame.

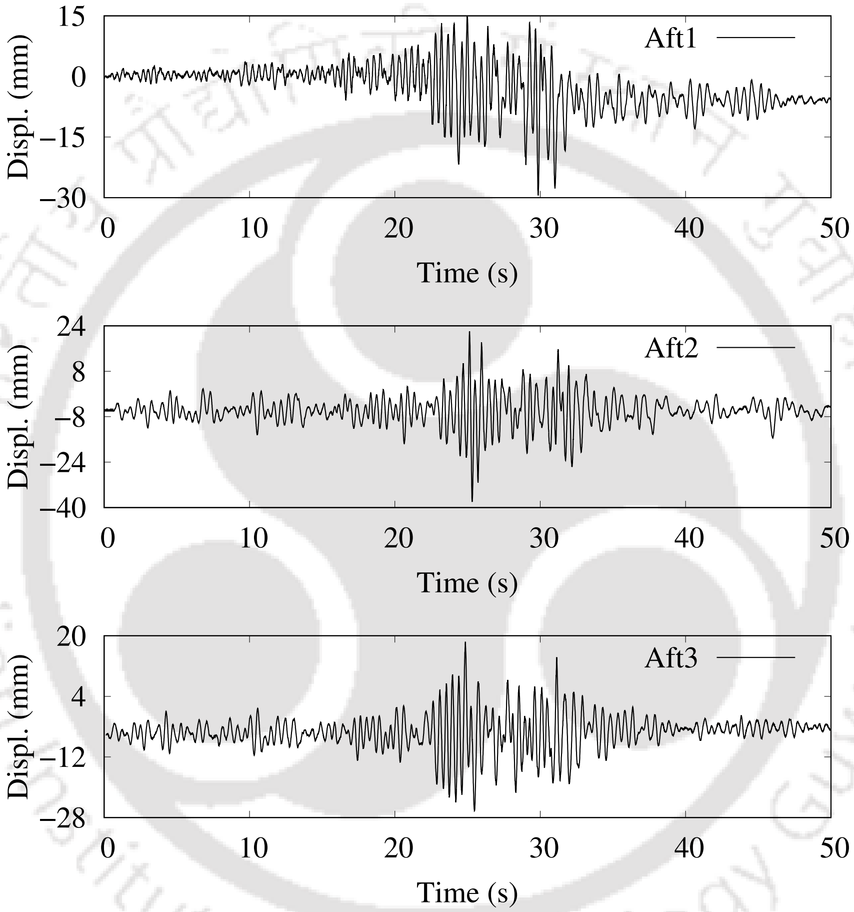

Figure 6.15 Relative Displacement at top of the damaged frame-A1 when tested with Aft1, Aft2 and Aft3 (10 kN gravity loading)

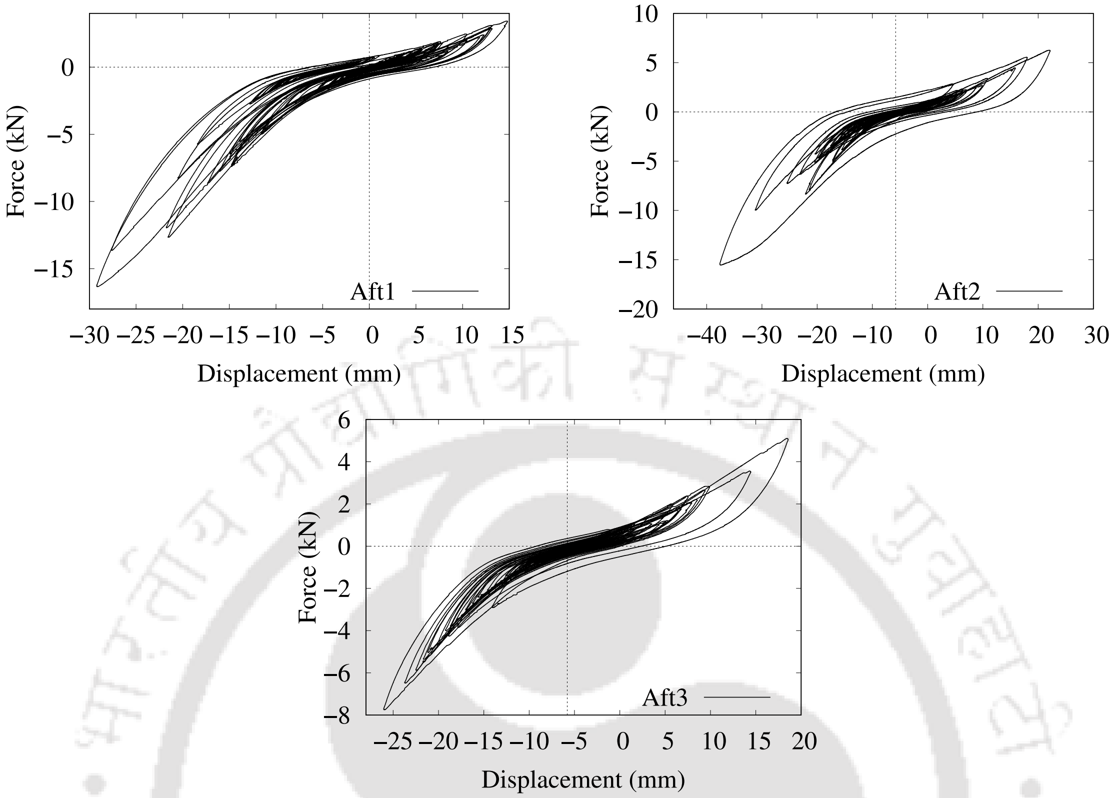

Figure 6.16 Hysteresis curve of the already damaged frame-A2 for pseudo-static testing to inflict damage due to Aft1, Aft2 and Aft3 (10 kN gravity loading)

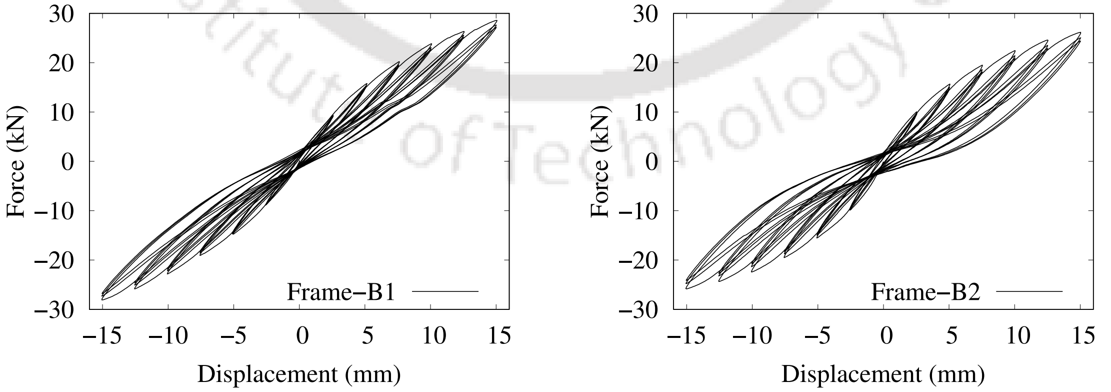

Figure 6.17 Hysteresis curves of frames-B1 and B2 for slow-cyclic testing to inflict main shock damage corresponding to 15 mm lateral displacement (20 kN gravity loading)

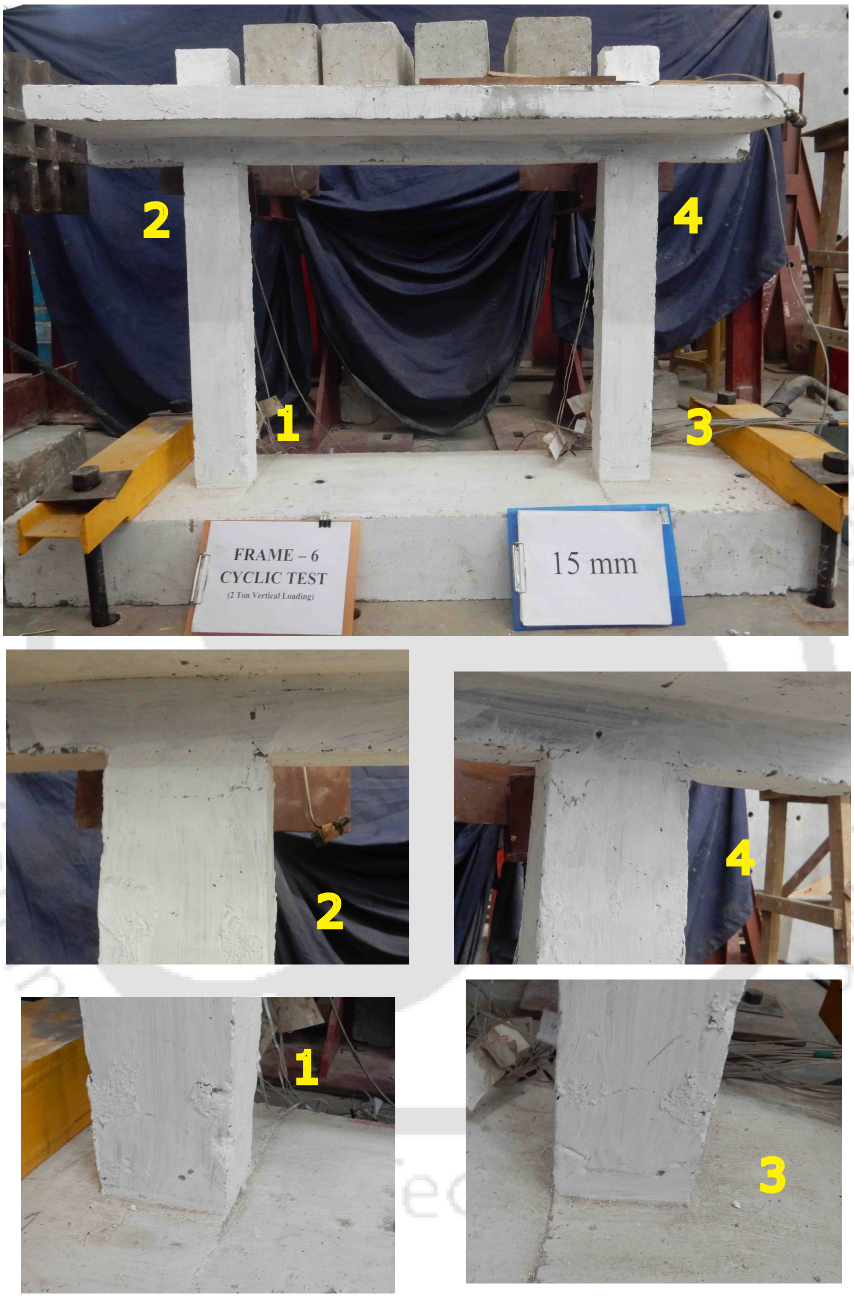

Figure 6.18 Damaged frame-B1 due to main shock damage corresponding to 15 mm displacement by slow-cyclic testing (20 kN gravity loading)

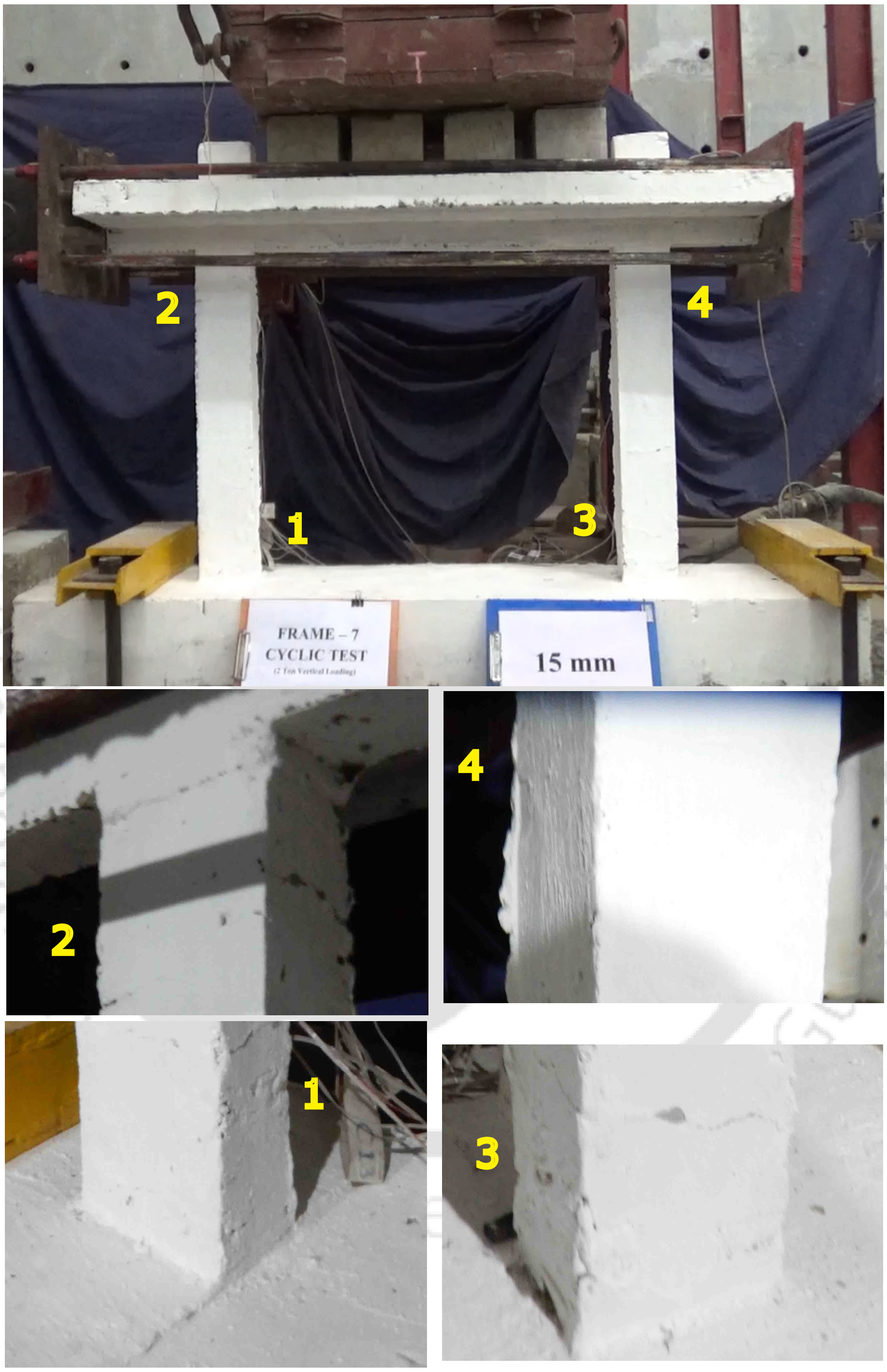

Figure 6.19 Damaged frame-B2 due to main shock damage corresponding to 15 mm displacement by slow-cyclic testing (20 kN gravity loading)

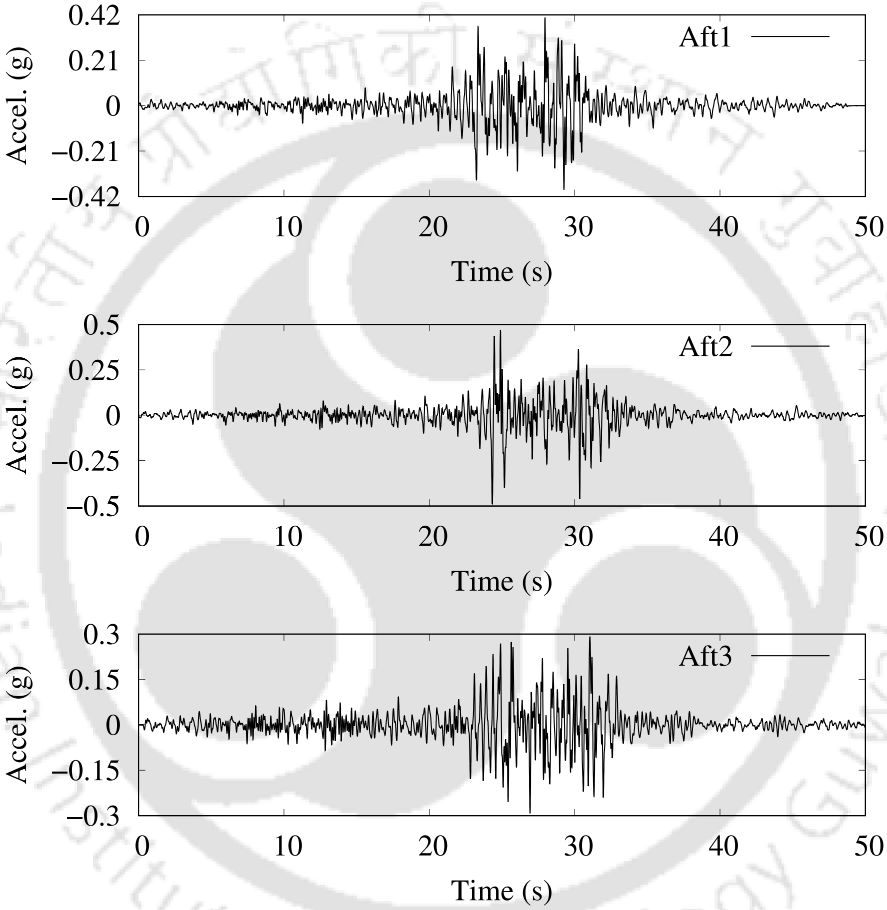

Figure 6.20 Acceleration recorded on the shake table when the damaged frame-B1 tested with Aft1, Aft2 and Aft3 (20 kN gravity loading)

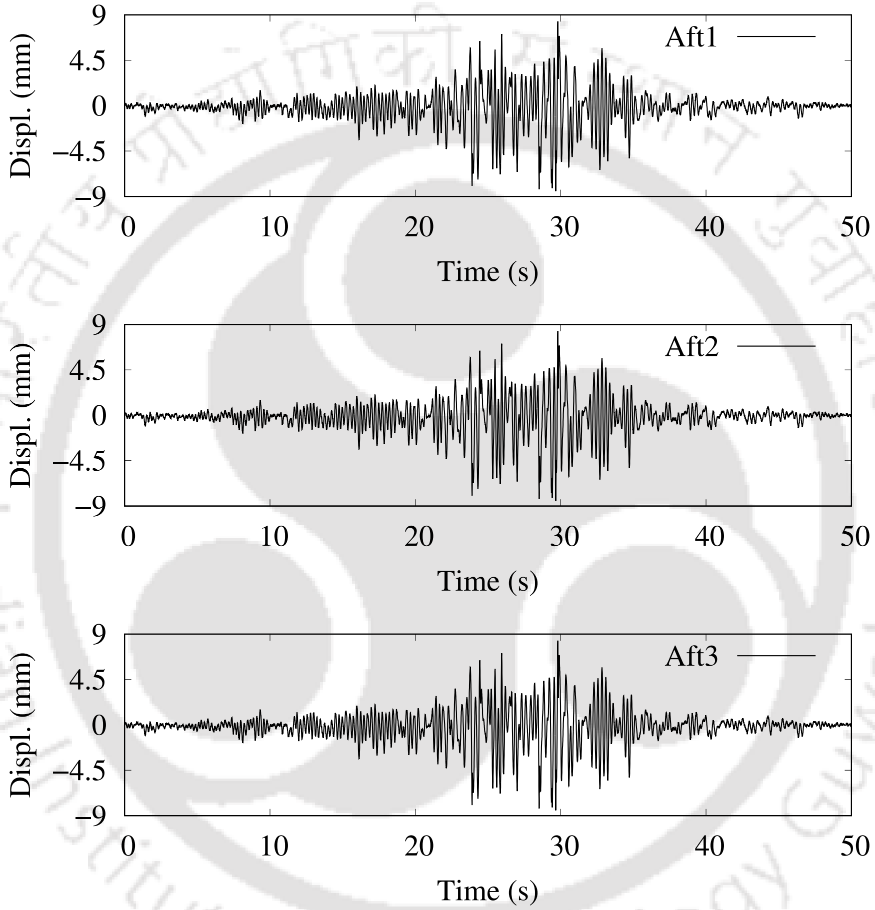

Figure 6.21 Relative Displacement at top of the main shock damaged frame-B1 when tested with Aft1, Aft2 and Aft3 (20 kN gravity loading)

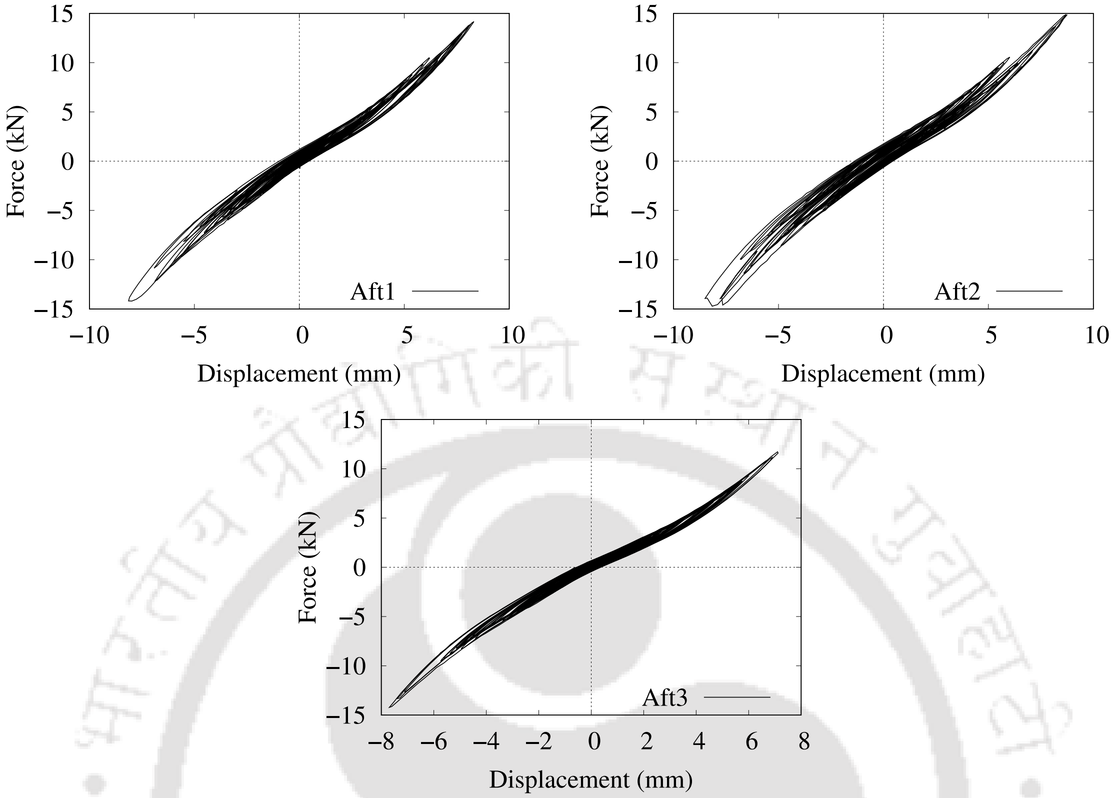

Figure 6.22 Hysteresis curve of the already damaged frame-B2 for pseudo-static testing to inflict damage due to Aft1, Aft2 and Aft3 (20 kN gravity loading)

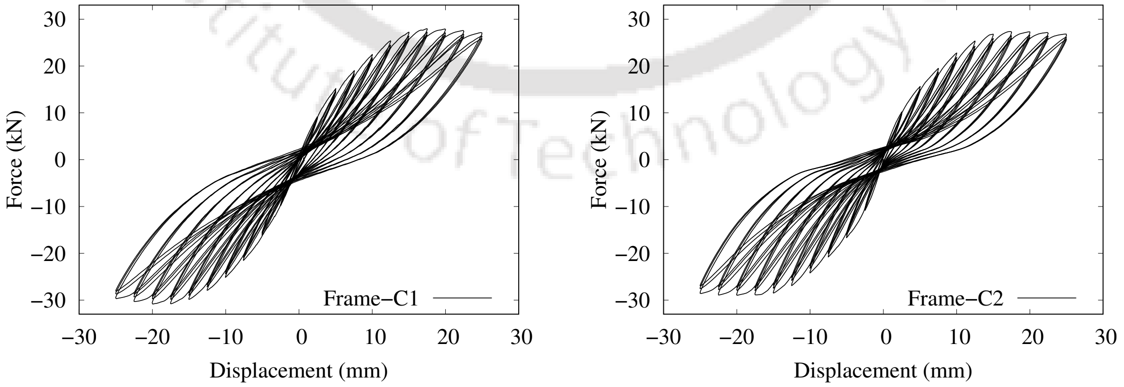

Figure 6.23 Hysteresis curves of frames-C1 and C2 for slow-cyclic testing to inflict main shock damage corresponding to 25 mm lateral displacement (20 kN gravity loading)

Figure 6.24 Damaged frame-C1 due to main shock damage corresponding to 25 mm displacement by slow-cyclic testing (20 kN gravity loading)

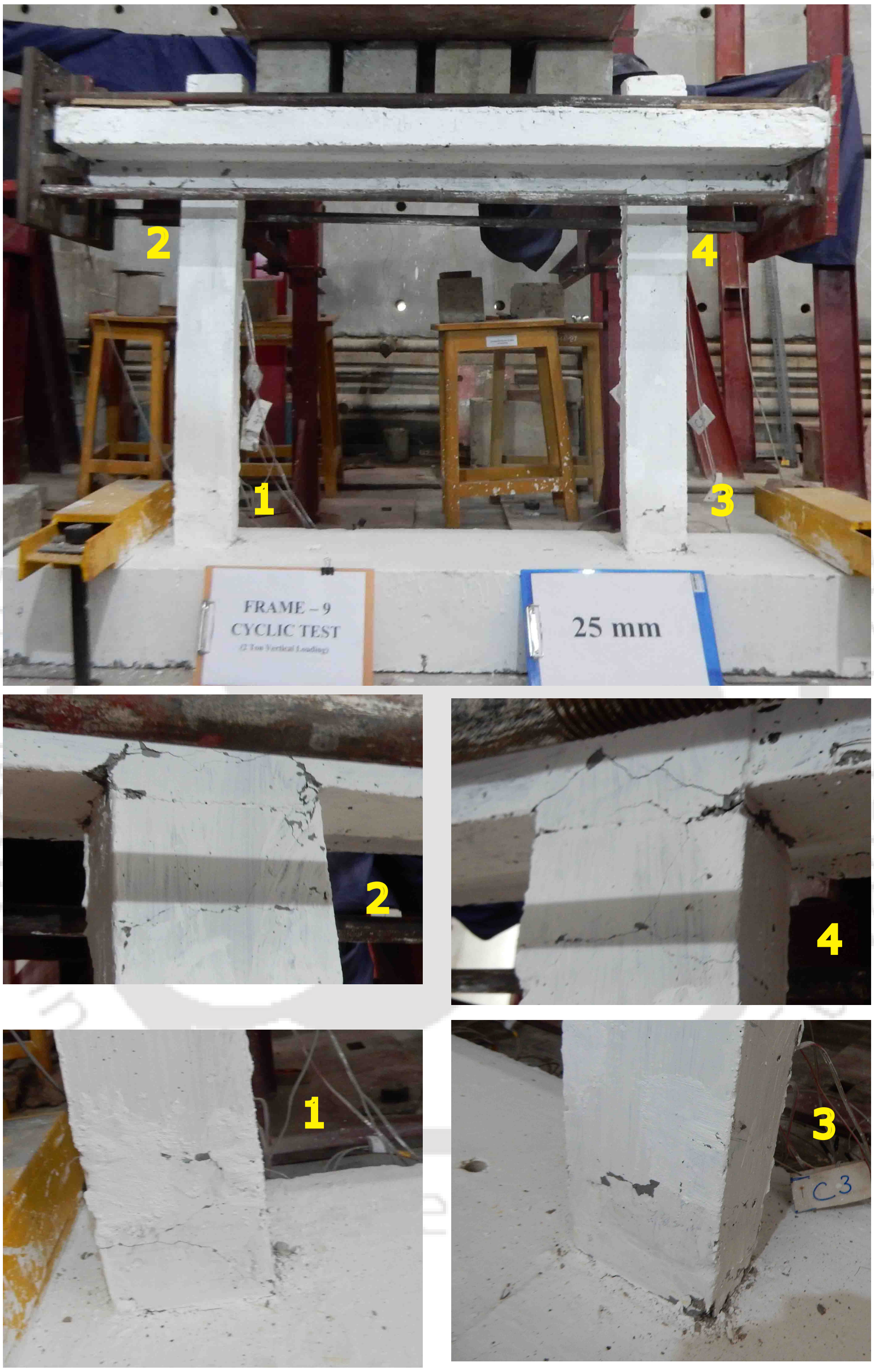

Figure 6.25 Damaged frame-C2 due to main shock damage corresponding to 25 mm displacement by slow-cyclic testing (20 kN gravity loading)

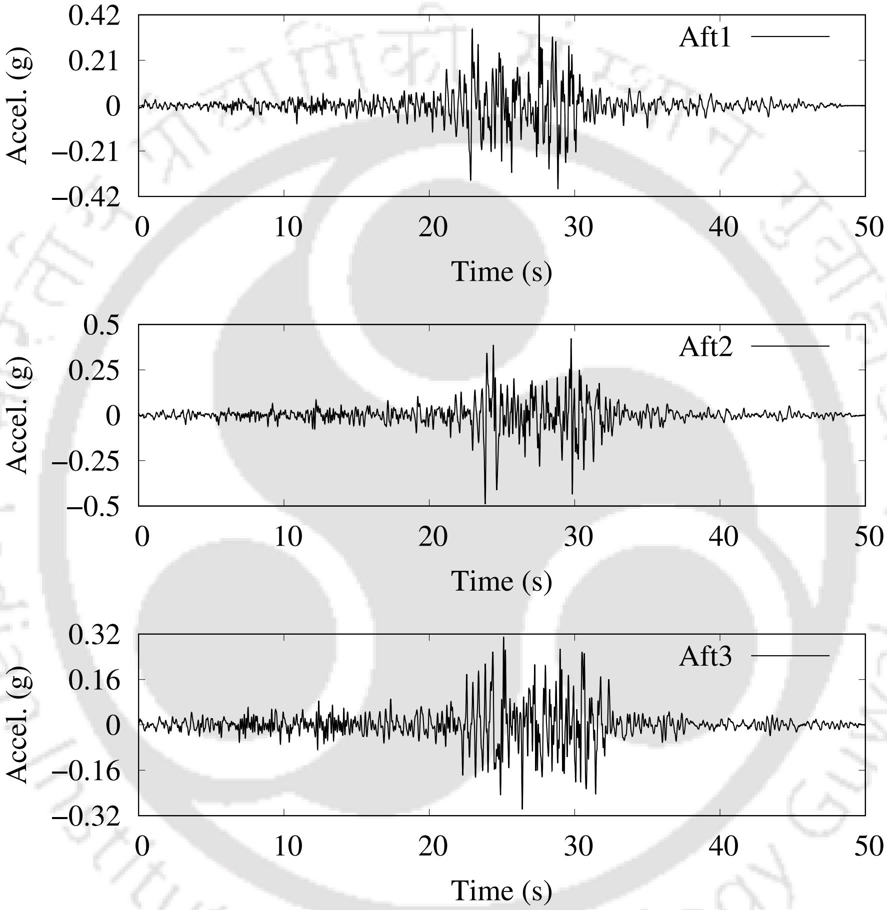

Figure 6.26 Acceleration recorded on the shake table when the damaged frame-C1 tested with Aft1, Aft2 and Aft3 (20 kN gravity loading)

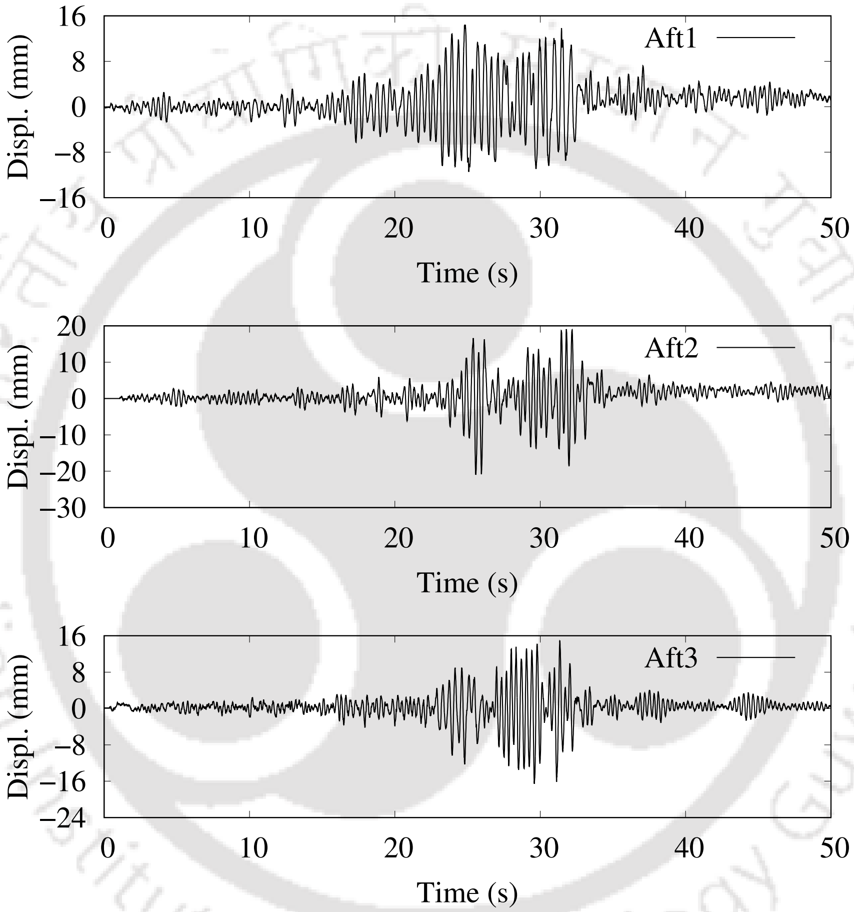

Figure 6.27 Relative Displacement at top of the damaged frame-C1 when tested with Aft1, Aft2 and Aft3 (20 kN gravity loading)

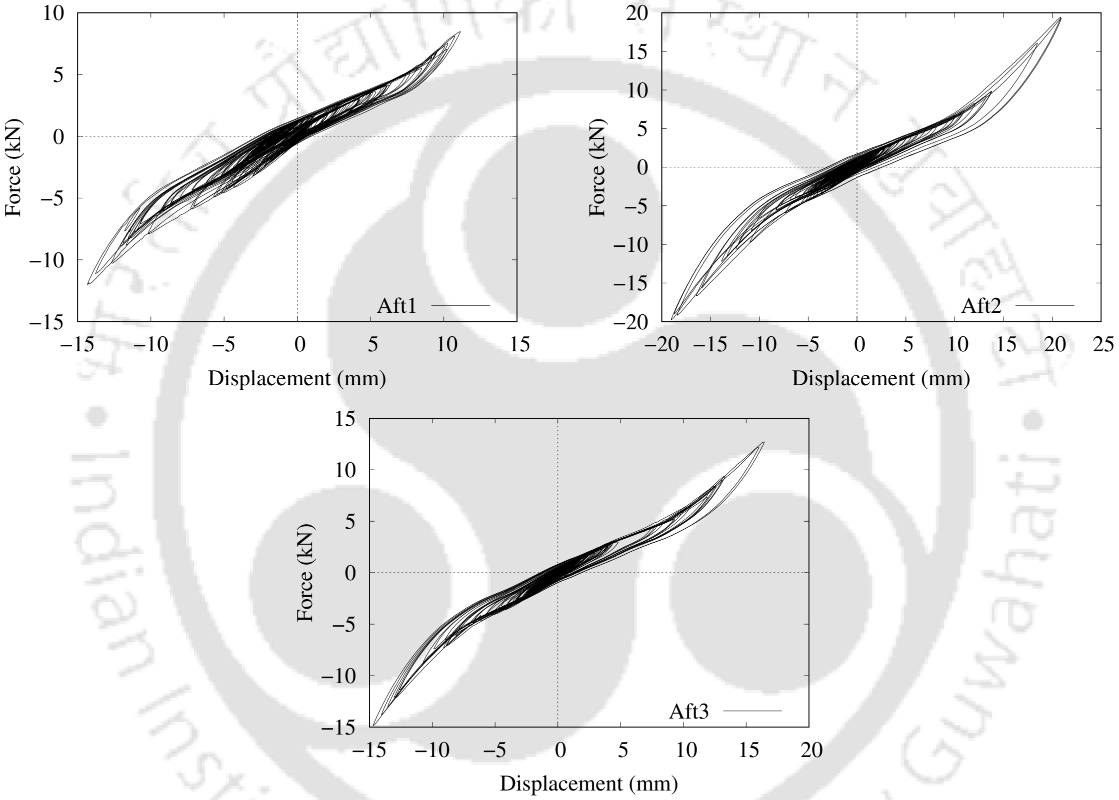

Figure 6.28 Hysteresis curve of the already damaged frame-C2 for pseudo-static testing to inflict damage due to Aft1, Aft2 and Aft3 (20 kN gravity loading)

6.6 Analytical Results

From the force-displacement data and frequency data from different tests, a trend has been observed between the drop in fundamental frequencies of the frame and the cumulative hysteresis energy dissipated. A plot of cumulative hysteresis energy with respect to fundamental frequencies of the structure after each testing stage is shown in Figure 6.29 for 10 kN and 20 kN loading cases and different initial damage cases corresponding to displacement levels of 45 mm, 25 mm and 15 mm. The damage corresponding to 45 mm displacement for 10 kN loading is more which resulted in a considerable drop in the frequency of the structure compared to that corresponding to 15 mm and 25 mm displacement for 20 kN loading. Also, the frequency drop due to all the aftershock ground motions (Aft1, Aft2 and Aft3) is less compared to that due to initial damage inflicted by slow-cyclic testing even for similar amount of hysteresis energy dissipation. This is because the deformation due to the initial damage is higher than that due to the aftershocks even though the hysteresis energy dissipated due to initial damage and all the aftershocks are similar. It has been calculated from the experimental data that the total hysteresis energy dissipated due to all the aftershock ground motions (Aft1 to Aft3) is about 99%, 62% and 12% of the hysteresis energy due to initial damage corresponding to 15 mm (20 kN loading), 25 mm (20 kN loading) and 45 mm (10 kN loading) lateral displacement, respectively. The decrease in percentage between these three cases is due to the relatively lesser increase in hysteresis energy due to all aftershocks compared to the increase in hysteresis energy due to the initial damage because of the same level of PGAs of the three aftershocks used in all the tests. Also, it has been observed, with increasing initial damage, the drop in frequency due to aftershocks also increases, which is seen in Figure 6.29. From the study on the trends of the frequency drop with the cumulative hysteretic energy dissipated, an attempt is made to develop a relation connecting the cumulative hysteretic energy dissipated and the frequency. From Figure 6.29(b) for 20 kN loading case, an exponential trend is observed between the cumulative hysteretic energy and the frequency of the structure, which is not clearly visible for 10 kN loading case due to lesser experimental results. Hence, an exponential form is adopted for the relation as follows

$$f = g_1 f_0 \exp\left[g_2 \sum_{i=1}^{m} \left\{ I_i \left(\frac{E_{H_i}}{F_y x_u} \right) \rho_{axial} \right\} + g_3 \sum_{i=1}^{m} \left\{ I_i \left(\frac{D_i}{x_u} \right) \rho_{axial} \right\} \right] \tag{6.1}$$

Here, m is the maximum number of events present in any sequence (in the present study $m = 4$), I_i is an indicator which is 1 if up to ith event is considered for the purpose of regression (for both coefficient determination and prediction) and is 0 otherwise, f is the frequency at any stage of damage, f_0 is the frequency of the undamaged structure, ρ_{axial} is the axial-load ratio on the columns of the frame specified as percentage, E_{H_i} is the cumulative hysteretic energy dissipated up to ith event, D_i is a measure of size of displacement in hysteresis cycles for the ith event which is determined as 1.5 times the RMS value of the deformations in the hysteresis cycles (the deformations being measured from one end to other end of a hysteresis cycle), F_y is the yield strength of the structure which is obtained from the monotonic force-displacement curve of structure by the method by Park (1988), x_u is the failure displacement of the structure when subjected to monotonic loading, g_1, g_2 and g_3 are the regression coefficients. From regression analysis by least-squares method, the values of g_1, g_2 and g_3 are obtained as 0.8492, -0.1323 and -0.0080, respectively. As expected, the values of g_2 and g_3 are negative, as with increase in energy dissipation and increase in the deformation size, the drop in the fundamental frequency will increase. Though the value of g_1 is close to 1.0 but not 1.0 (as it is supposed to be since for zero hysteresis energy dissipation, the model should estimate the initial fundamental frequency i.e. f_0), the main focus is on the estimation of the frequency of the damaged structure and not the undamaged one. The inclusion of the hysteresis loop size term (D_i) in the model is important, as without this term, the model will estimate the same drop in frequency for a smaller hysteresis loop case and a larger hysteresis loop case, which is not so. The estimated values of frequency from the model for the observed cumulative hysteretic energy dissipated are also plotted in Figure 6.29. It can be seen that the predicted values of frequency are mostly close to observed ones. For Frame-C2, the estimated frequency is a little less compared to that of the observed ones. It needs to be said that, the initial frequency of frames shown in Figure 6.29 for the estimated ones are the observed values and not estimated from the model. As said before, this model is not used for the estimation of initial frequency but the frequency of the damaged structure. The model has been developed using the experimental data for low axial load ratios of 1.5% and 3.0% and hence it is applicable only in these ranges of axial load ratios. Experimental tests are required to be carried out for other axial load ratios to study their effects on the frequency drop. Also, it is possible that a single model which works for a wide range of axial load ratios may not be sufficient i.e. there may be variations in the coefficients with axial load ratios because of which the coefficients may be required to expressed as some function of the axial load ratio.

The experimental data from all the tests are used for the final calibration of the analytical RC frame model separately for 10 kN and 20 kN gravity loading. Figure 6.30 shows the response of the analytical model calibrated with the cyclic pushover curve for 10 kN loading when cyclically loaded upto 45mm. Figure 6.31 shows the response of the analytical model calibrated with the cyclic pushover curve for 20 kN loading when cyclically loaded upto 15mm. Figures 6.32 shows the response of the analytical model calibrated with the cyclic pushover curve for 20 kN loading when cyclically loaded upto 25mm. The analytical models have been also calibrated with the force-displacement data from the pseudo-static test due to Aft1, Aft2 and Aft3. In all the cases, the calibrations have been performed by matching the hysteresis energy of the analytical model with that from the experimental data for each stage of testing. Table 6.1 shows the comparison of the hysteresis energy from the analytical model and the experimental testing for each stage of testing. The calibrated values of the `pinching4` material

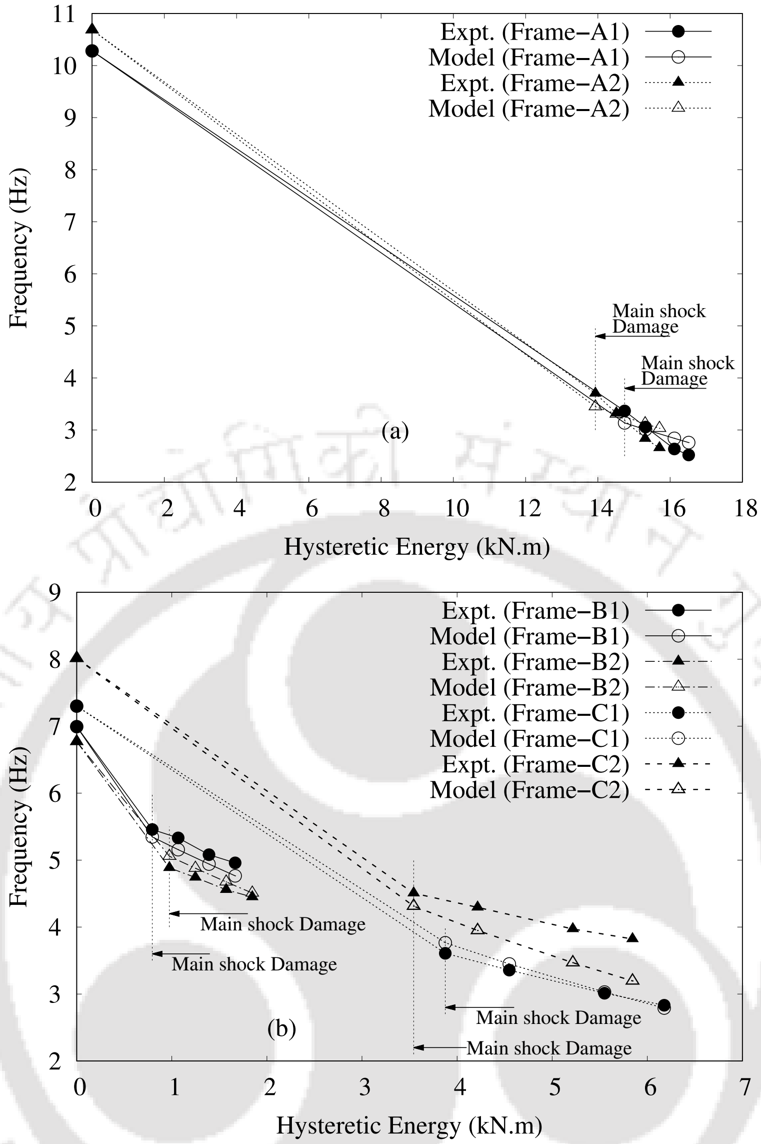

Figure 6.29 Drop in natural frequency of the RC frames with cumulative hysteretic energy dissipated for with (a) 10 kN and (b) 20 kN gravity loadings - experimental (line with solid points) and fitted model (line with hollow points)

model for 10 kN and 20 kN loading cases are shown in tables 6.2 and 6.3, respectively. Also from the calibrated analytical model, *ODI*s at each stage of testing for different gravity loadings and initial damages are calculated which are shown in table 6.4.

The calibration of the analytical model at the material level is advantageous in the sense that this calibrated material can be used in other analytical models of any scale. Usage of the calibrated material models in full-scale structures is beneficial in carrying out comprehensive and rigorous analyses which are difficult and very time-consuming or not possible via experimental testings. In usual practice, analytical models are calibrated against experimental data and the calibrated material models are used in other analytical models which may not be tested experimentally but are subjected to analysis. Similarly, from the analytical models calibrated

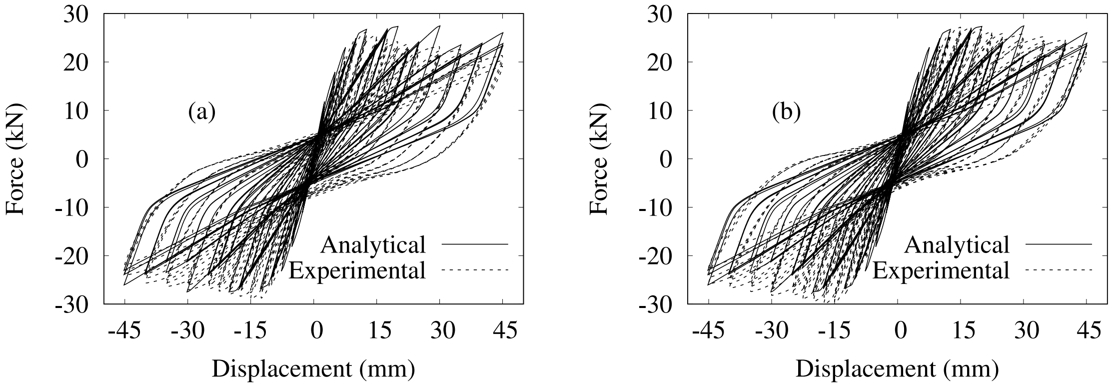

Figure 6.30 Comparison of experimental and analytical cyclic pushover curves of frames (a) A1 and (b) A2 for main shock damage corresponding to 45 mm displacement by slow-cyclic testing (10 kN gravity loading)

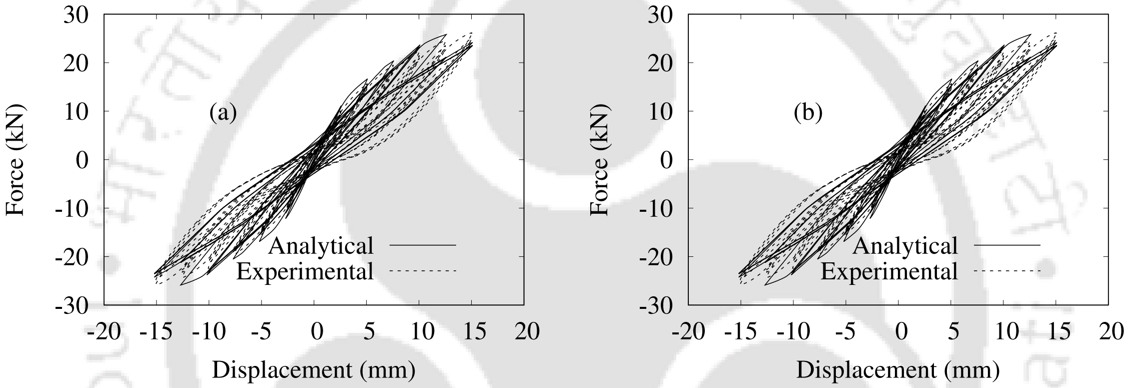

Figure 6.31 Comparison of experimental and analytical cyclic pushover curves of frames (a) B1 and (b) B2 for main shock damage corresponding to 15 mm displacement by slow-cyclic testing (20 kN gravity loading)

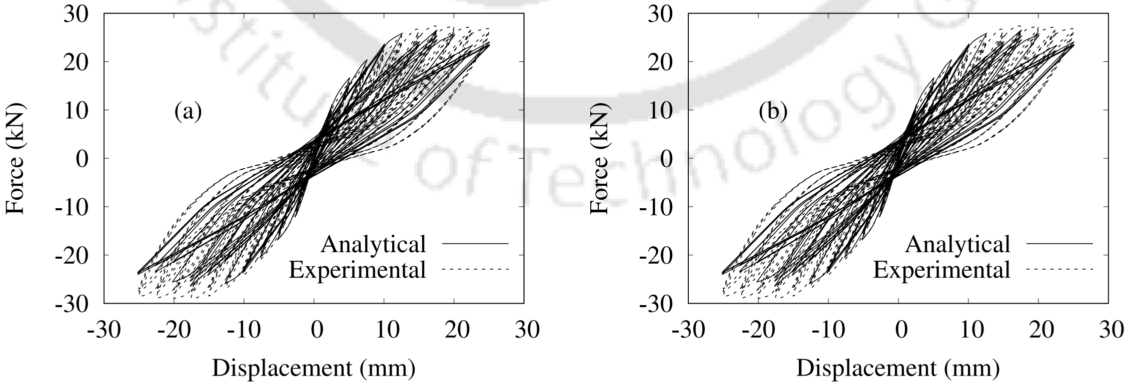

Figure 6.32 Comparison of experimental and analytical cyclic pushover curves of frames (a) C1 and (b) C2 for main shock damage corresponding to 25 mm displacement by slow-cyclic testing (20 kN gravity loading)

Table 6.1 Comparison of the hysteresis energy from the experimental testing and from the calibrated analytical models

Frames	Hysteresis Energy (kN.m)				Cumulative Hysteresis Energy (kN.m)			
	Initial Damage	Aft1	Aft2	Aft3	Initial Damage	Aft1	Aft2	Aft3
A1	14.739	0.579	0.799	0.395	14.739	15.318	16.117	16.512
A2	13.931	0.579	0.799	0.395	13.931	14.510	15.309	15.704
Analytical	12.999	0.403	0.912	0.442	12.999	13.402	14.314	14.756
B1	0.794	0.274	0.324	0.275	0.794	1.068	1.392	1.667
B2	0.974	0.274	0.324	0.275	0.974	1.248	1.572	1.847
Analytical	1.141	0.259	0.271	0.211	1.141	1.400	1.671	1.882
C1	3.876	0.673	1.001	0.628	3.876	4.549	5.550	6.178
C2	3.542	0.673	1.001	0.628	3.542	4.215	5.216	5.844
Analytical	3.921	0.503	0.951	0.576	3.921	4.424	5.375	5.951

Table 6.2 The values of parameters of `Pinching4` model for the calibration of the analytical frame model with 10 kN gravity loading with the experimental data

Envelope Parameters				Parameters Controlling Loading-Reloading Pathway							
Parameter	Values	Param.	Val.	Param.	Val.	Param.	Val.	Param.	Val.	Param.	Val.
ePf1	18.000	eNf1	-18.000	rDispP	0.34	gK1	0.10	gD1	0.30	gF1	0.00
ePf2	35.216	eNf2	-35.216	rForceP	0.40	gK2	0.50	gD2	0.30	gF2	0.00
ePf3	29.977	eNf3	-29.977	uForceP	-0.35	gK3	0.20	gD3	0.10	gF3	0.00
ePf4	29.977	eNf4	-29.977	rDispN	0.34	gK4	0.10	gD4	0.10	gF4	0.00
ePd1	0.00070	eNd1	-0.00070	rForceN	0.40	gKLim	1.00	gDLim	1.00	gFLim	0.00
ePd2	0.00240	eNd2	-0.00240	uForceN	-0.35	gE	10.00				
ePd3	0.03050	eNd3	-0.03050			dmgType	energy				
ePd4	0.05050	eNd4	-0.05050								

Table 6.3 The values of parameters of `Pinching4` model for the calibration of the analytical frame model with 20 kN gravity loading with the experimental data

Envelope Parameters				Parameters Controlling Loading-Reloading Pathway							
Parameter	Values	Param.	Val.	Param.	Val.	Param.	Val.	Param.	Val.	Param.	Val.
ePf1	18.000	eNf1	-18.000	rDispP	0.40	gK1	0.00	gD1	0.00	gF1	0.00
ePf2	36.836	eNf2	-36.836	rForceP	0.50	gK2	1.00	gD2	0.60	gF2	0.00
ePf3	31.977	eNf3	-31.977	uForceP	-0.35	gK3	0.00	gD3	0.00	gF3	0.00
ePf4	29.977	eNf4	-29.977	rDispN	0.40	gK4	0.10	gD4	0.10	gF4	0.00
ePd1	0.00071	eNd1	-0.00071	rForceN	0.50	gKLim	1.00	gDLim	1.00	gFLim	1.00
ePd2	0.00340	eNd2	-0.00340	uForceN	-0.35	gE	10.00				
ePd3	0.00800	eNd3	-0.00800			dmgType	energy				
ePd4	0.05700	eNd4	-0.05700								

Table 6.4 *ODI* values at different stages of testing for different gravity loadings and initial damages calculated from the analytical frame model

Loading	Displacement Level for Main Shock ODI	*ODI*			
		Main shock	Aft1	Aft2	Aft3
10 kN	45 mm	0.926	0.942	0.980	0.998
20 kN	15 mm	0.137	0.147	0.157	0.165
	25 mm	0.349	0.369	0.405	0.427

in the present work, the material model from the analytical model with 20 kN loading is applied in the 1-storey, 2-storey and 5-storey frames considered in Chapter 5. The calibrated material model from the analytical model with 20 kN loading has been taken since it's axial load ratio (3.0%) is closest to the axial load ratios (9% to 18%) in the columns of the 1-storey, 2-storey and 5-storey frames than the 10 kN loading case (1.5% axial load ratio). The periods of 1-storey, 2-storey and 5-storey frames after modelling with the calibrated material model are found to be 0.330 s, 0.463 s and 1.007 s, respectively, which are close to the periods of the frames (0.329 s, 0.460 s and 0.960 s for 1-storey, 2-storey and 5-storey frames, respectively) considered in Chapter 5. The analyses performed in Chapter 5 to develop the design guidelines are repeated on these frames for some sequences to validate the guidelines. Sequence ensembles SEQ12, SEQ18 and SEQ24 have been selected for performing the analyses. From the analysis results, a similar trend in increase in safety with increase in material strength as seen from Tables 5.16 to 5.27 are observed. The average estimates of *ODI* are found to be close to that obtained from previous analyses in Chapter 5. 1-storey, 2-storey and 5-storey frames are found to be safe for all the aftershocks (AS1 to AS4) with respect to average *ODI*, which is also seen in the previous chapter. With respect to maximum *ODI*, 1-storey, 2-storey and 5-storey frames are safe against all the aftershocks of SEQ18 and SEQ24 without any increase in material strength, as observed in previous chapter. 1-storey frame is not safe against any aftershocks of SEQ12 with respect to maximum *ODI* as per current analysis, whereas 1-storey is made safe by 15% increase in strength against all the aftershocks as per the previous analysis. Even then, the percentage decrease in the maximum *ODI* with increase in material strength is found to be similar between these two analyses. 2-storey frame is made safe against all the aftershocks of SEQ12 with respect to maximum *ODI* with 10% increase in material strength which is also seen in the previous chapter. 5-storey frame is safe against all the aftershocks of SEQ12 with respect to maximum *ODI* without any increase in material strength, whereas in the previous analysis, 5-storey frame is made safe with 15% increase in material strength. Inspite of this difference, it is seen from previous analysis that maximum *ODI* for AS4 of SEQ12 on the original 5-storey frame is made from 1.17 to 0.94 with 15% increase in material strength, whereas in the current analysis, this maximum *ODI* is reduced from 0.98 to 0.90. Most importantly, it is observed from the current analysis that the *ODI*s due to main shocks are in the irreparable zone for all the increase in material strengths for the different structures which is also observed in the previous analysis. Although some local differences are observed between the earlier and present results, which may be due to the effect of pinching in the present material model, the general trend observed from the present results is in line with the trend observed in the earlier results. Hence, the results from the present analysis validates the usage of the proposed 10% to 15% additional material safety in arresting the collapse of RC frames against a majority of MASs.

6.7 Summary

In the present study, an experimental study of additional damages due to the aftershocks on already damaged structures is performed. For the experimental study, quarter-scale RC bare frames are constructed. Two loading cases corresponding to 1.5% and 3.0% axial-load ratio are considered in this study to consider structures of different time-periods. The main shock damage in the frame is inflicted by controlled slow-cyclic testing. The effects of the aftershocks on the already damaged frames are studied by testing them against aftershock ground motions via dynamic testing. Due to the inability to obtain hysteresis data of the frame for the aftershock shaking during dynamic testing, an alternate method is attempted to determine the hysteresis data. In this method, a second frame is considered with similar initial undamaged properties as that of the frame used for dynamic testing. The second frame is subjected to the same main shock damage as that of the first frame, but the second frame is subjected to aftershocks by pseudo-static testing with the relative displacements of the first frame due to aftershocks during dynamic testing. The hysteresis data obtained for the second frame for aftershock shaking is considered to be same as that for the first frame. The frequencies of the frames at different stages of the testing are measured by impact-testing or white-noise testing. It is found that the frequencies of the frames at each stage of testing or damage follow an exponential trend with respect to the cumulative hysteresis energy dissipated by the frames. A mathematical model is developed for the estimation of frequencies of the frames at any stage of damage based on the initial frequency of the structure, cumulative hysteresis energy dissipated, axial load ratio and size of displacement cycle. Analytical models of the RC frames for the cases of 1.5% and 3.0% axial load ratios are calibrated with the experimental results. The calibrated material model is used in RC frame models used in the previous chapter for performing analysis to validate the design modification proposed in the previous chapter. Some important conclusions of the present study are as follows.

- The additional damages due to aftershocks increase with the increase in the initial damage of the structures due to main shock.
- A decreasing exponential trend has been observed between the frequencies of the structure at different stages of damage and the cumulative hysteretic energy dissipated.
- The effect of the size of deformations in hysteresis cycles is found to be significant in the reduction of the frequency of the structure, that for similar hysteresis energy dissipation, hysteresis cycles with larger deformation show larger frequency drop compared to that with smaller deformation.
- A mathematical model has been developed for the prediction of natural frequency at the end of any event based on the initial frequency of the structure, cumulative hysteresis energy dissipated, axial load ratio and size of displacement cycle.

- The usage of 10% to 15% additional material safety in design as proposed in the previous chapter to arrest the collapse of RC frames against a majority of MASs has been validated via analysis of RC frames using the calibrated material model.

Chapter 7

CONCLUSIONS

The effects of the aftershocks are not considered in the conventional seismic design of structures due to which structures may withstand the main shock but become weak to resist the successive aftershocks. The main objective of the present work is the investigation of additional damages due to aftershocks on main shock damaged structures and the development of design modification to account for the effects of the aftershocks in the design. A detailed study of the additional damages due to the aftershocks requires an ensemble of aftershocks for a main shock and for some specified scenario of the aftershocks, which may not be available from the recorded database, due to which ground motions are required to be simulated. A simulation technique has been developed wherein an ensemble of scenario-specific ground motions can be simulated via a scaling relationship of frequency-dependent energy arrival curves based on some seismological parameters. A simulation technique has also been developed for the simulation of an ensemble of realistic aftershock ground motions from a recorded main shock ground motion and for some specified scenario of the aftershocks. The main shock-aftershock ground motions simulated using the developed methods have been used for the nonlinear time-history analysis of some building frames which have been designed as per codal provisions, to study the additional damages due to the aftershocks. In addition to the study of the additional damages due to the aftershocks on an analytical level, an experimental study on the additional damages due to aftershocks has also been carried out, for which quarter-scale RC frames have been tested. Finally, some design modification has been proposed to consider the effects of the aftershocks in the design. The major conclusions from the present work are listed below.

- A new method for the simulation of nonstationary ground motion samples, from frequency-dependent instantaneous energy arrivals of wavelet coefficients of recorded motions, based on the Priestley process assumption has been proposed. The ground motion samples simulated from this method show good agreement with recorded motion with respect to the nonstationary characteristics in statistical sense. At the response spectrum level, the minimum and maximum levels of response are able to capture the recorded trend quite satisfactorily. The simulation technique follows Priestley process, thereby ensures that the simulated ground motion ensembles follow zero-mean Gaussian distribution. With respect to different ground motion parameters, their mean from the simulated ensemble are close to those of the recorded motion.

- An empirical scaling model for scenario-specific frequency-dependent instantaneous energy arrival in terms of some seismological parameters has been proposed using which scenario-specific ensembles of ground motions have been simulated, which exhibit expected trends in terms of median PSV and median SMD. Any number of ground motions for a scenario can be simulated using this method, which will be beneficial for performing any scenario-specific statistical analysis. The simulated samples of an ensemble for a scenario show variability in their temporal features as well as in their strengths. In a scenario-specific ensemble, variability in spectral estimates is high whereas the variability in SMD is significantly less.
- A procedure has been further devised to modify the frequency-dependent estimated energy arrival, using the proposed scaling model, so that the simulated ensemble becomes fully compatible, in terms of both median and standard deviation, with any target GMPE. Moreover, the GMPE compatibility algorithm has been found to be capable of producing lognormal distribution of derived PSV spectra, which is desirable when the GMPE for PSV yields lognormal distribution. When GMPE compatible ensemble is simulated for 5% damping PSV spectrum, it is found to be compatible with PSV spectra for damping ratios ranging from 2% to 10%.
- The proposed process-specific simulation of fully nonstationary earthquake ground motions has been improved in view of extraction of deterministic slow-varying modulation, including a shift from the wavelet domain to the decomposed time-history domain for more efficient reconstruction.
- A conditional scaling model for energy arrival curves of aftershocks, from the known preceding main shock, has been proposed from which aftershock ground motions have been simulated. The simulated aftershock ground motion samples show the expected trend against the seismological scenarios.
- The conditional scaling model has been found to perform better than the unconditional scaling model in capturing the recorded response spectra through the 10 and 90 percentile PSV spectra and SMD of simulated motions.
- An approximate version of the conditional scaling model for aftershocks has also been developed for situations when aftershock data are inadequate for carrying out fresh regression analysis for the development of a conditional scaling model. The approximate conditional model produces results comparable to that of a freshly regressed conditional scaling model. Hence, a conditional scaling model, if not an approximate one, should be used in lieu of an unconditional scaling model for better prediction.

- The analytical study has shown that when the largest aftershock (magnitude-wise) is smaller than the main shock by 0.5 or more, single-event-based designed flexible (taller) frames are likely to be safe against collapse. However, for sequences with the largest aftershock smaller than the main shock by 0.3, they cannot withstand the aftershocks, especially for shallower events. Hence, the effects of aftershocks should necessarily be considered in the design of structures.

- The consideration of P-Delta effect in the analysis of structures is crucial for the proper estimation of the additional damages due to the aftershocks. Hence, in any analysis using the main shock aftershock sequences for aftershock damage estimation, P-Delta effect should not be avoided.

- The order in which the aftershocks are arranged in the sequence affects the order of average ODI at the end of each aftershock. Here, the aftershocks are arranged in descending order of their magnitudes, hence the average ODI showing some saturation in increase with the number of aftershocks.

- The time-frequency characteristics of the preceding main shock may play an important role in the future aftershock-induced damage. It was observed that the main shock motion with longer SMD is likely to have higher final ODI in comparison with a main shock motion having smaller SMD.

- It has been found that the consideration of an additional material safety factor of 10–15% in design can make the properly designed RC frames safe against collapse from a large proportion of main shock-aftershock sequences. Hence, in the design of RC frames against main shock-aftershock sequences, the material safety factor with an increase of 10–15% should be used.

- For all material safety factors (10%-20%) considered here, the ODI at the end of main shock is more than 0.4 (irreparable damage), except for a few cases, which indicates that a solution is available through the proposed additional material safety where the design against the main shock will not be too conservative according to the current seismic design philosophy, even for a critical scenario for aftershocks.

- From the experimental study, it is seen that the drop in natural frequency of the structures due to aftershock response increases with the initial damage caused by the main shock. Hence, experimentally it shows that the additional damage due to the aftershocks depends on the initial main shock damage.

- The experimental data showed a decreasing exponential trend between the frequencies of the structure at different stages of damage and the cumulative hysteretic energy dissipated. Also, reduction in the frequency of the structure is found to be affected by the size of the deformations in the hysteresis cycles, i.e., for similar hysteresis energy dissipation, hysteresis cycles with larger deformation show larger frequency drop compared to that with smaller deformation.

- Based on the experimental data, an empirical relationship has been developed for the prediction of natural frequency at the end of any event in the MAS in terms of the initial frequency, cumulative hysteresis energy, axial load ratio and size of displacement cycle.
- The proposed strategy of applying additional material safety factor in design has been validated via analysis of RC frames with the material models that are calibrated using the experimental data. These analyses using the calibrated material models also showed that the ODI due to main shocks are in the irreparable zone for all the material safety factors as observed in the previous analysis of the frames.

Limitations in the present work are list below.

- The analytical study considered only bare frames and the effects of infills on the additional damages due to aftershocks were not considered.
- The model has been developed using the experimental data for low axial load ratios of 1.5% and 3.0% and hence it is applicable only in these ranges of axial load ratios.

Scope of the future work includes the following.

- Scaling models can be developed from ground motion database of different regions to simulate ground motions with different time-frequency characteristics that are not produced by the scaling models developed here. Hence, the time-frequency characteristics of the ground motions may be considered comprehensively for investigating their effects on the additional damages due to the aftershocks.
- Other nonlinear parameters like inter-storey drift, frequency drop etc can be considered in the analytical study to see how these parameters represent the additional damages due to the aftershocks and are sensitive to them.
- Analytical study on the performance of infilled frames against main shock-aftershock sequences can be done to see the effects of infills on the additional damages due to the aftershocks.
- Experimental tests can be carried out for other axial load ratios (other than 1.5% and 3.0%) to study their effects on the frequency drop.

REFERENCES

Abdollahzadeh, G., Mohammadgholipour, A., and Omranian, E. (2019). Seismic evaluation of steel moment frames under mainshock–aftershock sequence designed by elastic design and PBPD methods. *Journal of Earthquake Engineering*, 23(10):1605–1628.

Abrahamson, N. A. (1992). Non-stationary spectral matching. *Seismological Research Letters*, 63(1):30.

Abrahamson, N. A. and Silva, W. (2008). Summary of the Abrahamson & Silva NGA ground-motion relations. *Earthquake Spectra*, 24(1):67–97.

Alarcon, C., Hube, M. A., Jünemann, R., and de la Llera, J. C. (2015). Characteristics and displacement capacity of reinforced concrete walls in damaged buildings during 2010 Chile earthquake. *Bulletin of Earthquake Engineering*, 13(4):1119–1139.

Amadio, C., Fragiacomo, M., and Rajgelj, S. (2003). The effects of repeated earthquake ground motions on the non-linear response of SDOF systems. *Earthquake engineering and structural dynamics*, 32(2):291–308.

Amin, M. and Ang, A. H. S. (1968). Nonstationary stochastic models of earthquake motions. *Journal of the Engineering Mechanics Division*, 94(2):559–584.

Ang, A. H. S. (1988). Seismic damage assessment and basis for damage-limiting design. *Probabilistic Engineering Mechanics*, 3(3):146 – 150.

Atkinson, G. M. and Boore, D. M. (2006). Earthquake ground-motion prediction equations for eastern North America. *Bulletin of the seismological society of America*, 96(6):2181–2205.

Atkinson, G. M. and Goda, K. (2010). Inelastic seismic demand of real versus simulated ground-motion records for cascadia subduction earthquakes. *Bulletin of the Seismological Society of America*, 100(1):102–115.

Atkinson, G. M., Worden, C. B., and Wald, D. J. (2014). Intensity prediction equations for North America. *Bulletin of the Seismological Society of America*, 104(6):3084–3093.

Atzori, S., Tolomei, C., Antonioli, A., Merryman Boncori, J. P., Bannister, S., Trasatti, E., Pasquali, P., and Salvi, S. (2012). The 2010–2011 Canterbury, New Zealand, seismic sequence: multiple source analysis from InSAR data and modeling. *Journal of Geophysical Research: Solid Earth*, 117(B8).

Basha, S. H. and Kaushik, H. B. (2016). Behavior and failure mechanisms of masonry-infilled RC frames (in low-rise buildings) subject to lateral loading. *Engineering Structures*, 111: 233–245.

Basu, B. and Gupta, V. K. (1998). Seismic response of SDOF systems by wavelet modelling of nonstationary processes. *Journal of Engineering Mechanics*, 124(10):1142–1150.

Basu, B. and Gupta, V. K. (2000). Stochastic seismic response of single-degree-of-freedom systems through wavelets. *Engineering Structures*, 22(12):1714–1722.

Boore, D. M. and Atkinson, G. M. (2008). Ground-motion prediction equations for the average horizontal component of PGA, PGV, and 5%-damped PSA at spectral periods between 0.01 s and 10.0 s. *Earthquake Spectra*, 24(1):99–138.

Campbell, K. W. and Yousef Bozorgnia, Y. (2008). NGA ground motion model for the geometric mean horizontal component of PGA, PGV, PGD and 5% damped linear elastic response spectra for periods ranging from 0.01 to 10s. *Earthquake Spectra*, 24(1):139–171.

Campbell, K. W. and Bozorgnia, Y. (2010). A ground motion prediction equation for the horizontal component of cumulative absolute velocity (CAV) based on the PEER-NGA strong motion database. *Earthquake Spectra*, 26(3):635–650.

Caughey, T. K. and Stumpf, H. J. (1961). Transient response of a dynamic system under random excitation. *Journal of Applied Mechanics*, 28(4):563–566.

Cecini, D. and Palmeri, A. (2015). Spectrum-compatible accelerograms with harmonic wavelets. *Computers and Structures*, 147:26–35.

Chan, C. H. and Wu, Y. M. (2013). Maximum magnitudes in aftershock sequences in Taiwan. *Journal of Asian Earth Sciences*, 73:409 – 418.

Conte, J. P. and Peng, B. F. (1997). Fully nonstationary analytical earthquake ground-motion model. *Journal of Engineering Mechanics*, 123(1):15–24.

Das, S. *Aftershock ground motion: characterization and effects on damage-based seismic design*. PhD thesis, Indian Institute of Technology Kanpur, (2009).

Das, S. and Gupta, V. K. (2008). Wavelet-based simulation of spectrum-compatible aftershock accelerograms. *Earthquake Engineering & Structural Dynamics*, 37(11):1333–1348.

Das, S. and Gupta, V. K. (2010). Scaling of response spectrum and duration for aftershocks. *Soil Dynamics and Earthquake Engineering*, 30(8):724–735.

Das, S. and Gupta, V. K. (2011). A wavelet-based parametric characterization of temporal features of earthquake accelerograms. *Engineering Structures*, 33(7):2173–2185.

Das, S. and Hazra, B. (2018). Frequency-dependent principal component analysis of multi-component earthquake ground motions. *Earthquake Engineering and Structural Dynamics*, 47(5):1360–1366.

Das, S., Gupta, V. K., and Srimahavishnu, V. (2007). Damage-based design with no repairs for multiple events and its sensitivity to seismicity model. *Earthquake Engineering and Structural Dynamics*, 36(3):307–325.

De Guzman, P. and Ishiyama, Y. (2004). Collapse assessment of building structures using damage index. In *Proceedings of the 13th WCEE*.

Deodatis, G., Ellingwood, B. R., and Frangopol, D. M. (2014). *Safety, reliability, risk and life-cycle performance of structures and infrastructures*. CRC Press Boca Raton.

Der Kiureghian, A. and Crempien, J. (1989). An evolutionary model for earthquake ground motion. *Structural Safety*, 6(2-4):235–246.

Di Sarno, L. and Amiri, S. (2019). Period elongation of deteriorating structures under mainshock-aftershock sequences. *Engineering Structures*, 196:109341.

Galasso, C., Zareian, F., Iervolino, I., and Graves, R. W. (2012). Validation of ground-motion simulations for historical events using SDoF systems. *Bulletin of the Seismological Society of America*, 102(6):2727–2740.

Goda, K. (2012). Nonlinear response potential of mainshock–aftershock sequences from Japanese earthquakes. *Bulletin of the Seismological Society of America*, 102(5):2139–2156.

Goda, K. (2015). Record selection for aftershock incremental dynamic analysis. *Earthquake Engineering & Structural Dynamics*, 44(7):1157–1162.

Goda, K. and Taylor, C. A. (2012). Effects of aftershocks on peak ductility demand due to strong ground motion records from shallow crustal earthquakes. *Earthquake Engineering & Structural Dynamics*, 41(15):2311–2330.

Gülkan, P., Clough, R. W., Mayes, R. L., and Manos, G. C. (1990). Seismic testing of single-story masonry houses: Part 1. *Journal of Structural Engineering*, 116(1):235–256.

Gupta, V. K., Nielsen, S. R., and Kirkegaard, P. H. (2001). A preliminary prediction of seismic damage-based degradation in RC structures. *Earthquake engineering & structural dynamics*, 30(7):981–993.

Hainzl, S., Christophersen, A., Rhoades, D., and Harte, D. (2016). Statistical estimation of the duration of aftershock sequences. *Geophysical Journal International*, 205(2):1180–1189.

Hartzell, S. H. (1978). Earthquake aftershocks as green's functions. *Geophysical Research Letters*, 5(1):1–4.

Hatzigeorgiou, G. D. and Beskos, D. E. (2009). Inelastic displacement ratios for SDOF structures subjected to repeated earthquakes. *Engineering Structures*, 31(11):2744–2755.

Holzer, T. L. Implications for earthquake risk reduction in the united states from the Kocaeli, Turkey, earthquake of august 17, 1999. Technical report, (2000).

Hu, S., Gardoni, P., and Xu, L. (2018). Stochastic procedure for the simulation of synthetic main shock-aftershock ground motion sequences. *Earthquake Engineering and Structural Dynamics*, 47(11):2275–2296.

Huang, W., Qian, J., and Fu, Q. S. (2012). Damage assessment of RC frame structures under mainshock-aftershock seismic sequences. In *15th World Conference on Earthquake Engineering*. Lisbon, Portugal.

IS 13920. Indian standard code of practice for ductile detailing of concrete structures subjected to seismic forces. Standard, Bureau of Indian Standard, New Delhi, (1993).

IS 1893. Criteria for earthquake resistant design of structures -part 1: General provisions and buildings. Standard, Bureau of Indian Standard, New Delhi, (2002).

IS 456. Plain and reinforced concrete – code of practice. Standard, Bureau of Indian Standard, New Delhi, (2000).

IS 875 (Part I). Code of practice for design loads (other than earthquake) for buildings and structures : Part i dead loads - unit weights of building materials and stored materials. Standard, Bureau of Indian Standard, New Delhi, (1987).

IS 875 (Part II). Code of practice for design loads (other than earthquake) for buildings and structures : Part ii imposed loads. Standard, Bureau of Indian Standard, New Delhi, (1987).

Iyama, J. and Kuwamura, H. (1999). Application of wavelets to analysis and simulation of earthquake motions. *Earthquake Engineering and Structural Dynamics*, 28(3):255–272.

Jeon, J. S., DesRoches, R., Brilakis, I., and Lowes, L. N. (2012). Aftershock fragility curves for damaged non-ductile reinforced concrete buildings. In *15th World Conference on Earthquake Engineering*. Lisbon, Portugal.

Joyner, W. B. and Boore, D. M. (1986). On simulating large earthquakes by green's–function addition of smaller earthquakes. *Earthquake Source Mechanics*, 37:269–274.

Joyner, W. B. and Boore, D. M. (1993). Methods for regression analysis of strong-motion data. *Bulletin of the Seismological Society of America*, 83(2):469–487.

Kamae, K., Irikura, K., and Pitarka, A. (1998). A technique for simulating strong ground motion using hybrid green's function. *Bulletin of the Seismological Society of America*, 88 (2):357–367.

Karabalis, D. L., Cokkinides, G. J., Rizos, D. C., and Mulliken, J. S. (2000). Simulation of earthquake ground motions by a deterministic approach. *Advances in Engineering Software*, 31(5):329–338.

Kaushik, H. B. and Dasgupta, K. (2013). Assessment of seismic vulnerability of structures in Sikkim, India, based on damage observation during two recent earthquakes. *Journal of Performance of Constructed Facilities*, 27(6):697–720.

Kazama, M. and Noda, T. (2012). Damage statistics (summary of the 2011 off the Pacific Coast of Tohoku earthquake damage). *Soils and Foundations*, 52(5):780–792.

Kim, T. H., Lee, K. M., Chung, Y. S., and Shin, H. M. (2005). Seismic damage assessment of reinforced concrete bridge columns. *Engineering Structures*, 27(4):576 – 592.

Kunnath, S. K., Reinhorn, A. M., and Lobo, R. F. IDARC version 3.0: A program for the inelastic damage analysis of reinforced concrete structures. Technical report, Multidisciplinary Center for Earthquake Engineering Research, (1992).

Lee, K. and Foutch, D. A. (2004). Performance evaluation of damaged steel frame buildings subjected to seismic loads. *Journal of Structural Engineering*, 130(4):588–599.

Lee, W. H. K., Shin, T. C., and Wu, C. F. CWB free-field strong-motion data from 30 early aftershocks of the 1999 Chi-Chi earthquake: Processed acceleration data files on CD-ROM, CWB strong-motion data series CD-003. Seismological Observation Center of Central Weather Bureau: Taipei, Taiwan, (2001a).

Lee, W. H. K., Shin, T. C., and Wu, C. F. CWB free-field strong-motion data from three major aftershocks of the 1999 Chi-Chi earthquake: Processed acceleration data files on CD-ROM, CWB strong-motion data series CD-002. Seismological Observation Center of Central Weather Bureau: Taipei, Taiwan, (2001b).

Li, Q. and Ellingwood, B. R. (2007). Performance evaluation and damage assessment of steel frame buildings under main shock–aftershock earthquake sequences. *Earthquake engineering & structural dynamics*, 36(3):405–427.

Li, S., Zuo, Z., Zhai, C., Xu, S., and Xie, L. (2016). Shaking table test on the collapse process of a three-story reinforced concrete frame structure. *Engineering Structures*, 118:156–166.

Li, Y., Song, R., Van de Lindt, J., Nazari, N., and Luco, N. (2012). Assessment of wood and steel structures subjected to earthquake mainshock-aftershock. In *15th world conference on earthquake engineering, Lisbon, Portugal*.

Liang, J. (2005a). Simulation of non-stationary ground motion processes (i). *Acta Seismologica Sinica*, 18(2):226–238.

Liang, J. (2005b). Simulation of non-stationary ground motion processes (ii). *Acta Seismologica Sinica*, 18(3):368–374.

Liang, J., Ray Chaudhuri, S., and Shinozuka, M. (2007). Simulation of nonstationary stochastic processes by spectral representation. *Journal of Engineering Mechanics*, 133(6):616–627.

Lin, Y. Y. and Miranda, E. (2010). Estimation of maximum roof displacement demands in regular multistory buildings. *Journal of Engineering Mechanics*, 136(1):1–11.

Mazzoni, S., McKenna, F., Scott, M. H., Fenves, G. L., and Others. (2005). OpenSees command language manual. *Pacific Earthquake Engineering Research (PEER) Center*.

Miramontes, D., Merabet, O., and Reynouard, J. M. (1996). Beam global model for the seismic analysis of RC frames. *Earthquake Engineering & Structural Dynamics*, 25(7):671–688.

Mukherjee, S. and Gupta, V. K. (2002a). Wavelet-based generation of spectrum-compatible time-histories. *Soil Dynamics and Earthquake Engineering*, 22(9-12):799–804.

Mukherjee, S. and Gupta, V. K. (2002b). Wavelet-based characterization of design ground motions. *Earthquake Engineering and Structural Dynamics*, 31(5):1173–1190.

Mukhopadhyay, S., Das, S., and Gupta, V. K. (2019). Wavelet-based generation of accelerogram-consistent, spectrum-compatible motions: New algorithms and short-period overestimation. *Soil Dynamics and Earthquake Engineering*, 121:327–340.

Nader, M. N. and Astaneh-Asl, A. (1996). Shaking table tests of rigid, semirigid, and flexible steel frames. *Journal of Structural Engineering*, 122(6):589–596.

Nazari, N., Van de Lindt, J. W., and Li, Y. (2015a). Quantifying changes in structural design needed to account for aftershock hazard. *Journal of Structural Engineering*, 141(11):04015035.

Nazari, N., Van de Lindt, J. W., and Li, Y. (2015b). Effect of mainshock-aftershock sequences on woodframe building damage fragilities. *Journal of Performance of Constructed Facilities*, 29(1):04014036.

Neam, A. S. and Taghikhany, T. (2016). Prediction equations for generalized interstory drift spectrum considering near-fault ground motions. *Natural Hazards*, 80(3):1443–1473.

Ordaz, M., Arboleda, J., and Singh, S. K. (1995). A scheme of random summation of an empirical green's function to estimate ground motions from future large earthquakes. *Bulletin of the Seismological Society of America*, 85(6):1635–1647.

Oyarzo-Vera, C. and Chouw, N. (2008). Effect of earthquake duration and sequences of ground motions on structural responses. In *The 10th International Symposium on Structural Engineering for Young Experts*. Changsha, China.

Papadopoulos, A. N., Kohrangi, M., and Bazzurro, P. (2019). Correlation of spectral acceleration values of mainshock-aftershock ground motion pairs. *Earthquake Spectra*, 35(1): 39–60.

Papadrakakis, M., Fragiadakis, M., and Lagaros, N. D. (2011). *Computational methods in Earthquake Engineering*. Springer.

Park, R. (1988). Ductility evaluation from laboratory and analytical testing. In *Proceedings of the 9th world conference on earthquake engineering, Tokyo-Kyoto, Japan*, volume 8, pages 605–616.

Paulay, T. and Priestly, M. J. N. *Seismic Design of Reinforced Concrete and Masonry Buildings*, pages i–xxiii. John Wiley & Sons, Inc., (2009).

Peng, L., Huang, G., Chen, X., and Yang, Q. (2018). Evolutionary spectra-based time-varying coherence function and application in structural response analysis to downburst winds. *Journal of Structural Engineering*, 144(7):04018078.

Priestley, M. B. (1965). Evolutionary spectra and non-stationary processes. *Journal of the Royal Statistical Society. Series B (Methodological)*, 27(2):204–237.

Qin, X. and Chouw, N. (2017). Shake table study on the effect of mainshock-aftershock sequences on structures with sfsi. *Shock and Vibration*, 2017.

Raghunandan, M., Liel, A. B., and Luco, N. (2015). Aftershock collapse vulnerability assessment of reinforced concrete frame structures. *Earthquake Engineering & Structural Dynamics*, 44(3):419–439.

Rezaeian, S. and Der Kiureghian, A. (2008). A stochastic ground motion model with separable temporal and spectral nonstationarities. *Earthquake Engineering and Structural Dynamics*, 37(13):1565–1584.

Rezaeian, S. and Der Kiureghian, A. (2010). Simulation of synthetic ground motions for specified earthquake and site characteristics. *Earthquake Engineering and Structural Dynamics*, 39(10):1155–1180.

Rezaeian, S. and Der Kiureghian, A. (2012). Simulation of orthogonal horizontal ground motion components for specified earthquake and site characteristics. *Earthquake Engineering & Structural Dynamics*, 41(2):335–353.

Rezaeian, S. and Sun, X. (2014). Stochastic ground motion simulation. *Encyclopaedia of Earthquake Engineering*, pages 1–15.

Ruiz-Garcia, J. (2012). Mainshock-aftershock ground motion features and their influence in building's seismic response. *Journal of Earthquake Engineering*, 16(5):719–737.

Ruiz-García, J. and Aguilar, J. D. (2015). Aftershock seismic assessment taking into account postmainshock residual drifts. *Earthquake Engineering & Structural Dynamics*, 44(9):1391–1407.

Ryu, H., Luco, N., Uma, S. R., and Liel, A. B. (2011). Developing fragilities for mainshock-damaged structures through incremental dynamic analysis. In *Ninth Pacific Conference on Earthquake Engineering, Auckland, New Zealand*.

Shokrabadi, M., Burton, H. V., and Stewart, J. P. (2018). Impact of sequential ground motion pairing on mainshock-aftershock structural response and collapse performance assessment. *Journal of Structural Engineering*, 144(10):04018177.

Song, R., Li, Y., and van de Lindt, J. W. (2014). Impact of earthquake ground motion characteristics on collapse risk of post-mainshock buildings considering aftershocks. *Engineering Structures*, 81:349–361.

Spanos, P. D. and Failla, G. (2004). Evolutionary spectra estimation using wavelets. *Journal of Engineering Mechanics*, 130(8):952–960.

Spence, R. and D'Ayala, D. (1999). Damage assessment and analysis of the 1997 Umbria-Marche earthquakes. *Structural engineering international*, 9(3):229–233.

Stavridis, A., Koutromanos, I., and Shing, P. B. (2012). Shake-table tests of a three-story reinforced concrete frame with masonry infill walls. *Earthquake Engineering & Structural Dynamics*, 41(6):1089–1108.

Stone, W. C. and Taylor, A. W. Seismic performance of circular bridge columns designed in accordance with AASHTO/CALTRANS standards. Technical report, US Department of Commerce, National Institute of Standards and Technology, (1993).

Takewaki, I., Moustafa, A., and Fujita, K. (2012). *Improving the earthquake resilience of buildings: the worst case approach*. Springer Science & Business Media.

Tang, W. H. and Ang, A. H. S. (2007). *Probability Concepts in Engineering: Emphasis on Applications to Civil and Environmental Engineering*. Wiley.

Trifunac, M. D. and Brady, A. G. (1975). A study on the duration of strong earthquake ground motion. *Bulletin of the Seismological Society of America*, 65(3):581–626.

Trifunac, M. D. and Lee, V. W. (1989). Empirical models for scaling pseudo relative velocity spectra of strong earthquake accelerations in terms of magnitude, distance, site intensity and recording site conditions. *Soil Dynamics and Earthquake Engineering*, 8(3):126–144.

Trifunac, M. D. and Lee, V. W. (1990). Frequency dependent attenuation of strong earthquake ground motion. *Soil Dynamics and Earthquake Engineering*, 9(1):3–15.

Tso, W. K., Zhu, T. J., and Heidebrecht, A. C. (1993). Seismic energy demands on reinforced concrete moment-resisting frames. *Earthquake Engineering & Structural Dynamics*, 22(6): 533–545.

Twigden, K., Li, X., Ali, M., Oyarzo-Vera, C., and Chouw, N. (2010). Effect of harmonic excitation sequences on structures. In *2010 NZSEE Conference*. Auckland,New Zealand.

Twigden, K. M., Oyarzo-Vera, C. A., and Chouw, N. (2011). Experimental study of earthquake sequence effect on structures. In *Proceedings of the Ninth Pacific Conference on Earthquake Engineering*. Auckland, New Zealand.

Wen, W., Zhai, C., Ji, D., Li, S., and Xie, L. (2017). Framework for the vulnerability assessment of structure under mainshock-aftershock sequences. *Soil Dynamics and Earthquake Engineering*, 101:41–52.

Wen, W., Zhai, C., and Ji, D. (2018). Damage spectra of global crustal seismic sequences considering scaling issues of aftershock ground motions. *Earthquake Engineering & Structural Dynamics*, 47(10):2076–2093.

Williams, M. S. and Sexsmith, R. G. (1995). Seismic damage indices for concrete structures: a state-of-the-art review. *Earthquake spectra*, 11(2):319–349.

Yamamoto, Y. and Baker, J. W. (2013). Stochastic model for earthquake ground motion using wavelet packets. *Bulletin of the Seismological Society of America*, 103(6):3044–3056.

Yamane, Y., Nagano, M., Hida, T., and Tanuma, T. (2016). Height-wise distribution of maximum interstory drift angles in super high-rise rc buildings based on earthquake response analysis models for structural design. *AIJ Journal of Technology and Design*, 22(50):93–98.

Žarnić, R., Gostič, S., Crewe, A. J., and Taylor, C. A. (2001). Shaking table tests of 1:4 reduced-scale models of masonry infilled reinforced concrete frame buildings. *Earthquake engineering & structural dynamics*, 30(6):819–834.

Zembaty, Z., Kowalski, M., and Pospisil, S. (2006). Dynamic identification of a reinforced concrete frame in progressive states of damage. *Engineering Structures*, 28(5):668 – 681.

Zhai, C. H., Wen, W. P., Chen, Z., Li, S., and Xie, L. L. (2013). Damage spectra for the mainshock-aftershock sequence-type ground motions. *Soil Dynamics and Earthquake Engineering*, 45:1–12.

Zhai, C. H., Wen, W. P., Li, S., Chen, Z., Chang, Z., and Xie, L. L. (2014). The damage investigation of inelastic SDOF structure under the mainshock-aftershock sequence-type ground motions. *Soil Dynamics and Earthquake Engineering*, 59:30–41.

Zhao, B., Taucer, F., and Rossetto, T. (2009). Field investigation on the performance of building structures during the 12 May 2008 Wenchuan earthquake in China. *Engineering Structures*, 31(8):1707–1723.

LIST OF PUBLICATIONS

International Journals

- V.L. Nithin, Das, S., and Kaushik, H. B. (2017). Wavelet-based simulation of scenario-specific nonstationary accelerograms and their GMPE compatibility, *Soil Dynamics and Earthquake Engineering*, 99, 56-67.
- V.L. Nithin, Das, S., and Kaushik, H. B. Stochastic simulation of fully nonstationary aftershock ground motions from known preceding main shock, *Soil Dynamics and Earthquake Engineering* (Accepted).
- V.L. Nithin, Das, S., and Kaushik, H. B. Seismic safety of RC frames against main shock-aftershock sequences (To be submitted).
- V.L. Nithin, Das, S., and Kaushik, H. B. Experimental study of damage in RC frames due to main shock aftershock sequence (To be submitted).

International Conferences

- V.L. Nithin, Das, S., and Kaushik, H. B. (2017) Seismic scenario specific ground motion simulations consistent with ground motion prediction equation, *16th World Conference on Earthquake Engineering*, Paper No. 2143, Santiago, Chile.
- V.L. Nithin, Das, S., and Kaushik, H. B. (2020) Stochastic conditional simulation of aftershock accelerograms given the parent main shock motion, *17th World Conference on Earthquake Engineering*, Sendai, Japan (Abstract accepted).